



Substrate functionalization with functional particle patterns

DOCTORAL THESIS

by

Qaiser Ali Khan

Institute of Chemistry of New Materials
University of Osnabrück

Supervisor: Prof. Dr. Martin Steinhart

Date: January 2022

Osnabrück

The doctoral thesis is submitted to partially fulfill the requirements for
'Doctor rerum naturalium' degree

Presented by Qaiser Ali Khan; Date of birth: 02.04.1991

to the Institute of Chemistry of New Materials, University of Osnabrück

1st Reviewer: Prof. Dr. Martin Steinhart

2nd Reviewer: Prof. Dr. Markus Haase

Acknowledgments

First of all, I would like to thank Prof. Dr. Martin Steinhart for his advice, great discussions, support, and being available almost all of the time. I am also very thankful for giving me the opportunity to join the ERC project 646742 INCANA and help with my Ph.D. research.

I would like to thank Prof. Dr. Joachim Wollschläger for the fruitful discussions about magnetic stamping and characterizations. Many thanks to Kevin Ruwisch for measurements with the vibrating-sample magnetometer and Jannis Thien for X-ray photoelectron spectroscopy measurements and analysis. I am very grateful to Dr. Karsten Küpper for conducting specialized XPS measurements, discussion about magnetic stamping, and his support.

I would like to thank Prof. Dr. Artur Erbe, Dr. Anna Eichler-Volf, Dr. Larysa Baraban and Yara Alsaadawi, from Helmholtz-Zentrum Dresden-Rossendorf (HZDR) for their support and the collaboration in several projects during this research work.

I would like to thank Prof. Dr. Yogendra Kumar Mishra for providing Zinc-oxide tetrapods, his fruitful discussions, and measurements of samples with a Helium ion microscope at the Mads Clausen Institute, University of Southern Denmark.

I am also very thankful to Prof. Dr. Dirk Enke and Alexander Grimm for nitrogen sorption measurements at the Institute of Chemical Technology at Universität Leipzig.

I would like to thank Prof. Dr. Markus Haase for his support and examination of my doctoral thesis. Jonas Klein's technical support for QCM measurements is gratefully acknowledged. I would like to thank Dr. Karsten Kömpe and Kerstin Rucker for their assistance with UV-Vis spectroscopy and FTIR measurements. I am also very thankful to Dr. Marius Ciobanu for discussing titania mesoporosity.

Many thanks to the most important people, Claudia Heß, Christine Schulz-Köbel, Brigitte Hartmann-Azanza, and Heinrich Tobergte, for their assistance in getting familiar with different devices and support. Many thanks to Barbara Gunkel for all her wonderful support and help with administrative issues.

A big thanks to all my colleagues for their help, support, and knowledge. Thank you so much Dr. Mercedes Runge, Dr. Michael Philippi, Fernando Vázquez-Luna, Markus Geuß, Ruža Periz, Wajiha Akram, and Fatih Alarслан. Many thanks to Dr. Helmut Schäfer for helping me from time to time with the XRD device and characterization.

Last but not least, I would like to heartfully thank my parents, family, and wife Elizbit for their continuous help, unconditional support, and encouragement.

Table of Contents

1 Introduction	1
2 State-of-the-art	4
2.1 Fabrication of patterned surfaces	5
2.1.1 Self-assembly of particles into patterned surfaces	7
2.2 Fundamentals of wettability on surfaces	8
2.2.1 Wetting on smooth surfaces	8
2.2.2 Wetting on rough surfaces	10
2.3 Surface modifications of patterned surfaces for modification of wetting properties	11
2.3.1 Switchable water wettability	12
2.3.1.1 Switchable wettability of titania (TiO ₂)	13
2.4 Janus particles/membranes	15
2.4.1 Fabrication of Janus particles/ membranes	15
2.4.1.1 Phase separation	16
2.4.1.2 Masking	16
2.4.1.3 Self-assembly	17
2.5 Fabrication of ring-like structures	18
2.6 Contact printing (CP)	20
2.7 Soft nanoimprint lithography (NIL)	25
3 Experimental	26
3.1 Materials and methods	27
3.1.1 Materials	27
3.1.2 Chemicals	27
3.1.3 Methods	28
3.1.3.1 Scanning electron microscopy (SEM)	28
3.1.3.2 Atomic Force Microscopy (AFM)	28
3.1.3.3 Contact angle measurements	29
3.1.3.4 X-ray photoelectron spectroscopy (XPS)	29

3.1.3.5 Nitrogen sorption measurements	29
3.1.3.6 Quartz crystal microbalance (QCM)	30
3.1.3.7 Vibrating-sample magnetometer (VSM)	30
3.1.3.8 Other instrumentations	30
3.1.4 Size and shape analysis	31
3.2 Procedures	32
3.2.1 Preparation of substrates and template surfaces	32
3.2.1.1 Preparation of FTO substrates	32
3.2.1.2 Preparation of silicon (Si) substrates	32
3.2.1.3 Silanization of macroporous silicon (mSi)/silicon (Si) substrate	32
3.3 Syntheses and Fabrication methods	33
3.3.1 Topographically patterned TiO ₂ substrates as a platform for wetting metamaterials	33
3.3.1.1 Fabrication of the PDMS secondary mold	33
3.3.1.2 Synthesis of titania (TiO ₂) sol-gel precursor solutions	33
3.3.1.3 Fabrication of patterned holey TiO ₂ films	34
3.3.1.3.1 Self-assembly of SiO ₂ microparticles inside TiO ₂ macropores	35
3.3.1.3.2 Surface chemistry of self-assembled SiO ₂ microparticles	35
3.3.1.3.3 Switchable water wettability	37
3.3.2 Site-selective orthogonal modifications of SiO ₂ microparticles in PS- <i>b</i> -P2VP and PS- <i>b</i> -P4VP substrates	39
3.3.2.1 Fabrication of patterned PS- <i>b</i> -P2VP and PS- <i>b</i> -P4VP substrates	39
3.3.2.1.1 Modification of infiltrated SiO ₂ microparticles inside PS- <i>b</i> -P2VP or PS- <i>b</i> -P4VP macroporous substrates	39
3.3.3 Fabrication of hollow microrings	43
3.3.3.1 Synthesis of titania (TiO ₂) sol-gel solution	43
3.3.3.2 Synthesis of chitosan-graphene oxide (CS-GO) hydrogel	43
3.3.3.3 Synthesis of gold (Au) precursor solution	43
3.3.3.4 Fabrication of hollow chitosan (CS)/CS-GO microrings	44
3.3.3.5 Fabrication of hollow titania (TiO ₂) microrings	45
3.3.3.6 Fabrication of hollow gold (Au) microrings	45
3.3.4 Magnetic induced insect-inspired capillary nanostamping (MA-IICN)	46
3.3.4.1 Synthesis of zinc oxide tetrapods (T-ZnO)	46

3.3.4.2 Fabrication of zinc oxide tetrapod (T-ZnO) pellets _____	46
3.3.4.3 Fabrication of PS- <i>b</i> -P2VP/T-ZnO porous composite stamps _____	47
3.3.4.3.1 Fabrication of PS- <i>b</i> -P2VP/T-ZnO porous composite stamps with a tip-like contact surface (TC) _____	47
3.3.4.3.2 Fabrication of PS- <i>b</i> -P2VP/T-ZnO porous composite stamps with holey contact surfaces (HC) _____	49
3.3.4.4 Stamping procedure _____	49
3.3.4.4.1 Stamp holder _____	49
3.3.4.4.2 Stamping process _____	50
3.3.4.4.2.1 Setup I _____	52
3.3.4.4.2.2 Setup II: _____	53
3.3.4.4.2.3 Setup III: _____	54
3.3.4.4.2.4 Setup-IV: _____	55
4 Topographically patterned TiO₂ substrates as a platform for wetting metamaterials ____	56
4.1 Patterned TiO₂ holey films _____	57
4.1.1 Self-assembly of SiO ₂ microparticles inside TiO ₂ holey films (<i>p</i> TiO ₂ _SiO ₂ template) _____	61
4.1.1.1 Surface Chemistry of <i>p</i> TiO ₂ _SiO ₂ templates _____	62
4.1.1.1.1 Adsorption of hydrophobic molecules on <i>p</i> TiO ₂ _SiO ₂ templates _____	62
4.1.1.1.2 PS- <i>b</i> -P2VP polymeric rods in <i>p</i> TiO ₂ _SiO ₂ templates _____	66
4.1.1.1.3 Gold metallic layer on SiO ₂ microparticles in <i>p</i> TiO ₂ _SiO ₂ templates ____	67
4.2 Applications _____	68
4.2.1 Water wettability _____	68
4.2.1.1 Switchable water wettability _____	74
4.2.1.1.1 Reversible wettability switching by the adhesively bonded tape method	74
4.2.1.1.2 Wettability Switching by heat treatment _____	76
4.2.1.2 Water droplet evaporation dynamics _____	80
5 Site-selective modification of SiO₂ microparticles in macroporous-nanoporous substrates	87

5.1 Fabrication of PDMS stamps _____	88
5.2 Fabrication of PS-<i>b</i>-P2VP and PS-<i>b</i>-P4VP macroporous-nanoporous substrates	89
5.2.1 Self-assembly of SiO ₂ microparticles inside porous block copolymer substrates _	90

5.2.1.1 Site-selective orthogonal modifications of SiO ₂ microparticles inside PS- <i>b</i> -P2VP with gold and K ₂ Cr ₂ O ₇	91
5.2.1.2 Site-selective orthogonal modifications of SiO ₂ microparticles inside PS- <i>b</i> -P4VP with 1-dodecanethiol and APTES	92
6 Hollow microrings by a one-step direct imprinting method	95
6.1 Fabrication of PDMS secondary mold	96
6.2 Fabrication of hollow microrings	96
6.2.1 Chitosan (CS) and chitosan-graphene oxide (CS-GO) hydrogel microrings	96
6.2.1.1 Morphological characterization of chitosan (CS) hydrogel microrings	99
6.2.1.2 Morphological characterization of chitosan-graphene oxide (CS-GO) hydrogel microrings	102
6.2.2 Fabrication of titania (TiO ₂) microrings	105
6.2.2.1 Morphological characterization of titania (TiO ₂) microrings	106
6.2.3 Fabrication of Gold (Au) microrings	111
6.2.3.1 Morphological characterization of gold (Au) microrings	111
6.3 Self-assembly of SiO₂ microparticles inside hollow microrings of TiO₂	115
6.4 Self-assembly of SiO₂ microparticles in hollow microrings of Au	116
7 Magnetic assisted insect-inspired capillary nanostamping (MA-IICN)	117
7.1 Design of stamps	118
7.1.1 PDMS secondary mold	118
7.1.2 Zinc oxide tetrapods (T-ZnO)	119
7.1.3 PS- <i>b</i> -P2VP/T-ZnO porous composite stamp with tip contact surfaces (TC)	120
7.1.4 PS- <i>b</i> -P2VP/T-ZnO porous composite stamp with holey contact surfaces (HC)	125
7.1.5 Stamping of magnetic nanoparticle model inks	127
7.1.5.1 Setup I	129
7.1.5.2 Setup II	131
7.1.5.2.1 In-plane magnetic field	133
7.1.5.2.2 Out-of-plane magnetic field	134
7.1.5.2.2.1 Effect of external magnetic field	134
7.1.5.2.2.2 Stamping by tip contact surfaces (TC) composite stamps	136
7.1.5.2.2.3 Stamping by holey contact surfaces (HC) composite stamps	141

7.1.5.3 Setup III	144
7.1.5.3.1 In-plane magnetic field	145
7.1.5.3.2 Out-of-plane magnetic field	146
7.1.5.3.2.1 Effect of external magnetic field	146
7.1.5.3.2.2 Stamping by tip contact surface (TC) composite stamps	147
7.1.5.3.2.3 Stamping by holey contact surface (HC) composite stamps	152
7.1.5.4 Setup IV	155
7.1.5.4.1 Out-of-plane magnetic field	156
7.1.5.4.2 In-plane magnetic field	158
7.1.5.4.2.1 Effect of magnetic field exposure time	158
7.1.5.4.2.2 Effect of external magnetic field	159
7.1.5.4.2.3 Stamping by tip contact surface (TC) composite stamps	160
8 Conclusion	165
9 References	169
10 Appendix	183
10.1 List of abbreviations	183
10.2 List of publications	185
10.3 Curriculum vitae	186
10.4 Declaration	187

1 Introduction

Colloidal particles can be deposited on smooth [1, 2] or on topographically patterned substrates to generate various particle patterns and structures.[3]

On the one hand, various methods have been developed for generating particle patterns on smooth surfaces, including dip-coating,[4] nanosphere lithography,[5] particle transfer printing (pTP),[6], and capillary stamping.[7] Printing dispersions of nanoparticle inks is associated with many challenges; for example, nanoparticles tend to agglomerate and form clusters due to high surface energies.[8] Well-defined printed patterns may result from an appropriate combination of substrate and ink characteristics.[8] Schmidt *et al.*[7] reported capillary stamping with continuous pore network silica stamps with a spongy mesoporous system. Several particulate inks, including nanodiamonds and fullerenes nanoparticles, were printed on smooth surfaces.

On the other hand, topographically patterned holey substrates can be precisely filled with monodisperse colloidal particles for modifying the structure of materials' surfaces.[3, 9, 10] This substrate modification is crucial for many practical applications, e.g., sensing and catalysis, as well as the use of the modified substrates as replicative masks and templates for replication molding.[11, 12]. Many different methods have been used to self-assemble colloidal particles on topographically patterned surfaces.[10, 13-16]

The modification of the surfaces of the particles themselves is an additional approach to further functionalize substrates modified with particle patterns and plays a significant role in modern materials science.[17] Surface modifications of nano and microparticles self-assembled in patterns on surfaces are complex and require further research.[17] Various site-specific modification techniques were developed for the fabrication of Janus particles (J.P.s)/membranes (J.M.s) and patchy particles.[17-21] The current state-of-the-art approaches are limited to specific materials, size limitations, and tedious fabrication procedures.[22]

The aim of this thesis is the development of functional particle patterns on substrates to modify the properties and functions of the substrates. Two classes of model substrates are fabricated;

(1) topographically patterned surfaces, in which microparticles of different sizes are deposited, and (2) smooth substrate surface, patterned by printing the magnetic nanoparticle aggregates.

(1) Topographically patterned model substrates are prepared by replication molding.

(i) Patterned Titania (TiO_2) substrates patterned with macropores are modified by the self-assembly of silica (SiO_2) microparticles with different sizes inside the macropores. Different routes are applied to modify the surface chemistry of self-assembled SiO_2 microparticles inside the TiO_2 macropores. By silica microparticle deposition and modification of the latter, the wettability of the macroporous TiO_2 is reversibly switched from the hydrophobic state to a persistent super-hydrophilic state and *vice versa*. For wettability switching from hydrophilic to hydrophobic, the infiltrated self-assembled SiO_2 particles can be detached from the macropores. Heating the substrates results in wettability switching from hydrophobic to hydrophilic. High adhesion of water droplets to patterned TiO_2 and all modified patterned TiO_2 substrates having SiO_2 microparticles is observed in all hydrophobic states, and even upon tilting and vigorously moving the substrates, the droplets remain strongly pinned. The evaporation dynamics of water droplets are studied on all modified surfaces, including sessile water droplet shape evolution during evaporation.

ii) In the second example for topographically patterned surfaces, poly(styrene-*block*-2-vinyl pyridine) PS-*b*-P2VP and poly(styrene-*block*-4-vinyl pyridine) PS-*b*-P4VP macroporous substrates are fabricated. SiO_2 microparticles are deposited inside the macroporous-nanoporous substrates for site-selective orthogonal modifications to fabricate Janus particles. The top surface and the bottom surface of the SiO_2 microparticles can be modified independently due to the nanoporous fine structure of the macroporous block copolymer substrates.

iii) Smooth substrates are structured with hollow microrings of chitosan (C.S.), chitosan-graphene oxide (CS-GO), gold (Au), and TiO_2 to generate the third example of a topographically patterned surface. The microrings of TiO_2 are exemplarily used as confinement structures for SiO_2 microparticles. SiO_2 microparticles are also self-assembled around Au microrings. This research aims to replicate high-quality

microstructures of different materials under specific imprint pressure and thermal treatment. The main advantage of this method is a single-step process, reproducibility, simplicity, and applicability for many different materials.

SiO₂ microparticles with different sizes are deposited in macroporous patterned substrates using the simple spin-coating method for functional applications in all topographically patterned surfaces, including TiO₂, block-copolymer substrates (PS-*b*-P2VP and PS-*b*-P4VP), and microrings (TiO₂ and Au). The SiO₂ microparticles self-assembled on patterned substrates are modified either selectively, or the whole surface of the desired substrate is modified.

(2) The study of the second model system aims at improvements of magnetic nanoparticle deposition onto smooth model substrates. A capillary stamping approach combined with external permanent magnetic fields or electromagnets is realized to print magnetic nanoparticle-based inks on smooth substrates. The stamping of magnetic nanoparticles is developed as a model embodiment for magnetic assisted insect-inspired capillary nanostamping (MA-IICN). The external magnetic field is applied to the substrate to print magnetic nanoparticle aggregates. For this purpose, a porous composite stamp consisting of zinc oxide tetrapods (T-ZnO) as an ink reservoir system attached to a topographically patterned PS-*b*-P2VP stamping layer is developed. Magnetic Fe₃O₄ nanoparticles are printed with the help of PS-*b*-P2VP/T-ZnO stamps with either tip contact surface (round or square-shaped) or with holey contact surfaces having round or square-shaped holes. The significant advantages of the method include overcoming the tedious printing of nanoparticles, the need for re-inking steps, and the simplicity of the method.

2 State-of-the-art

2.1 Fabrication of patterned surfaces

Patterned surfaces have been fabricated with different methods, for example, electrostatic powder spraying,[23] sol-gel syntheses,[24] self-assembly processes,[25] template methods,[26] soft lithography,[27] hot embossing lithography,[28] and direct imprinting.[29] Direct imprinting has been widely used to fabricate various micro-and nanostructures consisting of oxides.[30-32] The sol-gel method is the most established route for inorganic coatings because of its simplicity, low cost, and ease to control. Templating methods are the easiest and reproducible way to fabricate desired patterns, either positive or negative replicas of the templates.[33] The substrate-based manufacturing processes can be classified into three main groups: additive, subtractive, and structuring manufacturing technologies (Figure 2-1).[34] Additive manufacturing includes screen printing, lithographic printing, and offset printing methods commonly used in industries. The stamp is first inked with a material of interest, following contact of the inked stamp to a counter substrate, and releasing the stamp generates a pattern on the target substrate.[35] The subtractive transfer method involves the deposition of a continuous ink layer on a donor substrate, following stamp contact with donor surface, which selectively removes material in the areas of contact.[35] In the laser ablation or photolithography method, the deposited material is removed from the substrate to generate patterns. Imprinting, wetting/de-wetting, or bonding technologies fall in structuring technologies.[35] The imprint resist cured by heat during imprinting generating structure on substrates.[36]

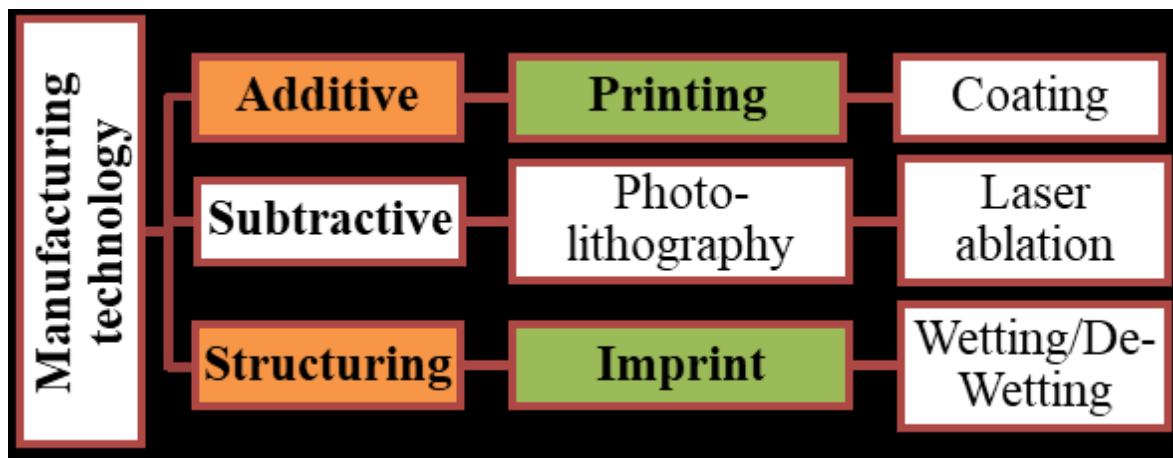


Figure 2-1 Classification scheme of substrate-based manufacturing technologies.

Fabrication of patterned surfaces received significant attention due to their use in various applications. For example, a micropatterned metal current collector film on a flexible graphene substrate enhanced supercapacitors' electrochemical performance.[37] Patterned polydimethylsiloxane films were used as optical strain sensors,[38] and micro/nanostructure Ti-6Al-4V surfaces patterned by pulsed lasers were used as antireflective coatings with an average reflectance of 3.1%.[39] Patterned poly(lactic-co-glycolic acid) electrospun nanofibrous films were surface-modified with bFGF, a basic fibroblast growth factor (bFGF), and 3,4-dihydroxyphenylalanine (DOPA) and used for wound healing.[40] Micro/nanostructured aluminum was employed as an oil-triggered surface for switchable wettability.[41] Figure 2-2 shows the list of different top-down approaches and the typical length scales.[42]

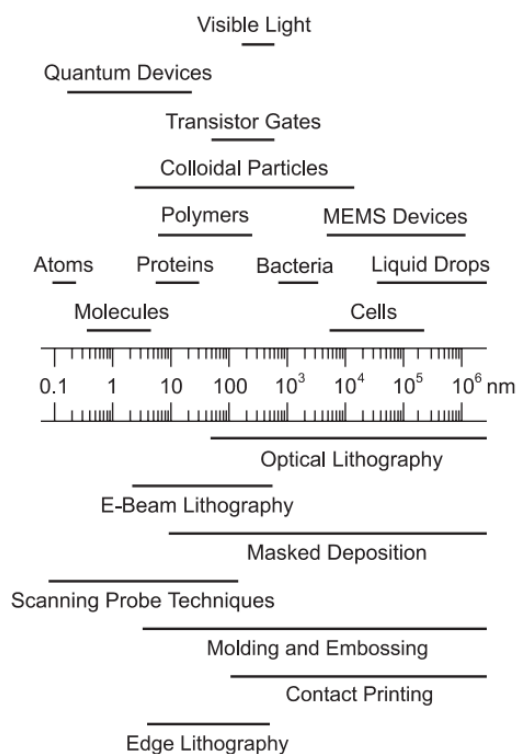


Figure 2-2 A list of top-down methods for patterning (below the scale) and the range of specific natural and artificial object dimensions (above the scale). It was adapted with permission from ref,[42] copyright 2004 WILEY-VCH Verlag GmbH & Co. KGaA, Weinheim.

2.1.1 Self-assembly of particles into patterned surfaces

Self-assembly of colloidal particles on topographically patterned surfaces has been broadly investigated for many practical applications, for example, as replicative masks or templates in mold replication methods such as soft lithography, hot embossing, and nanoimprinting.[11] Patterned holey substrates can be filled with monodisperse particles for modifying the structure of material surfaces, as studied by many researchers.[3, 9, 10] Yu *et al.*[13] reported a self-assembly approach based on physical confinement and templating monodisperse polystyrene (PS) beads within a packing cell composed of two glass substrates. Xia *et al.*[43] showed different arrangements (monomer, dimer, hexagon, square, and pentagon) of PS beads arranged in surfaces patterned with cylindrical holes by simply controlling the ratio of diameter and depth of holes in patterned arrays. Stelling *et al.*[44] reported electrostatic modeling of substrate for controlled placement of PS particles into Au nanohole arrays. Deying *et al.*[10] used a spin-coating method to assemble SiO₂ nanoparticles in cylindrical holes and nanoscale grooves. SiO₂ particles with ≈ 80 nm diameter were assembled in cylindrical holes and in grooved silicon patterned wafers. Nanoparticles tend to agglomerate, and guiding nanoparticles into precise locations is a challenging task. Asbahi *et al.*[14] reported a dip-coating technique to position sub-10 nm particle clusters in ordered arrays. Wittenberg *et al.*[15] reported a preparation technique called “squeegee” for settling monodisperse silica (SiO₂) beads coated with lipid bilayers into microwells of a silicon wafer. Miele *et al.*[16] showed self-organization of gold nanoparticles inside nanochannels by using simulations (atomistic molecular dynamics, MD) and live self-assembly behavior using in-situ liquid-cell transmission electron microscopy (LC-TEM).

Different forces are exerted on colloidal microparticles, e.g., contact force, electrostatic force, van der Waals force, hydrodynamic force, and capillary force (Figure 2-3).[45] Fujita *et al.*[45] used an immersed free surface (IFS) simulation model to simulate the drying of a colloidal solution on a substrate. Immersion capillary forces, which are attractive forces exerted between the spheres, may result in physical contact among microparticles. Meniscus-induced force plays the primary role in arranging and placing microparticles into macropores. Capillary forces among particles facilitate physical contact, and meniscus meniscus-induced force plays the primary role in arranging and placing particles into pores. Essential factors for the process

of ordering inside macropores can be due to immersion capillary forces and hydrodynamic flux.[45-48] Landau-Verwey-Overbeek (DLVO) numerical modeling is the most used theory to investigate the interactions on the shape of the patterns left by evaporated drops.[48]

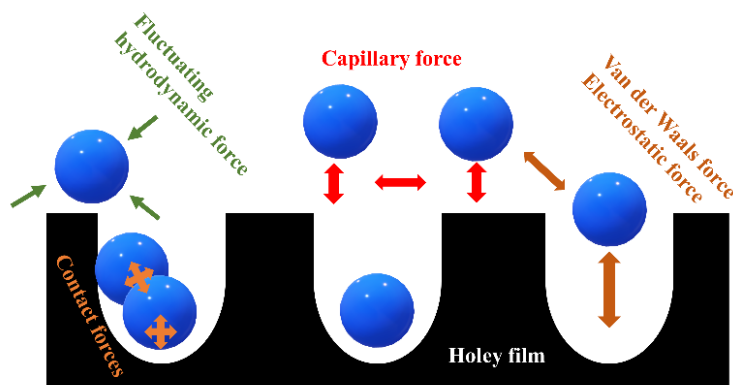


Figure 2-3 Schematic illustration of forces exerted on colloidal microparticles, which results in the confinement of microparticles inside holey arrays.

2.2 Fundamentals of wettability on surfaces

2.2.1 Wetting on smooth surfaces

Wettability is an important property, and applications related to wettability play an essential part in nature and technology.[49-51] The hydrophobic surface properties of lotus leaves,[52] lady's mantle leaves,[53] and hydrophilic surface properties of *Ruellia devosiana*,[54] Spanish moss,[54] and *Artemisia tridentate* [55] have been known for a longer time. Inspired by their surface structures, many researchers replicated different functional material structures for their use in practical applications.[56-60]

Generally, the macroscopic water contact angle has been used to evaluate the wettability of surfaces.[60] When a drop of a liquid impinges on a surface, either the liquid spreads entirely over the surface, showing a continuous increase in the radius of the area enclosed by the three-phase (solid, vapor, and liquid) contact line or a sessile drop of liquid settles on the surface, and the three-phase contact line advances only up to a finite contact radius. As the radius of a drop grows beyond the capillary length $l_c = \sqrt{\gamma_{LV}/\rho g}$, [61] where γ_{LV} is liquid-vapor

interfacial tension, ρ is liquid density, and g is the gravitational acceleration, the shape of the drop changes to a “pancake” shape of constant thickness, and the main driving force is now gravity. Both van der Waals and electrostatic forces determine whether a given surface is wettable or non-wettable by a given fluid. If surface charges are absent, van der Waals forces are responsible in both cases for the mode, in which fluids spread over a solid surface, and the wetting films' equilibrium thickness.[62] The disjoining pressure $\Pi_d = -dg_t/d_h$ is the force per unit area, obtained as the derivative of $-g_t$ with respect to the distance. Where g_t is the total Gibbs energy of interaction, and h is the distance between the surfaces of the semi-infinite plates.[63] The van der Waals interaction includes all intermolecular interactions, i.e., dipole-dipole, dipole-induced dipole, and induced dipole-induced dipole interactions. The so-called Hamaker constant A in $\Pi_d = A/6\pi l^3$ gives the amplitude of the interactions. Where l is the thickness of liquid film on a solid substrate. In repulsive cases, where the film tends to thicken, the $A > 0$.[62]

The spreading parameter $S = \gamma_{SV} - \gamma_{SL} - \gamma_{LV}$ controls the thermodynamic wettability of the surface. Where: γ_{SL} , γ_{SV} , and γ_{LV} are the solid-liquid, solid-vapor, and liquid-vapor interfacial tensions, respectively. When S is negative, a drop with a finite contact angle θ (Young's angle) is formed in the equilibrium. If S is positive, the equilibrium state corresponds to the spontaneous spreading of the liquid (contact angle is zero).[64] Three types of wetting usually occur upon liquid contact to a solid surface. Total wetting ($S \geq 0$), partial ($S < 0$), and pseudo-partial wetting ($S < 0$).[65] Complete wetting relates to a microscopically thick layer of liquid absorbed at the surface, and the equilibrium spreading coefficient is zero. If a drop of liquid settles on a surface, the contact angle value can be quantitatively calculated using Young's Equation 2-1.[62, 66]

$$\cos \theta = (\gamma_{SV} - \gamma_{SL}) / (\gamma_{LV}) \quad \text{Equation 2-1}$$

Three surface tensions are involved upon liquid drop contact on a solid surface: γ_{SL} , γ_{SV} , γ_{LV} , respectively, the solid-liquid, solid-vapor, and liquid-vapor surface tensions (Figure 2-4a). The surface tensions here are defined when the solid, liquid, and gas phases are in mechanical equilibrium with each other.[62]

In this case, the solid-vapor interface tension is now equal to the sum of the solid-liquid and liquid-vapor tensions.[62] The pseudo-partial wetting regime, also characterized by $A < 0$ is the combination of a non-zero Young contact angle at the macro scale and a zero microscopic

contact angle. The presence of an ultra-thin liquid film across the main drop indicates a microscopic zero contact angle.[67]

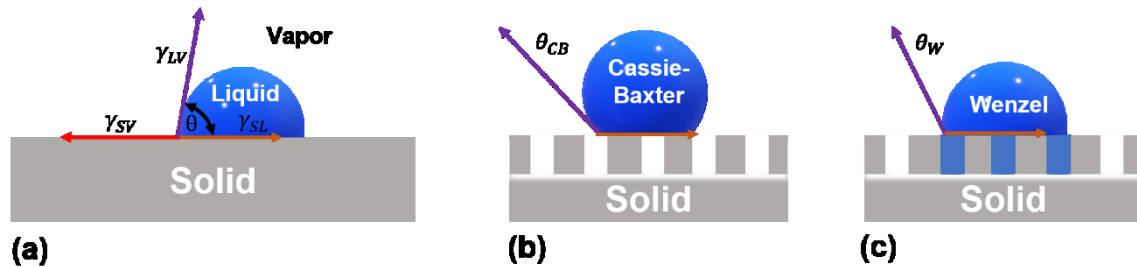


Figure 2-4 Schematic diagram of a liquid drop on a solid flat surface, Young's law a), Cassie-Baxter state, in which a drop of liquid on substrate stays suspended on top and does not penetrate surface asperities b), and the Wenzel state where the liquid penetrates the asperities of the surface. θ , θ_{CB} and θ_W are Young's, Cassie-Baxter, and Wenzel's contact angles, respectively.

2.2.2 Wetting on rough surfaces

The liquid droplets act differently on different surfaces; Wenzel showed that a droplet of liquid on a rough surface might form contact with the entire exposed surface area of the rough surface (Figure 2-4c) and form a sessile droplet with a smooth liquid-vapor interface.[68] Young's equation was thus modified by introducing the surface roughness factor, r , defined by the ratio of the actual solid-liquid contact area and its projection onto a flat plane (Equation 2-2).

$$\cos \theta_W = r \cos \theta \quad \text{Equation 2-2}$$

Whereas in the Cassie-Baxter case,[69] a liquid does not penetrate the hollow of the grooved surface (Figure 2-4b) as shown in Equation 2-3.[70]

$$\cos \theta_{CB} = f_1 \cos \theta_1 + f_2 \cos \theta_2 \quad \text{Equation 2-3}$$

Where f_1 and f_2 are area fractions with contact angles of θ_1 and θ_2 of a binary composite surface. The Cassie-Baxter regime is often applied for chemically patterned surfaces [71], and the Wenzel regime is often applied for patterned topographical surfaces.[72] Both the Wenzel

and the Cassie-Baxter state are based on the consideration of the contact area between the liquid and solid affecting the contact angle. However, it has been reasoned by Gao and McCarthy [73] that three-phase contact lines alone are essential in determining wettability, and the interfacial area within the contact boundary is irrelevant. Many other findings support McCarthy's arrangements. For example, Bartell [74] discussed that contact angles are not altered by surface irregularities at the bottom of the droplet, Extrand *et al.*[75] discussed that the contact angle is controlled by a three-phase structure at the contact line, not the liquid-solid interface underneath the droplet. Wenzel's and Cassie's models corroborate the notion that the interfacial free energies and the contact area are essential for determining wettability. However, Gao and McCarthy [73] argued that the contact areas are not crucial in determining wettability.

2.3 Surface modifications of patterned surfaces for modification of wetting properties

To manipulate wettability, surface free energy, roughness, chemical composition, porosity, surface chemistry, tension, and surface charges are the governing properties to be considered.[76] Figure 2-5 shows the wettability alteration of liquids due to surface energy of substrate surface and liquid surface tension changes. Specific surface treatments of substrates can be done to increase the surface-free energy. Change in surface chemistry has a strong influence on surface energy change.[76]

Depending on the application, patterned surfaces can be modified by different methods to make them either (super) hydrophilic or (super) hydrophobic. For wettability transitions, changing the chemistry of patterned surfaces with different molecules (hydrophobic or hydrophilic) is a commonly used surface modification method.[77-79] Zhen *et al.*[77] showed the superhydrophobicity (water contact angle, WCA $\approx 160.6^\circ \pm 1.5^\circ$) of patterned aluminum (Al) surfaces via the nanosecond laser ablation process, after chemical modification with (heptadecafluoro-1,1,2,2-tetradecyl) triethoxysilane. Reiner *et al.*[78] showed hydrophobicity (WCA $\approx 120.6^\circ \pm 3.2^\circ$) of a silicon wafer with regular patterns of spikes fabricated by X-ray lithography. The silicon patterned specimen was hydrophobized with Au-thiol (1-hexadecanethiol). Chao-

Hua *et al.*[79] fabricated hydrophobic cotton fibers via polyhedral oligomeric silsesquioxane (POSS) based polymers grafting on the fiber's surface.

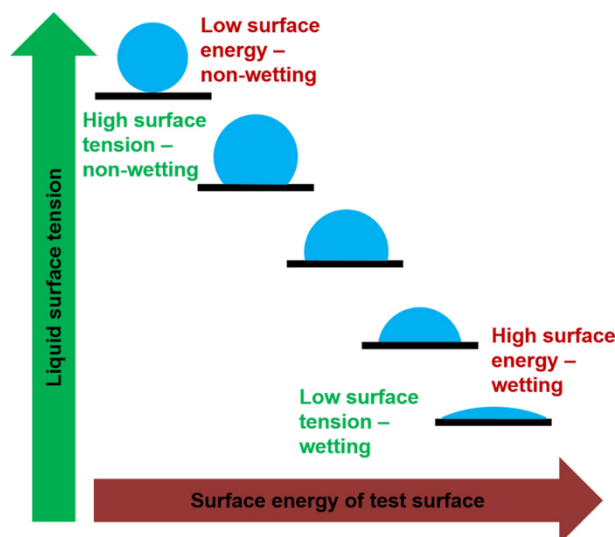


Figure 2-5 Change in wettability due to surface energy of test surface and liquid surface tension. It is adapted with permission from the ref,[76] Springer Science+Business Media, LLC, part of Springer Nature 2020.

2.3.1 Switchable water wettability

Switchable wettability has attracted enormous attention and interest in academia, for it is possible to use in practical applications.[80, 81] Different methods have been established to design surfaces, which respond to external stimuli for wettability switching. Temperature, electric potential, UV light, pH values, and magnetic fields are external stimuli used for switching between wetting states.[82] Among these stimuli, light has gained much interest because of advantages, such as non-contamination of the surface, non-contact, and remote control of the stimulus.[83] After the discovery of ultraviolet (UV) light-induced photocatalytic activity of TiO_2 , [84, 85] the wettability of various metal oxides (TiO_2 , ZnO , SnO , WO_3 , V_2O_5 , CeO_2 , CuO , MoO_3 , Fe_2O_3 , Cr_2O_3 , and In_2O_3) was investigated.[86]

2.3.1.1 Switchable wettability of titania (TiO₂)

Titanium dioxide (TiO₂) has received enormous attention and interest in academia, especially its synthesis and physical properties. Titania is used as a paint pigment, electrochromic material, self-cleaning coating, antifogging coating, photocatalyst, photovoltaics, and electrical energy storage material.[87] Many studies deal with TiO₂ surface wettability and reversible transition between hydrophobic and hydrophilic properties.[88-90]

The contact between liquids and solid surfaces is ubiquitous. It underlies a broad range of physical phenomena as well as and technical processes. For example, sessile droplets, which can be immobilized on topographically patterned substrates,[91] have received significant interest as chemical and biological assays.[91] In this context, two phenomena are of relevance: surface wettability and evaporation.[92] The manipulation of surface wettability by surface patterning attracts ongoing interest, but a predictive understanding of the interplay between wettability and surface patterning has remained premature.[93-96] Wettability management is, nevertheless, being considered as an important property of functional surfaces.[97] Other efforts were directed to the minimization of the wettability of surfaces.[98] Evaporation management is likewise important.[99] Limiting cases for the evaporation of sessile droplets are the constant contact radius (CCR) mode and the constant contact angle (CCA) mode.[100] If the evaporating liquid contains non-volatile components, ring-like deposits (“coffee rings”)[101] form at the positions of three-phase gas-liquid-solid contact lines if a sessile droplet evaporates in the CCR mode. It is, for example, desired to suppress the formation of coffee rings when volatile components of droplets deposited by inkjet printing evaporate.[102] On the other hand, the formation of coffee rings has intentionally been exploited to pattern substrates.[103] Frequently observed stick-slip motions of the gas-liquid-solid contact line of evaporating sessile droplets have been interpreted as a sequence of CCR (stick) and CCA (slip) phases.[104] Many studies have reported TiO₂ surface wettability and reversible transition between hydrophobic and hydrophilic nature.[88-90] The surface roughness and pore morphology could affect the surface wettability of mesoporous TiO₂ films.[105]

The switching of superhydrophobic to a superhydrophilic state can be done with continuous illumination of the TiO₂ surface with UV light and usually takes at least a few hours.[106] Zhou *et al.*[107] showed the transition from super-hydrophobic to super-hydrophilic under UV irradiation and reversible switching to super-hydrophobic by placing the sample in the dark at 60 °C. Yunlu *et al.*[108] described switchable super-wettability of TiO₂ nanoparticles modified

with a 1H,1H,2H,2H-perfluorooctyl(trimethoxy)silane (PFOS) coating. In this study, the transition of super-hydrophobic (water contact angle, WCA $\approx 165^\circ$) to super-hydrophilic (water contact angle, WCA $\approx 0^\circ$) was triggered by exposure to UV irradiation, followed by heating at 120 °C for 90 mins to gain reversible hydrophobicity. UV irradiation and heating were repeated for 5-10 cycles until the surface did not transit back to a superhydrophobic state. Kobayashi *et al.*[109] reported the combined use of UV light and direct current bias voltage to make wettability switching time from the hydrophobic to the hydrophilic state short. 1/10th shortened the switching time between these two states compared to TiO₂ thin films subjected only to UV irradiation. Besides the limitation of continuous illumination of UV light for maintaining the hydrophilic state, some other challenges include the loss of wettability switching due to microstructural changes. Kang *et al.*[110] reported the combination of shape memory polymers and UV-irradiation of TiO₂ nanoparticles, which shows excellent responsivity between superhydrophobicity and superhydrophilicity. The need for continuous UV light illumination for maintaining hydrophilic properties restricts the use of TiO₂ films for practical applications due to the lack of UV illumination in the dark or during rainy seasons, where the hydrophobic properties recover.[111] Gan *et al.*[112] reported multilayer assembly of TiO₂ nanoparticle and polyethylene glycol (PEG) for non-UV activated superwetting characteristics. Here the authors reported that hydrophilic characteristics of the TiO₂ film were preserved even after 15 cycles of continuous drying and wetting; however, the continuous drying and wetting affect the superhydrophilic quality of the film and destroy the superhydrophilic characteristics. The other drawback is the need for a higher number of multilayer coatings requirements to achieve superhydrophilic characteristics.

The continuous UV light illumination for hydrophilic property restricts the use of TiO₂ film for practical applications due to the lack of UV illumination in the dark or raining seasons. The dark and longer rainy seasons result in the recovery of hydrophobic properties and hence impede the practical application of TiO₂ films.[111] Therefore, considering this limitation, many research groups have explored the persistent hydrophilicity of TiO₂ film without using UV light.[113, 114] However, these all works focused on the non-reversible wettability of TiO₂ surfaces without UV. It has remained challenged to fabricate TiO₂ based films with switchable wettability without any external stimuli (i.e., UV light) and a film with a persistent super-hydrophilic state for practical applications.

2.4 Janus particles/membranes

Janus particles (J.P.s)/membranes (J.M.s) are particles or membranes that have two sides with different chemical or physical properties. In recent years J.P.s and J.M.s have attracted advanced research attention for their use in many different application areas, including catalysis, electrochemical sensors applications, biomedicine, and use as stabilizers.[115] Various morphologies of J.P.s have been designed and prepared, including dumbbell-shapes,[116] disk-shapes,[117] rod-shapes,[118] cones,[119] and mushroom-shapes.[120]

2.4.1 Fabrication of Janus particles/ membranes

For producing the combination of two different properties on single particles/membranes, for example, hydrophilicity and hydrophobicity or some other physiochemical properties, various site-specific modification techniques were developed. Three major categories for the fabrication of Janus particles are phase separation, masking techniques, and self-assembly (Figure 2-6).[18]

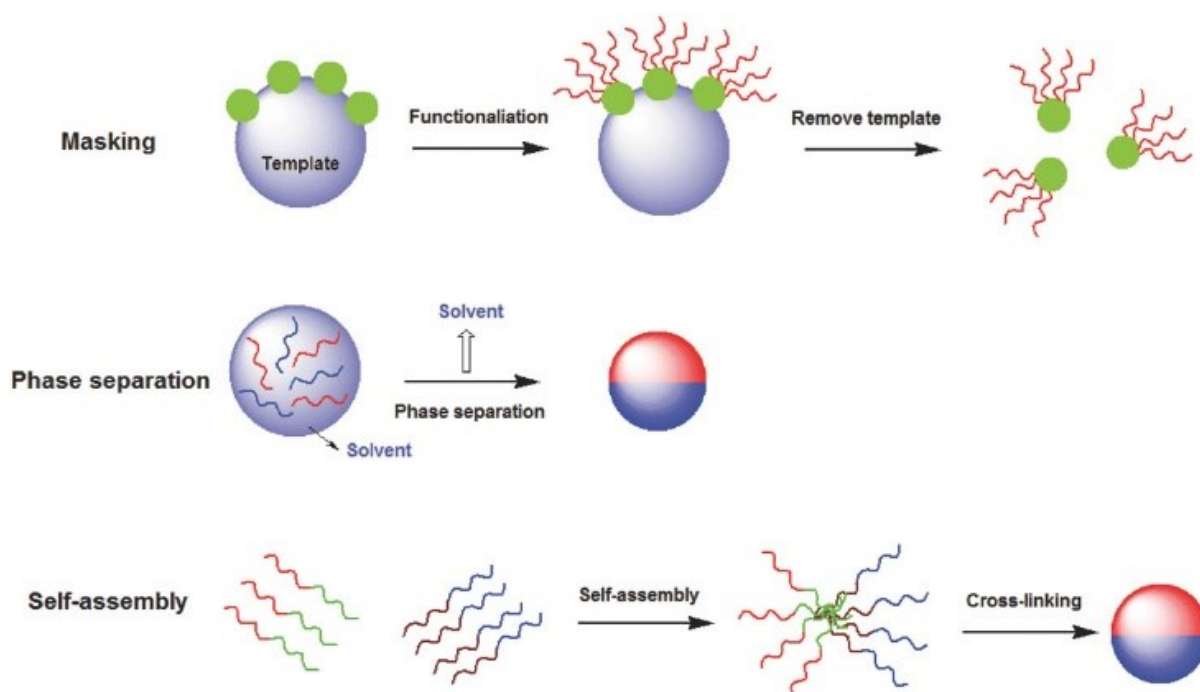


Figure 2-6 Schematic diagram showing three strategies for the preparation of Janus nanoparticles. Figure 2-6 is adapted with permission from the ref,[18] copyright 2018 WILEY-VCH Verlag GmbH & Co. KGaA, Weinheim.

2.4.1.1 Phase separation

The phase separation method may yield J.P.s of different types, e.g., inorganic, nanocrystalline, and polymeric. The phase separation strategy has been widely used for synthesizing polymeric J.P.s. Two approaches are usually involved in the phase-separation strategy: either interaction between polymers and other non-polymeric materials or between different polymers.[18] Fan *et al.*[121] developed an emulsion interfacial polymerization approach to synthesize uniform polystyrene-based J.P.s with controlled topological and chemical anisotropy. Liu *et al.*[19] used nonsolvent thermally induced phase separation (NTIPS) to fabricate a dual-layer membrane, which consisted of a thin hydrophobic PVDF top-layer and a relatively thick hydrophilic PVDF-PVA sub-layer. The resulting Janus membrane was used for membrane distillation application. The stable salt rejection above 99.5 % over continuous membrane distillation run is reported. Tian *et al.*[122] reported the fabrication of Janus dimers from tunable phase separation to utilize glycidyl methacrylate (GMA) and stearyl methacrylate (SMA) as a model system. With the addition of only 1 % cross-linked agent mostly Janus dimers are elongated and assemble into colloidal clusters.

2.4.1.2 Masking

Different types of masking techniques are used for the production of J.P.s. In the masking method, the exposed surface of the particles deposited on any substrate is modified chemically towards a specific function. The other side, which is the protected part, is not modified. For polymeric or other inorganic J.P.s, the masking process can be achieved by trapping or depositing the particles on a solid substrate or absorbing particles at the interface between two fluid phases.[18] Masking can be achieved by different methods: hard templating, templating by particles, Pickering emulsion, and polymeric single-crystal templating.[123] Wang *et al.*[124] reported the production of amphiphilic Janus gold nanoparticles by combining “solid-state grafting to” and “grafting from” methods. Two different types of polymeric chains were

decorated on the opposite sides of gold nanoparticles. Amphiphilic PEO-Au-PMMA and PEO-Au-PtBA and hydrophilic PEO-Au-PAA nanoparticles were synthesized by this method. Hong *et al.*[125] used oil-water emulsions. The colloidal particles were immobilized at an interface between vitrified wax and water upon cooling the emulsion to room temperature. The exposed surface of the immobilized particles was then chemically modified. Afterward, the wax was dissolved, and the resulting particles could be further chemically modified. Wu *et al.*[21] used a Pickering emulsion template method to fabricate Janus graphene oxide (GO) nanosheets modified by amino-containing chemicals. The wax in an aqueous Pickering emulsion protects one side of GO while the outer surface is functionalized with amino-containing chemicals with epoxy groups. Tan *et al.*[126] reported a scaling up production method to fabricate Janus TiO₂ particles using simple spin-coating and UV induced partial photodegradation. The functionalized TiO₂ particles were first spin-coated on a substrate. Then, the particle film was placed under UV light. The UV light induces the photodegradation of the surface coatings only, exposed to the light.

2.4.1.3 Self-assembly

Zhu and co-workers [127] reported unimolecular polymeric J.P.s consisting of a polystyrene-*b*-poly(2-vinylpyridine)-*b*-poly(ethylene oxide) (PS-*b*-P2VP-*b*-PEO or SVEO) triblock copolymer. The chemical cross-linking induced micellization of an amphiphilic ABC triblock copolymer in the common solvent DMF was employed to fabricate polymeric Janus nanoparticles. Dong and co-workers [128] described a method to synthesize spherical polymeric Janus particles. The polymeric JPs were synthesized by using a combination of self-assembly of simple ABC linear poly(methyl methacrylate)-*block*-poly(2-(cinnamoyloxy)ethyl methacrylate)-*block*-poly(2-dimethylaminoethylmethacrylate)(PMMA-*b*-PCEMA-*b*-PDMAEMA) triblock terpolymers into nanostructured micellar dimers with different sizes and crosslinking of the conjunction between the opposite hemispheres. Poggi *et al.*[20] synthesized polymeric Janus nanoparticles by combining the self-assembly of block copolymers in thin films and polymer grafting for surface modification.

2.5 Fabrication of ring-like structures

Ring-like structures have been fabricated using classical particle lithography, also known as colloidal lithography. Patterned surfaces are first fabricated by assembling spherical particles into organized 2-D or 3-D patterns, then used as a structural template or mask. Usually, a surface mask of silica or latex mesospheres is used for preparing a pattern.[129] First, a solution of silica or latex mesospheres is deposited on the substrate, which spontaneously assembles on the substrate during solvent evaporation (due to capillary force). Then the material of interest is deposited, and after removal of the template, ring-like structures are generated. Bayati *et al.*[130] demonstrated the fabrication of metal nanorings on flat substrates using templating and capillary nanofabrication, as shown in Figure 2-7.

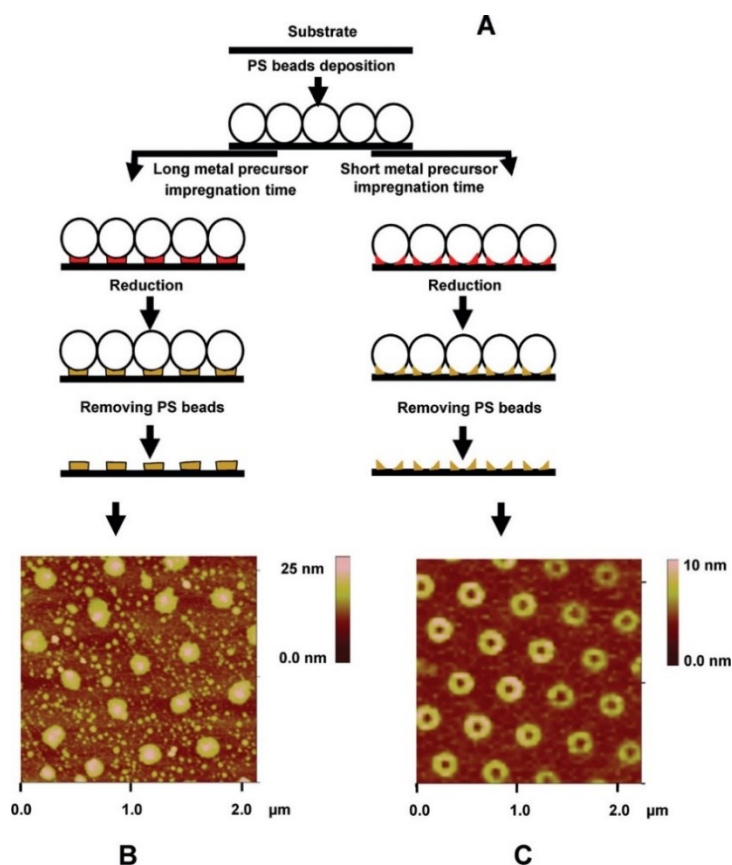


Figure 2-7 A: Schematic process illustration for the fabrication of nanofeatures. AFM images of the platinum, Pt (B) nanodisks, and (C) nanorings. Figure 2-7 is reprinted with permission from the ref,[130] Copyright 2010 American Chemical Society.

In the first step, polystyrene (PS) beads are deposited on the substrate, followed by the deposition of metal precursor solution into the interstices between the PS beads. After removing excess salt, followed by the reduction of the metal precursor solution, removal of the PS mask generates the metal nanorings. Yan *et al.*[131] reported the fabrication of polystyrene, poly(methyl methacrylate), TiO₂, and poly (trimethylolpropane trimethacrylate) ring-like structures using an assembly of silica particles 1100 nm in diameter as the template. The silica particle layer was then filled with a solution of the nonvolatile polymer. Removing the silica particles by exposure to hydrofluoric acid (HF) resulted in ring-like structures. The same group reported the preparation of gold rings on a mica sheet by using porous polymeric templates.[132]

2.6 Contact printing (CP)

Microcontact printing (μ CP) is a versatile technique mainly used for precisely replicating microstructure surfaces or fabricating surface patterns. Kumar and Whitesides [133] were the first to develop μ CP in 1993. They used PDMS stamps to fabricate patterned self-assembled thiol monolayers on Au substrates. The μ CP can also be used for protein patterning, biomolecule imprinting, and chemical group grafting.[134] The typical process of μ CP is schematically illustrated in Figure 2-8. After fabricating a stamp with pre-defined geometric patterns, the stamp is coated with ink. After the conformal contact formation of the inked stamp with the substrate, followed by soft stamp removal, printed ink patterns remain on the receiving substrate.[134] Since μ CP development, several variations of μ CP have been developed, including magnetic field-assisted microcontact printing (μ CP),[135] electrical microcontact printing (e- μ CP),[136] and vacuum-assisted microcontact printing (mCP).[137]

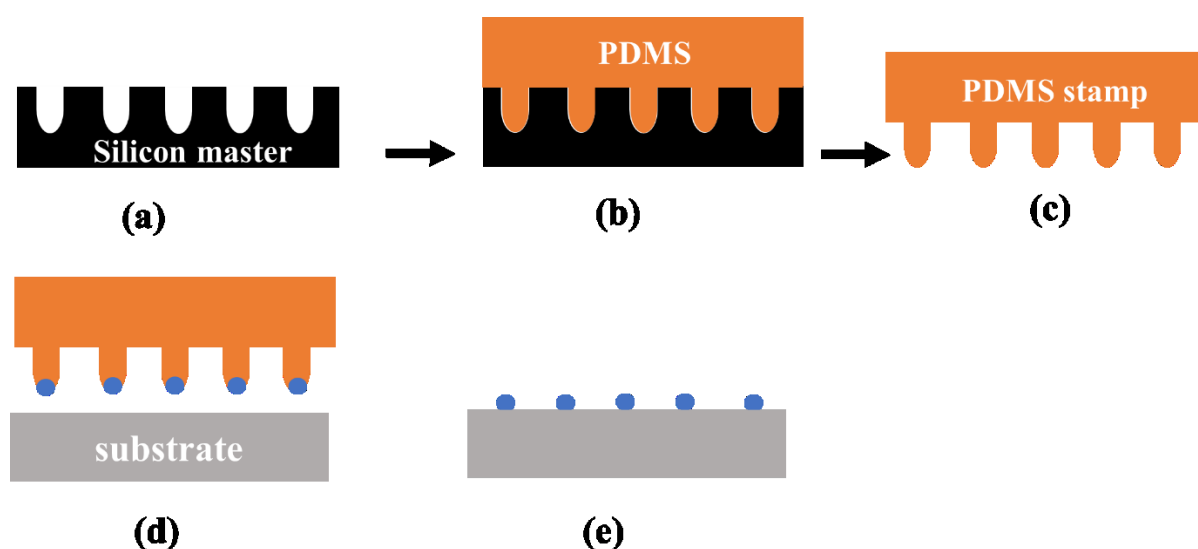


Figure 2-8 Schematic illustration of microcontact printing (μ CP). Preparation of a PDMS stamp and its use. (a), (b) PDMS precursor (orange) is molded against a master Si template (black). (c) After curing and detachment, a negative PDMS replica of the Si master is obtained. (d) The desired particles or molecules are first absorbed onto the PDMS stamp, and after drying, the stamp is brought in contact with a receiving substrate, which results in patterns of molecules or particles printed on the substrate (e).

The force applied on the stamp during μ CP is an important parameter for the realization of homogenous patterns. The pressure applied in the stamping process is improved by magnetic

field-assisted μ CP.[135] Good homogeneity of the printed patterns can be achieved by using the automated magnetic field-assisted μ CP method. In this method, a tunable external magnetic field is used to control the applied force on the stamp during the stamping process. The PDMS prepolymer and iron powder were mixed to prepare a magnetized PDMS layer. The magnetized layer of iron particles is attached to the upper side of the standard PDMS stamp layer, resulting in a composite stamp consisting of iron particles embedded in a PDMS top layer and a structural PDMS layer at the bottom. After placing the magnetic stamp under a magnetic field gradient, the stamp is attracted by the magnetic field source. The magnetic pressure generated results in a magnetic stamp being pressed on the substrate.[135] Typically, resolutions of 10 μ m can be realized by using this method. A fluorescent dye Cy3 line with a width of 10 μ m was printed on a glass slide in this way.[135] The major disadvantage of this method is the preparation process of the magnetized PDMS layer, as it demands a homogeneous mixture of highly viscous PDMS prepolymer formulation with iron powder. Non-homogenous magnetic PDMS stamps result in non-uniform magnetic forces and affect the substrate's ink distribution.[138]

Another variation of μ CP introduced by Jacobs *et al.*[136] is based on patterning thin-film electrets by applying a voltage between gold-coated PDMS stamps and the backside of an *n*-doped silicon substrate. The patterned surface of PDMS is firstly made electrically conductive with gold (Au). An approximately 80 nm thick PMMA film is coated on the *n*-doped Si wafer. Then the metal-coated PDMS stamp is placed on top of the PMMA film. After placing the PDMS stamp on top of PMMA, a voltage of 10 to 20 V between the Au coating on the PDMS and the backside of the Si wafer is applied. After turning off the potential and removing the PDMS stamp, a PMMA pattern remains on the substrate.

The alignment of stamp and printing pressure control in μ CP was improved by the simple vacuum pressure control method.[137] A vacuum was applied using a syringe at the stamp inner side and suctioning the air between the substrate and stamp. This negative pressure developed inside the stamp assists the conformal contact between substrate and stamp patterns.

Lee *et al.*[6] developed the particle transfer printing (pTP) method. In the pTP method, particle arrays were first deposited on a substrate. PDMS stamp conformal contact with the colloidal particles and detachment of the PDMS stamp results in attachment of the colloidal particles on the contact surface of the patterned PDMS stamp. The stamp with particles is then brought in

contact with a receiving substrate coated by a water layer. Retraction of the PDMS stamp results in the deposition of colloidal particle patterns on the receiving substrate. Santhanam *et al.*[139] reported the fabrication of a patterned close-packed array of Au nanoparticles on a receiving substrate by using a PDMS stamp. The Au nanoparticles floating on a water surface were picked up with the help of a PDMS stamp, and upon conformal contact of PDMS stamp with a solid substrate resulted in the formation of Au nanoparticle arrays on the receiving substrate. A typical particle transfer printing process is schematically shown in Figure 2-9.

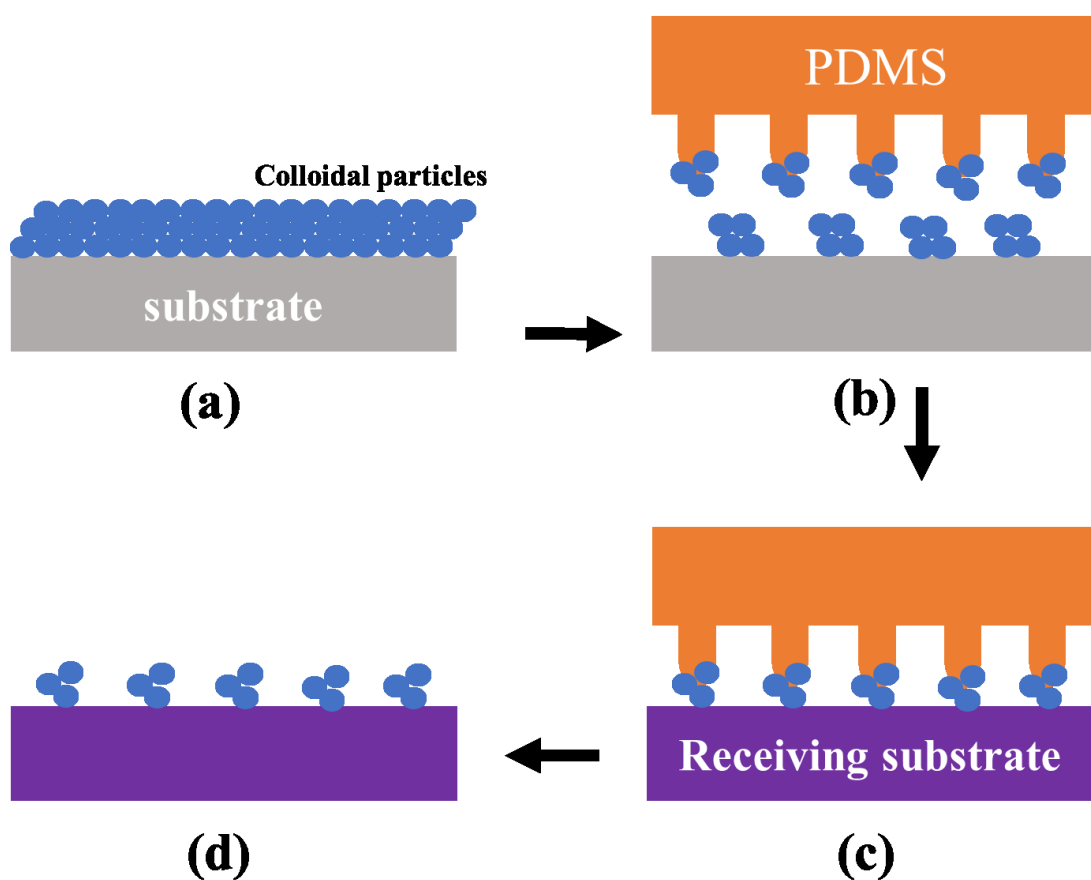


Figure 2-9 Schematic illustration of particle transfer printing. (a) The colloidal particles are first deposited on a first substrate, (b) The patterned PDMS stamp is brought into conformal contact with the colloidal particles and then detached. (c-d) The PDMS stamp having colloidal particles attached to its contact surface is brought into contact with a second receiving substrate.

Ling *et al.*[140] demonstrated particle transfer printing of 3D-patterned particles of various shapes and dimensions onto the target β -cyclodextrin-covered substrates. In Figure 2-10, an

example of particle transfer printing is shown, where single and double-layer particle networks are printed on β -cyclodextrin-covered substrates.[140] Wolf and his team[141] reported nanoparticle printing by transferring dry nanoparticles assembly from PDMS templates to the plain substrate. This group developed the fabrication of lines, arrays, and complex arrangements of nanoparticles with single-particle resolution. Yao *et al.*[142] showed patterning of colloidal silica particles using the lift-up soft lithography method. The colloidal silica microspheres with diameters of 232 to 231 nm were self-assembled on a silicon substrate, followed by lift-up with the help of a PDMS stamp having patterned features after conformal contact at 100 C for 3 h. Upon removing the PDMS stamp from the silicon substrate, the stamp with particles was cooled to room temperature, leaving the corresponding silica particles pattern on the substrate.

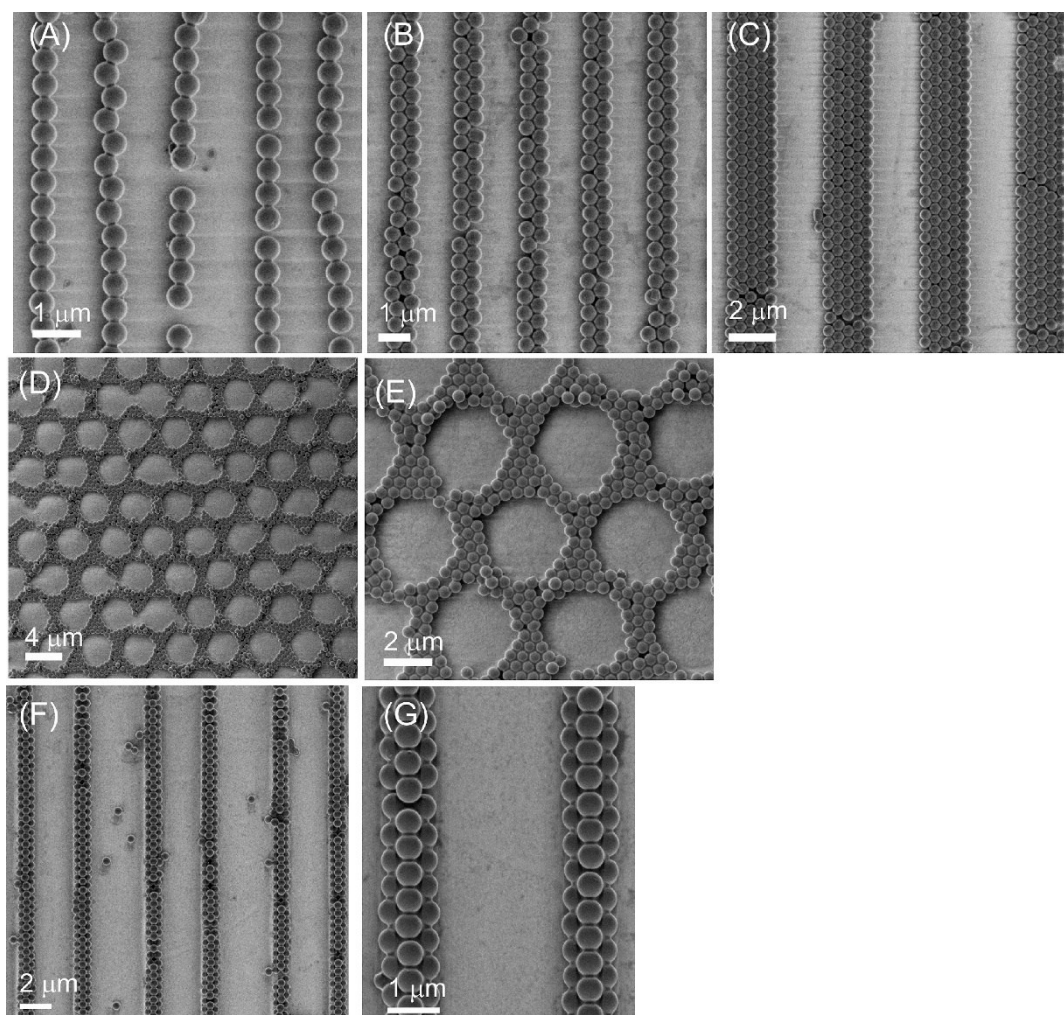


Figure 2-10 An example of the particle transfer printing method. (A-G) SEM images of the different patterns of particles transferred by particle transfer printing. Figure 2-10 is reprinted with permission from the ref,[140] copyright 2010 American Chemical Society.

Flexography is a reel-to-reel contact printing technology, which works as continuous reproduction of already defined patterns on flexible substrates.[143] Hart and co-workers reported that the high-resolution direct printing of colloidal inks could be achieved with the flexographic printing method.[144] The nanoparticle-based ink is loaded into a polymer-CNT stamp via immersion or spin coating, followed by stamp contact with the counter substrate. Transfer of ink patterns to the substrate, which matches the polymer-CNT stamp pattern, happens. Teng and co-workers[145] demonstrated a flexographic printing method for direct printing of Au nanoparticles. Printed AuNPs with an average size of approximately 60 nm were used for biosensing applications.

The contact printing methods relying on solid elastomeric stamps, such as PDMS stamps, allow simultaneous patterning of large substrate areas.[133, 146] However, the significant limitations of these methods include ink depletion after a few stamp-substrate contacts and throughput limitations.[147] Other drawbacks are the missing continuous ink supply to the contact surfaces of the stamps. To solve these problems, Xu *et al.*[148] reported porous stamps of ((poly(ether sulfone)(PES)/poly(vinylpyrrolidone)(PVP)) and ((poly(etherimide)(PEI)/poly(vinylpyrrolidone)(PVP)). The microstructured stamps were fabricated by the phase separation micromolding (PS μ M) method.

Capillary stamping with porous stamps is a parallel additive substrate patterning method that overcomes the problem of ink depletion, and that is a high throughput method.[7, 147, 149, 150] Schmidt *et al.*[7] reported stamping with mesoporous silica stamps. The stamps were prepared via sol-gel synthesis. The major characteristics of the stamps were the continuous pore system for ink supply and the stamping of sub-micron features of various inks under ambient conditions. The stamp was used to print various model inks; nanodiamonds suspensions, metallopolymer and block copolymers solutions, and solutions of small organic molecules.[147]

Hou *et al.*[150] reported the scanner-based capillary stamping combining polymer penlithography (PPL) and capillary stamping. The stamp is based on a rigid, controlled porous silica glass (CPG) layer and a porous polystyrene/poly-2-vinylpyridine block copolymer stamping layer. Even after 800 consecutive stamping cycles without reinking, the inks were deposited on the substrate without pattern quality deterioration.

2.7 Soft nanoimprint lithography (NIL)

Nanoimprint lithography (NIL) is low cost, high throughput, and high-resolution method to fabricate micro/nanoscale patterns.[151] The elastomeric stamp, which acts as a template, is used in the NIL technique to pattern structures. The malleable resist underneath the stamp having surface topography is pressed, and heat is applied. The pattern is transferred with excellent reliability.[151] The negative of the mold pattern imprint on the substrate. This method is the first variant of NIL is known as thermal embossing NIL (TE-NIL), as shown in Figure 2-11. Other developed approaches of NIL are step and flash imprint lithography (S-FIL),[152] metal-assisted chemical imprinting (Mac-Imprint),[153] laser shock imprinting,[154] UV-nanoimprint lithography,[155], and solid-state superionic stamping (S4).[156] Magnetic force-assisted thermal nanoimprint lithography (MF-TNIL) is a recent variation of the NIL method. MF-TNIL allows low-cost fabrication of nanoarrays.[138] MF-TNIL uses a permanent external magnet above the non-magnetic PDMS stamp for uniform imprinting pressure during the imprinting step. The PDMS stamp, magnetic plate, and laminated plastic sheet are sandwiched between the iron plate and external magnet. The drawback of this method can be the non-precise control of magnetic pressure.[138] Yang and co-workers developed magnetic soft mold imprint technology to fabricate microlens arrays.[157]

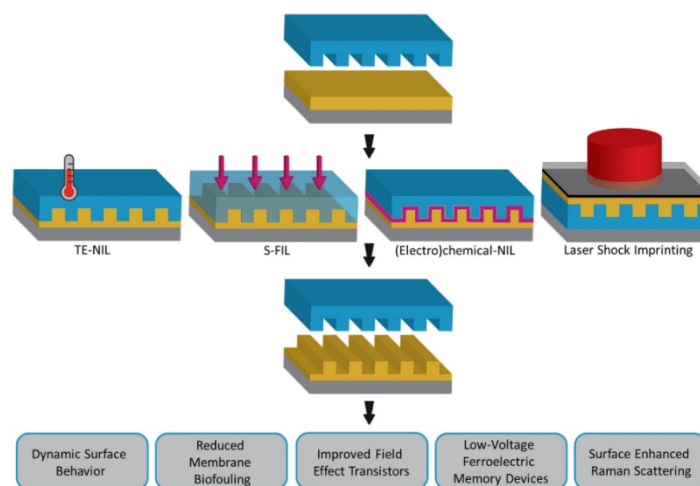


Figure 2-11 Nanoimprint lithography (NIL). Figure 2-11 is adapted with permission from the ref,[153] copyright 2020 Elsevier Ltd.

3 Experimental

3.1 Materials and methods

3.1.1 Materials

Fluorine-doped tin oxide-coated glass (FTO, $7\Omega/\text{sq}$) was purchased from Sigma Aldrich. Two types of macroporous silicon (mSi) templates were provided by SmartMembranes (Halle/Saale, Germany): 1) trigonal pore array, pitch $1.5\ \mu\text{m}$, $0.8\ \mu\text{m}$ pore length, $0.9\ \mu\text{m}$ pore diameter, round pore bottoms, 2) square pore arrays, pitch $12\ \mu\text{m}$, total pore length $7.26\ \mu\text{m}$ including etching pits with a depth of $4.23\ \mu\text{m}$, $6.0\ \mu\text{m}$ pore opening diameter, and $3.5\ \mu\text{m}$ pore bottom diameter. External permanent magnets (NdFeB, $20*5\text{mm}^2$ (diameter*height), Grade 52), and (NdFeB, $6*1\text{mm}^2$ (diameter*height), Grade 52) were purchased from Maqna otom® Group GmbH. Super-hydrophobic cover glasses ($18*18\ \text{mm}^2$) were purchased from Paul Marienfeld GmbH & Co. KG, Germany. Silicon (Si) wafers (thickness $380\ \mu\text{m}$) were provided by Siegert wafer GmbH.

3.1.2 Chemicals

Sylgard 184 kit was purchased from Dow Corning. Tetrabutyl orthotitanate (TBOT, 99+%), hydrogen tetrachloroaurate (III) hydrate ($\text{HAuCl}_4 \times \text{H}_2\text{O}$), 99.9% (metal basis), Au 49% min and 1-dodecanethiol (98%) were purchased from Alfa Aesar. N-Aminoethyl-aza-2,2-dimethyl-4-methylsilacyclopentane (hereafter referred to as cycloazasilane), acetylacetone (AcAc, 99+%), and hydrochloric acid (HCl, 37%) were bought from Gelest, Acros Organics, and Merck, Germany, respectively. Anhydrous ethanol (EtOH, 99.5%) was obtained from VWR International. 1H,1H,2H,2H-Perfluorodecyltrichlorosilane (FDTS, purity 97%; stabilized with Cu) was purchased from ABCR GmbH. Diethanolamine (DEA, 99.9%), Chitosan (CS, high molecular weight), toluene (99.8%), potassium hydroxide (KOH, pellets), Pluronic F-127, potassium dichromate ($\text{K}_2\text{Cr}_2\text{O}_7$, 99.5%), and glacial acetic acid (HAc, 99.9%) were purchased from Sigma Aldrich. Sodium hydroxide (NaOH, pellets, 99%) was purchased from ORG Laborechemie GmbH. Mucosal detergent was obtained from Brand GmbH. Poly(styrene-*block*-4-vinyl pyridine) (PS-*b*-P4VP; M_n (PS)=128.0 g/mol; M_n (P4VP)=35.0 g/mol, $M_w/M_n=1.10$, and poly(styrene-*block*-2-vinyl pyridine) (PS-*b*-P2VP; M_n (PS)= 89.500 g/mol; M_n

(P2VP) = 25.500 g/mol, $M_w/M_n = 1.18$) was supplied by Polymer Source. Aqueous suspensions containing 100mg/mL silica (SiO₂) microparticles with a diameter of 4.07 μm and 10 mg/ml silica (SiO₂) nanoparticles of 50nm were purchased from Bangs Laboratories, Inc and Alpha Nanotech, respectively. Aqueous suspensions of 5 wt.% silica (SiO₂) microparticles with diameters of 143nm, 501nm, 755nm, and 985nm, as well as SiO₂-NH₂ microparticles 976 nm in diameter, were purchased from microparticles GmbH, Germany. 5 nm iron oxide superparamagnetic nanoparticles (magnetite, Fe₃O₄) in water (5mg/ml) were purchased from Cytodiagnosics Inc, Canada. Water-based ferrofluid with magnetic particle diameter (magnetite Fe₃O₄) of 10 nm having a particle concentration of 1.2 vol-% was provided by Ferrotec USA. Aqueous dispersions of graphene oxide (GO) in water (0.4 wt.%) were obtained from Graphenea. Zinc oxide (T-ZnO) tetrapods powder provided by Mads Clausen Institute, University of Southern Denmark.

3.1.3 Methods

3.1.3.1 Scanning electron microscopy (SEM)

SEM was performed with a Zeiss Auriga scanning electron microscope using a secondary electron chamber detector (SESI) and an in-lens detector. SEM was carried out at an accelerating voltage of 8 keV in the case of titania samples, 15 keV in the case of block copolymer films, and 1.9 keV in the case of printed magnetic nanoparticle aggregates. Before imaging, all samples were sputter-coated (Emitech K575X) with platinum/iridium alloy.

3.1.3.2 Atomic Force Microscopy (AFM)

AFM was performed in contact mode using an NTEGRA microscope (NT-MDT) and CSG01/Pt GOLDEN SILICON cantilevers bought from TipsNano (silicon; tip curvature radius 35 nm; resonant frequency between 4 kHz and 17 kHz; force constant between 0.003 N m⁻¹ and 0.31 N m⁻¹).

3.1.3.3 Contact angle measurements

A drop shape analyzer Krüss DSA100 was used for water contact angle (WCA) measurements at a temperature of 23 °C and relative humidity of 31%. Sessile water droplets with a volume of 2 µL were deposited on the substrates for each measurement. Each reported value is the average of six measurements on three different samples at different locations.

3.1.3.4 X-ray photoelectron spectroscopy (XPS)

X-ray photoelectron spectroscopy (XPS) measurements were performed under an ultra-high vacuum in an ESCA-unit Phi 5000 VersaProbe III with a base pressure of less than 10^{-9} mbar. A monochromatic Al K α X-ray source with excitation energy of 1486.6 eV was used. The X-ray beam size was set to 100 µm. Both an ion gun and an electron gun were used to prevent the charging of the samples. The take-off angle was 45° for all measurements. The XP spectra were calibrated using the Carbon C 1s (284.5 eV) peak.[158] Origin was used for Lorentz fitting and analyzing the XP spectra of all TiO₂ based templates. For fitting chitosan (CS) and chitosan-graphene oxide (CS-GO) hydrogel XPSPEAK41 software was used.

For site-selective modification of SiO₂ microparticles in macroporous-nanoporous substrates, the XPS measurements were performed employing a PHI Versaprobe III spectrometer equipped with a monochromatic Al K α , micro-focused scanning X-ray source. To compensate for charging effects, a dual-beam charge neutralization method was used. Calibration was performed according to the position of the C1s line (284.8 eV).

3.1.3.5 Nitrogen sorption measurements

Nitrogen sorption measurements of TiO₂ were performed on a "Surfer," distributed by the company "Porotec" (Germany). Data evaluation was carried out using the "ASiQ" Software from the company "Quantachrome Corporation"(Florida, USA). The temperature of the measurement was liquid nitrogen temperature (-196°C). BET evaluation was done in a pressure range between $p/p_0 = 0.05-0.3$.

3.1.3.6 Quartz crystal microbalance (QCM)

The thickness of the Ti and Au layers was estimated by using the method described elsewhere.[159] An AT-cut eQCM quartz having a well-defined area was coated with metal and weighed before and after deposition using GAMRY eQCM 10 M quartz crystal microbalance. The deposition conditions were kept the same as metal deposition on samples.

3.1.3.7 Vibrating-sample magnetometer (VSM)

Magnetic stamping and characterizations were performed using LakeShore VSM Model 7407 at room temperature. Different magnetic field strengths were applied for stamping magnetic nanoparticles under the magnetic field influence; 0.2T, 0.6T, 1.0T, and 1.4T for approximately 10 sec both **in-plane** and **out-of-plane** geometries. The magnetic inked stamp is placed on a silanized silicon substrate and then attached to the VSM sample holder. The sample holder was placed carefully at the central position between two pickup coils. After a magnetic field application for 10 sec, the silicon counter substrate and the stamp were detached from the VSM sample holder. Then, the stamp was carefully detached from the surface of the silanized silicon substrate. More details can be found in section 3.3.4.4.2.4.

3.1.3.8 Other instrumentations

The SiO₂ filled particles inside each macropore were coated with titanium (Ti) and gold (Au) by thermal evaporation. Thermal evaporation was performed in a vacuum chamber at 10⁻⁴ mbar using a Balzers BAE 120 evaporator. The thermal evaporator was equipped with a Maxtek thickness monitor (MODEL TM-350), used for thickness measurements during deposition. The self-assembly of SiO₂ particles in patterned arrays was done under 2000 rpm for 1 min using a spin coater G3P-8 from Specialty Coating Systems. A sonicator Elmasonic P from Elma was used for sonication at a frequency of 35 kHz. Oxygen plasma treatment was performed at 100 W with Diener Femto plasma cleaner supplied by Diener electronic GmbH. High-temperature treatments were done using a Muffle furnace (Nabertherm GmbH). The stamp was prepared in custom build computer-controlled furnaces under a vacuum. Sputtering of gold was done with JEOL JFC-1200 fine coater.

3.1.4 Size and shape analysis

ImageJ software was used to analyze the size and shape of the obtained stamped spots or particles if not mentioned otherwise. The evaluation was done by evaluating corresponding SEM images. To make the corresponding SEM images binary, the threshold was selected so that with changing the brightness and contrast, the sizes of stamped spots did not change. The particle diameter, d , and side-lengths l of square-shaped aggregates were calculated using equations 3-1 and 3-2, respectively. The area A [160] values were obtained from the ImageJ processed data, and then d was calculated with OriginLab.

$$d = \sqrt{4 \cdot \frac{A}{\pi}} \quad \text{Equation 3-1}$$

$$d = \sqrt{A} \quad \text{Equation 3-2}$$

The circularity [159, 160] and aspect ratio were calculated using equations 3-3 and 3-4. The circularity and the aspect ratio of an object describe the deviation of the shape of an object from an ideal circle. The circularity and aspect ratio of an ideal circle is equal to 1.

$$\text{Circularity} = 4\pi \cdot \frac{A}{\text{perimeter}^2} \quad \text{Equation 3-3}$$

$$\text{Aspect ratio} = \frac{\text{major axis}}{\text{minor axis}} \quad \text{Equation 3-4}$$

The plot-line profile in the case of the square edge length of square-shaped stamped aggregates was analyzed with Image J.

3.2 Procedures

3.2.1 Preparation of substrates and template surfaces

3.2.1.1 Preparation of FTO substrates

For TiO₂ holey film or hollow ring fabrication, the FTO glasses (15*15*2.2 mm³) were first rinsed with 3 wt.% mucasol detergents in water, followed by successive ultrasonication in acetone, ethanol, and DI water for 15 min followed by drying in an argon flow. The cleaned FTO glasses were treated with oxygen plasma at 100 W for 10 min before drop-casting of TiO₂ sol-gel solution.

3.2.1.2 Preparation of silicon (Si) substrates

For TiO₂, Au, CS, and CS-GO hollow microrings fabrication, the silicon substrate was ultrasonicated in acetone, ethanol, and DI water for 15 minutes and dried in an argon flow. The cleaned silicon glasses were treated with oxygen plasma at 100 W for 10 min before drop-casting of TiO₂ sol-gel, Au, CS, or CS-GO solution.

3.2.1.3 Silanization of macroporous silicon (mSi)/silicon (Si) substrate

For silanization, the mSi and silicon substrates were subjected to successive ultrasonication in acetone, ethanol, and DI water for 15 min, followed by drying in an argon flow. The cleaned mSi and Si substrates were treated with oxygen plasma at 100 W for 10 min before silanization. The primary mold mSi templates and silicon substrates for printing were hydrophobically modified with FDTS following a procedure described elsewhere.[161] Briefly, mSi templates and silicon substrates were modified by vapor deposition at 100 °C for 5 h and 100 °C for 2 h under room pressure respectively.

3.3 Syntheses and Fabrication methods

3.3.1 Topographically patterned TiO₂ substrates as a platform for wetting metamaterials

3.3.1.1 Fabrication of the PDMS secondary mold

PDMS secondary molds were fabricated using a mSi template as a primary mold, which was hydrophobically modified with FDTS as described above (see section 3.2.1.3). Then, degassed PDMS prepolymer formulation (base: curing agent = 10:1) was poured onto the modified mSi template and cured overnight at 70 °C. The degassing of PDMS was done in a vacuum desiccator. After curing, the PDMS secondary mold was a negative replica of the macroporous silicon template.

3.3.1.2 Synthesis of titania (TiO₂) sol-gel precursor solutions

TiO₂ sol-gel precursor solution was synthesized following a procedure described elsewhere.[162, 163] Briefly, 2 g of F127 was added to \approx 68 mL of anhydrous ethanol (EtOH) under stirring. Then, 8 mL of concentrated HCl (37%) was added slowly to the mixture and allowed to mix for 30 mins at room temperature under vigorous stirring (F127/EtOH/HCl). Separately, \approx 5.9 mL of TBOT was added to \approx 68 mL of EtOH and 4 mL of AcAc under vigorous stirring at room temperature for about 30 mins (TBOT/EtOH/AcAc). Finally, \approx 74 mL of F127/EtOH/HCl solution was added to the \approx 75 mL solution mixture of TBOT/EtOH/AcAc under vigorous magnetic stirring (speed: \approx 500 rpm) for 1 h at room temperature. After stirring (speed: \approx 500 rpm) for 23 h at room temperature, the solution had an orange color, and the volume of the final concentrated solution was \approx 23 mL. The molar ratio of F127: TBOT was adjusted to 0.00015:0.0173. Pluronic F127 was used as a structure-directing agent and TBOT as the inorganic precursor for TiO₂. AcAc [87] and HCl [164] were used to control the sol-gel chemistry of the Ti-precursor and slow the rates of hydrolysis and condensation. TBOT precursor has two major advantages over other precursors (for example,

titanium (IV) isopropoxide, titanium (IV) chloride, and titanium (IV) ethoxide): (i) n-butanol can be in situ released, acting as swelling agent or cosurfactant and (ii) its higher linearity and larger dimensions.[162, 165]

3.3.1.3 Fabrication of patterned holey TiO₂ films

20 μL of the synthesized TiO₂ sol-gel precursor solution was drop-cast onto cleaned FTO glass (see section 3.2.1.1 for the cleaning procedure). Directly after deposition of TiO₂ sol, the PDMS secondary mold attached to a steel block with double-sided polyimide tape was pressed against the TiO₂ sol-gel precursor solution located on FTO glass (Figure 3-1a-d).

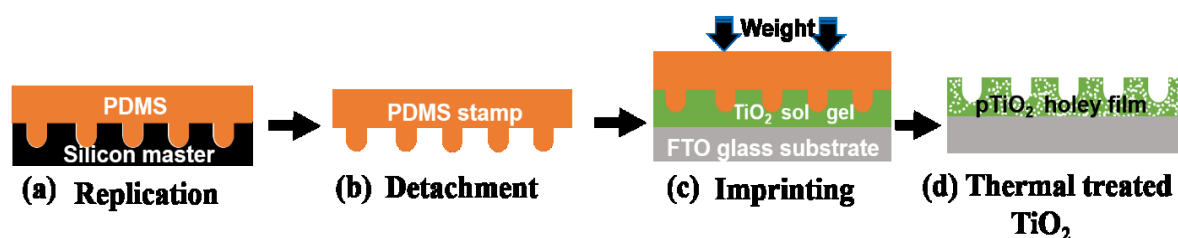


Figure 3-1 Patterned titania (*p*TiO₂) holey films and their preparation. Schematic illustration of the fabrication of *p*TiO₂ holey films. (a) PDMS pre-polymer is poured onto a surface-modified primary silicon mold and then cured. (b) Detachment yielded a secondary PDMS mold, which is a negative replica of the primary silicon mold. (c) TiO₂ sol-gel solution is cast onto an FTO glass substrate and then sandwiched between PDMS stamp and FTO glass substrate while the additional load is applied. (d) After thermal treatment, a macroporous/mesoporous TiO₂ film (*p*TiO₂ holey) forms on the FTO glass substrate.

The mass of the steel block was 40 g, and together with double-sided polyimide tape, it was 40.06 g. The thickness of the PDMS secondary mold was approximate. 4 mm, having a mass of approximately 0.34 g and the contact area of the PDMS secondary molds on the TiO₂ films was approximate. 10 mm x 10 mm. The total mass of steel block, PDMS secondary mold, and polyimide tape summed to 40.40 g. The pressure exerted on the TiO₂ sol-gel precursor solution amounted to 3.95 kN m⁻². The whole setup was heated from RT to 250 °C in the air at a heating rate of 5°C/min, kept at 250°C for 2h and then cooled to 60 °C at a cooling rate of 5°C/min (Figure 3-1c). The PDMS secondary mold and the steel block were detached at 60 °C. The holey macroporous TiO₂ film was then heated to 450°C at a heating rate of 5°C/min under

ambient atmosphere and kept for 1 h at this temperature to obtain solvent-free and crystallized holey titania films. [166] The obtained patterned TiO₂ film (*p*TiO₂) (10 x10 mm²) having macropores at the position of PDMS pillars was mechanically stable, transparent, and crack-free (Figure 3-1d).

3.3.1.3.1 Self-assembly of SiO₂ microparticles inside TiO₂ macropores

SiO₂ microparticles were deposited into the TiO₂ macropores using a simple spin coating method. The *p*TiO₂ film was first treated with oxygen plasma with 100 W for 10 min to hydrophilize [16] the surfaces of the macropores to ensure water retention inside the channels, followed by heating at 350 °C for 15 mins. Then, the samples were taken out and spin-coated with 20μL of 0.5 wt.% aqueous solutions of SiO₂ microparticles at 2000 rpm for 1 min using a spin coater G3P-8 from Specialty Coating Systems. After spin coating, the samples were heat-treated at 350 °C for 15 minutes to generate hybrid TiO₂/SiO₂ (*p*TiO₂_SiO₂) patterned arrays. The subsequent heat treatment helps increase the adhesion of SiO₂ particles to the TiO₂ microwells.

3.3.1.3.2 Surface chemistry of self-assembled SiO₂ microparticles

The surface chemistry of self-assembled SiO₂ microparticles inside TiO₂ macropores was modified by three different routes, (1) adsorption of a) cycloazasilane, b) FDTS, and c) 1-dodecanethiol, (2) Au metal caps coated on the SiO₂ particles inside the TiO₂ macropores by thermal evaporation, and (3) block-copolymer rods attached to the filled particles.

(1) For *p*TiO₂_SiO₂ template surface modification with cycloazasilane (*p*TiO₂_SiO₂@cycloazasilane), the *p*TiO₂_SiO₂ templates were kept in 10 ml of a 2 vol-% solution of cycloazasilane in toluene for 2 h at room temperature. The obtained *p*TiO₂_SiO₂@cycloazasilane templates were successively rinsed with toluene, ethanol, and

water. The substrates were then blown dry with argon. The same procedure was applied to modify $p\text{TiO}_2\text{-SiO}_2\text{@Au}$ templates with 1-dodecanethiol ($p\text{TiO}_2\text{-SiO}_2\text{@Au@1-dodecanethiol}$). The $p\text{TiO}_2\text{-SiO}_2$ template was also modified with perfluorodecyltrichlorosilane molecules ($p\text{TiO}_2\text{-SiO}_2\text{@FDTS}$) by a vapor deposition method at 100 °C for 5 h under room pressure.

(2) The SiO_2 microparticles inside each macropore were coated with titanium (Ti) and gold (Au) by thermal evaporation ($p\text{TiO}_2\text{-SiO}_2\text{@Au}$) (Figure 3-2). Thermal evaporation was performed in a vacuum chamber at 10^{-4} mbar using a Balzers BAE 120 evaporator. A ≈ 20 nm thick Au layer was deposited after a ≈ 5 nm Ti layer deposition serving as an adhesion promoter. The thermal evaporator was equipped with a Maxtek thickness monitor (MODEL TM-350), which was used for thickness measurement during deposition. The thickness of the Ti and Au layers was estimated by using the method described in section 3.1.3.6.

(3) After modification of $p\text{TiO}_2\text{-SiO}_2$ templates with FDTS, 20 μL of a 10 wt.% solution of PS-*b*-P2VP in toluene was cast on the modified $p\text{TiO}_2\text{-SiO}_2$ templates. The latter was then placed under the Petri dish to slow down solvent evaporation for 24 h at room temperature. The PS-*b*-P2VP bulk film was detached after sonification for 15 mins in ethanol, followed by bulk layer removal with scalpels (Figure 3-3).

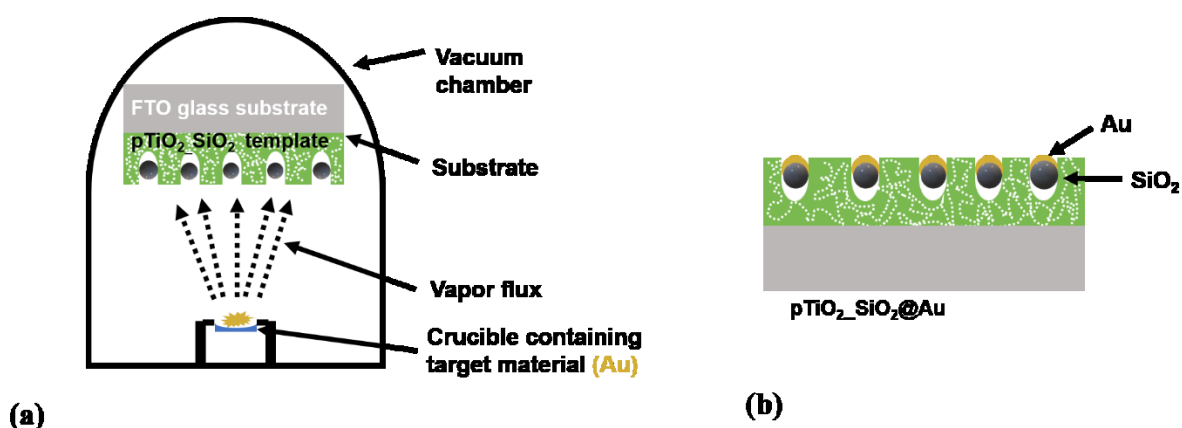


Figure 3-2 Schematic showing thermal evaporation setup for deposition of gold (Au) layer on SiO_2 microparticles in $p\text{TiO}_2\text{-SiO}_2(143\text{nm})$ template (a), and (b) the resulting $p\text{TiO}_2\text{-SiO}_2(143\text{nm})\text{@Au}$ template after thermal evaporation.

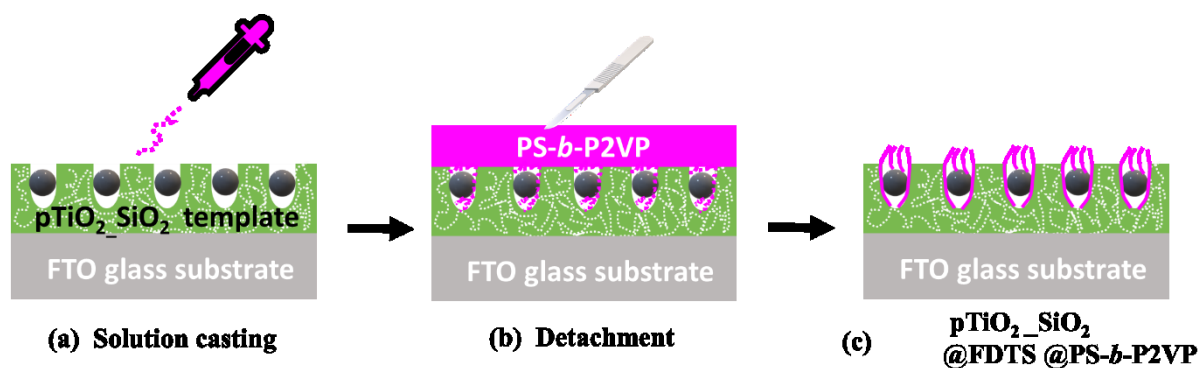


Figure 3-3 Schematic showing the fabrication of PS-*b*-P2VP block copolymer rods inside the $p\text{TiO}_2\text{-SiO}_2$ template; (a) solution casting of PS-*b*-P2VP block copolymer solution in toluene, (b) bulk layer removal with the help of scalpels after complete evaporation, and (c) the resulting fabricated $p\text{TiO}_2\text{-SiO}_2$ template along with PS-*b*-P2VP rods.

3.3.1.3.3 Switchable water wettability

A simple and ease of wettability reversal of TiO_2 based surface from hydrophobic state to persistent super-hydrophilic state and vice versa was reported. TiO_2 is intrinsically hydrophilic; by texturing, the TiO_2 film surface has the potential to increase hydrophilicity.[167] Texturing of semiconducting metal oxide (TiO_2) patterned microwells was achieved with the self-assembly of different sizes of SiO_2 microparticles inside arrays. The scheme in Figure 3-4 shows the wettability exchange between the different stages. A direct imprinting method was performed to fabricate TiO_2 holey patterned arrays, which showed the hydrophobic property (Figure 3-4a). After the self-assembly of different sizes of SiO_2 microparticles inside TiO_2 holey film, the super-hydrophilic property is achieved (Figure 3-4b). For gaining the hydrophobic state, the surface chemistry of SiO_2 particles embedded in TiO_2 arrays is modified with different hydrophobic molecules (Figure 3-4c). For wettability switching from hydrophilic to hydrophobic, the infiltrated self-assembled SiO_2 particles can be detached from the microwells to restore the native hydrophobic state. For wettability switching from hydrophobic to hydrophilic, by heating the substrates, the transition can occur. High adhesion of water droplets to the surfaces was observed in all hydrophobic states, and even upon tilting and vigorously moving substrates, the droplet remained strongly pinned. The evaporation dynamics study of water droplets is performed on all modified surfaces, including sessile water droplet shape evolution during evaporation.

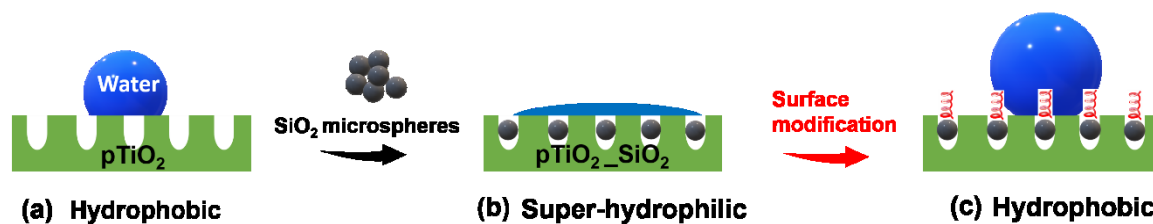


Figure 3-4. Wettability management of topographically patterned TiO₂. a) TiO₂ topographically patterned with arrays of macropores ($p\text{TiO}_2$) is hydrophobic. b) Deposition of SiO₂ microspheres into the macropores of $p\text{TiO}_2$ ($p\text{TiO}_2\text{-SiO}_2$) changes the wettability to hydrophilic. c) Chemical modification of $p\text{TiO}_2\text{-SiO}_2$ switches the wettability again to hydrophobic.

3.3.2 Site-selective orthogonal modifications of SiO₂ microparticles in PS-*b*-P2VP and PS-*b*-P4VP substrates

3.3.2.1 Fabrication of patterned PS-*b*-P2VP and PS-*b*-P4VP substrates

100 mg of PS-*b*-P4VP were dissolved in 4 mL of toluene and shook for 48 hours to completely dissolve the polymer. 100 μ L of the PS-*b*-P4VP solution was dropped on top of a PDMS secondary mold negative replica (10 x10 mm²) obtained from a silicon master template with a 6 μ m pore opening diameter (see section 3.3.1.1) left at room temperature for 24 hours in a ventilated hood for solvent evaporation. The dried polymer films were then heated at 200 °C for 18 hours in an argon atmosphere. Then, the films were swelled in ethanol at 60 °C for 4 hours for pore generation using a protocol established elsewhere [168, 169]. The ethanol is selective to P2VP domains and swells upon heating of PS-*b*-P2VP. The swelling of the P2VP domains leads to the plastic deformation of the non-swollen PS matrix. With changing the swelling time, the pores sizes can be tuned. The films were removed from the ethanol and immediately placed with the square pore mouths facing upwards on top of a glass substrate previously cleaned with oxygen plasma. Finally, the polymer films were placed in an oven at 40 °C overnight for drying. The second set of block-copolymer PS-*b*-P2VP membranes was also fabricated. 100 μ g of PS-*b*-P2VP were dissolved in 1 mL of toluene and mixed for 48 hours to completely dissolve the polymer. 100 μ L of the PS-*b*-P2VP solution was dropped on top of a PDMS secondary mold negative replica obtained from a silicon master template with 0.9 μ m pore diameter (see section 3.3.1.1). The other steps followed were the same as described above.

3.3.2.1.1 Modification of infiltrated SiO₂ microparticles inside PS-*b*-P2VP or PS-*b*-P4VP macroporous substrates

SiO₂ microparticles with diameters of 4.07 μ m and 0.755 μ m were infiltrated into the macropores of macroporous PS-*b*-P4VP and PS-*b*-P2VP substrates, respectively. First, the macroporous PS-*b*-P4VP or PS-*b*-P2VP films were fixed on a glass substrate. The SiO₂

microparticles were deposited inside the PS-*b*-P2VP and PS-*b*-P4VP macropores by spin-coating. The surface of the substrates patterned with macropores was first treated with oxygen plasma 100 W for 2 min to hydrophilize [16] the macropores to ensure water retention inside the macropore channels, followed by heating at 50 °C for 15 mins. Then, the samples were taken out and spin-coated with 20 μ L of 0.5 wt.% aqueous solutions of the SiO₂ microparticles at 2000 rpm for 1 min using a spin coater G3P-8 from Specialty Coating Systems. After spin coating, the samples were heat-treated at 50 °C for 15 minutes to generate hybrid PS-*b*-P2VP/SiO₂ and PS-*b*-P4VP/SiO₂ patterned substrates.

After the infiltration of 4.07 μ m SiO₂ microparticles inside the macropores of the macroporous PS-*b*-P4VP substrates, the top side of the embedded SiO₂ microparticles along with the patterned PS-*b*-P4VP membrane was sputtered coated with a \approx 20 nm thick gold layer using a JEOL JFC-1200 fine coater. The top side of the embedded gold-coated SiO₂ microparticles was modified with 2 vol-% solutions of 1-dodecanethiol in ethanol at room temperature for 3 h. Then, the macroporous PS-*b*-P4VP/SiO₂ modified with 1-dodecanethiol was successively rinsed three times with ethanol and water. The substrates were then blown dry with Argon. The backside of the embedded SiO₂ microparticles inside PS-*b*-P4VP macropores was modified with (3-aminopropyl)triethoxysilane (APTES) using a home-built device shown in Figure 3-5. Figure 3-5 illustrates the modification method used for selective capping of infiltrated SiO₂ microparticles inside the PS-*b*-P4VP macropores.

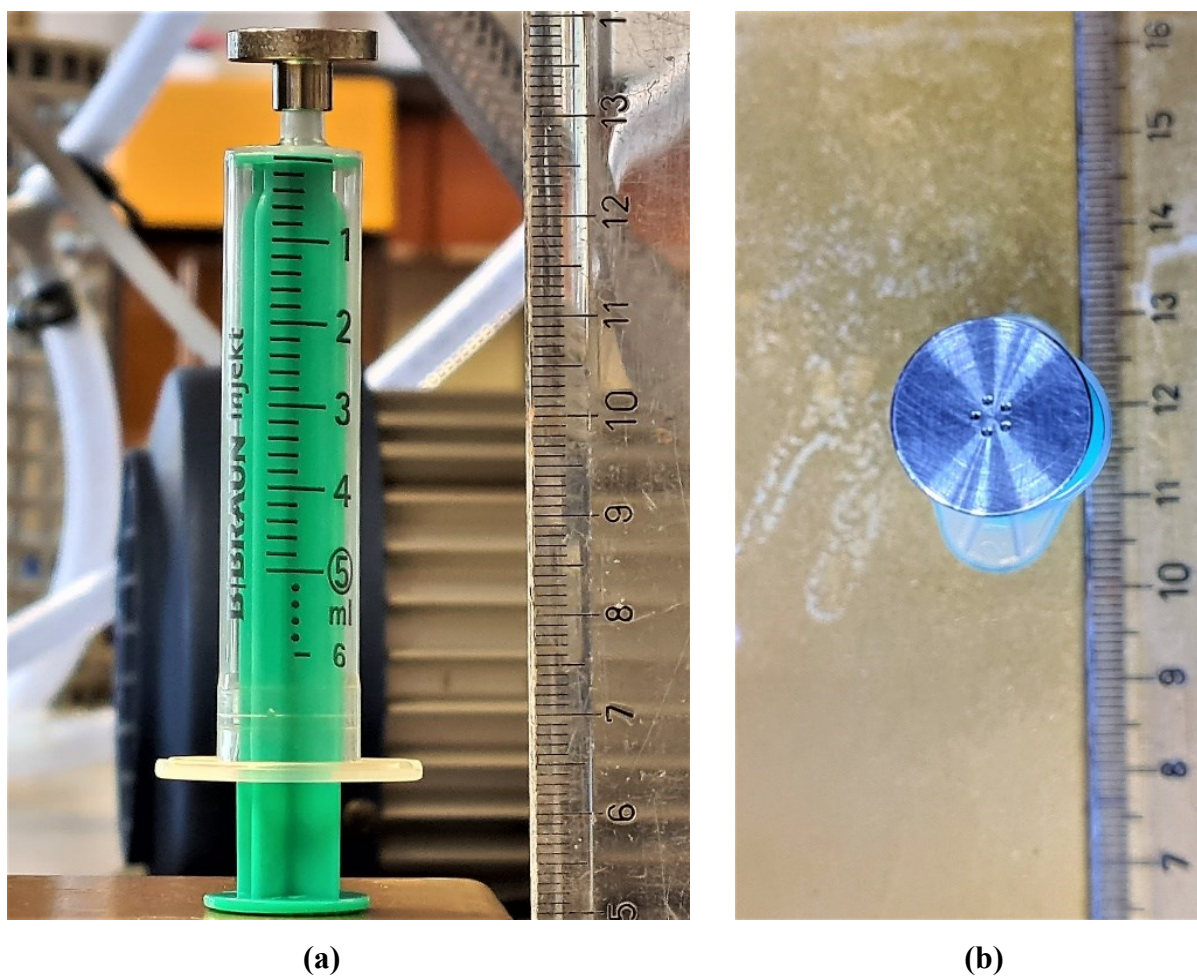


Figure 3-5 Photograph of a syringe part without needle used to modify embedded SiO_2 microparticles in PS-*b*-P4VP and PS-*b*-P2VP macroporous substrates (a) Syringe and the home-built device, which is fixed at the top needle side. (b) The top view photo of the home-built steel device with 5 small holes to supply selected modification solutions.

The macroporous PS-*b*-P4VP membranes infiltrated with SiO_2 microparticles and modified with 1-dodecanethiol were first detached from the glass slide with the help of a scalpel. The detached films were placed on the top side of the device (shown in Figure 3-5b) so that the 1-dodecanethiol modified surface faced the top. The backside was now modified with a 4 vol-% ethanolic solution of APTES injected from a syringe so that the solution was in contact with the backside of macroporous PS-*b*-P4VP membrane infiltrated with SiO_2 microparticles ($4.07 \mu\text{m}$) and modified with 1-dodecanethiol. The 4 vol-% ethanolic solutions of APTES solution go out within small holes in the steel device. APTES modification was done for 3 h at room temperature, followed by successively rinsing three times with ethanol and water. The

substrates were then blown dry with argon. Figure 3-6 shows the schematics of the modification of embedded SiO₂ particles inside the confined channel.

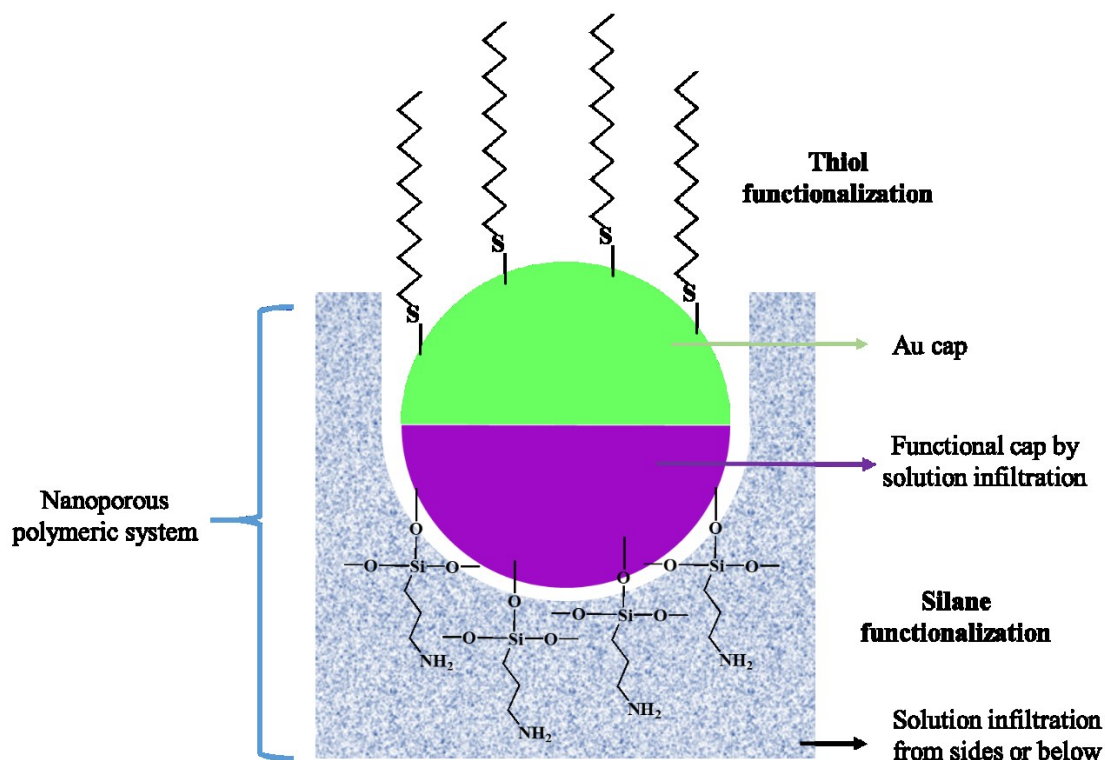


Figure 3-6 Schematics of the method used to selectively modify the top and bottom sides of SiO₂ microparticles inside the macropores of a patterned PS-*b*-P4VP substrate.

The same procedure described above was used to modify embedded SiO₂ microparticles with a diameter of 0.755 μm inside a patterned PS-*b*-P2VP substrate. The top side of the embedded SiO₂ microparticles and the patterned PS-*b*-P2VP substrate were sputter-coated with a ≈ 20 nm thick gold layer using a JEOL JFC-1200 fine coater. Then bottom side was modified with 2 mM of potassium dichromate following the same procedure as for APTES modification described above.

3.3.3 Fabrication of hollow microrings

3.3.3.1 Synthesis of titania (TiO₂) sol-gel solution

TiO₂ sol-gel solution was synthesized following the procedure described elsewhere.[170] Briefly, tetrabutyl titanate (TBOT) was added to a solution of anhydrous ethanol (ETOH) and diethanolamine (DEA) and mixed vigorously with a magnetic stirrer for 2 h separately. Glacial acetic acid (HAc) and DI water were mixed separately, followed by the dropwise addition to the TBOT solution. The solution was stirred for 24 h to get the final concentrated solution.

3.3.3.2 Synthesis of chitosan-graphene oxide (CS-GO) hydrogel

CS-GO hydrogel was synthesized following a procedure described elsewhere.[171] Briefly, 0.25 mL glacial acetic acid (HAc) was added to 49.75 mL deionized (DI) water. The solution was stirred for 15 min at room temperature. Then, 0.25 g chitosan powder was added to 24.8 g of the aqueous acetic acid solution to obtain a solution containing 0.5 wt.% CS. The solution was stirred by high-speed vortexing using a Vortex-Genie 2 for 15 mins at room temperature. 1 wt.% of CS-GO solution was synthesized by adding aqueous GO dispersion to the chitosan solution. The CS-GO solution was vigorously stirred for 24 hours at room temperature.

3.3.3.3 Synthesis of gold (Au) precursor solution

The gold precursor solution was synthesized by following procedures reported elsewhere.[172] 0.44 g NaOH was dissolved in 200 mL of DI water in a beaker (55 mM) and left for stirring for 30 mins at room temperature. In the other beaker, 0.164 g HAuCl₄ x H₂O was mixed in 130 mL of DI water (3.73 mM) and left for mixing in stirring for 15 mins. 10 mL of each solution were mixed in another beaker to produce a final 20 mL mixture and mixed in Vortex for 10 mins at 300 rpm.

3.3.3.4 Fabrication of hollow chitosan (CS)/CS-GO microrings

20 μL of 0.5 wt.% CS or 1 wt.% of CS-GO precursor solutions was drop cast on cleaned silicon substrates (see section 3.2.1.2 for cleaning procedure). Directly after deposition of the solutions, the PDMS secondary molds (PDMS square-shaped top elements with a diameter of $\approx 4.3 \mu\text{m}$) attached to a steel block with double-sided polyimide tape were pressed against the precursor solution located on the Si substrates as shown in Figure 3-7. Steel blocks with a mass of 40 g or 80g were used for different experiments. In the setup with a single steel block, the mass of the steel block was 40 g, and together with double-sided polyimide tape, it was 40.06 g. The thickness of the PDMS secondary mold was approximately 4 mm, and its mass amounted to approximately 0.34 g. The contact area of the PDMS secondary mold on the precursor solution was approximately 10 mm x 10 mm. The total mass of steel block, PDMS secondary mold, and polyimide tape summed up 40.40 g. The pressure exerted on the precursor solution amounted to 3.95 kN m^{-2} . The total mass of two steel blocks, PDMS secondary mold and polyimide tape, summed to 80.40 g. The pressure exerted on the precursor solutions amounted to 7.87 kN m^{-2} . The whole setup, in either case, was heated from RT to 160°C in the air at a heating rate of $5^\circ\text{C}/\text{min}$, kept at 160°C for 2h and then cooled to 60°C at a cooling rate of $5^\circ\text{C}/\text{min}$. The PDMS secondary mold and the steel block were detached at 60°C . The final substrate consisted of CS or CS-GO patterned hollow microrings.

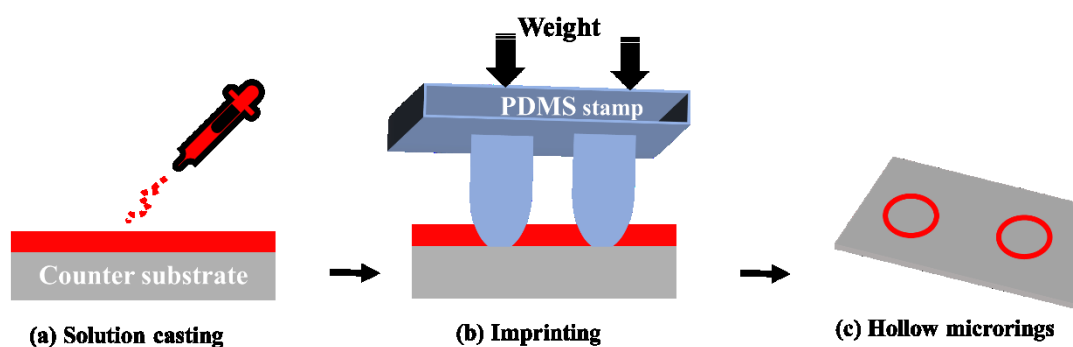


Figure 3-7 Hollow microrings and their preparation. Schematic illustration of the fabrication of hollow microrings. (a) The desired solution is cast onto Si or FTO substrates and (b) then sandwiched between PDMS stamp and substrates while the additional load is applied. (c) After thermal treatment, hollow microrings form on the substrates.

3.3.3.5 Fabrication of hollow titania (TiO₂) microrings

20 μ L of synthesized TiO₂ sol-gel precursor solution was drop cast onto cleaned FTO glass or Si substrates (see sections 3.2.1.1 and 3.2.1.2 for cleaning the substrates). Directly after deposition of the solution, the PDMS secondary mold attached to a steel block with double-sided polyimide tape was pressed against the precursor solution located on the FTO or Si substrates. Steel blocks with a weight of 40 g or 80g were used for different experiments. The whole setup was heated from RT to 250 °C in the air at a heating rate of 5°C/min, kept at 250°C for 2h and then cooled to 60 °C at a cooling rate of 5°C/min. The PDMS secondary mold and the steel block were detached at 60 °C. The TiO₂ microrings were then heated to 450°C at a heating rate of 5°C/min under ambient atmosphere and kept for 1 h at this temperature to obtain arrays of solvent-free and crystallized holey TiO₂ microrings.[166]

3.3.3.6 Fabrication of hollow gold (Au) microrings

To synthesize Au hollow microrings on cleaned Si substrates (see sections 3.2.1.2 for cleaning the substrates), 20 μ L of precursor solution was drop cast onto the cleaned Si substrates. Directly after deposition of the solution, the PDMS secondary mold attached to a steel block with double-sided polyimide tape was pressed against the precursor solution located on Si substrates. The whole setup was heated from RT to 140 °C in the air at a heating rate of 5°C/min, kept at 140°C for 2h and then cooled to 60 °C at a cooling rate of 5°C/min. The PDMS secondary mold and the steel block were detached at 60 °C. The microrings of Au were then heated to 450°C at a heating rate of 5°C/min under ambient atmosphere and kept for 1 h at this temperature.

3.3.4 Magnetic induced insect-inspired capillary nanostamping (MA-IICN)

3.3.4.1 Synthesis of zinc oxide tetrapods (T-ZnO)

Zinc oxide tetrapods (T-ZnO) was synthesized following the procedures reported elsewhere.[173, 174]

3.3.4.2 Fabrication of zinc oxide tetrapod (T-ZnO) pellets

For fabricating 3D ZnO pellets, 20mg of zinc oxide tetrapod (T-ZnO) powder was pressed in a mold (diameter, $d=13$ mm) with the help of a stainless-steel pressing tool carrying a mass m of approximately. 35 g, a diameter d of 13 mm and length l of approximately. 30 mm. The steel mold and a pressing tool of the Manual Hydraulic Press device (Graseby by Specac Limited) were used, as shown in Figure 3-8. The T-ZnO powder was pressed under a pressure of 0.65 kN m^{-2} in an ambient atmosphere for approximately 15 sec.



Figure 3-8 Fabrication of zinc oxide tetrapod (T-ZnO) pellets. (a) The stainless-steel pressing tool and (b) the resulting T-ZnO pellet with a diameter d of ≈ 13 mm and a thickness t of ≈ 1 mm.

3.3.4.3 Fabrication of PS-*b*-P2VP/T-ZnO porous composite stamps

Two porous composite stamps were fabricated with either tip as contact surfaces (TC) or holey contact surfaces (HC) as stamping layers.

3.3.4.3.1 Fabrication of PS-*b*-P2VP/T-ZnO porous composite stamps with a tip-like contact surface (TC)

A composite stamp consisting of block copolymer PS-*b*-P2VP stamping layer 2 attached to T-ZnO layer 1 is schematically shown in Figure 3-9a-f. The 3D T-ZnO pellet (diameter $d=13$ mm and thickness $t=1$ mm, mass $m=20$ mg) was heated for 1.25 h at 60 °C (Figure 3-9a). After heating, the pellet was removed and placed on a cleaned hydrophobic glass substrate (18*18 mm²). The pellet was infiltrated with 10 wt.% of PS-*b*-P2VP solution in toluene in two successive steps at room temperature (Figure 3-9b). 60 μL of PS-*b*-P2VP in toluene was infiltrated and kept under a petri dish on top. After a wait time of 10 minutes, the pellet was infiltrated again with 60 μL of PS-*b*-P2VP solution and then covered with a petri dish to slow evaporation. In total, 120 μL of a 10 wt.% solution of PS-*b*-P2VP in toluene was infiltrated in two steps in a T-ZnO pellet. The toluene was allowed to evaporate for 72 h at room temperature. In the next step, a PS-*b*-P2VP film was sandwiched between the infiltrated T-ZnO pellet and a surface-modified silicon master template with 0.9 μm pore diameter (mSi) (Figure 3-9c). The latter was hydrophobically modified with FDTs as described in section 3.2.1.3. As a result, the PS-*b*-P2VP bonded to T-ZnO layer 1 could be easily detached from the silicon master template with 0.9 μm pore diameter (mSi). The PS-*b*-P2VP film was prepared by drop-casting 140 μL of a 10 wt.% solution of PS-*b*-P2VP in toluene onto a superhydrophobic glass substrate (18*18 mm²). The superhydrophobic glass substrate was used for easy removal of PS-*b*-P2VP dried films. The toluene was allowed to evaporate for 72 h at room temperature. The whole sample consisted of a PS-*b*-P2VP film sandwiched between the T-ZnO infiltrated pellet. A surface-modified silicon master template was heated under a vacuum applying a pressure of 2.2 kN m⁻² on the sample using a weight. The sample was heated from room temperature to 200 °C at a heating rate of 5 °K/min and then kept for 1 min at 200 °C, then heated from 200 °C to 220 °C at a heating rate of 1 °K/min. After keeping for 2 h at 220 °C, the setup was cooled to room temperature at a cooling rate of -1 K/min. The composite stamp was detached from the

hydrophobic silicon master template by sonicating in ethanol for 5 mins (Figure 3-9d). The obtained PS-*b*-P2VP/T-ZnO composite stamp was treated with hot ethanol using a protocol established elsewhere [168, 169] to generate continuous nanopore systems in the PS-*b*-P2VP stamp layer 2 (Figure 3-9e). The PS-*b*-P2VP layer 2 bonded to T-ZnO layer 1 was treated with ethanol at 60 °C for 4 h. The ethanol is selective to P2VP domains and swells upon heating of PS-*b*-P2VP. The swelling of the P2VP domains leads to the plastic deformation of the non-swollen PS matrix. With changing the swelling time, the pores sizes can be tuned. The swelling-induced pore generation in PS-*b*-P2VP can result in volume expansion, which was prevented with the help of rigid T-ZnO reinforced support. Figure 3-10 shows the photograph of a PS-*b*-P2VP/T-ZnO composite stamp.

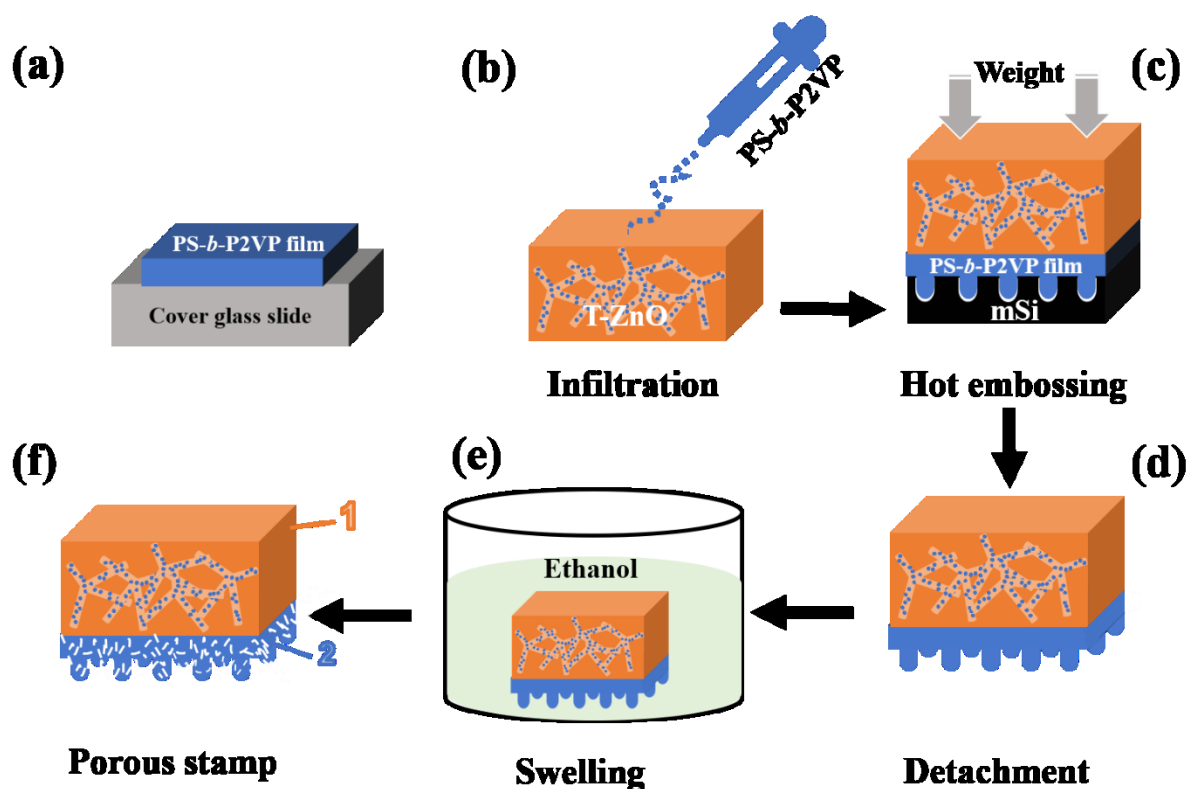


Figure 3-9 Schematic illustration of the fabrication of porous composite stamps consisting of block copolymer (PS-*b*-P2VP) and zinc oxide tetrapods (T-ZnO) composite. (a) PS-*b*-P2VP solution (blue) drying on a cover glass slide (grey) after drop cast. (b) Infiltration of PS-*b*-P2VP block copolymer solution into T-ZnO pellet (orange). (c) A PS-*b*-P2VP film is sandwiched between the infiltrated T-ZnO pellet and a hydrophobically modified silicon master template (mSi)(black) in a way that T-ZnO and mSi mold are in contact with the PS-*b*-P2VP. (d) The composite stamp (PS-*b*-P2VP/T-ZnO) was detached from the hydrophobically modified silicon master template after cooling to room temperature. (e) The PS-*b*-P2VP/ T-ZnO composite stamp is treated with hot ethanol to generate nanopores in PS-*b*-P2VP by

selective-swelling induced pore generation. (f) The result is a porous composite stamp system with T-ZnO layer 1 and PS-*b*-P2VP stamping layer 2.

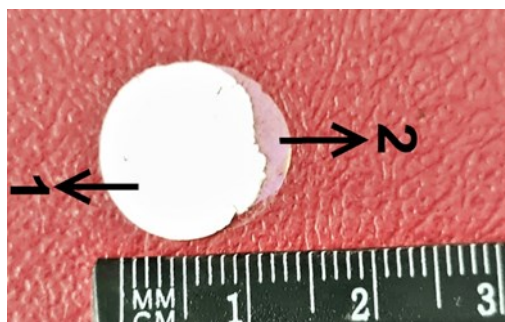


Figure 3-10 Photograph of a PS-*b*-P2VP/T-ZnO composite stamp. The porous T-ZnO layer 1 has a diameter $d=13$ mm. The porous PS-*b*-P2VP stamping layer 2 has a diameter of $d=13$ mm.

3.3.4.3.2 Fabrication of PS-*b*-P2VP/T-ZnO porous composite stamps with holey contact surfaces (HC)

The same procedure as described in section 3.3.4.3.1 was followed to fabricate composite stamps with holey contact surfaces. The PS-*b*-P2VP film was sandwiched between the T-ZnO infiltrated pellet and a secondary PDMS mold. All other steps were followed the same as described.

3.3.4.4 Stamping procedure

3.3.4.4.1 Stamp holder

A stamp holder made of aluminum having a length of approximately 35 mm with a weight of approximately 6 g was used. Figure 3-11 shows the stamp holder with a permanent external magnet (NdFeB, $6*1\text{mm}^2$ (diameter*height), Grade 52) embedded in a PDMS block layer (thickness $t \approx 5$ mm). The total weight is 6.9 g.



Figure 3-11 Photograph of stamp holder made of aluminum, having a PDMS layer with a permanent external magnet (NdFeB, $6 \times 1 \text{ mm}^2$ (diameter*height), Grade 52) embedded.

3.3.4.4.2 Stamping process

PS-*b*-P2VP/T-ZnO stamps with either tip contact surfaces (round or square-shaped) or with holey contact surfaces having round or square-shaped holes were used in the entire work. The same stamp holder (made of aluminum) was used in all setups I, II, and III (see below). Before inking, the backside of the PS-*b*-P2VP/T-ZnO composite nanoporous stamp, which is T-ZnO layer 2, was first treated with oxygen plasma for 2 min at 100 W. Then, approximately 24 μL of magnetic ink was infiltrated from the backside (T-ZnO layer 2) at RT and allowed for 3 min to infiltrate completely.

The complete wetting of the PS-*b*-P2VP layer verified the successful supply of ink from the T-ZnO backside. After infiltration with ink for 3 min at RT, the residual ink on the stamp was removed with a tissue. The easy flow of ink to the PS-*b*-P2VP layer from the T-ZnO layer may be due to the high porosity of the T-ZnO 3D pellet. The stamp is then glued to a PDMS layer already connected to the stamp holder with double-sided polyimide tape. The whole setup is brought into contact with the counterpart substrate for approximately 3-5 sec in the case of setups I, II, and III (Figure 3-12b) and 10 sec in the case of setup IV. The counterpart substrate was placed on PDMS support depending on the setup used. After conformal contact with the counterpart substrate, the whole stamp setup is detached (Figure 3-12c), resulting in the deposition of printed aggregates/square-array patterns on the counterpart substrate depending

on the used stamp and setup. The stamp's edges were cut with a scalpel to make it as smooth as possible before stamping. The stamping process presented in this work (setups I, II, and III) was carried out by hand. Hence, the stamping was performed by making the stamp contact with the counterpart surface with minimal or no pressure. The throughput was very high; at least 10 stamping cycles could be performed without re-inking. If not specified otherwise, stamps with a size of 5 x 5 mm² were used for every stamping process.

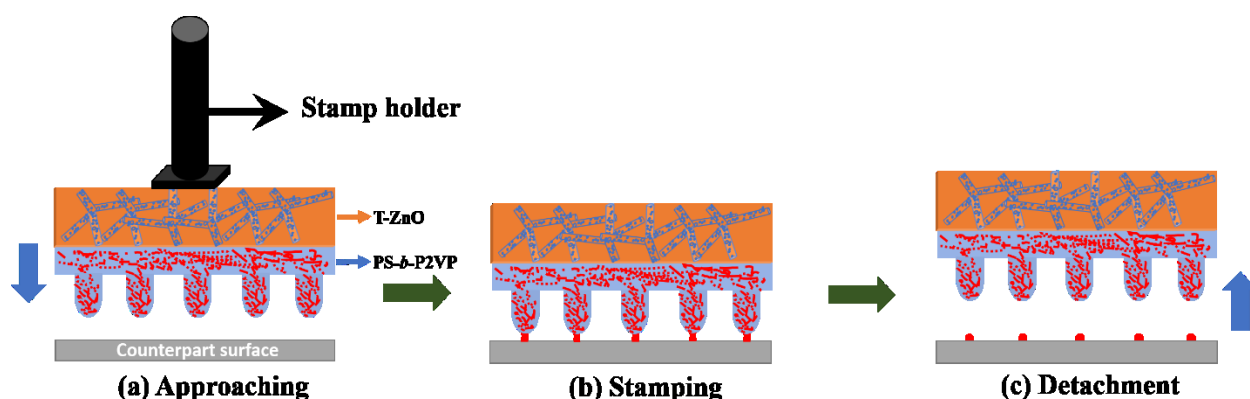


Figure 3-12 Illustration of a stamping process. (a; approach); the zinc oxide tetrapods (T-ZnO) and the porous PS-*b*-P2VP layer filled with magnetic ink (red, infiltrated from the backside). (b; Stamping) After infiltration with ink, the stamp is brought into contact with the counterpart substrate. (c; Detachment) The stamping step after conformal contact. After conformal contact with the counterpart, the stamp setup is detached, and printing aggregates on the substrate depending on the used stamp.

3.3.4.4.2.1 Setup I

The schematic in Figure 3-13 shows the setup I used for the stamping process with PS-*b*-P2VP/T-ZnO nanoporous composite stamps. The thickness of the PS-*b*-P2VP and T-ZnO layers of the PS-*b*-P2VP/T-ZnO nanoporous composite stamps is 0.065 mm and 1 mm, respectively. Before inking, the backside of the PS-*b*-P2VP/T-ZnO nanoporous composite stamp, which is the T-ZnO layer, was first treated with oxygen plasma for 2 min at 100 W. Then, approximately 24 μL of magnetic ink was infiltrated from the backside at RT and allowed for 3 min to infiltrate completely. The complete wetting of the PS-*b*-P2VP layer verified the successful supply of ink from the T-ZnO backside. After infiltration with ink for 3 min at RT, residual ink on the stamp was removed with a tissue. The stamp was now glued to a PDMS layer. The PDMS layer extended $10 \times 10 \text{ mm}^2$ and weighted approximately 0.58 g. The stamp glued to the PDMS layer was connected to a stamp holder with double-sided polyimide tape. The whole setup was brought into contact with the counterpart substrate. The counterpart substrate was placed on PDMS support. After conformal contact with the counterpart substrate, the whole stamp setup was detached and resulted in the deposition of aggregates or square arrays on the counterpart substrate depending on the used stamp.

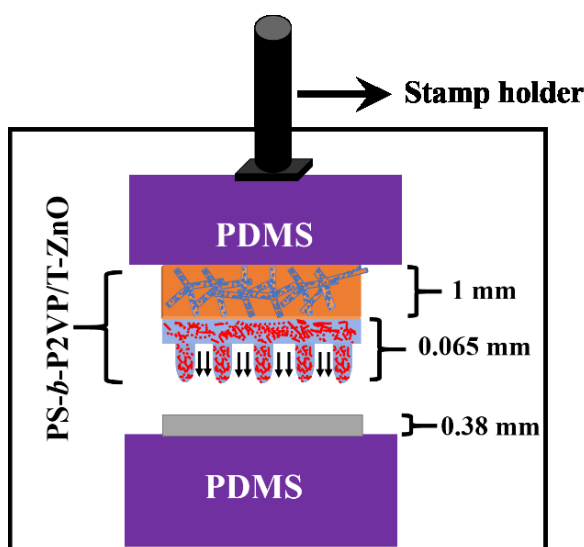


Figure 3-13 Schematic showing the experimental setup I for capillary stamping by PS-*b*-P2VP/T-ZnO nanoporous composite stamps. The zinc oxide tetrapods, T-ZnO, and block copolymer, PS-*b*-P2VP, are filled with magnetic ink (red, infiltrated from the backside). After infiltration with ink, the stamp is now glued to the PDMS layer. The stamp setup is brought into contact with the counterpart substrate. The counterpart substrate is placed on a PDMS support. The stamp setup after conformal contact with the counterpart substrate is detached. Depending on the used stamp, it results in aggregates/square arrays printed on the counterpart substrate.

3.3.4.4.2.2 Setup II:

The schematic in Figure 3-14 shows the setup II used for the stamping process referred to as magnetically induced stamping with PS-*b*-P2VP/T-ZnO nanoporous composite stamps. The stamp is brought into contact with the counterpart substrate. The counterpart substrate was placed on a PDMS support. All the dimensions and the setup were the same as the setup I, only with incorporating a permanent external magnet into the PDMS support placed below the counterpart substrate, as shown in Figure 3-14. After conformal contact with the counterpart substrate, the whole stamp setup was detached and resulted in aggregates/square arrays printed on the counterpart substrate depending on the used stamp.

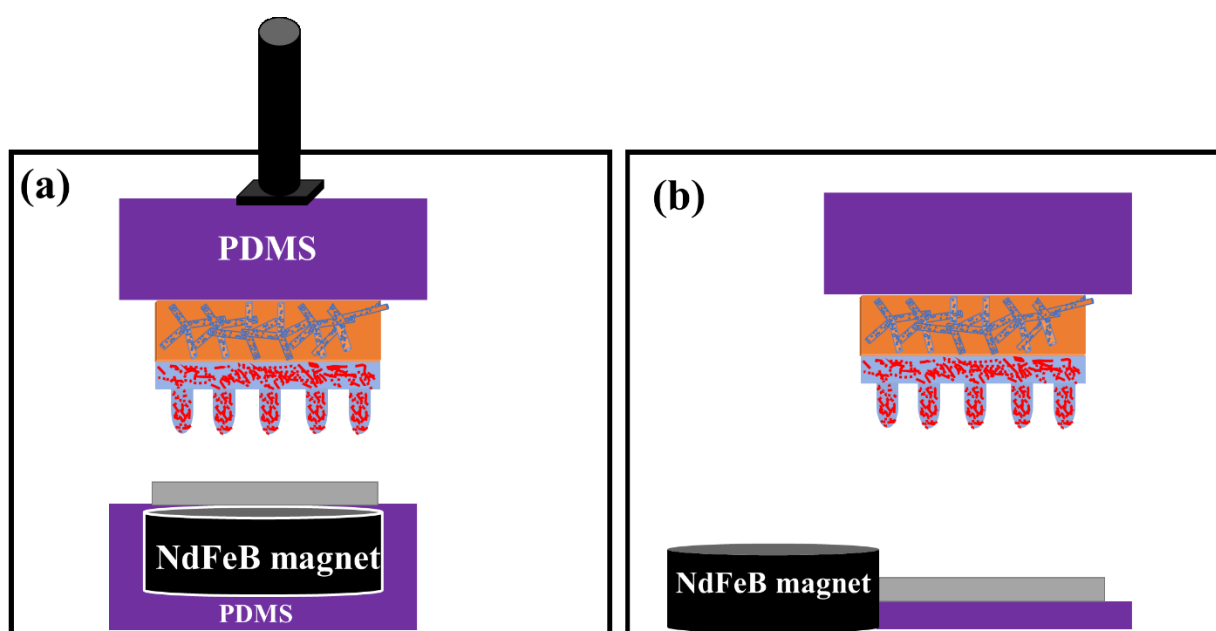


Figure 3-14 Schematic showing the experimental setup II for capillary stamping by PS-*b*-P2VP/T-ZnO nanoporous composite stamps. The zinc oxide tetrapods, T-ZnO, and block copolymer, PS-*b*-P2VP, are filled with magnetic ink (red, infiltrated from the backside). After infiltration with ink, the stamp is now glued to a PDMS layer. The stamp setup is brought into contact with the counterpart substrate. (a) **Out-of-plane geometry**, for generating a perpendicular magnetic field, the counterpart substrate is placed on external permanent magnets embedded in PDMS (NdFeB, 20*5mm² (diameter*height), Grade 52)). (b) **In-plane geometry** For generating a parallel magnetic field, the counterpart substrate is placed besides external permanent magnets embedded in PDMS (NdFeB, 20*5mm² (diameter*height), Grade 52)). After conformal contact with the counterpart, the stamp setup is detached, resulting in aggregates /square arrays printed on the counterpart substrate depending on the used stamp.

3.3.4.4.2.3 Setup III:

The schematic in Figure 3-15 shows the setup III used for the stamping process called magnetic induced stamping by means of PS-*b*-P2VP/T-ZnO nanoporous composite stamps. All the dimensions and the setup were the same as for setup II, only with the incorporation of a permanent external magnet (NdFeB, 6*1mm² (diameter*height), Grade 52)) into the PDMS layer glued to the stamp holder with double-sided polyimide tape. The stamp is brought into contact with the counterpart substrate. After conformal contact with the counterpart, the whole stamp setup is detached, resulting in the aggregates/square arrays printed on the counterpart substrate depending on the used stamp.

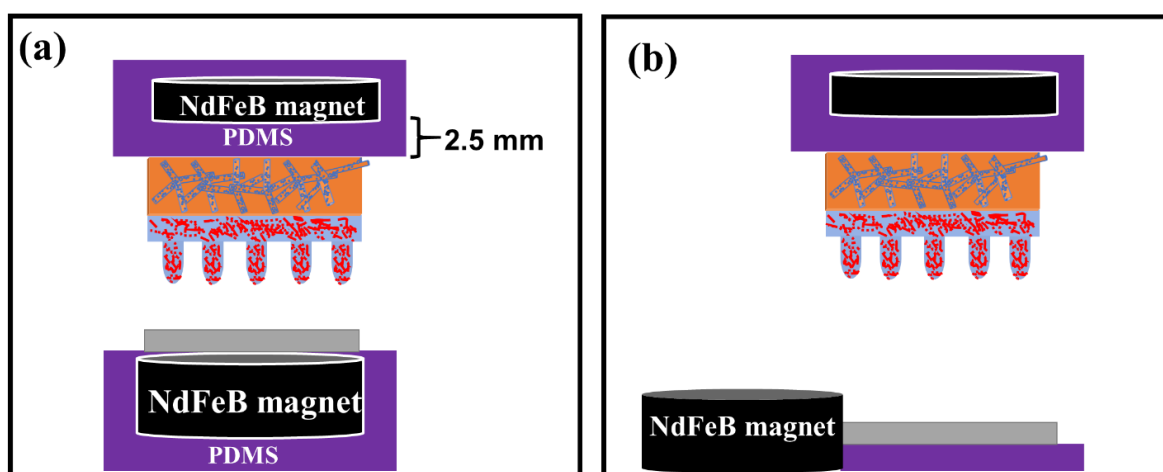


Figure 3-15 Schematic showing the experimental setup III for capillary stamping by means of PS-*b*-P2VP/T-ZnO nanoporous composite stamps. The zinc oxide tetrapods, T-ZnO, and the block copolymer, PS-*b*-P2VP, are filled with magnetic ink (red, infiltrated from the backside). After infiltration with ink, the stamp is now glued to a PDMS layer containing a small disc-like magnet (NdFeB, 6*1mm² (diameter*height), Grade 52)) glued to the stamp, and (a) **Out-of-plane geometry**, for generating a perpendicular magnetic field, the counterpart substrate is placed on external permanent magnets embedded in PDMS (NdFeB, 20*5mm² (diameter*height), Grade 52)). (b) **In-plane geometry**, for generating a parallel magnetic field, the counterpart substrate is placed besides external permanent magnets embedded in PDMS (NdFeB, 20*5mm² (diameter*height), Grade 52)). The stamp setup is brought into contact with the counterpart substrate. After conformal contact with the counterpart substrate, the stamp setup is detached, resulting in aggregates/square arrays printed on the counterpart substrate depending on the used stamp.

3.3.4.4.2.4 Setup-IV:

The schematic in Figure 3-16 shows the magnetic-induced stamping process by using a vibrating sample magnetometer (VSM). The PS-*b*-P2VP/T-ZnO nanoporous composite stamp is filled with magnetic ink (red, infiltrated from the backside). After infiltration with ink, the stamp (with contact surfaces facing towards silanized Si substrate) is first placed on silanized Si substrate attached with the help of PI tape. It is then glued to the sample holder rod. The printing was done by applying magnetic field H (for 10 sec), either in an **in-plane** or an **out-of-plane** geometry. In **in-plane** geometry, the stamp placed on silanized Si substrate was attached to the VSM sample rod so that Si substrate was fixed with the VSM sample holder, as shown in Figure 3-16a. For the **out-of-plane** geometry, the VSM sample holder with a stamp was rotated by an angle of 80° . The infiltrated ink stamp and the silicon counterpart surface attached to the VSM sample rod were placed carefully at the central position between two pickup coils.

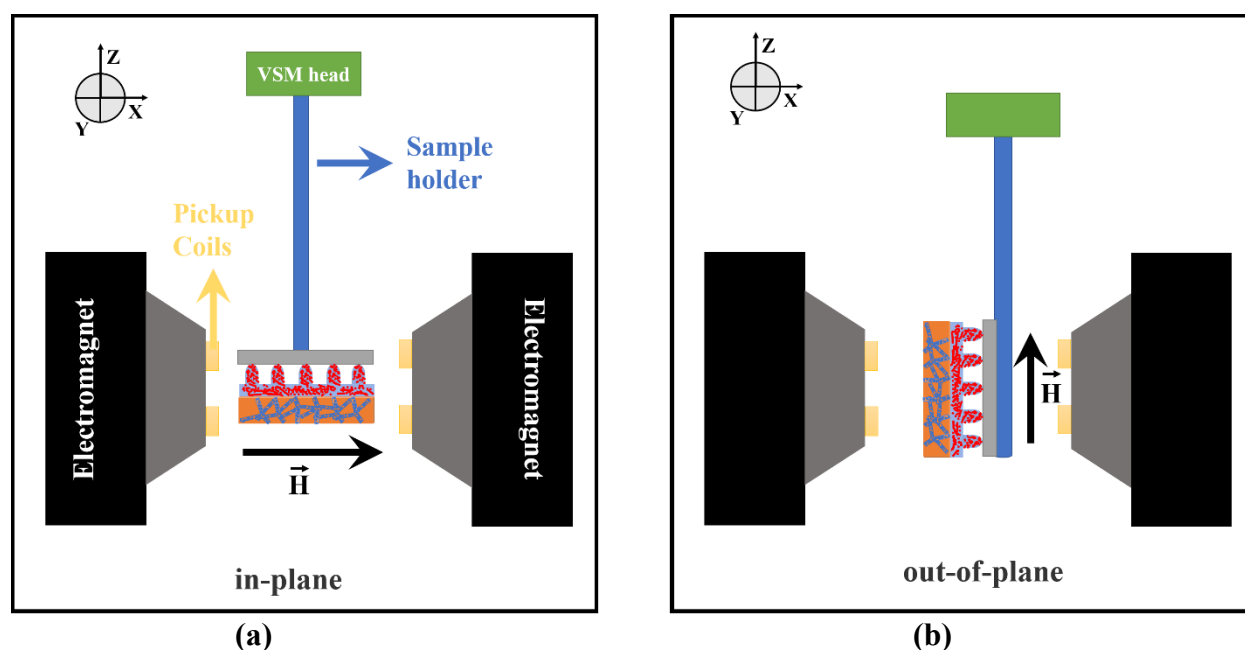


Figure 3-16 The schematic shows the magnetic-induced stamping process IV with PS-*b*-P2VP/T-ZnO nanoporous composite stamps using a vibrating sample magnetometer (VSM). After infiltration with ink, the stamp is glued to the VSM sample holder. Then printing was done by applying magnetic field H . (a) **in-plane geometry** and (b) **out-of-plane geometry**.

4 Topographically patterned TiO₂ substrates as a platform for wetting metamaterials

4.1 Patterned TiO₂ holey films

Patterned titania (*p*TiO₂) holey film was fabricated by direct imprinting [166] as described in section 3.3.1.3. 20 μ L of the synthesized TiO₂ sol-gel precursor solution was drop-cast onto cleaned FTO glass (see section 3.2.1.1 for the cleaning procedure). Directly after deposition of TiO₂ sol, the PDMS secondary mold attached to a steel block with double-sided polyimide tape was pressed against the TiO₂ sol-gel precursor solution located on FTO glass (see Figure 3-1a-d; section 3.3.1.3). Macropores in the film of the precursor sol-gel solution were obtained at the positions of PDMS pillars by direct imprinting. In the next step, patterned TiO₂ holey films were formed by calcination; the samples were heated to 450°C at a heating rate of 5°C/min and kept for 1 h at this temperature under the ambient atmosphere. The decomposition of the block copolymer template resulted in the formation of mesopores. Silanized macroporous silicon templates (mSi) were used as primary molds containing hexagonal arrays of macropores. The macropores with round pore bottoms had pore lengths of \approx 800nm, pore diameters of \approx 900nm, and interpore distances of \approx 1.5 μ m (Figure 4-1a-b). PDMS secondary molds were obtained by pouring PDMS prepolymer onto silanized mSi. After curing, the PDMS molds had pillars at the positions of the mSi macropores. The depth (\approx 800nm) and base diameter (\approx 900nm) of the PDMS pillars (Figure 4-1c-d) matched the dimensions of the macropores of the primary mSi molds. SEM images of *p*TiO₂ holey films fabricated by imprinting with PDMS secondary molds and subsequent thermal treatment are shown in Figure 4-1e-h. The pore diameter of the *p*TiO₂ macropores is \approx 890nm, and the interpore distance is \approx 1.5 μ m (Figure 4-1f). The thickness of the *p*TiO₂ holey film is approx. 500-530nm, and the pore depth amounted to \approx 400-415nm (Figure 4-1h). The decrease in the depth and diameter of the macropores in the *p*TiO₂ holey films compared to the mSi macropores is related to the decomposition of organic materials during imprinting and annealing.[30] During thermal imprinting and annealing, the decomposition of the organic components and the evaporation of the solvents results in shrinkage. The transferred TiO₂ imprint patterns were of high quality without any cracks or delamination from the FTO glass substrate. The delamination experiments were conducted by adhering polyimide tape on top of *p*TiO₂ holey films on the FTO glass substrates and then detaching them from the substrates.

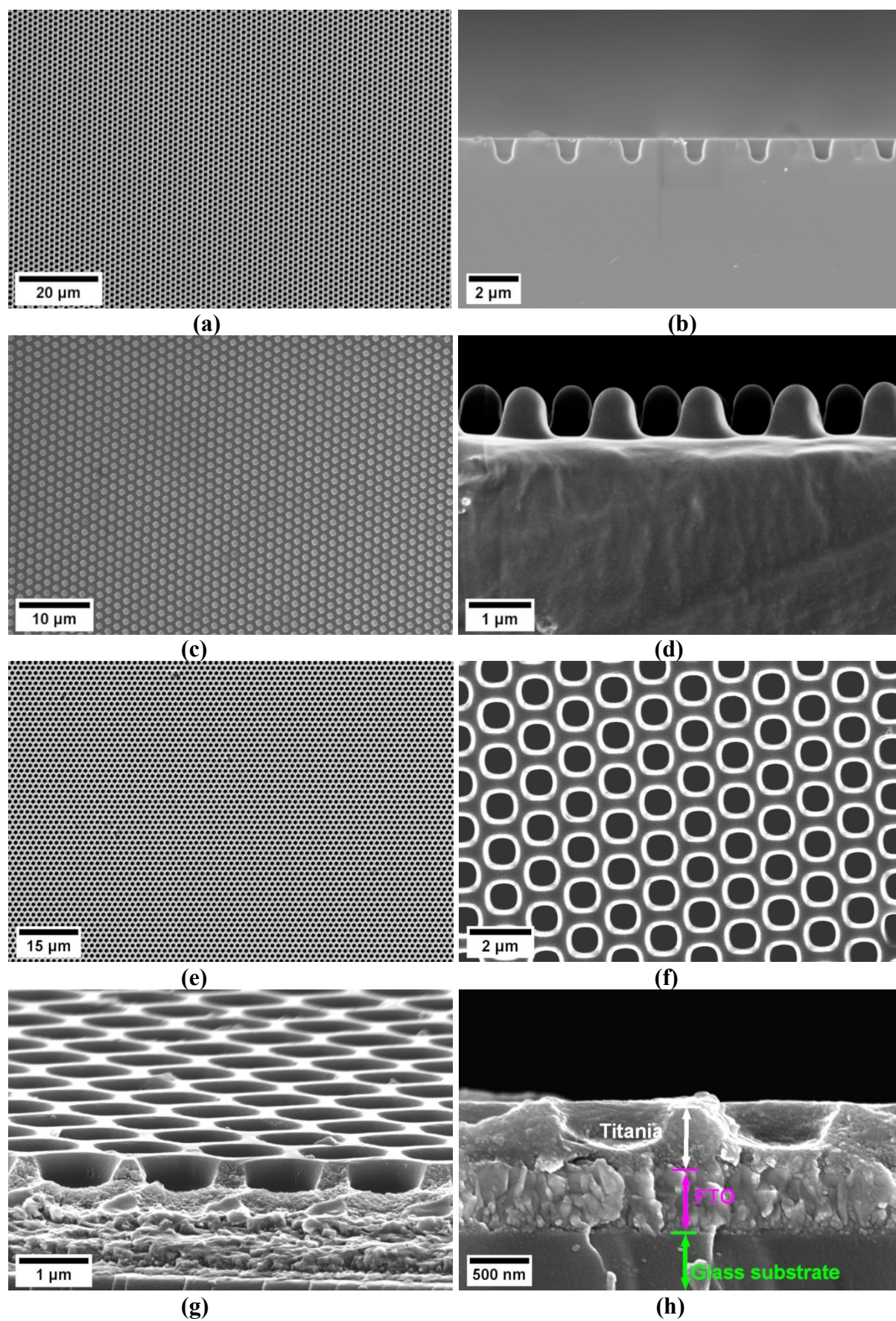


Figure 4-1 Patterned titania (*p*TiO₂) holey films and their preparation. Scanning electron microscopy (SEM) images of (a) the surface and (b) a cross-section of macroporous silicon (mSi) primary molds, of (c) the surface and (d) a cross-section of PDMS secondary molds as well as (e, f) the surface and (g, h) the cross-section of a (*p*TiO₂) holey film.

The X-ray diffraction (XRD) pattern of a synthesized TiO₂ sample annealed at 450 °C is shown in Figure 4-2. The TiO₂ sol-gel solution was deposited on a cleaned FTO glass substrate and then treated thermally. The thermal treatment followed is the same procedures as in the case of the fabrication of patterned TiO₂ holey films (see section 3.3.1.3). After the thermal treatment, the TiO₂ film was scratched with the help of a scalpel from the FTO substrate so that it was obtained in powder form for further analysis. The crystalline nature of the sample was confirmed by the occurrence of well-defined sharp Bragg diffraction peaks. By comparison with reference spectrum ICSD # 202243, the diffraction peaks at 2θ values of 25.28°, 37.78°, 48.05°, 53.88°, 54.77°, 62.55°, 68.77°, 70.11°, and 75.07° were assigned to the (101), (004), (200), (105), (211), (204), (116), (220), and (215) reflections of tetragonal anatase with the space group I41/amd. The absence of reflections emerging from other polymorphs such as rutile or brookite indicated the exclusive presence of anatase. The obtained XRD pattern agrees with previously reported XRD patterns of sol-gel synthesized TiO₂ annealed at 450°C.[166] The mean crystallite size of TiO₂ along the [101] direction estimated by the Debye-Scherrer method amounted to ≈ 8.2 nm, and lies close to values reported previously.[162]

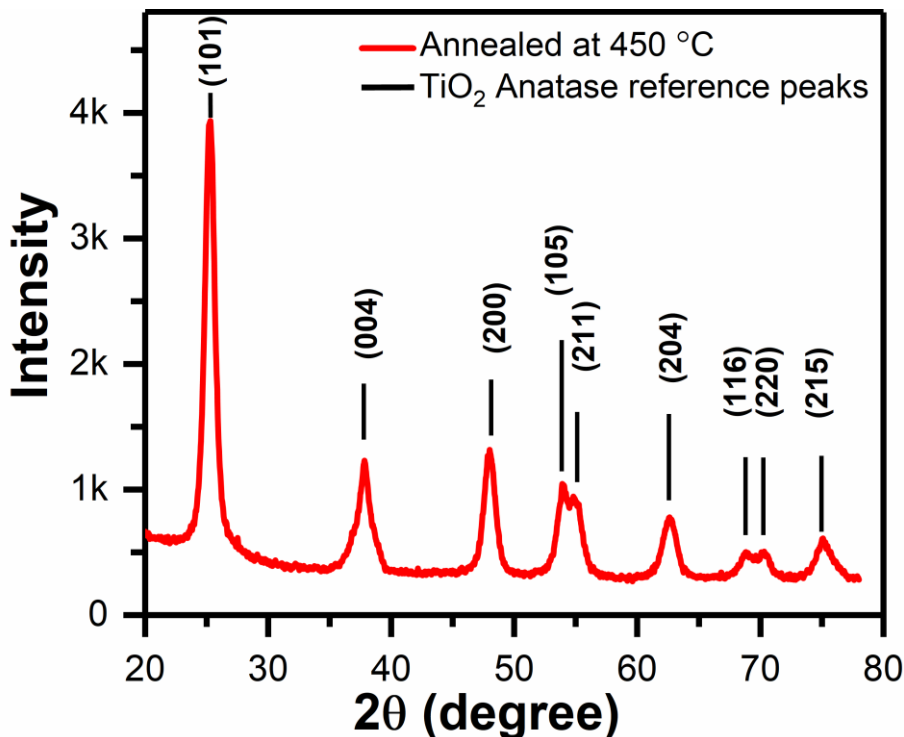


Figure 4-2 X-ray diffraction (XRD) pattern of sol-gel synthesized titania (TiO₂) showing the typical features of the anatase phase (ICSD # 202243).

Nitrogen sorption analysis of a TiO₂ sample annealed at 450 °C is shown in Figure 4-3. The sample was prepared in the same way as for XRD measurements. The Brunauer-Emmett-Teller (BET) isotherm in Figure 4-3a indicates a variety of a type IV isotherm with an H2 hysteresis,[175] which stands in good agreement with previously reported results.[162, 176] The hysteresis loop is typical of mesoporous materials that contain relatively uniform mesopores with a narrow diameter distribution. Figure 4-3b shows the pore size distribution. The mesopore size ranges between 5-10nm, with a most frequent pore size of approximately 7 nm. The BET surface area amounts to $\approx 99\text{m}^2.\text{g}^{-1}$. The porosity of the mesoporous TiO₂ amounted to $\approx 64.8\%$, as calculated according to $P = V_t / (V_t + V_{anatase}^*) \times 100$, [162] where P is the porosity. The total pore volume V_t is derived from the desorption branch of the isotherm at a relative pressure (p/p_0) value close to unity ($V_t \approx 0.48\text{ mL/g}$ at $p/p_0 = 0.994$). $V_{anatase}^*$ is the theoretical volume of solid pure anatase per gram and is determined by using equation $V_{anatase}^* = 1/\rho_{anatase}$ [162] The density $\rho_{anatase}$ of anatase was assumed to be 3.89g cm^{-3} . [177]

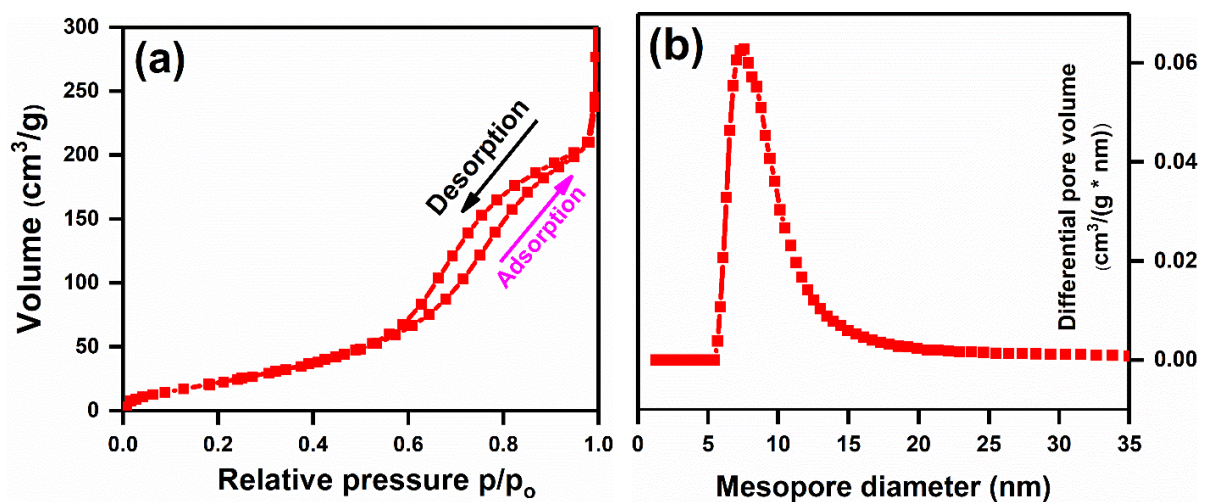


Figure 4-3 Nitrogen sorption measurements on mesoporous titania (TiO₂) powder synthesized by the sol-gel process a) BET isotherm (b) The Barret-Joyner-Halenda (BJH) pore size distribution derived from the adsorption branch of the BET isotherm, which shows a relatively narrow peak.

4.1.1 Self-assembly of SiO₂ microparticles inside TiO₂ holey films (*p*TiO₂-SiO₂ template)

Silica (SiO₂) microparticles with different sizes were deposited into each *p*TiO₂ macropore (*p*TiO₂-SiO₂ template) with the method described in section 3.3.1.3.1. Depending on the size of SiO₂ microparticles, a different arrangement was achieved and is shown in Figure 4-4a-d. SiO₂ microparticles within each pore adjusted their positions to form different arrangements. SiO₂ microparticles with diameters of 50nm and 143nm arranged themselves very homogeneously and well embedded (Figure 4-4a and 4-4b, respectively). However, different arrangements occurred in the case of SiO₂ microparticles with diameters of 501nm and 985nm. In the former case, the SiO₂ microparticles arranged themselves in two possible square and square arrangements with one additional particle on the bottom (Figure 4-4c). This pattern is not very regular because of the possibility of two different microparticle arrangements. A considerable portion of the macropores was filled with tetramer patterns. In the latter case, only a single SiO₂ microparticle (985nm) was located inside each macropore (Figure 4-4d). In the case of SiO₂ microparticle sizes of 50nm and 143nm, the confinement effect resulted in a stronger packing order of microparticles inside each pore. In the case of microspheres with a diameter of 501nm, the packing order fluctuated from stronger to weaker. The amino-functionalized silica (SiO₂-NH₂) microparticles with a diameter of 976 nm, which can further be functionalized selectively, were also successfully infiltrated into the macropores (not shown here).

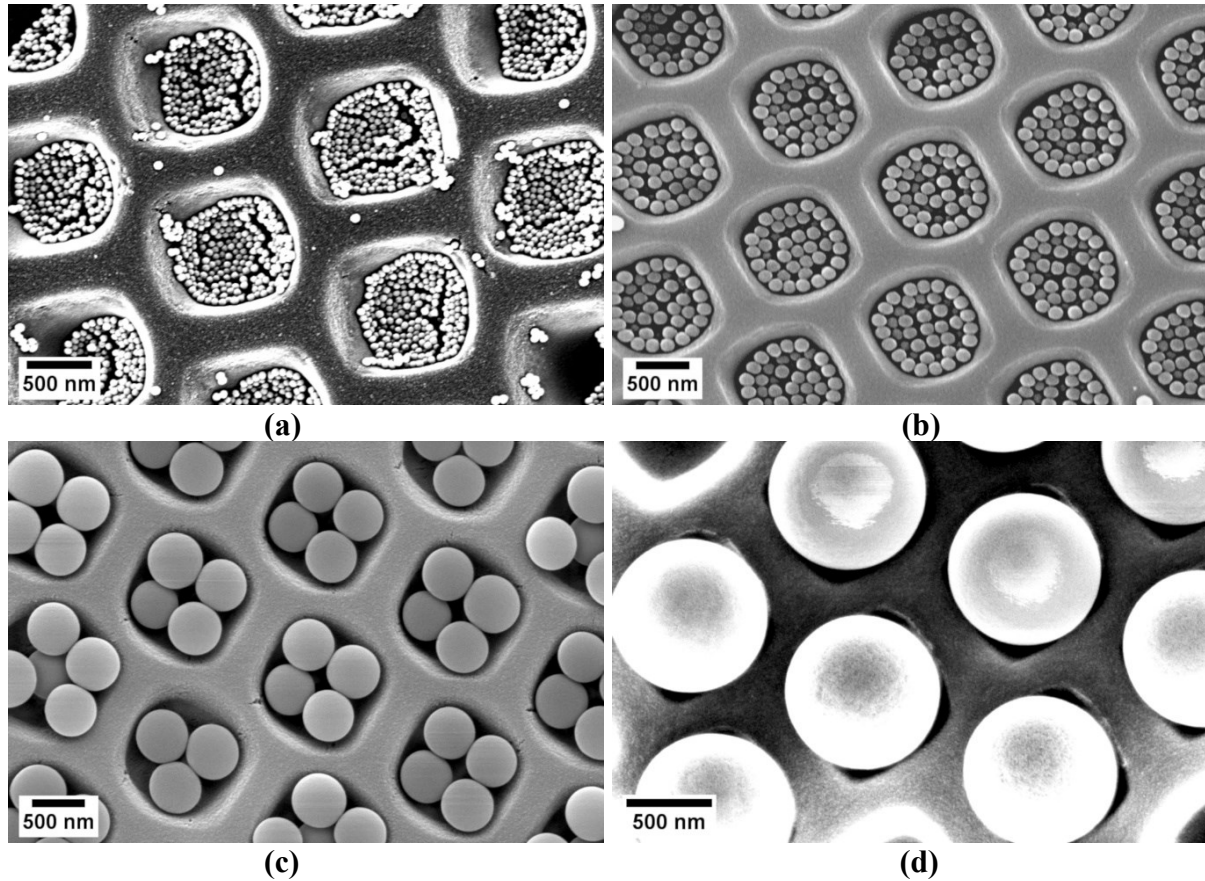


Figure 4-4. SEM (SEM) images of patterned titania films ($pTiO_2$) with macropores containing silica microspheres with different diameters of a) 50nm, ($pTiO_2_SiO_2(50nm)$) b) 143nm ($pTiO_2_SiO_2(143nm)$), c) 501nm ($pTiO_2_SiO_2(501nm)$) and d) 985nm ($pTiO_2_SiO_2(985nm)$).

4.1.1.1 Surface Chemistry of $pTiO_2_SiO_2$ templates

Three different routes were applied for changing the surface chemistry of TiO₂ holey film filled with SiO₂ microparticles ($pTiO_2_SiO_2$ template).

- (1) Adsorption of hydrophobic molecules on $pTiO_2_SiO_2$ template,
- (2) PS-*b*-P2VP polymeric rods in $pTiO_2_SiO_2$ template,
- (3) Gold metallic layer on SiO₂ microparticles in $pTiO_2_SiO_2$ template.

4.1.1.1.1 Adsorption of hydrophobic molecules on $pTiO_2_SiO_2$ templates

The $pTiO_2_SiO_2$ templates containing different sizes of SiO₂ microparticles “ $pTiO_2_SiO_2(50nm)$, $pTiO_2_SiO_2(143nm)$, $pTiO_2_SiO_2(501nm)$, and $pTiO_2_SiO_2(985nm)$ ” templates

were modified with three different hydrophobic molecules (cycloazasilane, FDTS, and with 1-dodecanethiol). Corresponding wide-scan X-ray photoelectron (WS-XP) spectra and high-resolution X-ray photoelectron (HR-XP) spectra are shown in Figures 4-5, 4-6 and 4-7. The WS-XP and HR-XP spectra of *p*TiO₂_SiO₂ (143nm) modified with cycloazasilane (“*p*TiO₂_SiO₂ (143nm)@cycloazasilane”) are shown in Figure 4-5a-f. The wide-scan XP spectrum shows peaks from all elements present in *p*TiO₂_SiO₂ (143nm)@cycloazasilane templates. The Si 2p peak of elemental silicon is known to appear at binding energy (B.E) of ≈ 99.6 eV.[178] Here, the Si 2p peak is shifted to the binding energy of ≈ 101.7 eV (Figure 4-5b). The appearance of the Si 2p peak within the binding energy range of 102-105 eV indicates the presence of SiO_x. [179] Lorentz fits of the O 1s peak in the corresponding HR-XP spectrum (Figure 4-5c) revealed the presence of two peaks assigned to lattice oxygen ions O²⁻ at a binding energy of ≈ 529.8 eV and to surface oxygen species chemically adsorbed, such as OH⁻ and carbonates at a binding energy of ≈ 531.7 eV.[180, 181] Figure 4-5d shows the HR-XP spectrum around the nitrogen N 1s peak. Lorentz fits revealed the presence of two N 1s peaks. The peak at a binding energy of ≈ 399.1 eV is attributed to the primary photoemission of N 1s, which can be assigned to NH₂, and the small peak at a binding energy of ≈ 400.4 eV is assigned to protonated or hydrogen-bonded amine groups (NH₃⁺, H...NH₂).[182-185] The HR-XP spectrum of the carbon C 1s peak is shown in Figure 4-5e and was also used to calibrate the XPS spectra. The C 1s peak was set to ≈ 284.5 eV.[186] Figure 4-5f shows an HR-XP spectrum containing the doublet separation between the Ti 2p_{1/2} and Ti 2p_{3/2} peaks at binding energies of ≈ 463.9 eV and ≈ 458.3 eV, respectively. The peak at a binding energy of 458.3 eV correlates with (titanium in the IV oxidation state) in TiO₂. [187]

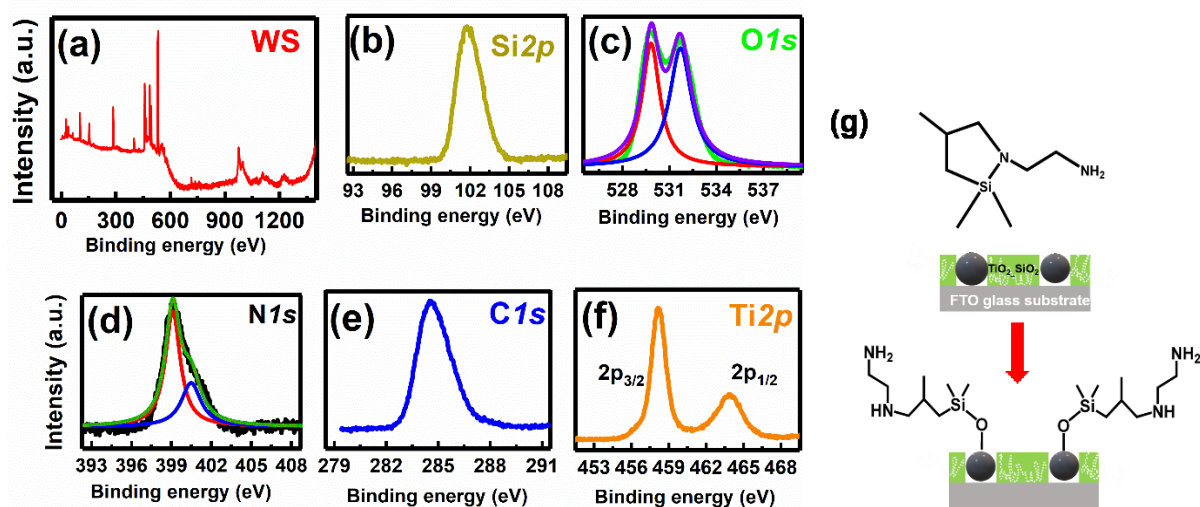


Figure 4-5 Wide-scan X-ray photoelectron (WS-XP) spectra and high-resolution X-ray photoelectron (HR-XP) spectra for a sample prepared by adsorption of cycloazasilane from toluene solution onto a *p*TiO₂/SiO₂ (143nm) template. (a) WS-XP spectrum, and (b-f) HR-XP spectra. (b) HR-XP spectrum of silicon 2p, and (c) HR-XP spectrum of oxygen 1s, where the purple curve is the sum of the red and blue curves showing good Lorentz fitting. (d) HR-XP spectrum of nitrogen 1s, where the green curve is the sum of the red, and blue curves show good Lorentz fitting. HR-XP spectra of (e) carbon 1s and (f) titanium 2p peaks. (g) Illustrations of cycloazasilane and a schematic sketch of adsorption on the template. Origin was used for fitting (Lorentz) and analyzing the XP spectra.

The WS-XP and HR-XP spectra of a *p*TiO₂/SiO₂(143nm) template modified with FDTS are shown in Figure 4-6a-f. The HR-XP spectrum of carbon C 1s (Figure 4-6b) shows four peaks. The corresponding Lorentz fits revealed the presence of a peak at a binding energy $\approx 292.1.8$ eV assigned to -CF₃ of a peak at a binding energy of the energy of ≈ 289.4 eV assigned to -CF₂, of a peak at a binding energy of ≈ 286.5 eV assigned to C=O and of a peak at a binding energy of ≈ 284.5 eV assigned to C-C. The components -CF₃ and -CF₂ can be attributed to functional groups in the FDTS molecules.[188-190] Lorentz fitting of an HR-XP spectrum measured around the O 1s peak revealed the presence of two peaks (Figure 4-6c). The peak at a binding energy of ≈ 529.7 eV is assigned to lattice oxygen ions O²⁻ and at a binding energy of ≈ 531.8 eV to surface oxygen species chemically adsorbed, such as OH⁻ and carbonates.[180, 181] The silicon Si 2p peak appears at a binding energy of ≈ 102.3 eV (Figure 4-6d), which indicates the presence of SiO_x. [179] Figure 4-6e shows the HR-XP spectrum around the fluorine 1s peak observed at a binding energy of ≈ 687.2 eV, further confirming the successful surface modification of *p*TiO₂/SiO₂(143nm) templates with FDTS. The position of the fluorine 1s peak is in line with previously reported values.[191] The HR-XP spectrum around the titanium Ti 2p photoelectron peaks shows the doublet separation between the 2p_{1/2} and 2p_{3/2}. The Ti 2p_{1/2} and 2p_{3/2} peaks appeared at binding energies of ≈ 463.9 eV and ≈ 458.2 eV (Figure 4-6f). The peak at a binding energy of 458.3 eV correlates with (titanium in the IV oxidation state) in TiO₂. [188]

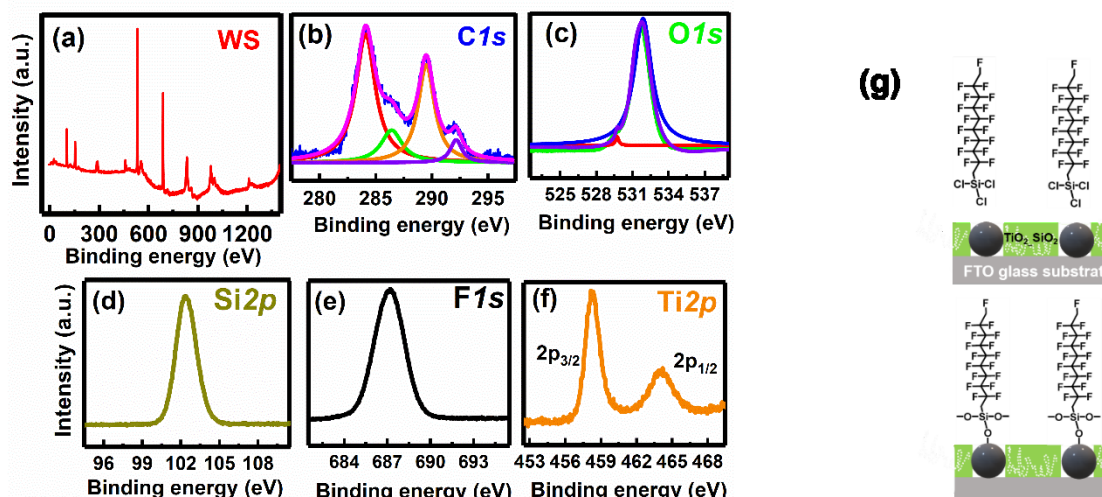


Figure 4-6 Wide-scan X-ray photoelectron (WS-XP) spectra and high-resolution X-ray photoelectron (HR-XP) spectra of a $p\text{TiO}_2/\text{SiO}_2(143\text{nm})$ template surface-modified with FDTs. (a) WS-XP spectrum, and (b-f) HR-XP spectra. (b) HR-XP spectrum the carbon 1s, where the pink curve is the sum of the green, orange, purple and red curves showing good Lorentz fitting. (c) HR-XP spectrum of the oxygen 1s, where the purple curve is the sum of the red, and blue curves show good Lorentz fitting. HR-XP spectra of (d) the silicon 2p, (e) the fluorine 1s, and (f) the titanium 2p peaks. (g) Illustrations of perfluorodecyltrichlorosilane and a schematic sketch of adsorption on the template. Origin was used for fitting (Lorentz) and analyzing the XP spectra.

The WS-XP and HR-XP spectra of a $p\text{TiO}_2/\text{SiO}_2(143\text{nm})$ template surface-modified with 1-dodecanethiol are shown in Figure 4-7a-e. The HR-XP spectrum of the carbon C 1s peak was used to calibrate the XPS spectra by setting the C 1s peak to 284.5 eV.[186] (Figure 4-7b). The oxygen O 1s peak at a binding energy of 531.9 eV is shown in Figure 4-7c. The gold Au 4f photoelectron spectrum shows a doublet separation between the $4f_{5/2}$ and $4f_{7/2}$. The $4f_{5/2}$ and $4f_{7/2}$ peaks occur at binding energies of ≈ 87.2 eV and ≈ 83.5 eV respectively (Figure 4-7d). The peak $4f_{5/2}$ represents the stable oxidation states of gold.[192] Figure 4-7e shows the HR-XP spectrum around the sulfur 2p peaks with a doublet structure. Lorentz fits revealed the presence of the $2p_{3/2}$ and the $2p_{1/2}$ at binding energies of ≈ 162.9 eV and ≈ 161.4 eV, respectively, which can be assigned to sulfur atoms bound to a gold surface.[193-198]

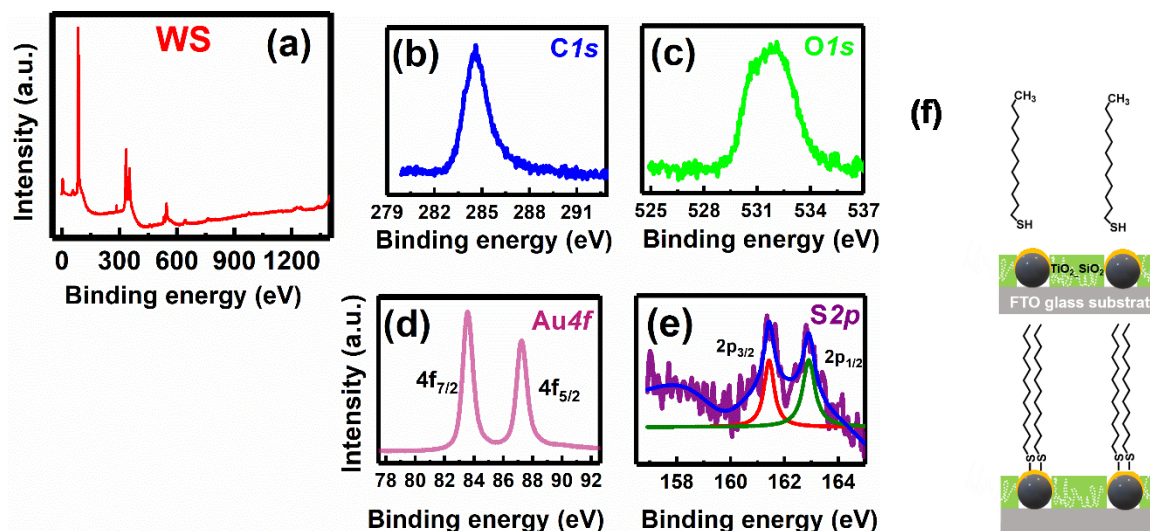


Figure 4-7 Wide-scan X-ray photoelectron (WS-XP) spectra and high-resolution X-ray photoelectron (HR-XP) spectra for a sample prepared by adsorption of the 1-Dodecanethiol molecule from toluene solution onto the $p\text{TiO}_2\text{-SiO}_2(143\text{nm})$ template. (a) The WS-XP spectrum, and (b-e) HR-XP spectra. HR-XP spectra of (b) carbon 1s, (c) oxygen 1s, (d) gold 4f. and (f) HR-XP spectrum of sulfur 2p, where the blue curve is the sum of the green, and red curves show good Lorentz fitting. Illustrations of 1-dodecanethiol and a schematic sketch of adsorption on the template Origin were used for fitting (Lorentz) and analyzing the XP spectra.

4.1.1.1.2 PS-*b*-P2VP polymeric rods in $p\text{TiO}_2\text{-SiO}_2$ templates

The schematic illustration shown in (Figure 3-3, see section 3.3.1.3.2) displays the fabrication of a $p\text{TiO}_2\text{-SiO}_2(143\text{nm})$ template filled with PS-*b*-P2VP rods. A $p\text{TiO}_2\text{-SiO}_2(143\text{nm})$ template was used, which was first modified with FDTs for easy detachment of polymeric film (see section 3.2.1.3 for modification procedure). A solution of PS-*b*-P2VP in toluene was cast on a modified $p\text{TiO}_2\text{-SiO}_2(143\text{nm})$ template. After complete evaporation of the solvent, the PS-*b*-P2VP bulk film was detached with scalpels to obtain sample $p\text{TiO}_2\text{-SiO}_2(143\text{nm})@\text{FDTs}@PS\text{-}b\text{-P2VP}$. SEM images of PS-*b*-P2VP rods emerging from a modified $p\text{TiO}_2\text{-SiO}_2(143\text{nm})$ template are shown in Figure 4-8 (a-c). Mostly, the PS-*b*-P2VP rods emerge from the small spaces between silica microparticles. PS-*b*-P2VP rods can be found in almost every filled macropore.

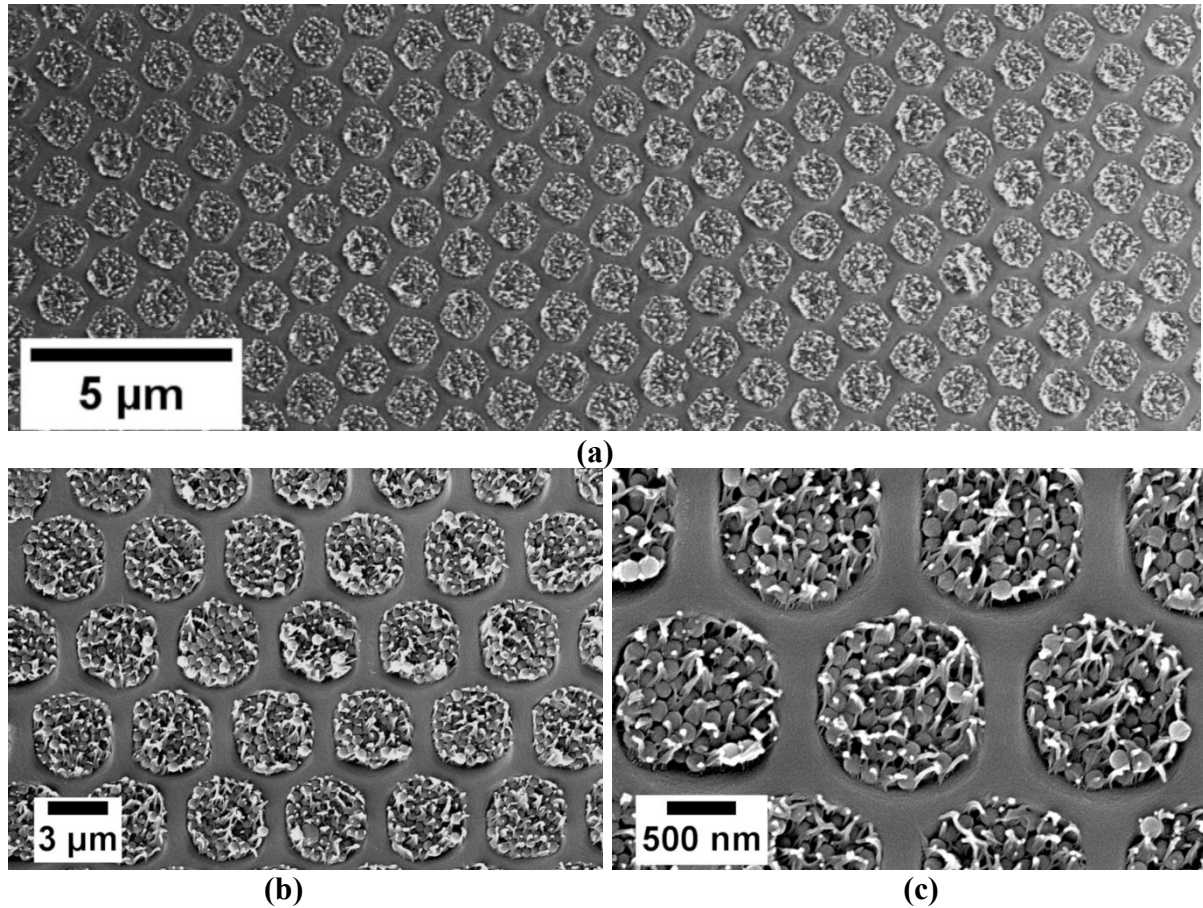


Figure 4-8 SEM images of PS-*b*-P2VP polymeric rods emerging from a modified $p\text{TiO}_2\text{-SiO}_2(143\text{nm})$ template; (a) large-field view and (b, c) details.

4.1.1.1.3 Gold metallic layer on SiO₂ microparticles in $p\text{TiO}_2\text{-SiO}_2$ templates

The SiO₂ (143nm) microparticles inside each macropore of $p\text{TiO}_2$ film were coated with a gold (Au) metallic layer by thermal evaporation (Figure 3-2, see section 3.3.1.3.2). A ≈ 20 nm thick Au layer was deposited after deposition of 5 nm Ti layer serving as adhesion promotor. The thickness of the Ti and Au layers was estimated by using the method described elsewhere.[159] The top-view SEM image of SiO₂ (143nm) microparticles coated with the Au metallic layer in $p\text{TiO}_2$ macropores by thermal evaporation is shown in Figure 4-9a. The uppermost silica microparticles located inside the $p\text{TiO}_2$ macropores are half-coated with a metallic Au layer. Figure 4-9b shows a cross-sectional SEM image of the Janus microparticles obtained in this way.

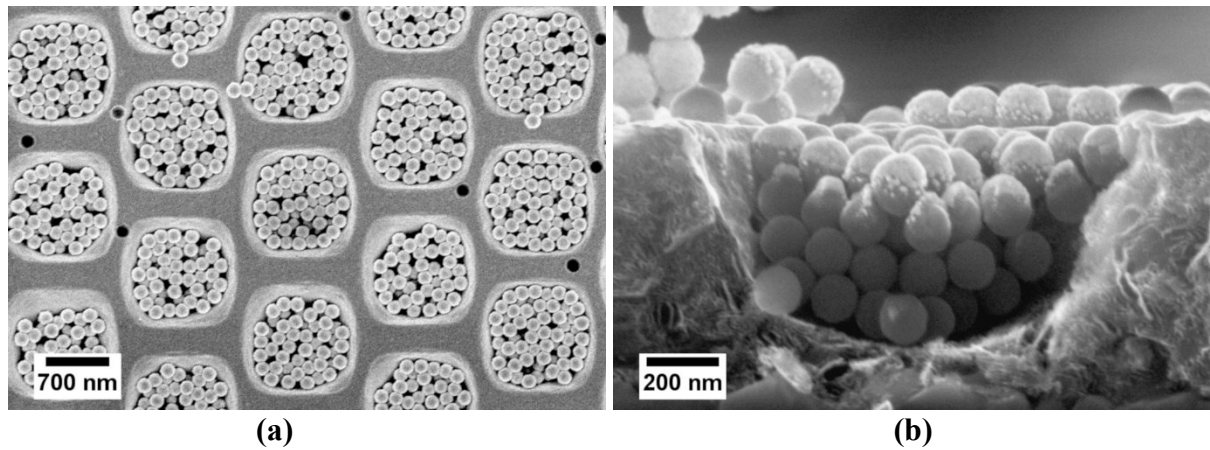


Figure 4-9 Schematic showing thermal evaporation setup for deposition of gold (Au) layer on SiO₂ microparticles in $p\text{TiO}_2\text{-SiO}_2(143\text{nm})$ template (a), and (b) the resulted $p\text{TiO}_2\text{-SiO}_2(143\text{nm})@Au$ template after thermal evaporation. SEM images of 143nm SiO₂ microparticles inside each $p\text{TiO}_2$ macropore coated with $\approx 20\text{nm}$ gold metal ($p\text{TiO}_2\text{-SiO}_2(143\text{nm})@Au$ template); (c) large-field top view, and (d) cross-section.

4.2 Applications

4.2.1 Water wettability

Figure 4-10 shows the changes in the apparent water contact angles after different surface treatments of $p\text{TiO}_2$ -based samples, and images of quiescent water drops on these samples are shown in Figure 4-11. A smooth titania film fabricated without imprinting with a PDMS stamp (without any regular holey arrays pattern, $w\text{pTiO}_2$) shows hydrophilic characteristics with an average θ_{WCA} of $\approx 25.6^\circ \pm 4.6^\circ$. The apparent θ_{WCA} increased from $\approx 25.6^\circ \pm 4.6^\circ$ to $\approx 108.5^\circ \pm 3.1^\circ$ when the titania film is imprinted with the PDMS stamp (TiO_2 patterning, $p\text{TiO}_2$). The hydrophobic characteristic displayed by $p\text{TiO}_2$ holey films is due to the difference in surface topography, and the interactions of the water and the solid at the three-phase contact line determine the contact angle behavior. The wettability of $p\text{TiO}_2$ holey films changed from hydrophobic to super-hydrophilic characteristics after deposition of different sizes of SiO₂ microparticles into the $p\text{TiO}_2$ macropores ($p\text{TiO}_2\text{-SiO}_2$). Water now spreads on the template. The $p\text{TiO}_2\text{-SiO}_2$ template surface, which is completely wet by water, can be converted in such

a way that it shows hydrophobic characteristics by surface modification with hydrophobic molecules (see section 3.3.1.3.2). The apparent θ_{WCA} of $pTiO_2_SiO_2(143nm)$ templates is $\approx 0^\circ$. The apparent θ_{WCA} of $pTiO_2_SiO_2(143nm)$ templates was increased from $\approx 0^\circ$ to $\approx 95.5^\circ \pm 5.0^\circ$ after surface modification with the cycloazasilane ($pTiO_2_SiO_2(143nm)@cycloazasilane$). The modification of the $pTiO_2_SiO_2(143nm)$ template with cyclic azasilane was confirmed by the increase in the apparent θ_{WCA} . [199] The deposition of gold layers with a thickness of ≈ 20 nm on $SiO_2(143nm)$ microparticles assembled in the $pTiO_2_SiO_2$ templates ($pTiO_2_SiO_2(143nm)@Au$) resulted in an increase in the apparent θ_{WCA} to $\approx 95.7^\circ \pm 3.7^\circ$. This observation is in line with the hydrophobic nature of pure Au. [200] The apparent water contact angle, θ_{WCA} of the $pTiO_2_SiO_2(143nm)@Au$ template was further increased by adsorption of 1-dodecanethiol on the gold surface, and the apparent θ_{WCA} increased to $\approx 116.4^\circ \pm 1.7^\circ$. The increase in the water contact angle results from the lowering of the surface energy caused by the surface modification with 1-dodecanethiol. [201] In the literature, the hydrophobic modification of a broad range of surfaces with FDTS is reported, often yielding superhydrophobic surfaces. [202, 203] Modification of the $pTiO_2_SiO_2(143nm)$ template with FDTS ($pTiO_2_SiO_2(143nm)@FDTS$) resulted in an increase in the apparent water contact angle θ_{WCA} to $\approx 124.0^\circ \pm 4.6^\circ$. The apparent θ_{WCA} is further increased after modification of $pTiO_2_SiO_2(143nm)@FDTS$ template with PS-*b*-P2VP rods. The template $pTiO_2_SiO_2(143nm)@FDTS@PS-b-P2VP$ shows an apparent θ_{WCA} of $\approx 134.5^\circ \pm 3.4^\circ$. The increase in the apparent θ_{WCA} appears to be related to the different surface topography. All the chemical surface treatments increased the apparent water contact angles, making the modified substrates more hydrophobic with a maximum apparent $\theta_{WCA} \approx 134.5^\circ \pm 3.4^\circ$ for $pTiO_2_SiO_2(143nm)@FDTS@PS-b-P2VP$. For all samples, $pTiO_2$ holey film, $pTiO_2_SiO_2(143nm)@cycloazasilane$, $pTiO_2_SiO_2(143nm)@Au$, $pTiO_2_SiO_2(143nm)@Au@1-dodecanethiol$, $pTiO_2_SiO_2(143nm)@FDTS@PS-b-P2VP$, and $pTiO_2_SiO_2(143nm)@FDTS$ pinning of water droplets on their surfaces were observed, and even upon tilting and vigorously moving the templates the droplets remained strongly pinned. The substrates were tilted manually from a horizontal to a vertical position and upside-down, and as illustrated in Figure 4-12a-f. The droplets pin on the hydrophobic surface despite the large inclinations of the hydrophobic templates.

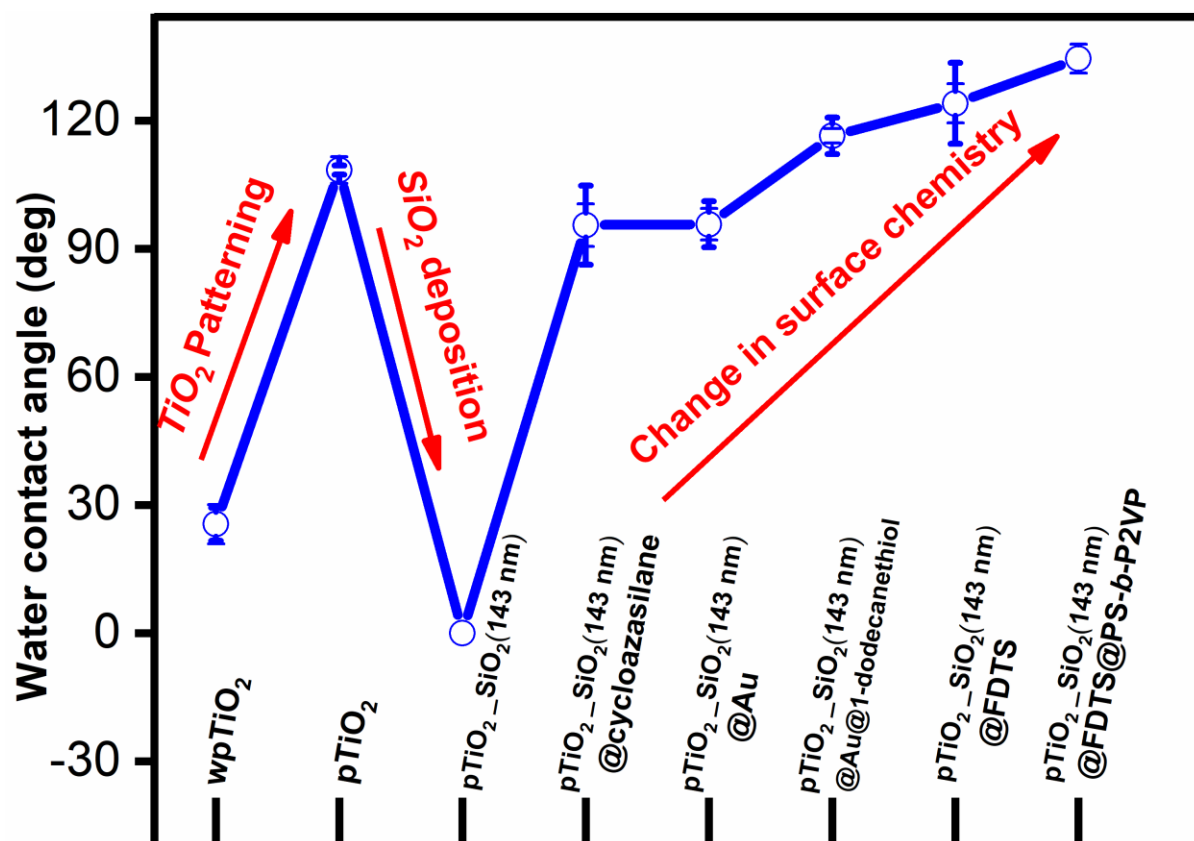


Figure 4-10 Apparent water contact angles (θ_{WCA}) of samples *wpTiO₂* (smooth TiO₂ film without macropores) and *pTiO₂* (macroporous TiO₂ without further modification), native and surface-modified *pTiO₂-SiO₂(143nm)* (macropores of *pTiO₂* are filled silica microparticles with a diameter of 143nm) as well as *pTiO₂-SiO₂(143nm)* after removal of the SiO₂ microspheres with carbon tape. (*pTiO₂@SiO₂* removed). Sample *pTiO₂-SiO₂(143nm)@cycloazasilane* denotes *pTiO₂-SiO₂(143nm)* additionally modified with cycloazasilane, sample *pTiO₂-SiO₂(143nm)@Au* denotes *pTiO₂-SiO₂(143nm)* additionally modified with gold, sample *pTiO₂-SiO₂(143nm)@Au@1-dodecanethiol* denotes sample *pTiO₂-SiO₂(143nm)@Au* additionally modified with of 1-dodecanethiol and sample *pTiO₂-SiO₂(143nm)@FDTS* denotes sample *pTiO₂-SiO₂(143nm)* additionally modified with FDTS. Each data point is the arithmetic mean of six measurements on different samples taken at 23 °C and relative humidity of 31%. The error bars indicate the standard deviations.

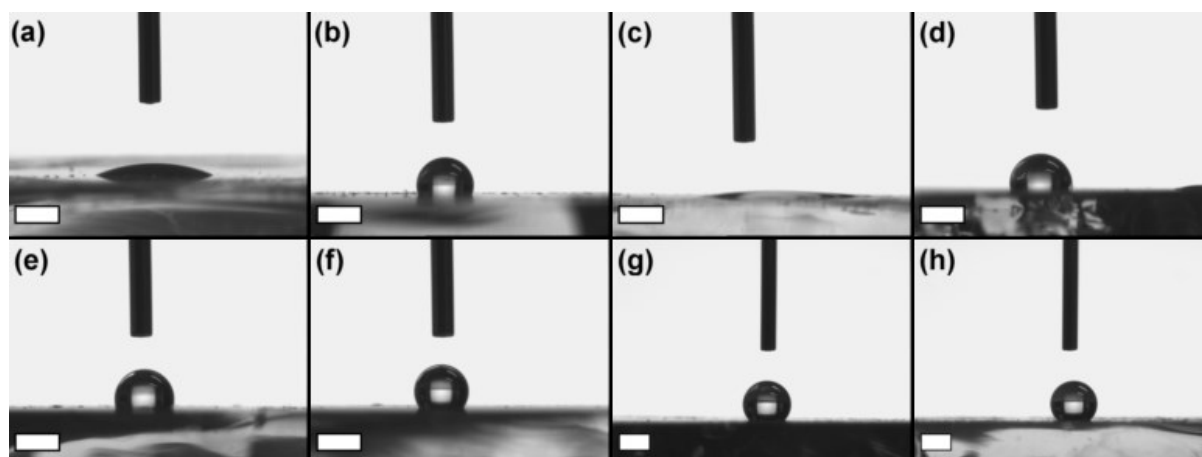


Figure 4-11 Photographs of sessile water droplets with a volume of 2 μ L on different samples; (a) *wp*TiO₂ (apparent $\theta_{WCA} \approx 25.6^\circ \pm 4.6^\circ$), (b) *p*TiO₂ (apparent $\theta_{WCA} \approx 108.5^\circ \pm 3.1^\circ$), (c) *p*TiO₂_SiO₂ (apparent $\theta_{WCA} \approx 0^\circ$), (d) *p*TiO₂_SiO₂(143nm)@cycloazasilane (apparent $\theta_{WCA} \approx 95.5^\circ \pm 5.0^\circ$), (e) *p*TiO₂_SiO₂(143nm)@Au (apparent $\theta_{WCA} \approx 95.7^\circ \pm 3.7^\circ$), (f) *p*TiO₂_SiO₂(143nm)@Au@1-dodecanethiol (apparent $\theta_{WCA} \approx 116.4^\circ \pm 1.7^\circ$), (g) *p*TiO₂_SiO₂(143nm)@FDTS (apparent $\theta_{WCA} \approx 124.0^\circ \pm 4.6^\circ$), and (h) *p*TiO₂_SiO₂(143nm)@FDTS@PS-*b*-P2VP (apparent $\theta_{WCA} \approx 134.5^\circ \pm 3.4^\circ$).

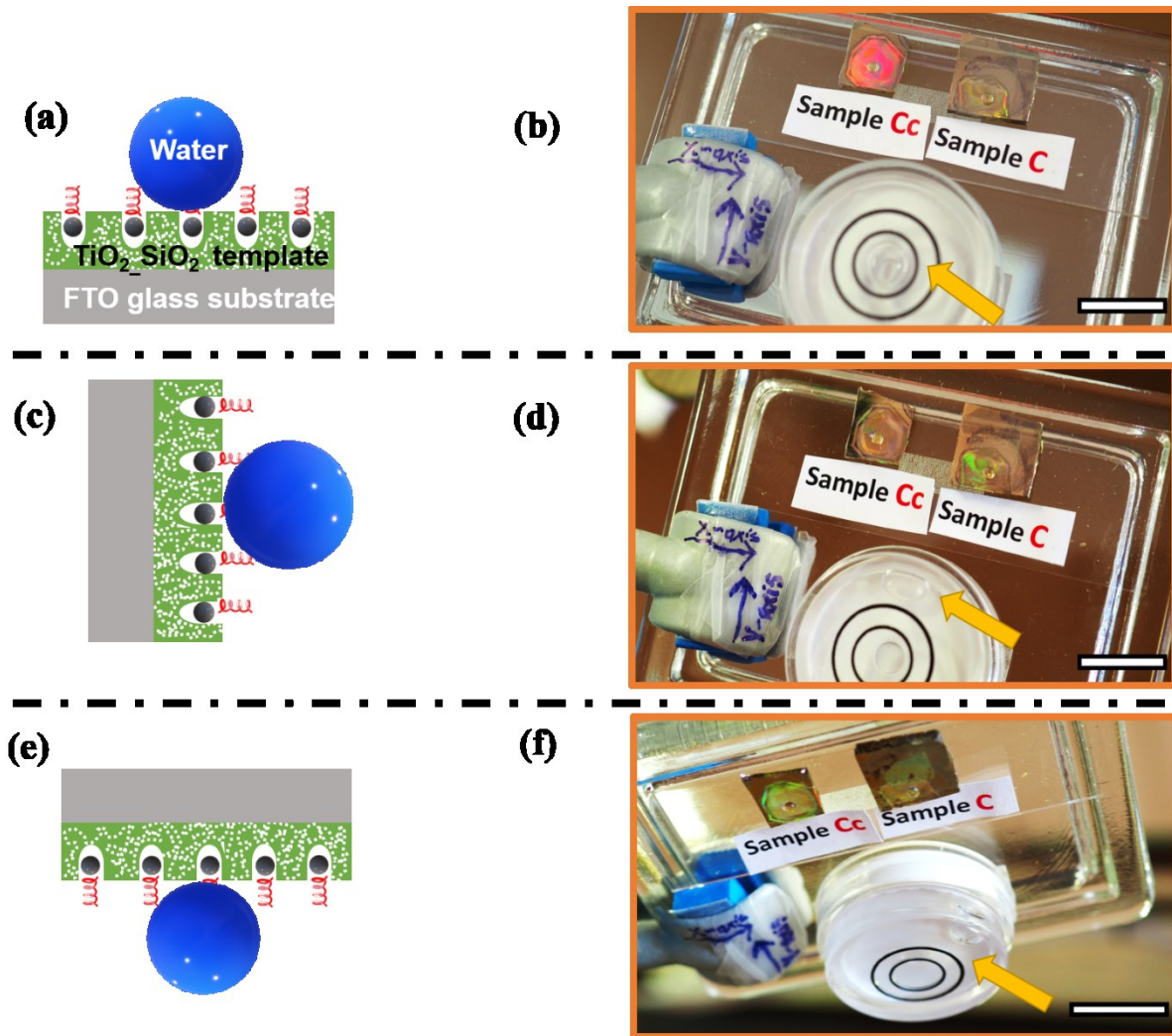


Figure 4-12 Schematics and photographs of water droplets with a volume of 2 μ L pinned on modified *p*TiO₂_SiO₂ templates. Sample C is *p*TiO₂_SiO₂(143nm)@Au, which is prepared by deposition of gold (Au) layers onto *p*TiO₂_SiO₂(143nm) templates by thermal evaporation. Sample Cc is *p*TiO₂_SiO₂(143nm)@Au@1-dodecanethiol, which is prepared after adsorption of 1-dodecanethiol on the gold film from toluene solution. Schematics and corresponding photographs of water droplets pinned (a-b) while the templates are in a horizontal position, (c-d) while the templates are in a vertical position, and (e-f) while the templates are turned upside-down. Water pinning experiments were conducted at a relative humidity of 40% at 23 $^\circ$ C. A spirit level was fixed on the supporting glass slide next to the samples. The position of the air bubble indicates the tilting of the entire setup, as indicated by a yellow arrow. The length of the scale bars in the images corresponds to 15 mm.

As discussed (Figure 4-4, see section 4.1.1), different sizes (50nm, 143nm, 501nm, and 985nm) of SiO₂ microparticles were deposited inside *p*TiO₂, resulting in *p*TiO₂_SiO₂ (50nm), *p*TiO₂_SiO₂ (143nm), *p*TiO₂_SiO₂ (501nm), and *p*TiO₂_SiO₂ (985nm) templates, respectively. The resulting templates after infiltration of the SiO₂ microparticles with different sizes are completely wetted by water. The effects of modifications with different hydrophobic molecules (see section 3.3.1.3.2 for surface modifications) on the wetting characteristics are shown in Figure 4-13. Figure 4-13 shows the apparent average water contact angle, θ_{WCA} of the modified templates, and Figure 4-14 shows images of quiescent water drops on modified samples.

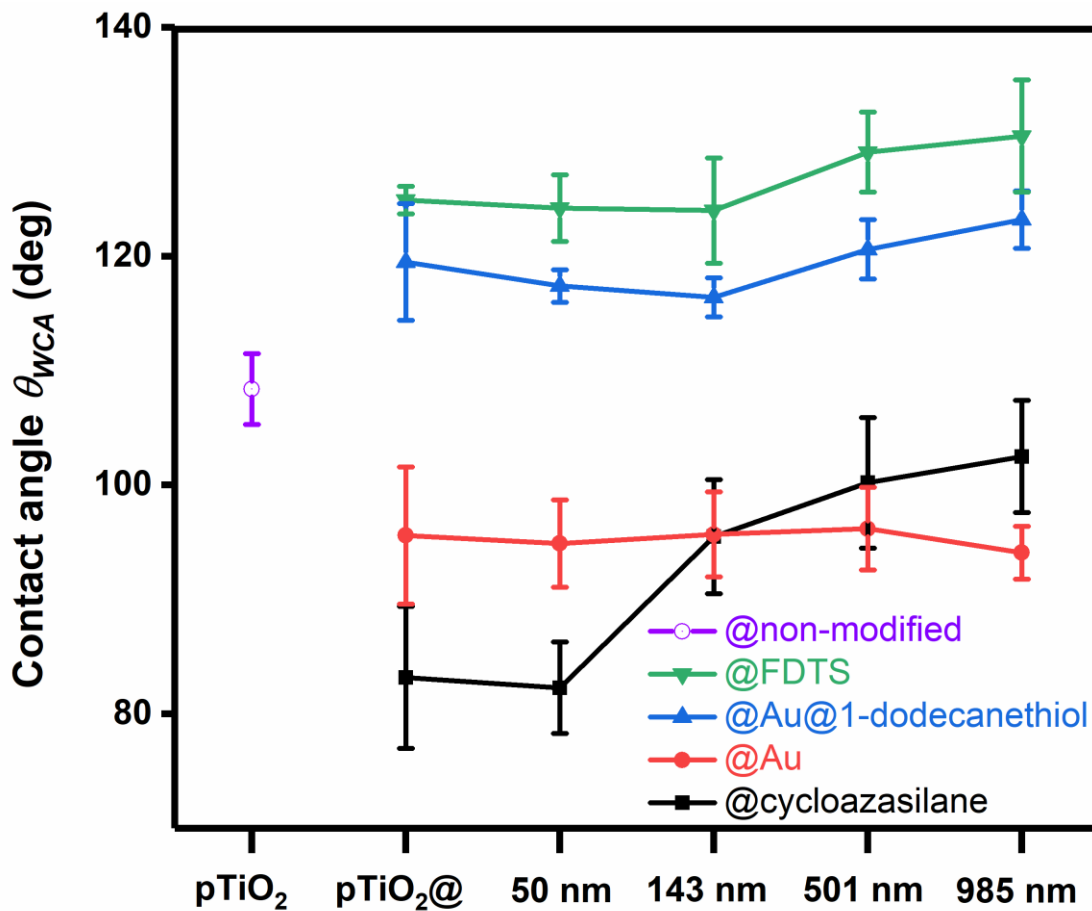


Figure 4-13 Apparent water contact angles θ_{WCA} of *p*TiO₂ (pink open circle) surface-modified *p*TiO₂ without SiO₂ microspheres (*p*TiO₂@) and surface-modified *p*TiO₂_SiO₂ with macropores filled with SiO₂ microspheres having diameters of 50nm, 143nm, 501nm, and 985nm. Solid green down-triangles denote samples coated with FDTS, solid blue up-triangles samples coated with gold and 1-dodecanethiol, solid red circles samples coated with gold, and solid black squares samples coated with cycloazasilane. Each data point is the arithmetic mean of six measurements on different samples taken at 23 °C and relative humidity of 31%.

With the increase in the size of the SiO₂ microparticles deposited into the *p*TiO₂ macropores, and after subsequent modification with 1-dodecanethiol, cycloazasilane, and with FDTS, θ_{WCA} increased (Figure 4-13). However, in the case of modification with a gold layer, θ_{WCA} remains almost the same for different sizes of deposited microparticles. The smaller SiO₂ microparticles (50nm) deposited into holey TiO₂ patterned films followed by modification with cycloazasilane (*p*TiO₂_SiO₂(50nm)@cycloazasilane) resulted in an apparent θ_{WCA} of $\approx 81.8^\circ \pm 1.7^\circ$. Deposition of SiO₂ microparticles with a diameter of 143nm inside holey TiO₂ patterned films followed by modification with cycloazasilane (*p*TiO₂_SiO₂(143nm)@cycloazasilane) resulted in an increase in the apparent θ_{WCA} to $\approx 91.5^\circ \pm 1.2^\circ$. The apparent θ_{WCA} was further increased by deposition of larger SiO₂ microparticles with a diameter of 501nm and 985nm onto holey TiO₂ patterned films and modification with cycloazasilane to $\approx 94.6^\circ \pm 1.2^\circ$ and $\approx 103.1^\circ \pm 1.7^\circ$, respectively.

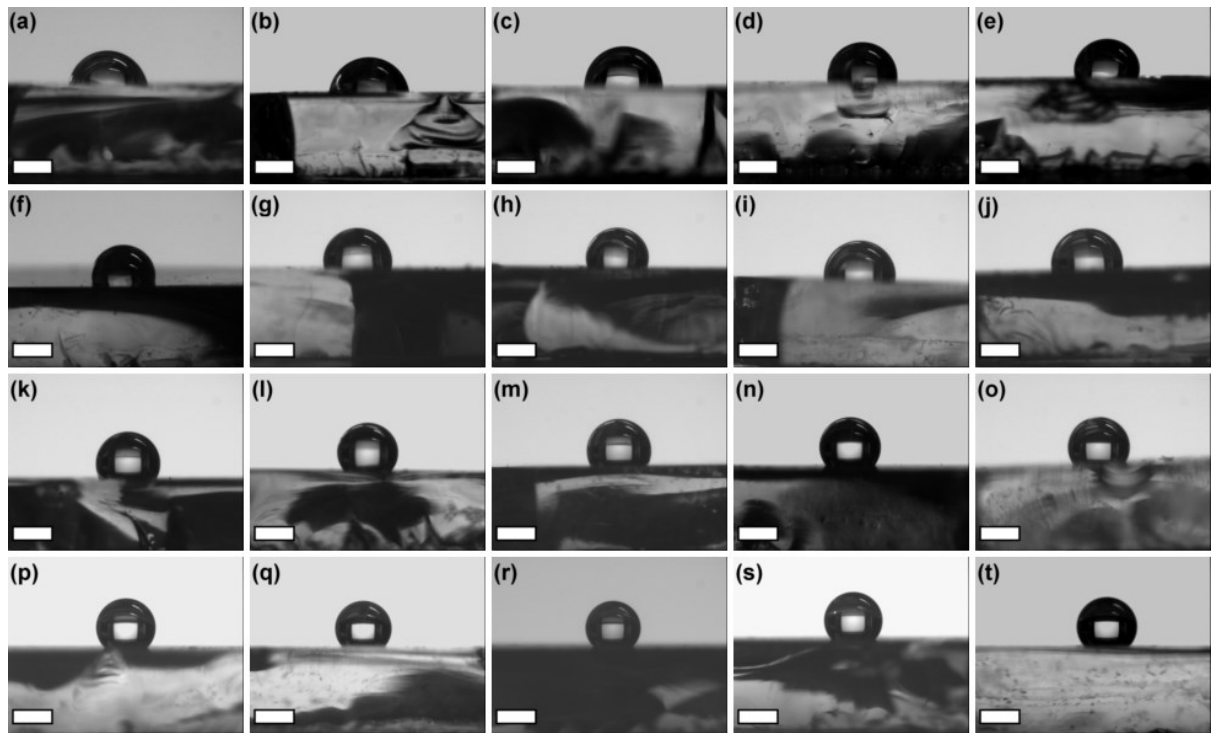


Figure 4-14 Photographs of sessile water droplets with a volume of 2 μ L on different samples; (a-e) different templates after surface modification with cycloazasilane from toluene solution; (a) *p*TiO₂, (b) *p*TiO₂_SiO₂(50nm), (c) *p*TiO₂_SiO₂(143nm), (d) *p*TiO₂_SiO₂(501nm) and (e) *p*TiO₂_SiO₂(985nm). (f-j) different templates after gold (Au) metallic layer deposition by thermal evaporation; (f) *p*TiO₂, (g) *p*TiO₂_SiO₂(50nm), (h) *p*TiO₂_SiO₂(143nm), (i) *p*TiO₂_SiO₂(501nm) and (j) *p*TiO₂_SiO₂(985nm). (k-o) different templates after adsorption of 1-dodecanethiol on the gold film from toluene solution; (k) *p*TiO₂, (l) *p*TiO₂_SiO₂(50nm), (m) *p*TiO₂_SiO₂(143nm), (n) *p*TiO₂_SiO₂(501nm) and (o) *p*TiO₂_SiO₂(985nm). (p-t) different templates after adsorption of FDTS; (p) *p*TiO₂, (q) *p*TiO₂_SiO₂(50nm), (r)

*p*TiO₂_SiO₂(143nm), (s) *p*TiO₂_SiO₂(501nm) and (t) *p*TiO₂_SiO₂(985nm). Water contact angle measurements were carried out at a room temperature of 23 °C and a relative humidity of 31%. The length of the scale bars in the images corresponds to 1 mm.

4.2.1.1 Switchable water wettability

4.2.1.1.1 Reversible wettability switching by the adhesively bonded tape method

Figure 4-15a-c schematically displays the method used to switch between a wettable state and a non-wettable state having a larger apparent water contact angle θ_{WCA} . The hydrophobic characteristics of *p*TiO₂ holey films (Figure 4-15a) are converted to super-hydrophilic characteristics by deposition of SiO₂ microparticles onto the *p*TiO₂ holey films (Figure 4-15b). The water now spreads on the sample surfaces. The initial hydrophobic state can be recovered by detaching the SiO₂ microparticles from the *p*TiO₂_SiO₂ template. The detachment was conducted with carbon or polyimide tape (Figure 4-15c). The tape was adhesively bonded to the *p*TiO₂_SiO₂(143nm) template by manually applying gentle pressure. Afterward, the tape was manually detached clusters of SiO₂ (143nm) microparticles formed ordered arrays replicating the arrangement of the macropores in *p*TiO₂_SiO₂. Figure 4-15d-e shows SEM images of SiO₂ (143 nm) microparticles picked up from *p*TiO₂_SiO₂ (143 nm) templates with carbon adhesive tape and the corresponding recovered *p*TiO₂ holey films, respectively

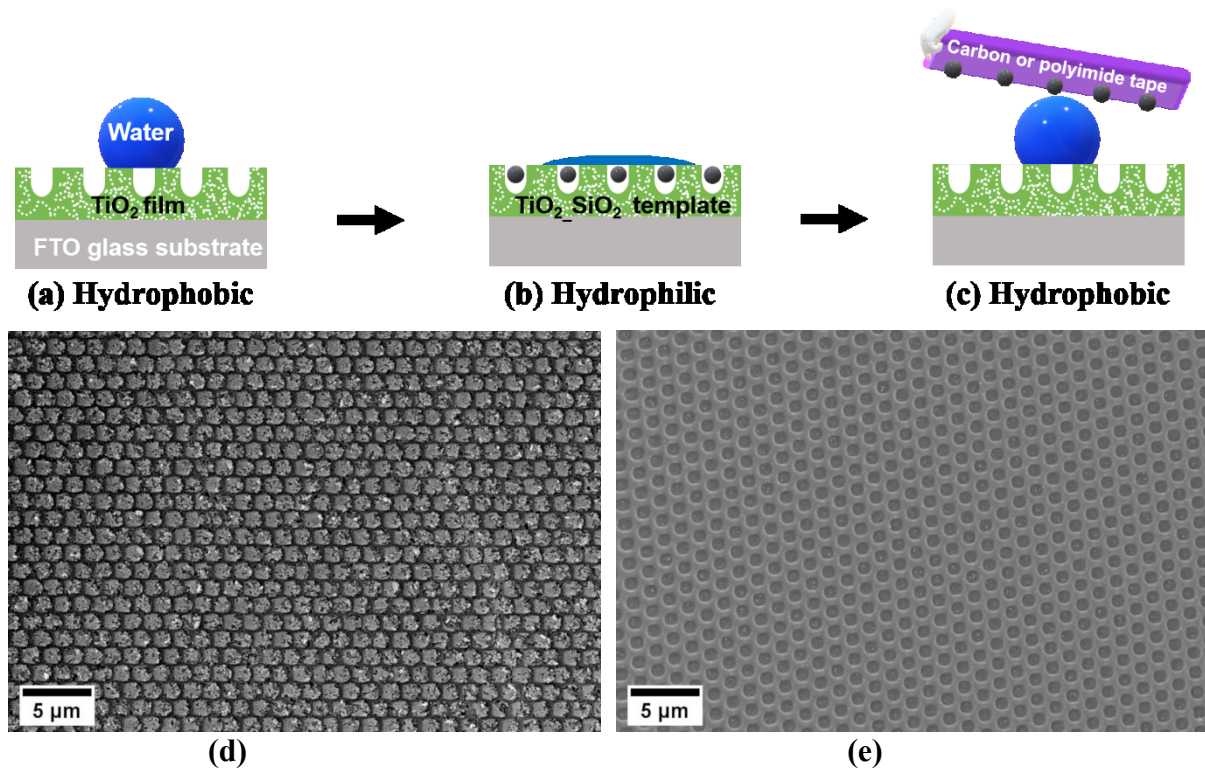


Figure 4-15 (a-c) Schematic showing the wettability transition from the wettable to non-wettable state and vice versa for *pTiO₂*. (a) Titania films imprinted with PDMS stamp (*pTiO₂*) show hydrophobic characteristics. (b) Deposition of SiO₂ microparticles (143nm) into the macropores of *pTiO₂* holey films (*pTiO₂_SiO₂(143nm)*) changes the wetting behavior to hydrophilic. (c) The detachment of the SiO₂ (143nm) microparticles with adhesive tape restores the hydrophobic character of *pTiO₂*. (d-e) SEM images of SiO₂(143nm) microparticles detached with carbon adhesive tape and the corresponding recovered *pTiO₂* holey film (e).

After detachment of SiO₂ (143nm) microparticles from the *pTiO₂_SiO₂(143nm)* template, which was completely wettable, the remaining *pTiO₂* template switched to the non-wettable state with a larger apparent water contact angle $\theta_{WCA} \approx 118.5^\circ \pm 5.2^\circ$ (when SiO₂ microparticles were detached with carbon tape), and $\theta_{WCA} \approx 110.1^\circ \pm 5.5^\circ$ (when SiO₂ microparticles were detached with polyimide tape) (Figure 4-16a-b). The initial apparent water contact angle θ_{WCA} of as-prepared *pTiO₂* amounted to $\approx 108.5^\circ \pm 3.1^\circ$ (see section 4.2.1 Figure 4-10). The empty *pTiO₂* holey film now can again be infiltrated with silica microparticles for switching between the two above discussed states.

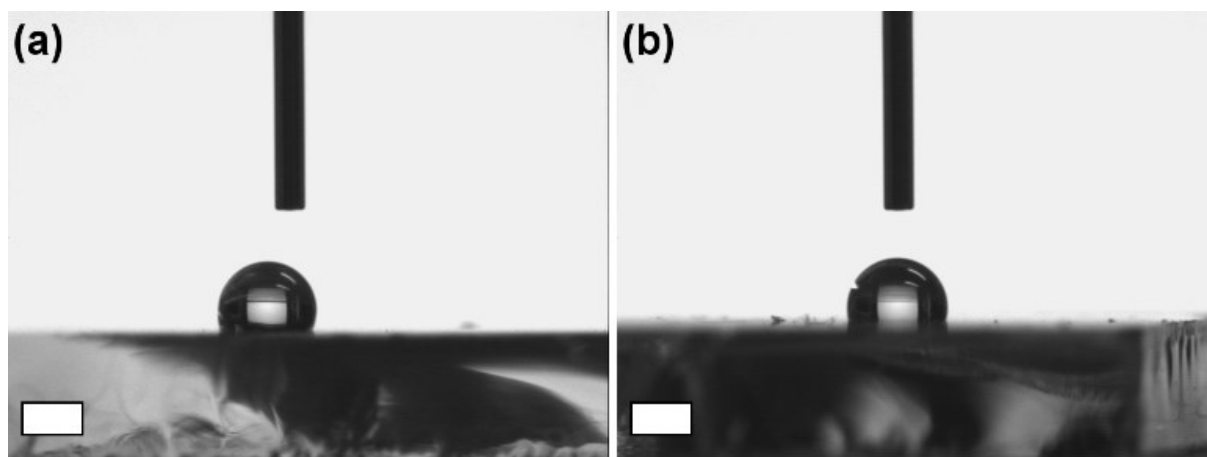


Figure 4-16 Photographs of sessile water droplets with a volume of 2 μL on $p\text{TiO}_2$ samples after detachment of SiO_2 microparticles (143nm) from $p\text{TiO}_2_ \text{SiO}_2(143\text{nm})$ template using (a) polyimide tape (apparent $\theta_{WCA} \approx 118.5^\circ \pm 5.2^\circ$) and (b) carbon tape (apparent $\theta_{WCA} \approx 110.1^\circ \pm 5.5^\circ$). Each value is the average of six measurements on different samples in each case. Water contact angle measurements were carried out at a room temperature of 23 $^\circ\text{C}$ and relative humidity of 31%. The length of the scale bars in the images corresponds to 1 mm.

4.2.1.1.2 Wettability Switching by heat treatment

As discussed in section 4.2.1, water spreads on $p\text{TiO}_2_ \text{SiO}_2$ (143nm) (apparent $\theta_{WCA} \approx 0^\circ$; Figure 4-10). The modification of $p\text{TiO}_2_ \text{SiO}_2$ (143nm) templates with different hydrophobic molecules resulted in a significant change in the wetting characteristics to non-wettable (Figure 4-10). For $p\text{TiO}_2_ \text{SiO}_2$ (143nm)@cycloazasilane, the apparent θ_{WCA} amounted to $95.5^\circ \pm 5.0^\circ$, for $p\text{TiO}_2_ \text{SiO}_2(143\text{nm})@ \text{Au}$ the apparent θ_{WCA} amounted to $95.7^\circ \pm 3.7^\circ$, for $p\text{TiO}_2_ \text{SiO}_2(143\text{nm})@ \text{Au}@1\text{-dodecanethiol}$ the apparent θ_{WCA} amounted to $116.4^\circ \pm 1.7^\circ$, for $p\text{TiO}_2_ \text{SiO}_2(143\text{nm})@ \text{FDTS}$ the apparent θ_{WCA} amounted to $124.0^\circ \pm 4.6^\circ$, and for $p\text{TiO}_2_ \text{SiO}_2(143\text{nm})@ \text{FDTS}@ \text{PS-}b\text{-P2VP}$ the apparent θ_{WCA} amounted to $134.5^\circ \pm 3.4^\circ$. The non-wettable state of the above-mentioned samples is again switched to a wettable state by heat treatment. Heat treatment reduced the apparent water contact angle (Figure 4-17). For all modified templates, the switching from non-wettable to wettable states was achieved by heating them to 600 $^\circ\text{C}$ for 30 mins in a muffle furnace under an ambient atmosphere. The templates were heated to 600 $^\circ\text{C}$ at a heating rate of 33 $^\circ\text{C}/\text{min}$, kept at this temperature for 30 minutes, and then directly removed from the muffle furnace. The reproducibility was checked by heat-treatment of three different samples for each sample type. Figure 4-17 shows the

change in the apparent water contact angles after heat treatments of *p*TiO₂ _SiO₂ (143nm) templates modified with various hydrophobic molecules, and Figure 4-18 photographs of sessile water drop on the heat-treated templates.

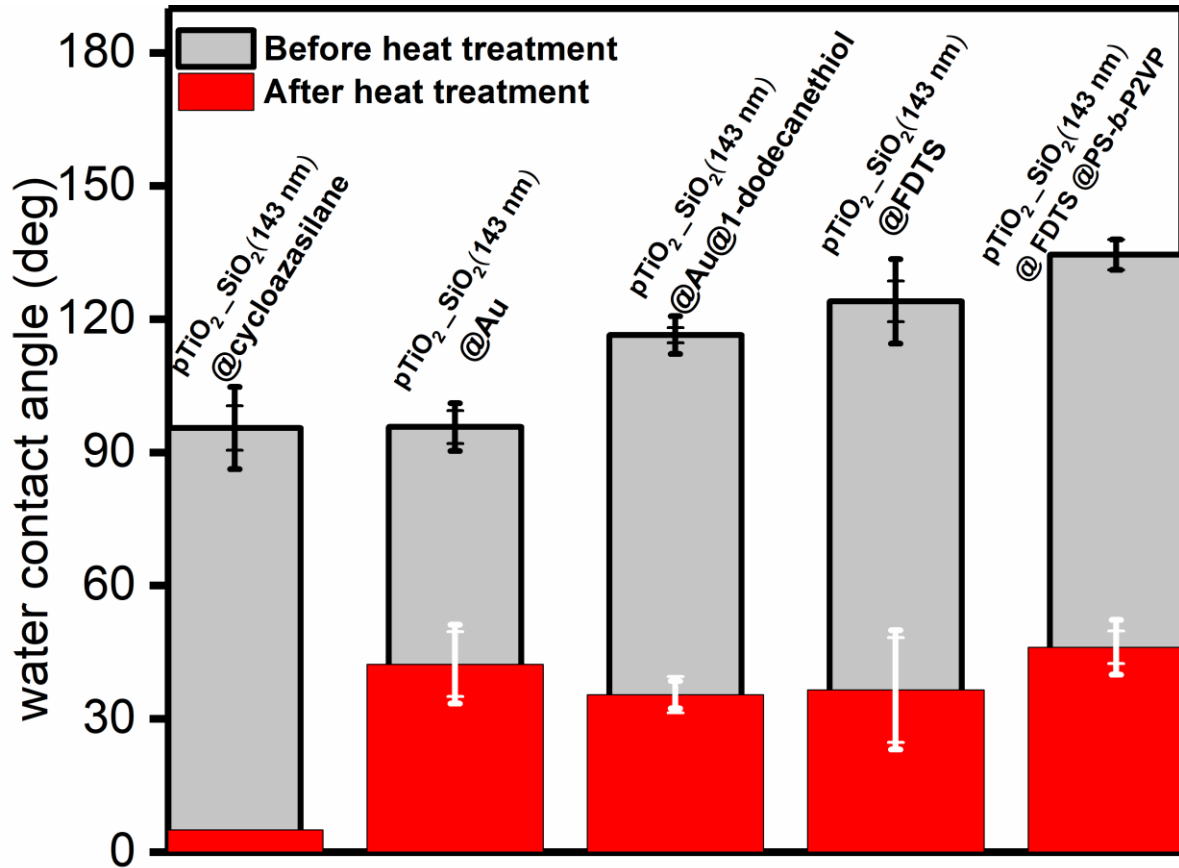


Figure 4-17 Apparent average water contact angles of different *p*TiO₂_SiO₂(143nm) samples after switching from non-wettable to the wettable state by heat treatment. The grey bar represents the water contact angles of the templates after modifications with different hydrophobic molecules before heat treatment. The red bar graph represents the decrease in apparent water contact angles after heat treatment for the switching of wettability. Each value is the average of six measurements on different samples. Water contact angle measurements were carried out at 23 °C and at a relative humidity of 31%.

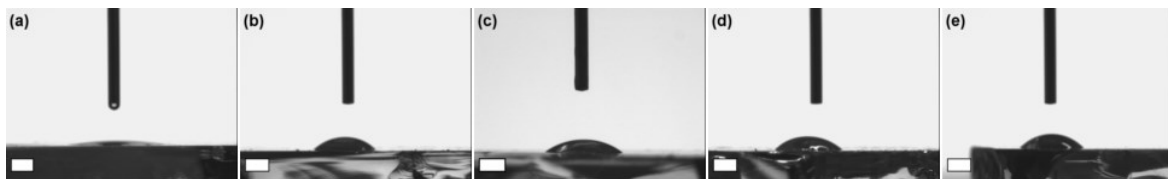


Figure 4-18 Photographs of sessile water droplets with a volume of 2 μ L on different p TiO₂/SiO₂ (143nm) samples after surface modification and heat treatment; (a) p TiO₂/SiO₂ (143nm)/cycloazasilane (apparent $\theta_{WCA} \approx 0^\circ$), (b) p TiO₂/SiO₂(143nm)/Au (apparent $\theta_{WCA} \approx 42.3^\circ \pm 7.3^\circ$), (c) p TiO₂/SiO₂(143nm)/Au@1-dodecanethiol (apparent $\theta_{WCA} \approx 35.4^\circ \pm 4.1^\circ$), (d) p TiO₂/SiO₂(143nm)/FDTS@PS-*b*-P2VP (apparent $\theta_{WCA} \approx 46.1^\circ \pm 6.2^\circ$), and (e) p TiO₂/SiO₂(143nm)/FDTS (apparent $\theta_{WCA} \approx 36.5^\circ \pm 5.8^\circ$). Water contact angle measurements were carried out at a temperature of 23 °C and relative humidity of 31%. The length of the scale bars in the images corresponds to 1 mm.

After heat treatment, the apparent θ_{WCA} of p TiO₂/SiO₂ (143nm)/cycloazasilane was lowered from $95.5^\circ \pm 5.0^\circ$ before heat treatment to $\approx 0^\circ$. In the case of p TiO₂/SiO₂(143nm)/Au templates, the apparent θ_{WCA} was reduced from $95.7^\circ \pm 3.7^\circ$ before heat treatment to $42.3^\circ \pm 7.3^\circ$ after the heat treatment. The thin gold film on top of the silica microparticles embedded in p TiO₂/SiO₂/Au macropores is assumed to be damaged after heating at 600 °C (Figure 4-19 a-f). This might be the reason for the switching from non-wettable to wettable. Figures 4-19 a-f shows detailed SEM images of p TiO₂/SiO₂(50nm)/Au, p TiO₂/SiO₂(143nm)/Au, p TiO₂/SiO₂(501nm)/Au, and p TiO₂/SiO₂(985nm)/Au templates after the heat treatment. The damage can be noticed with a series of broken pieces to the gold thin film on SiO₂ embedded microparticles in each case. Chunks of the dewetted gold film can be seen. The thin gold films, after heating to 500 C°, result in permanent damage to the film, as reported by other researchers.[204] A phenomenon called solid-state dewetting may occur. Solid-state dewetting occurs below the melting point of the corresponding metal and involves the surface diffusion of metal atoms and clusters. The formation of metal particles can result in substrates containing regular arrays of pits and indentations.[205] For p TiO₂/SiO₂(143nm)/FDTS templates, the apparent water contact angle θ_{WCA} is reduced from $124.0^\circ \pm 4.6^\circ$ before heat treatment to $36.5^\circ \pm 5.8^\circ$ after heat treatment. The apparent water contact angle θ_{WCA} of p TiO₂/SiO₂(143nm)/FDTS@PS-*b*-P2VP templates is also reduced from $\approx 134.5^\circ \pm 3.4^\circ$ before heat treatment to $46.1^\circ \pm 6.2^\circ$ after heat treatment.

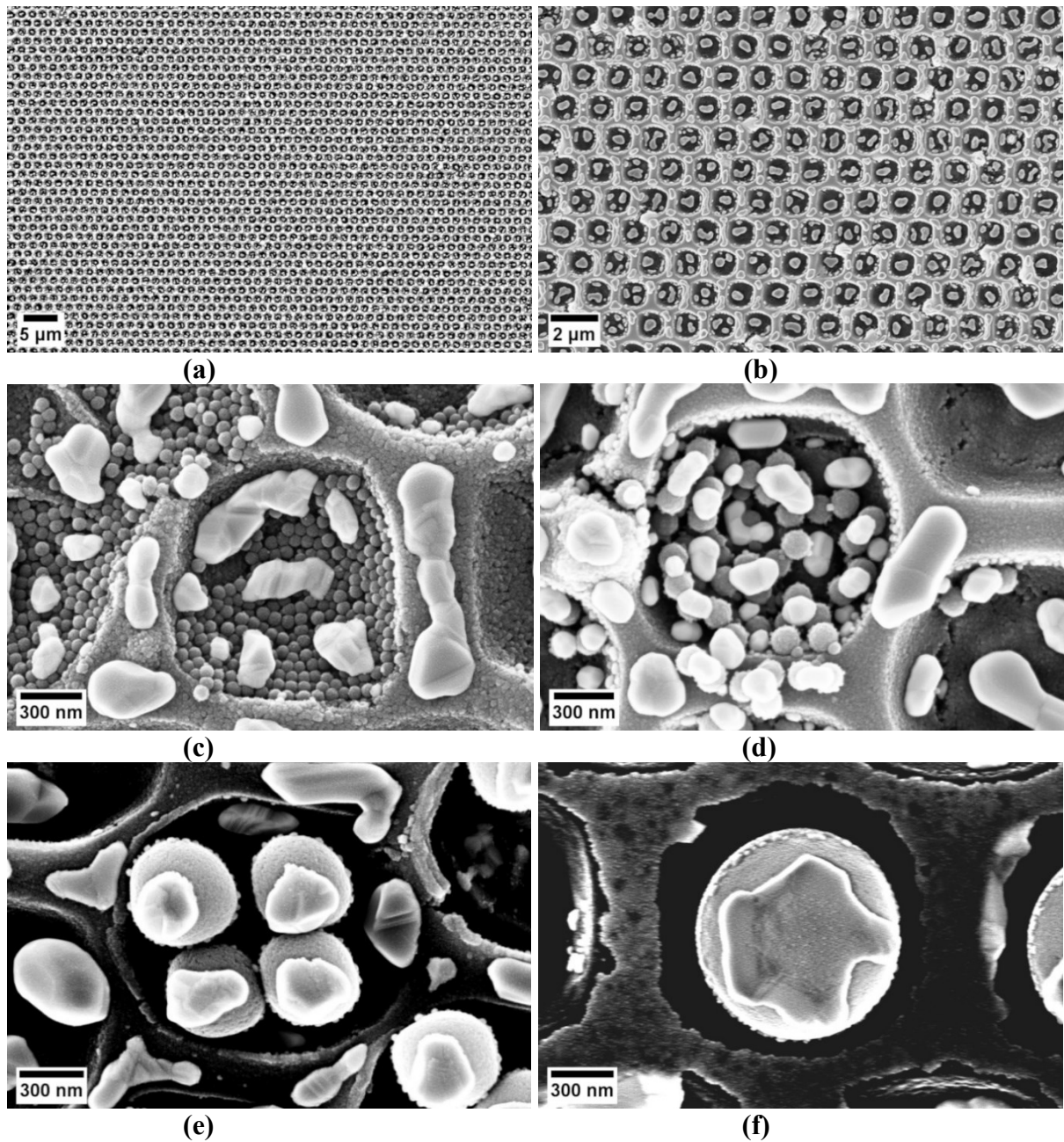


Figure 4-19 SEM images of templates after heat treatment for switching the wettability. (a) Large-field view and (b) detail of an unfilled region of $p\text{TiO}_2\text{-SiO}_2(50\text{nm})\text{-Au}$ template after heat treatment. (c) detail of a $p\text{TiO}_2\text{-SiO}_2(50\text{nm})\text{-Au}$, (d) detail of a $p\text{TiO}_2\text{-SiO}_2(143\text{nm})\text{-Au}$, (e) detail of a $p\text{TiO}_2\text{-SiO}_2(501\text{nm})\text{-Au}$, and (f) detail of a $p\text{TiO}_2\text{-SiO}_2(985\text{nm})\text{-Au}$ templates after heat treatment.

4.2.1.2 Water droplet evaporation dynamics

Figure 4-20 shows the shape evolution of sessile water droplets with an initial volume of 2 μL during evaporation on different templates. The shape evolution of sessile water droplets was analyzed for different surface modified templates ($p\text{TiO}_2$), which were infiltrated with different sizes of SiO_2 microparticles. Figure 4-21 shows images of an evaporating sessile water droplet with an initial volume of 2 μL evolution with time for templates ($p\text{TiO}_2\text{-SiO}_2$) filled with different sizes of SiO_2 microparticles and after surface modification with cycloazasilane from toluene solution. For all other templates mentioned in section 3.3.1.3.2, and with different surface modifications, the same procedure was used (not shown). Figure 4-22 shows the evolution of the dimensionless contact base radius ($r^*=r_e/r_0$) of a water droplet with the surface, where r_e is the base radius at the elapsed time, and r_0 is the contact base radius of the water droplet at an initial stage. For the templates modified with either cycloazasilane or with a gold metallic layer, the contact base radius remains nearly constant until the dimensionless time ($t^*=t_e/t_c$) of 0.8 and is identified as constant contact radius (CCR) mode. Where t_e is the elapsed evaporation time, and t_c is the time required for complete evaporation. For the templates modified with either 1-dodecanethiol on the gold film or with FDTS, the contact base radius remains nearly constant until the dimensionless time ($t^*=t_e/t_c$) of 0.6 and is identified as a constant contact radius (CCR) mode. In constant contact radius (CCR) mode, the pinning force between the water drop and substrate keeps a static contact line having a constant droplet radius.[206] At the initial stage of droplet evaporation, the droplet evaporation happened with a constant contact radius through contact angle decrease (Figure 4-22).

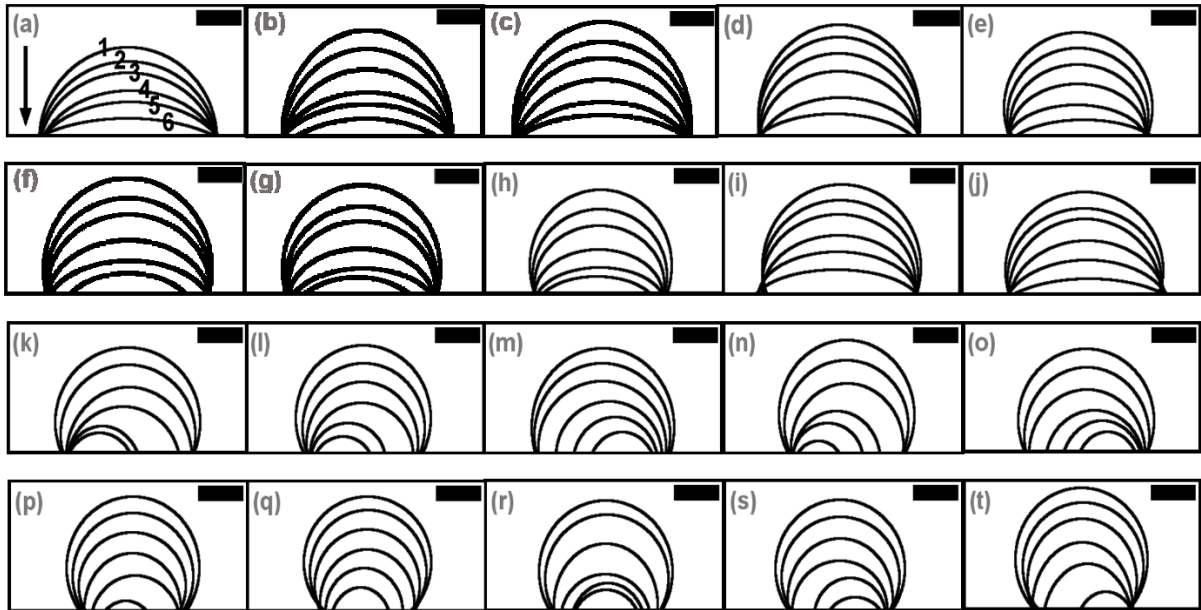


Figure 4-20 Shape evolution of sessile water droplets with an initial volume of 2 μL during evaporation on different templates. Droplet profiles are shown for different evaporation times; $t_1 = 0$ s is the time instant where evaporation started, and t_6 is the total time for evaporation. The shape evolution curve of sessile water droplets was generated after time interval ($t^* = t_i/t_f$) of 0.2 (where t_i is the time instant and t_f is total time for evaporation). The total time for evaporation (t_f) is calculated, when the water droplet is completely disappear as seen from the side view of drop shape analyzer Krüss DSA100. (a-e) different templates after surface modification with cycloazasilane from toluene solution; (a) $p\text{TiO}_2$ ($t_f \approx 12.6$ min), (b) $p\text{TiO}_2\text{-SiO}_2(50\text{nm})$ ($t_f \approx 13.9$ min), (c) $p\text{TiO}_2\text{-SiO}_2(143\text{nm})$ ($t_f \approx 15.9$ min), (d) $p\text{TiO}_2\text{-SiO}_2(501\text{nm})$ ($t_f \approx 15.6$ min) and (e) $p\text{TiO}_2\text{-SiO}_2(985\text{nm})$ ($t_f \approx 12.9$ min). (f-j) different templates after gold (Au) metallic layer deposition by thermal evaporation; (f) $p\text{TiO}_2$ ($t_f \approx 18.3$ min), (g) $p\text{TiO}_2\text{-SiO}_2(50\text{nm})$ ($t_f \approx 16.0$ min), (h) $p\text{TiO}_2\text{-SiO}_2(143\text{nm})$ ($t_f \approx 16.1$ min), (i) $p\text{TiO}_2\text{-SiO}_2(501\text{nm})$ ($t_f \approx 17.0$ min) and (j) $p\text{TiO}_2\text{-SiO}_2(985\text{nm})$ ($t_f \approx 17.0$ min). (k-o) different templates after adsorption of 1-dodecanethiol on the gold film from toluene solution; (k) $p\text{TiO}_2$ ($t_f \approx 19.9$ min), (l) $p\text{TiO}_2\text{-SiO}_2(50\text{nm})$ ($t_f \approx 20.2$ min), (m) $p\text{TiO}_2\text{-SiO}_2(143\text{nm})$ ($t_f \approx 21.0$ min), (n) $p\text{TiO}_2\text{-SiO}_2(501\text{nm})$ ($t_f \approx 20.3$ min) and (o) $p\text{TiO}_2\text{-SiO}_2(985\text{nm})$ ($t_f \approx 20.1$ min). (p-t) different templates after adsorption of FDTS; (p) $p\text{TiO}_2$ ($t_f \approx 21.1$ min), (q) $p\text{TiO}_2\text{-SiO}_2(50\text{nm})$ ($t_f \approx 19.9$ min), (r) $p\text{TiO}_2\text{-SiO}_2(143\text{nm})$ ($t_f \approx 20.0$ min), (s) $p\text{TiO}_2\text{-SiO}_2(501\text{nm})$ ($t_f \approx 21.0$ min) and (t) $p\text{TiO}_2\text{-SiO}_2(985\text{nm})$ ($t_f \approx 21.9$ min). Water contact angle measurements were carried out at a room temperature of 23 $^\circ\text{C}$ and a relative humidity of 31%. The length of the scale bars in the images corresponds to 0.5 mm.

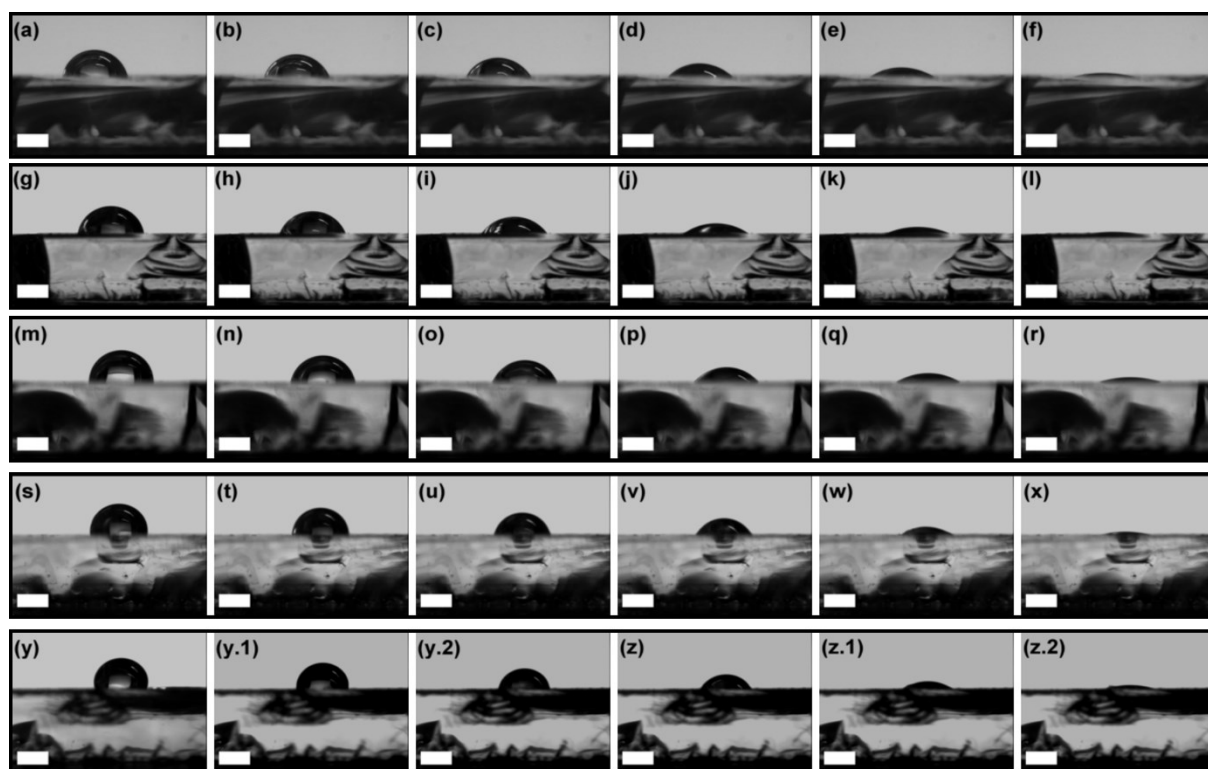


Figure 4-21 Images of an evaporating sessile water droplet with an initial volume of 2 μL placed on different templates after surface modification with cycloazasilane from toluene solution. The shape evolution curve of sessile water droplets was generated after a time interval ($t^*=t_i/t_f$) of 0.2 (where t_i is the time instant and t_f is the total time for evaporation). The total time for evaporation (t_f) is calculated when the water droplet is completely disappeared, as seen from the side view of drop shape analyzer Krüss DSA100. Time-dependent contact angle images during the natural evaporation from; (a-f) $p\text{TiO}_2@cycloazasilane$ ($t^*= 0, 0.2, 0.4, 0.6, 0.8,$ and 1.0 respectively), (g-l) $p\text{TiO}_2_SiO_2(50nm)@cycloazasilane$, (m-r) $p\text{TiO}_2_SiO_2(143nm)@cycloazasilane$, (s-x) $p\text{TiO}_2_SiO_2(501nm)@cycloazasilane$, and (y-z.2) $p\text{TiO}_2_SiO_2(985nm)@cycloazasilane$. Water contact angle measurements were carried out at a room temperature of 23 $^\circ\text{C}$ and relative humidity of 31%. The length of the scale bars in the images corresponds to 1 mm.

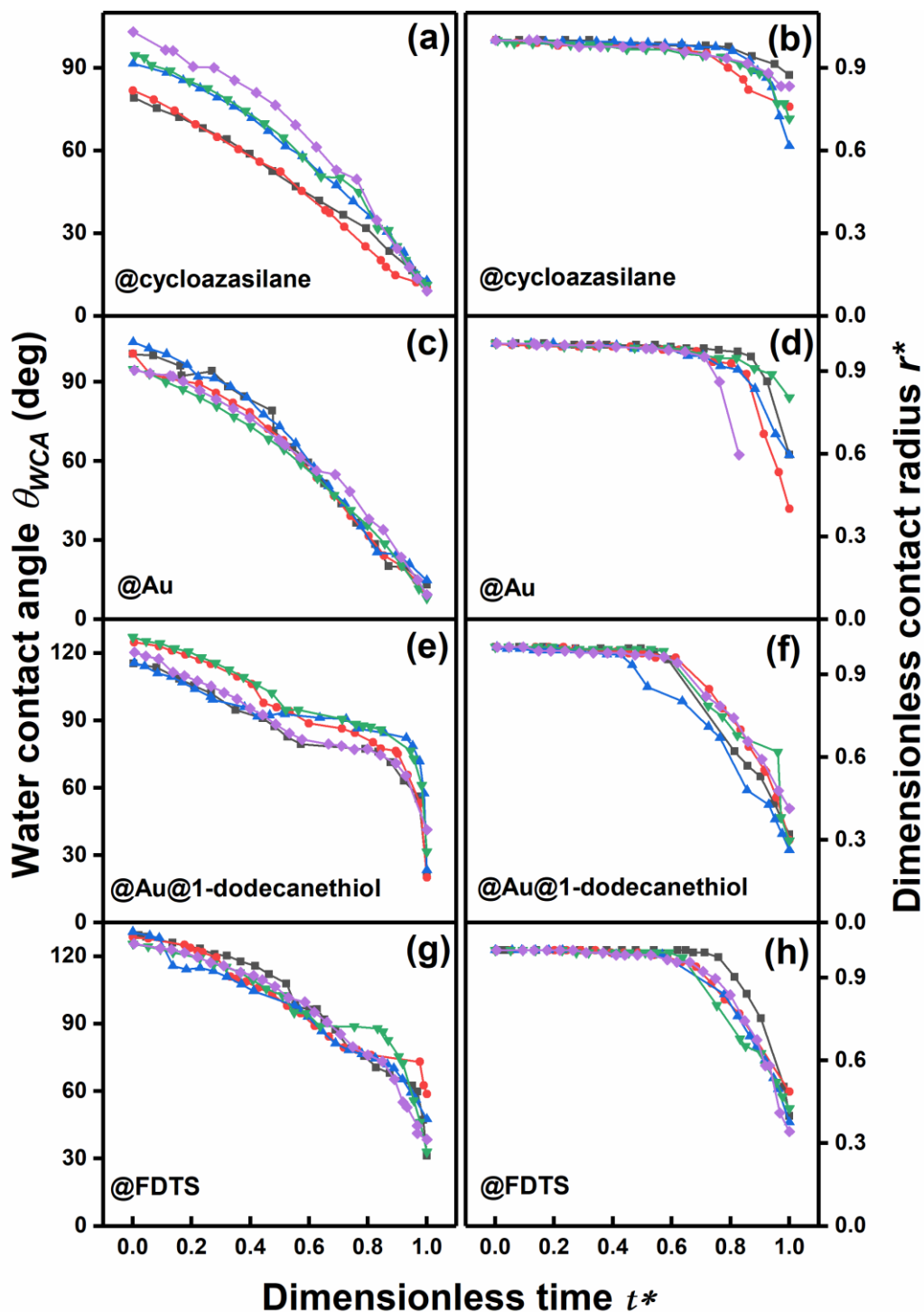


Figure 4-22 Contact angles and dimensionless contact radii $r^* = r_e/r_0$ of sessile water droplets with an initial volume of 2 μL on a), b) cycloazasilane-coated, c), d) gold-coated, e), f) gold and 1-dodecanethiol-coated and g), h) FDTS-coated $p\text{TiO}_2$ and $p\text{TiO}_2\text{-SiO}_2$ plotted against the dimensionless evaporation time $t^* = t_e/t_c$. t_e is the elapsed evaporation time, t_c the time required for complete evaporation, r^* the dimensionless contact radius, r_e the contact radius after the evaporation time t_e and r_0 the initial contact radius of the considered droplet. Black squares denote $p\text{TiO}_2$, red circles $p\text{TiO}_2\text{-SiO}_2(50\text{nm})$, blue up-triangles $p\text{TiO}_2\text{-SiO}_2(143\text{nm})$, green down-triangles $p\text{TiO}_2\text{-SiO}_2(501\text{nm})$ and pink squares $p\text{TiO}_2\text{-SiO}_2(985\text{nm})$. The lines are guides to the eyes. The measurements were carried out at 23 °C and relative humidity of 31%.

The base droplet contact radius (r_c) and droplet height (h) was verified and confirmed by calculating the apparent water contact angle using the relation $\theta_{WCA} = 2 \tan^{-1}(h/r_c)$. [207] Figure 4-23 shows the experimentally observed evolution of the apparent water contact angles, as well as calculated water contact angles, plotted against the dimensionless time (t^*). The small difference between experimental and calculated water contact angle values indicates that the measurements of r_c and h are valid. Figure 4-24 shows the optical microscopy images of the contact line of evaporation of sessile water droplets with an initial volume of 2 μL placed on different $p\text{TiO}_2\text{-SiO}_2$ templates modified with cycloazasilane. The contact line of the water droplet remains pinned till $t^*=0.8$, as described in Figure 4-24. After $t^*=0.8$, the contact angle decreases with the sudden decrease in contact radius.

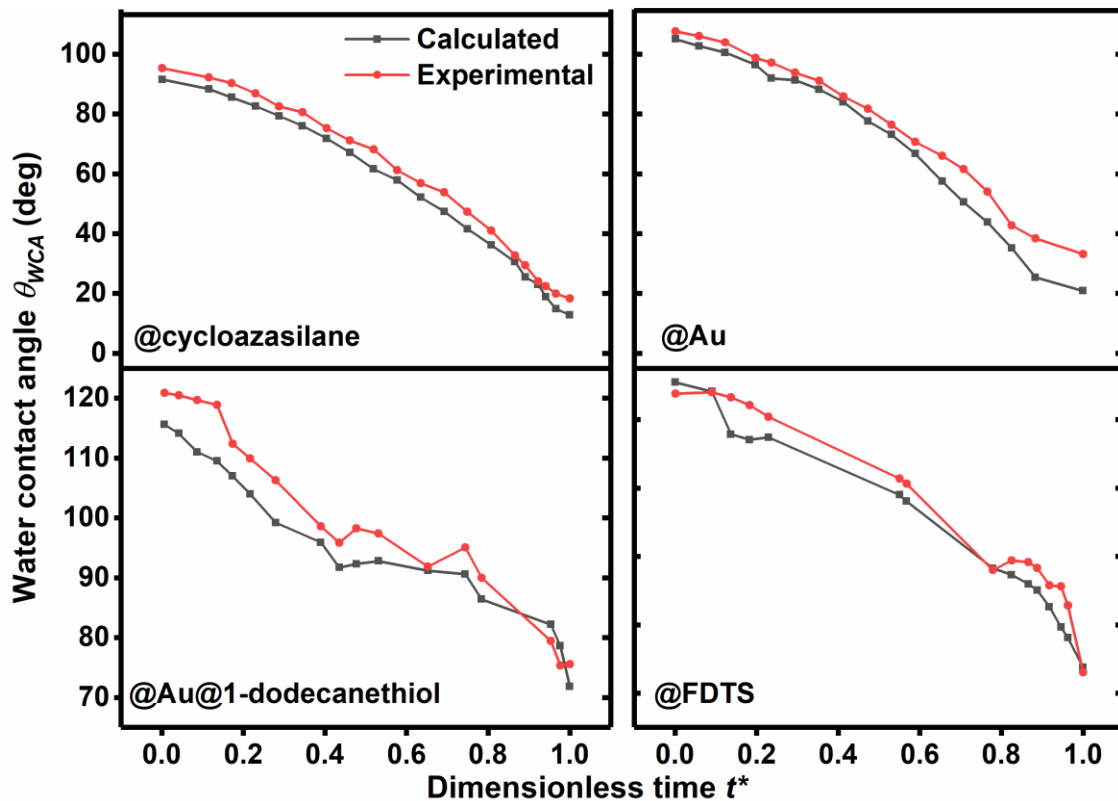


Figure 4-23 Comparison of experimentally measured apparent water contact angles and water contact angles calculated as $\theta_{WCA} = 2 \tan^{-1}(h/r_c)$ on $p\text{TiO}_2\text{-SiO}_2(143\text{nm})$ with different surface coatings plotted against the dimensionless evaporation time t^* . Measurements were carried out at 23°C and relative humidity of 31%. The lines are guides to the eyes.

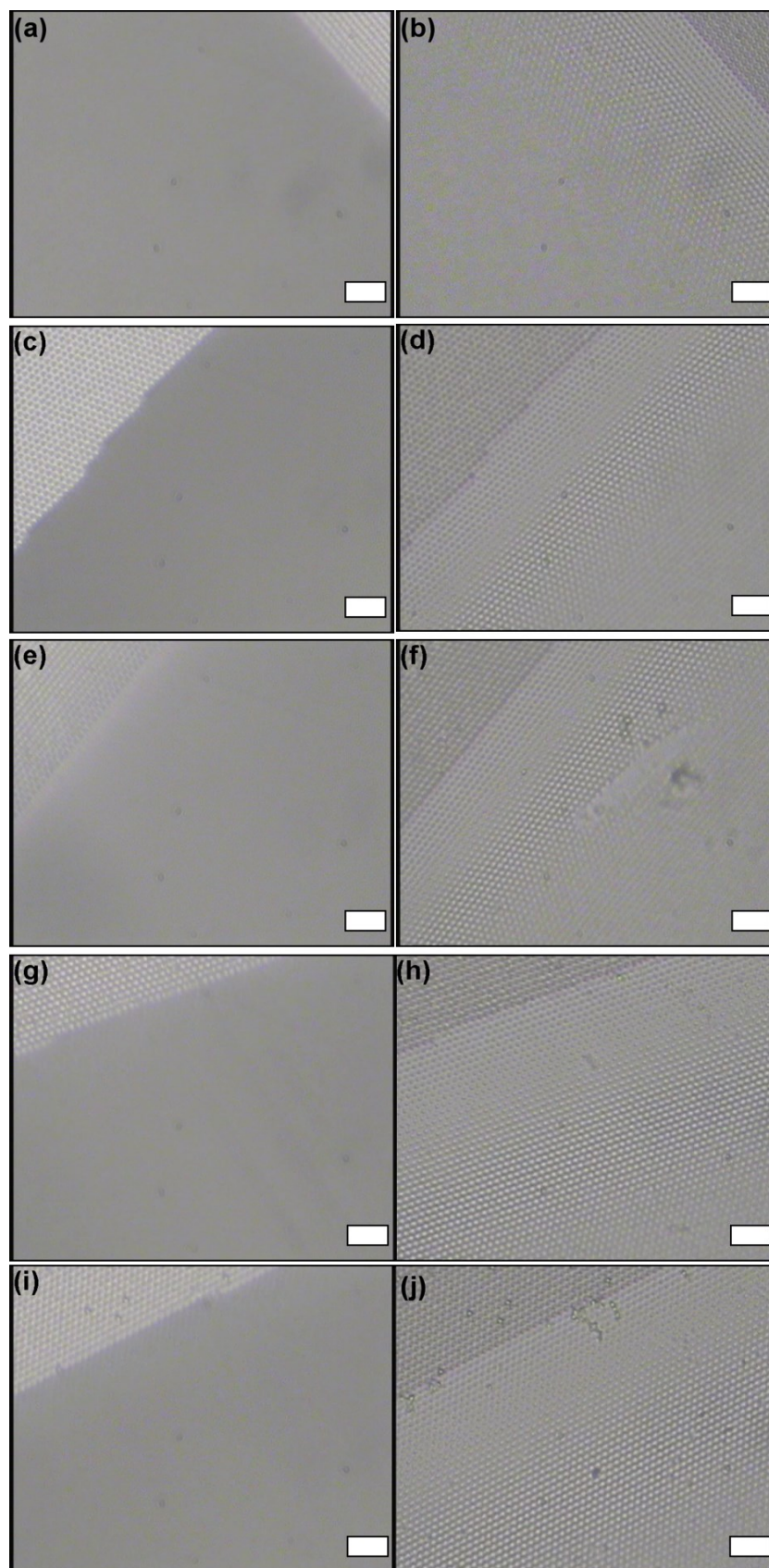


Figure 4-24 Optical microscopy images (60x magnification) of the contact line of evaporation of sessile water droplets with an initial volume of 2 μ L placed on different p TiO₂-SiO₂ templates modified with cycloazasilane. (a-b) p TiO₂@cycloazasilane, (c-d)

*p*TiO₂_SiO₂(50nm)@cycloazasilane, (e-f) *p*TiO₂_SiO₂(143nm)@cycloazasilane, (g-h) *p*TiO₂_SiO₂(501nm)@cycloazasilane, and (i-j) *p*TiO₂_SiO₂(985nm)@cycloazasilane. The left side panels are taken at ($t^*=t_e/t_c = 0$) and right-side panels at $t^*=0.8$; where t_e is the elapsed evaporation time, t_c is the time required for complete evaporation. The total time for evaporation (t_c) is calculated when the water droplet completely disappears, as seen from the inclined view. The scale bars for panels correspond to 10 μ m. The experiments were carried out at 23 °C at a relative humidity of 31%.

5 Site-selective modification of SiO₂ microparticles in macroporous-nanoporous substrates

5.1 Fabrication of PDMS stamps

The PDMS secondary molds were fabricated by pouring PDMS prepolymer onto silanized mSi (see section 3.3.1.1). Figure 5-1a, c shows SEM images of silanized macroporous silicon (mSi) templates used as a primary mold. The macropores with round pore bottoms had pore lengths of $\approx 0.8 \mu\text{m}$, pore diameters of $\approx 0.9 \mu\text{m}$, and interpore distances of $\approx 1.5 \mu\text{m}$ (Figure 5-1a), and the resulting PDMS secondary mold has dimensions of pore length ($\approx 0.79 \mu\text{m}$), and base diameter ($\approx 0.8 \mu\text{m}$) of the PDMS pillars (Figure 5-1b) approximately matched the dimensions of the macropores of the primary mSi mold. The pillar depth ($\approx 6.99 \mu\text{m}$) and base opening diameter ($\approx 5.06 \mu\text{m}$) of the PDMS pillars (Figure 5-1d) approximately match the dimensions of the macropores of the primary mSi mold (total pore length of $7.26 \mu\text{m}$, $6.0 \mu\text{m}$ pore opening diameter, and $3.5 \mu\text{m}$ pore bottom diameter) (Figure 5-1c).

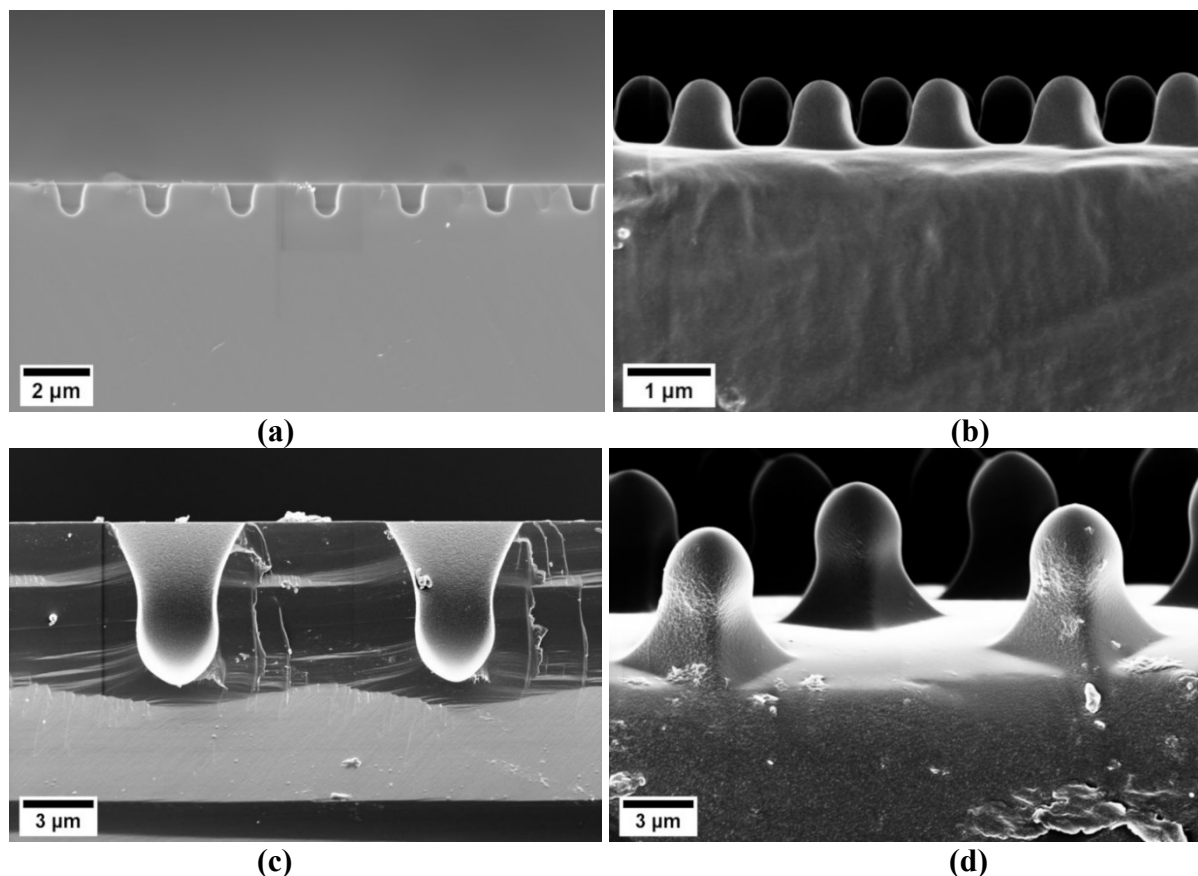


Figure 5-1 Cross-section SEM images of (a) macroporous silicon (mSi) primary mold with $0.9 \mu\text{m}$ pore base diameter, and resulting (b) PDMS secondary mold with a base diameter ($\approx 0.8 \mu\text{m}$) of the PDMS pillars. Cross-section SEM images of (c) macroporous silicon (mSi) primary

mold with 3.5 μm pore bottom diameter, and resulting (b) PDMS secondary mold with a base opening diameter ($\approx 5.06 \mu\text{m}$) of the PDMS pillars.

5.2 Fabrication of PS-*b*-P2VP and PS-*b*-P4VP macroporous-nanoporous substrates

The macroporous PS-*b*-P2VP and PS-*b*-P4VP polymeric substrates were fabricated using PDMS secondary molds (see sections 3.3.2.1). For the generation of continuous nanopores, the PS-*b*-P2VP or PS-*b*-P4VP substrate was treated with ethanol at 60 °C for 4 h using a protocol established elsewhere [168, 169]. The macroporous PS-*b*-P2VP substrates had a pore diameter of 0.9 μm and a pore length of 0.80 μm , as shown in Figure 5-2a-b. The topographically patterned macroporous PS-*b*-P4VP substrate had a macropore diameter of 5.3 μm and a macropore length of 8.6 μm (Figure 5-2c-d).

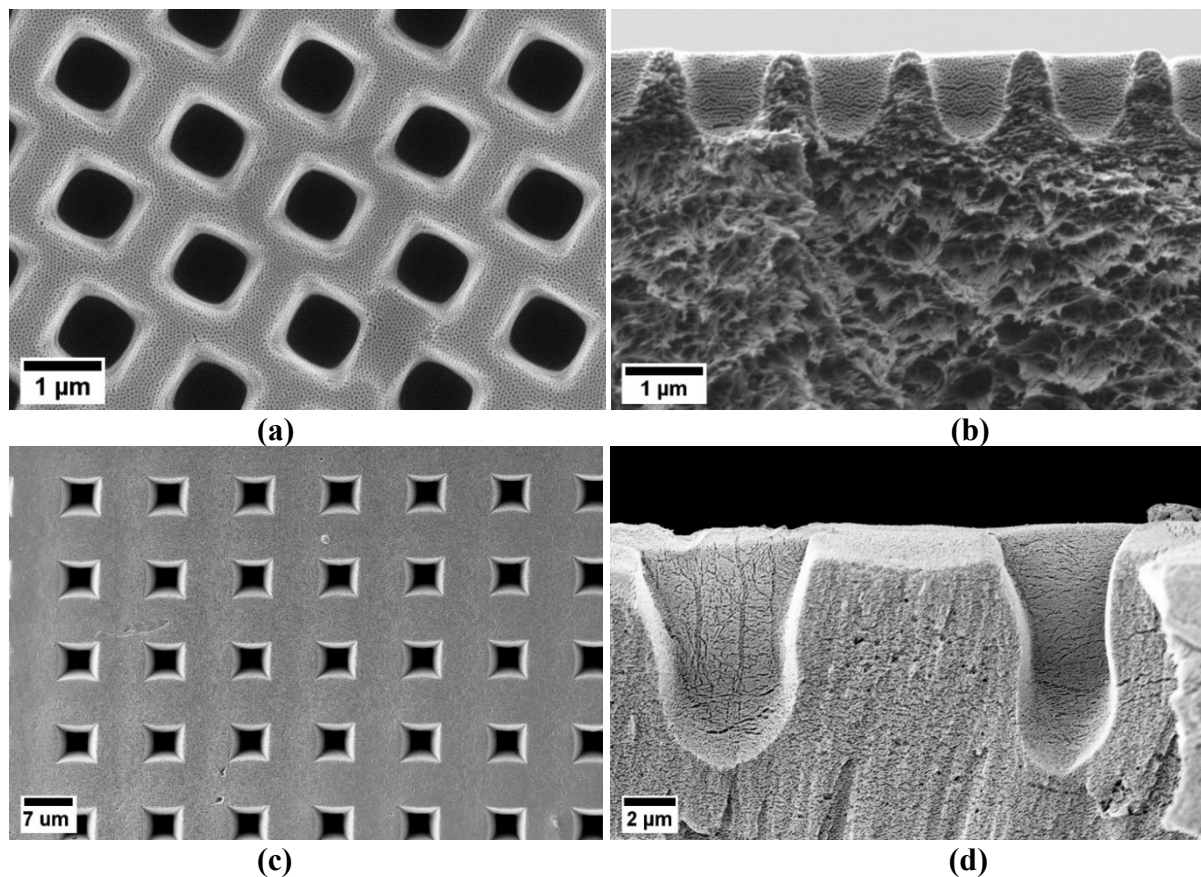


Figure 5-2 SEM images of a macroporous-nanoporous block copolymer substrates. (a-b) swelled PS-*b*-P2VP patterned substrate, (a) top view and (b) cross-sectional view. (c-d) swelled macroporous PS-*b*-P4VP substrate, (a) top view and (b) cross-sectional view.

5.2.1 Self-assembly of SiO₂ microparticles inside porous block copolymer substrates

SiO₂ microparticles with diameters of 4.07 μm and 0.755 μm were deposited into the macropores of PS-*b*-P4VP or PS-*b*-P2VP substrates according to the method described in the section 3.3.1.3.1. SiO₂ microparticles arranged themselves very homogenously and well embedded. One SiO₂ microsphere with a diameter of 0.755 μm can be seen in each PS-*b*-P2VP macropore (Figure 5-3a-b). The sizes of the SiO₂ microsphere sizes were selected in such a way that only one microsphere fitted into a macropore. Figure 5-3c-d shows the embedded of single 4.07 μm SiO₂ microparticles inside the macropores of the PS-*b*-P4VP substrate.

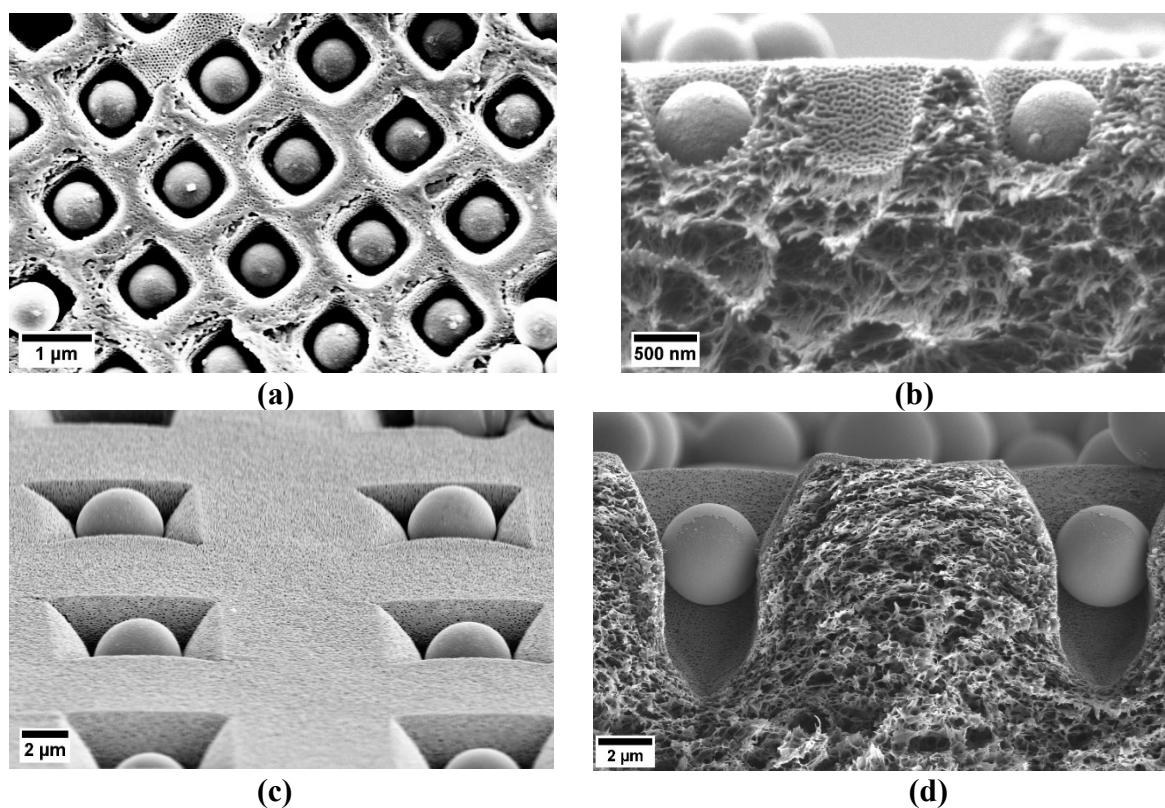


Figure 5-3 SEM images of patterned block-copolymer substrates with macropores containing silica microspheres. (a-b) SEM images of a PS-*b*-P2VP substrate containing SiO₂ microspheres

with a diameter of 0.755 μm in its macropores; (a) top view and (b) cross-sectional view. (c-d) SEM images of a PS-*b*-P4VP substrate containing SiO₂ microspheres with a diameter of 4.07 μm in its macropores; (c) tilted view and (d) cross-sectional view.

5.2.1.1 Site-selective orthogonal modifications of SiO₂ microparticles inside PS-*b*-P2VP with gold and K₂Cr₂O₇

For the site-selective orthogonal modification of 0.755 μm SiO₂ microparticles embedded inside the macropores of PS-*b*-P2VP membranes, the methods described in section 3.3.2.1.1 were applied. For the mapping of the elemental composition, EDX characterization was performed. Figure 5-4b-e reveals the distribution of the relevant elements on a modified SiO₂ microparticle located in a substrate macropore. The presence of Cr and O at the lower part of the SiO₂ particle supports the successful modification of infiltrated solution through the nanoporous channel.

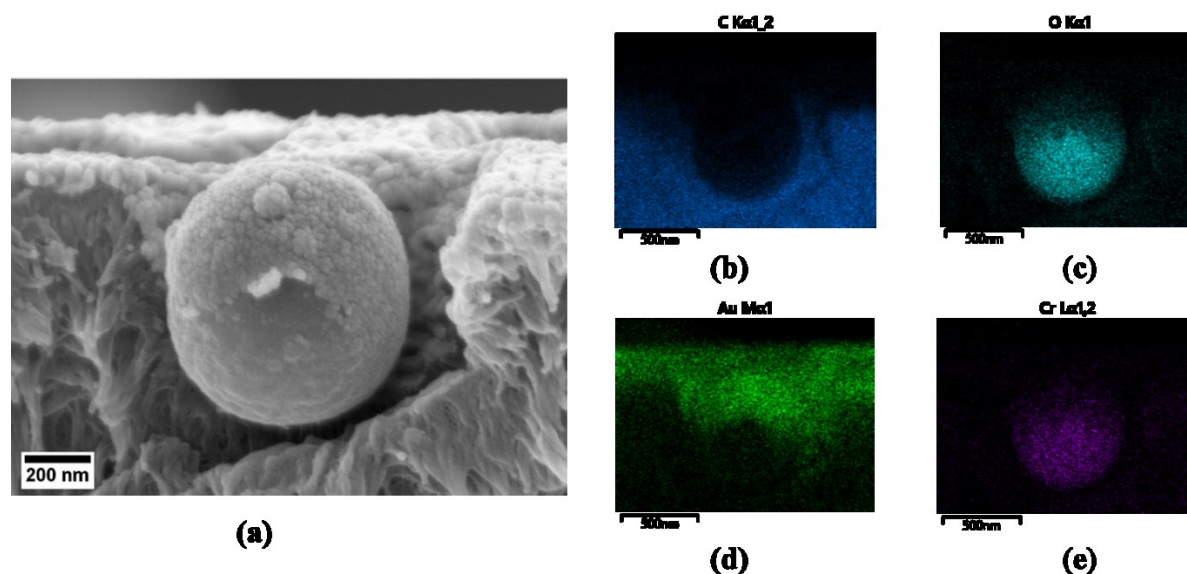


Figure 5-4 (a) SEM image for the EDX elemental mapping of 0.755 μm SiO₂ particles embedded inside a macropore of a PS-*b*-P2VP membrane. (b-e) EDX elemental mappings of the SEM image shown in a); EDX maps of (b) C K $\alpha_{1,2}$, (c) O K α_1 , (d) Au M α_1 , and (e) Cr L $\alpha_{1,2}$.

5.2.1.2 Site-selective orthogonal modifications of SiO₂ microparticles inside PS-*b*-P4VP with 1-dodecanethiol and APTES

In section 3.3.2.1.1, the modification method for the site-selective orthogonal modification of embedded SiO₂ microparticles with 1-dodecanethiol and APTES molecules is described. The top-most SiO₂ microparticle (diameter: 4.07 μm) facing upward was modified with 1-dodecanethiol. For this purpose, the embedded SiO₂ microparticles were sputter-coated with a ≈ 20 nm thick gold layer, then modified with 1-dodecanethiol. The thiol molecules on the Au surface are chemisorbed due to a robust thiolate-Au bond.[208] APTES is among the organosilanes, which are mostly used as a coupling agent for further functionalization of silica surfaces.[209] Wang *et al.*[210] reported surface modification of SiO₂ colloidal spheres with APTES. The presence of the APTES amino groups was advantageous for enhancing CO₂ gas sensing performance. Issa *et al.*[211] reported grafting of poly(ethylene oxide) monomethyl ether (MPEO) on APTES-modified colloidal SiO₂ nanoparticles. The PS-*b*-P4VP/SiO₂ substrate containing SiO₂ microparticles 4.07 μm in diameter was selectively modified with 1-dodecanethiol and APTES.

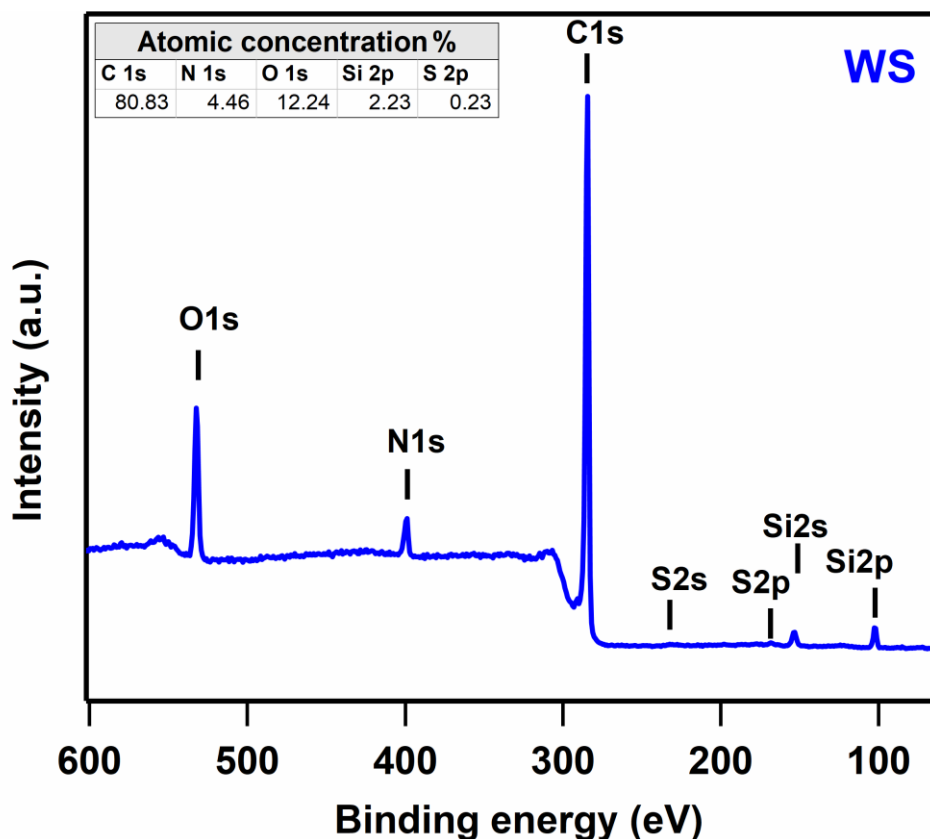


Figure 5-5 Wide-scan X-ray photoelectron (WS-XP) spectrum of SiO₂ microparticles embedded in a PS-*b*-P4VP/SiO₂ substrate after modification with 1-dodecanethiol and APTES.

Corresponding wide-scan X-ray photoelectron (WS-XP) spectra and high-resolution X-ray photoelectron (HR-XP) spectra are shown in Figures 5-5 and 5-6, respectively. The embedded SiO₂ microparticles inside the macropores were exposed on both modified sides for XPS measurements. For this, the sample PS-*b*-P4VP/SiO₂ substrate film containing SiO₂ microparticles 4.07 μm in diameter modified with 1-dodecanethiol and APTES was first to cut into half and then placed cross-sectionally in the cross-sectional sample holder. The wide-scan XP spectrum shows peaks from all elements (Si 2p, O 1s, N 1s, C 1s, S 2s, S 2p) present in PS-*b*-P4VP/SiO₂ substrate modified with 1-dodecanethiol and APTES.

High-resolution X-ray photoelectron (HR-XP) spectra shown in Figure 5-6 evidence the successful modification of the SiO₂ microparticles embedded inside the macropores. Figure 5-6a shows the HR-XP spectrum around the sulfur 2p peaks with a two-peak structure, revealing the presence of the S 2p peaks at binding energies of ≈163.7 eV and ≈168.5 eV, respectively, which can be assigned to sulfur atoms bound to a gold surface.[193-198] The lower S 2p peak has a very weak duplet peak 2p_{1/2}, and S 2p_{3/2} at 161.9 eV and 163.7 eV, which is indicative of a metal sulfide, and the peak at 168.5 eV shows the presence of a high oxidation state form of sulfur.[212, 213] So, in the sample, the presence of a form of sulfur in a high oxidation state (S 2p BE > 166 eV) such as in sulfonate (–SO₃H) groups was detected by XPS.[214] The presence of the sulfur S 2p peak at 161.9 eV suggests the bounding of sulfur atoms to the gold surface as a thiolate species in agreement with results reported by others.[214] As shown in Figure 5-6b, the peaks at B.E of 227.6 eV and 231.9 eV correspond to the sulfur S 2s peaks.[215, 216] The unmodified SiO₂ microparticles in the PS-*b*-P4VP/SiO₂ substrate show no clear peaks of S 2p and S 2s, suggesting successful modification of top-sided of embedded SiO₂ microparticles in macropores with 1-dodecanethiol. The unmodified SiO₂ microparticles are the microparticles that were assumed not to be successfully modified during the modification process. The unmodified SiO₂ microparticles were noticed after some tries during measurements. The presence of N 1s peak at B.E of 399.5 eV shown in Figure 5-6c indicates the presence of amino groups and, therefore, of APTES.[217]

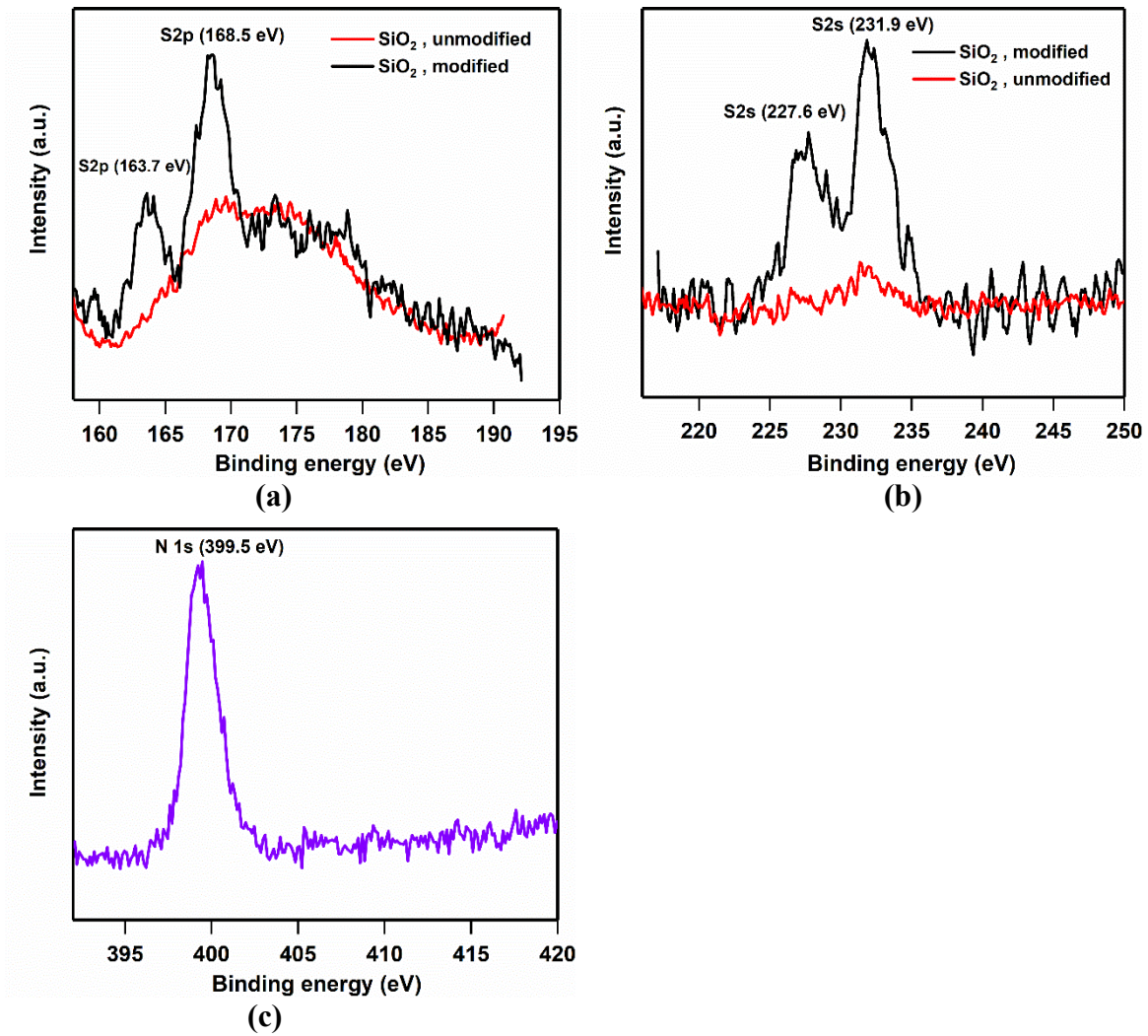


Figure 5-6 High-resolution X-ray photoelectron (HR-XP) spectra of SiO₂ microparticles embedded in a PS-*b*-P4VP/SiO₂ substrate modified and unmodified with 1-dodecanethiol and APTES. (a) HR-XP spectrum of sulfur 2p, and (b) HR-XP spectrum of sulfur 2s. (c) HR-XP spectrum of nitrogen 1s taken after the modification.

6 Hollow microrings by a one-step direct imprinting method

6.1 Fabrication of PDMS secondary mold

PDMS secondary molds were obtained by pouring PDMS prepolymer onto silanized mSi. After curing, the PDMS molds had pillars at the positions of the mSi macropores (see section 3.3.1.1). The pillar depth ($\approx 6.99 \mu\text{m}$) and base opening diameter ($\approx 5.06 \mu\text{m}$) of the PDMS pillars (see Figure 5-1d in section 5.1) approximately match the dimensions of the macropores of the primary mSi mold (total pore length of $7.26 \mu\text{m}$, $6.0 \mu\text{m}$ pore opening diameter, and $3.5 \mu\text{m}$ pore bottom diameter) seen in Figure 5-1c section 5.1.

6.2 Fabrication of hollow microrings

All microrings were fabricated by using a method described in section 3.3.3, Figure 3-7. Imprinting pressure is an essential factor affecting pattern quality and mold durability.[218] The effect of imprint pressure on height h , diameter d of hollow microrings, and width w of the rim have been described. The pattern transferred from a secondary elastomeric stamp (PDMS having pillars with $3.5 \mu\text{m}$ pore bottom diameter) consists of hollow microrings. The pressure was adjusted by applying to add different weights of steel blocks on top of the stamp. Two imprinting pressures with the value of $\approx 3.95 \text{ kN m}^{-2}$ and $\approx 7.87 \text{ kN m}^{-2}$ were applied to the transfer pattern.

6.2.1 Chitosan (CS) and chitosan-graphene oxide (CS-GO) hydrogel microrings

The CS and CS-GO were synthesized as described in section 3.3.3.2. The hollow microrings of chitosan (CS) and chitosan-graphene oxide (CS-GO) hydrogel was fabricated using the imprint method described in section 3.3.3.4. Corresponding wide-scan X-ray photoelectron (WS-XPS) spectra and high-resolution X-ray photoelectron (HR-XPS) spectra are shown in Figures 6-1 and 6-2, respectively. The CS or CS-GO solution was spin-coated on silicon substrates at 2000 rpm for XPS measurements for 1 min. The wide-scan XPS spectrum shows peaks from all elements (O 1s, N 1s, C 1s) present. HR-XPS spectra were measured to verify

the successful fabrication of chitosan (CS) and chitosan-graphene oxide (CS-GO) hydrogel nanocomposite. For this purpose, HR-XP of both CS and CS-GO nanocomposite were measured. The HR-XP spectrum around the N 1s peak measured on a chitosan (CS) film is shown in Figure 6-2a. The obtained curve can be deconvoluted into three peaks, which can be related to the amine (C-NH₂) peak at a binding energy of 399.4 eV, the amide (C-NHC=O) peak at a binding energy of \approx 400.5 eV and protonated amine species (C-NH₃⁺) at a binding energy of \approx 401.7 eV. The presence of N 1s at the measured binding energy values agrees with values reported in the literature.[171, 219] However, there are no noticeable peak shape changes in the N 1s spectra; only a shift of the amine peak from the binding energy of \approx 399.4 (CS) to the binding energy of 399.1 eV (CS-GO) occurred (Figure 6-2c). The C 1s spectrum of CS can be deconvoluted into three peaks at binding energies of 284.5, 286.13, and 287.5 eV that can be assigned to C-C, C-O, and C=O groups (Figure 6-2b). The HR-XP spectra around the C 1s peak of CS-GO could also be deconvoluted into three peaks at binding energies of 284.5, 286.13, and 287.5 eV that could be ascribed to C-C, C-O, and C=O groups (Figure 6-2d). However, as compared to the C 1s peak obtained for CS, the wider peak at 287.5 eV obtained for GO indicates the presence of C=C, alongside with C-C characteristic peak at 284.5 eV. Furthermore, the intensity of the C-O and C=O peaks in the CS-GO nanocomposite is due to the contribution of graphene oxide.[219]

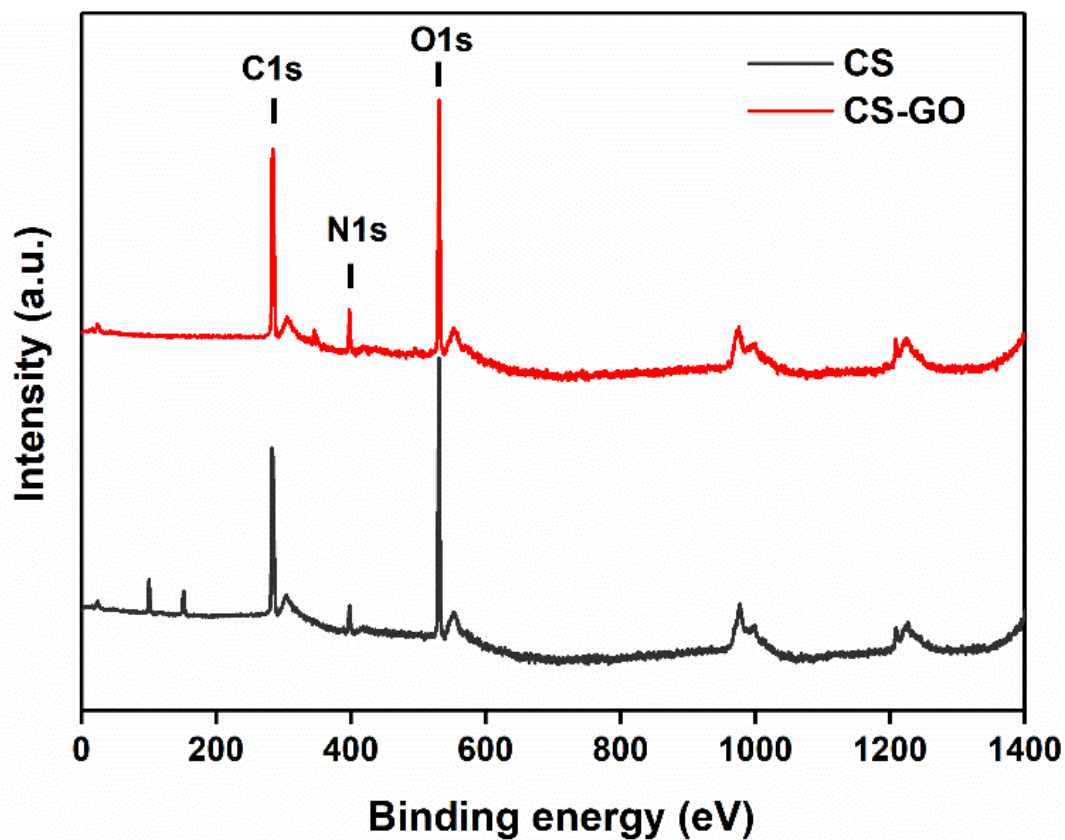


Figure 6-1 Wide-scan X-ray photoelectron (WS-XP) spectrum of CS and CS-GO hydrogel films.

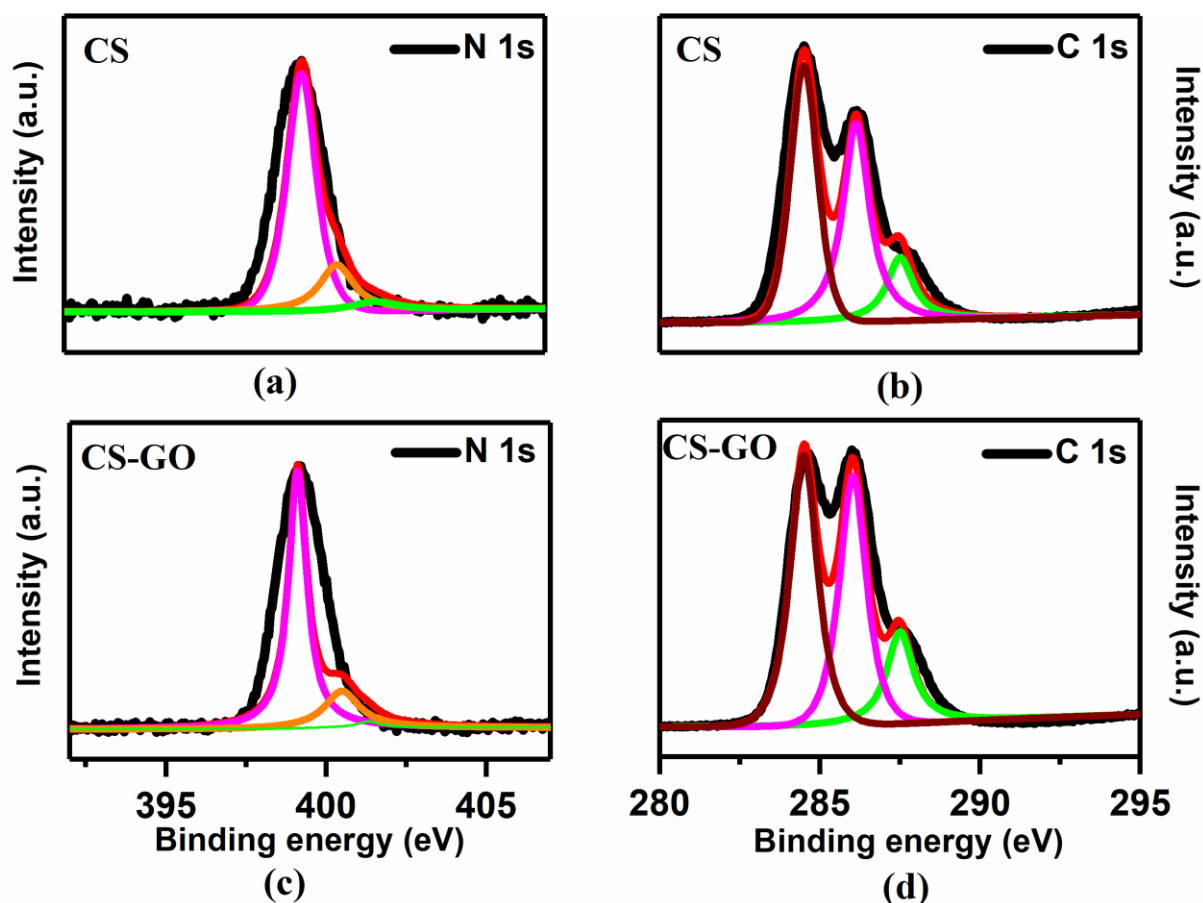


Figure 6-2 High-resolution X-ray photoelectron (HR-XP) spectra of CS and CS-GO hydrogel films. (a) HR-XP spectra of the region of the nitrogen N 1s peak, and (b) in the region of the carbon C 1s peak in the CS film. (c) HR-XP spectra of the region of the nitrogen N 1s peak, and (d) of the region of the carbon C 1s peak for the CS-GO film.

6.2.1.1 Morphological characterization of chitosan (CS) hydrogel microrings

Figure 6-3a-b shows the SEM images of hollow microrings of CS imprinted on Si substrate with an imprint pressure of 3.95 kN m^{-2} . The hollow microrings of CS are hexagonally arranged and have long-range order and almost no defects. The order of printed CS hollow microrings can be clearly seen from detailed magnified SEM images (Figure 6-3b). The hollow microrings' surface topography and height profile are characterized using atomic force microscopy (AFM). Figure 6-3c-d shows an AFM image to analyze the height of the hollow microrings. The average height of the eight hollow microrings amounted to $79.53 \pm 13.82 \text{ nm}$ measured with AFM. The measurement was done with AFM using the contact mode and extracting a line

profile of the measured data (Figure 6-3d). The average thickness of the rims calculated from 8 microrings from the AFM image amounted to $1.56\pm 0.35\ \mu\text{m}$. The hollow microrings of CS were analyzed according to the procedure described in chapter 3.1.4. and a total of 86 hollow microrings of CS was evaluated from a binarized SEM image. The analyzed hollow microrings have a diameter of $\approx 2.65\pm 0.17\ \mu\text{m}$, a circularity of $\approx 0.95\pm 0.09$, and an average aspect ratio of $\approx 1.07\pm 0.07$ (Figure 6-3e-g). Under the optimal thermal and pressure conditions, the precursor solution is attracted to the walls of the protruding mold section. It results in the transfer of the pattern.[220]

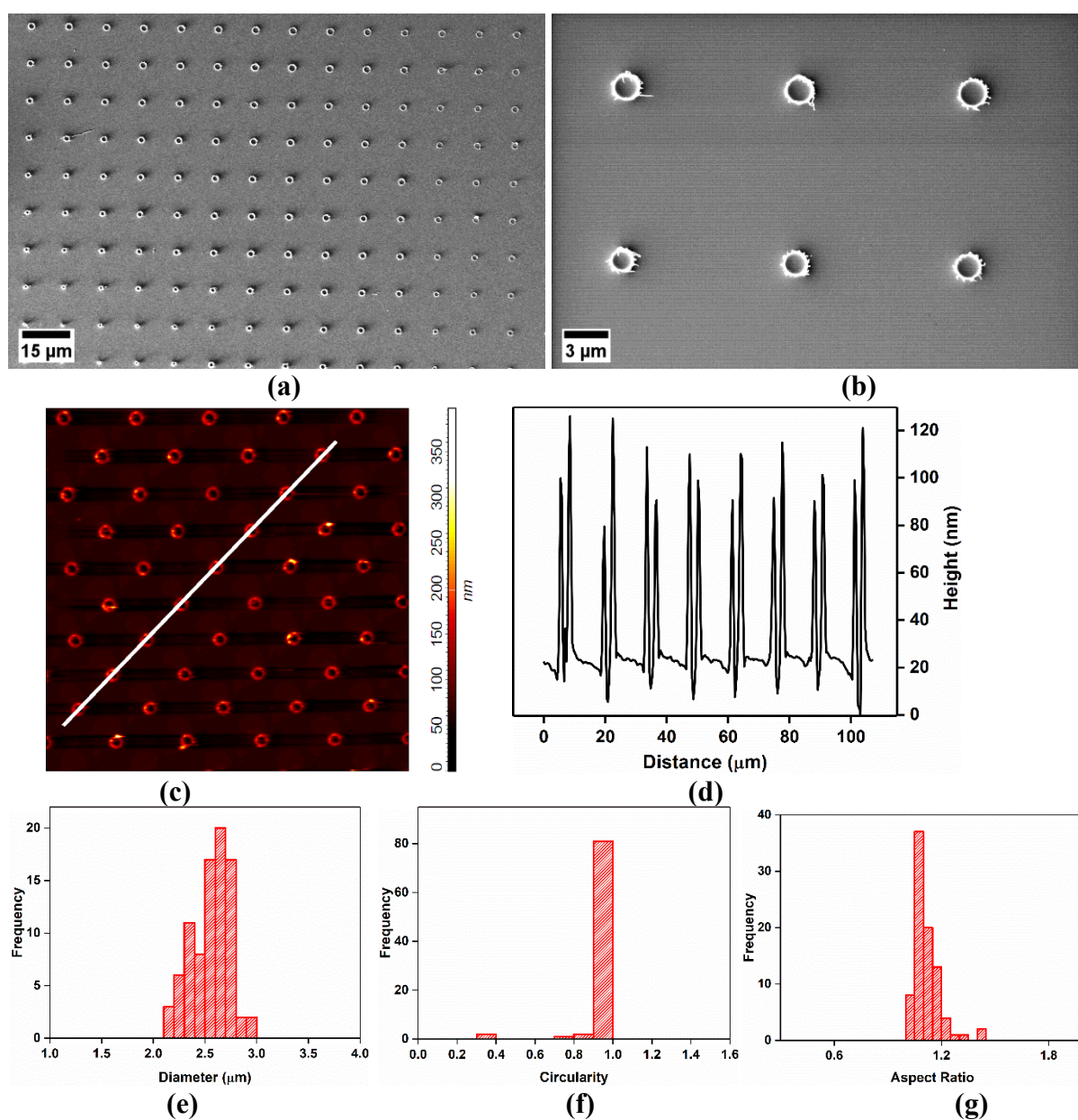
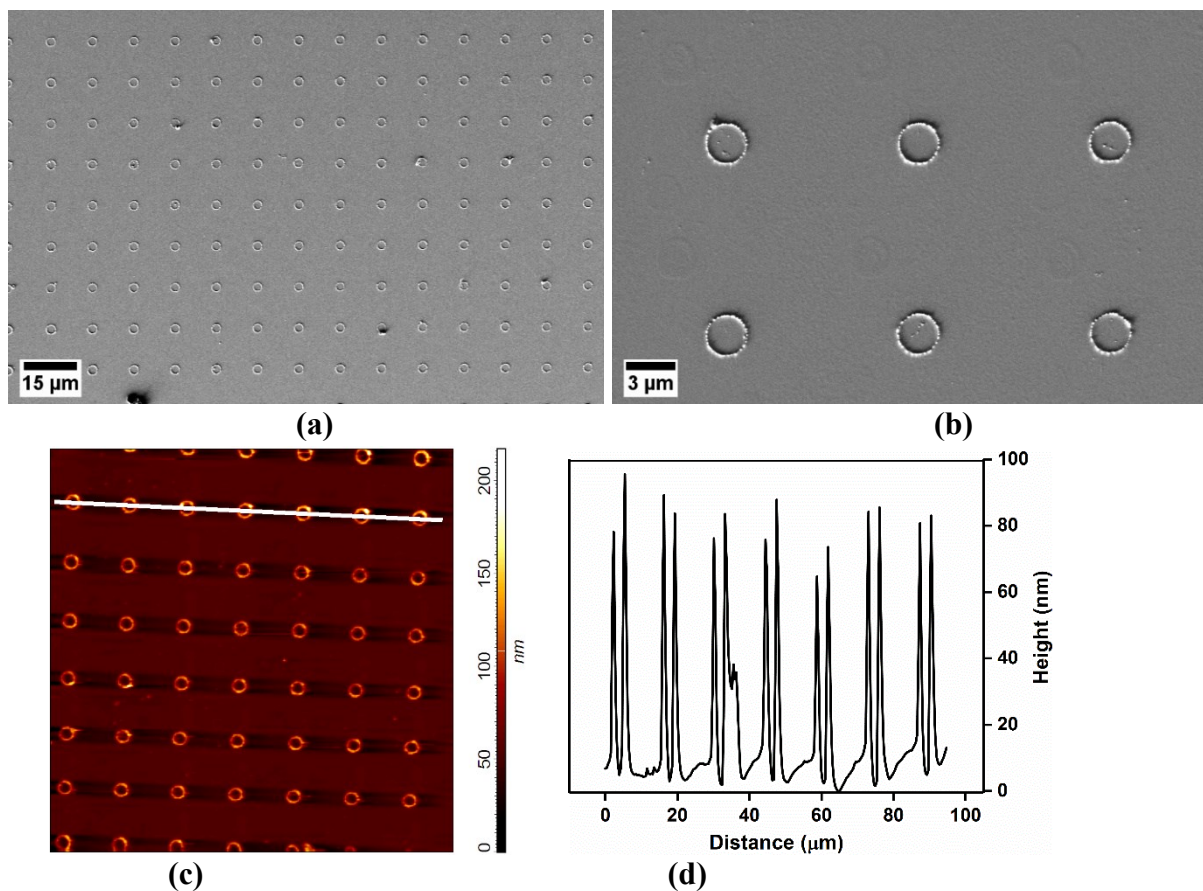


Figure 6-3 Imprinted hollow microrings of chitosan (CS) hydrogel on a silicon (Si) substrate fabricated under 3.95 kN m^{-2} imprint pressure. (a-b) SEM images; (a) large-area top view, and (b) detail top view. (c) Atomic force microscopy (AFM) image ($100 \times 100 \mu\text{m}^2$), and (d) topographic line scan along the white line in c). (e-f) Histograms of (e) the diameters, (f) the circularities, and (g) the aspect ratios of 86 analyzed microrings.

Figure 6-4a-b shows the SEM images of hollow microrings of CS imprinted on a Si substrate with an imprint pressure of 7.87 kN m^{-2} . The hollow microrings of CS are hexagonally arranged and have long-range order with few defects. Figure 6-4c-d shows an AFM image to analyze the height of the hollow microrings. The average height of the seven hollow microrings amounted to $81.52 \pm 7.57 \text{ nm}$ measured with AFM. The line profile is extracted from the measured data (Figure 6-4d). The average thickness of the rims calculated from 7 microrings from the AFM image amounted to $1.62 \pm 0.30 \mu\text{m}$. A total of 86 hollow microrings of CS were evaluated from a binarized SEM image according to the procedure described in chapter 3.1.4. The hollow microrings have a diameter of $\approx 3.15 \pm 0.09 \mu\text{m}$, a circularity of $\approx 0.75 \pm 0.09$, and an average aspect ratio of $\approx 1.12 \pm 0.07$ (Figure 6-4 e-g).



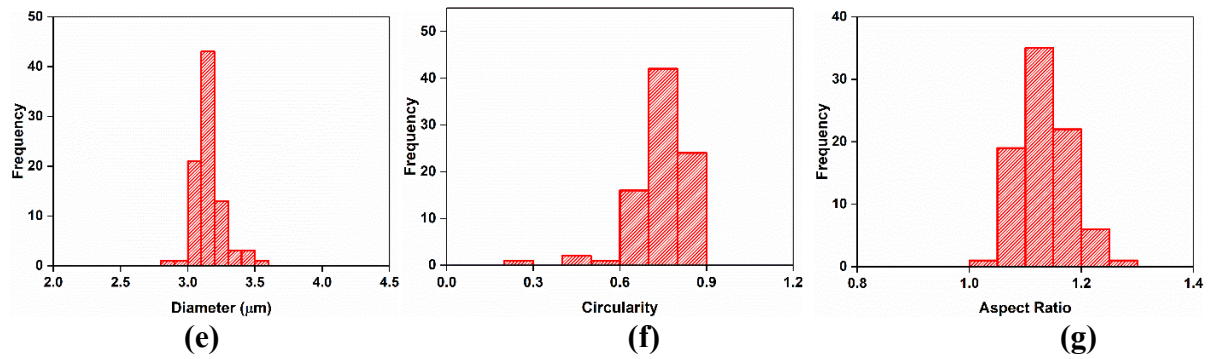


Figure 6-4 Imprinted hollow microrings of chitosan (CS) hydrogel on a silicon (Si) substrate fabricated under 7.87 kN m^{-2} imprint pressure. (a-b) SEM images; (a) large-area top view, and (b) detail top view. (c) AFM image ($100 \times 100 \mu\text{m}^2$), and (d) topographic line scan along the white line in c). (e-f) Histograms of (e) the diameters, (f) the circularities, and (g) the aspect ratios of 86 analyzed microrings.

6.2.1.2 Morphological characterization of chitosan-graphene oxide (CS-GO) hydrogel microrings

Figure 6-5a-b shows the SEM images of hollow microrings of CS-GO imprinted on a Si substrate with an imprint pressure of 3.95 kN m^{-2} . The hollow microrings of CS-GO are hexagonally arranged and have long-range order with some defects. The hollow microrings' surface topography and height profile were characterized using atomic force microscopy (AFM). Figure 6-5c-d shows an AFM image to analyze the height of the hollow microrings. The average height of the six hollow microrings amounted to $29.31 \pm 4.86 \text{ nm}$ measured with AFM. A topographic line profile of the measured data was extracted from the AFM image (Figure 6-5d). The average thickness of the rims calculated from 6 microrings from the AFM image amounted to $1.73 \pm 0.30 \mu\text{m}$. The hollow microrings of CS-GO were analyzed according to the procedure described in chapter 3.1.4 and total of 129 hollow microrings of CS-GO were evaluated from a binarized SEM image. The analyzed hollow microrings diameter of $\approx 2.50 \pm 0.42 \mu\text{m}$, a circularity of $\approx 0.75 \pm 0.16$, an average aspect ratio of $\approx 1.30 \pm 0.13$ (Figure 6-5e-g).

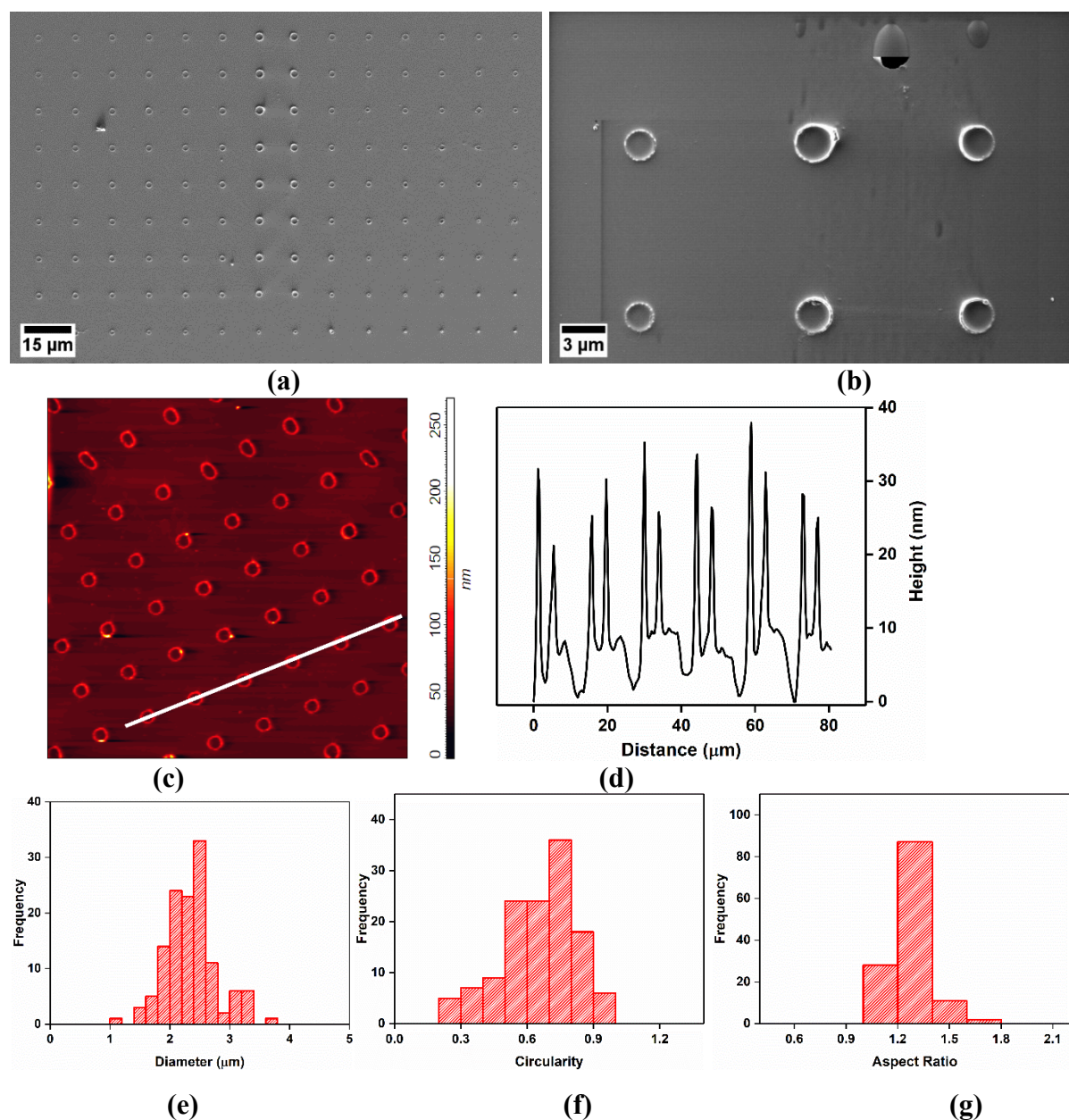


Figure 6-5 Imprinted hollow microrings of chitosan-graphene oxide (CS-GO) hydrogel on a silicon (Si) substrate fabricated with 3.95 kN m^{-2} imprint pressure. (a-b) SEM images; (a) large-area top view, and (b) detail top view. (c) AFM image ($100 \times 100 \mu\text{m}^2$), and (d) a topographic line scan along the white line in c). (e-f) Histograms of (e) the diameters, (f) the circularities, and (g) the aspect ratios of 129 analyzed micron hollow microrings.

Figure 6-6a-b shows the SEM images of hollow microrings of CS-GO imprinted on Si substrate with imprint pressure of 7.87 kN m^{-2} . The hollow microrings of CS are hexagonally arranged, have long-range order, and have few defects. Figure 6-6c-d shows an AFM image to analyze the height of the hollow microrings, and the average height of the hollow microrings amounted

to 37.34 ± 5.15 nm. A topographic line profile was extracted from the measured data (Figure 6-6d). The average thickness of the rims calculated from 7 microrings from the AFM image amounted to 1.84 ± 0.34 μm . A total of 91 hollow microrings of CS-GO were evaluated from a binarized SEM image having a diameter of $\approx 2.67 \pm 0.09$ μm , a circularity of $\approx 0.75 \pm 0.13$, an average aspect ratio of $\approx 1.05 \pm 0.01$ (Figure 6-6 e-g).

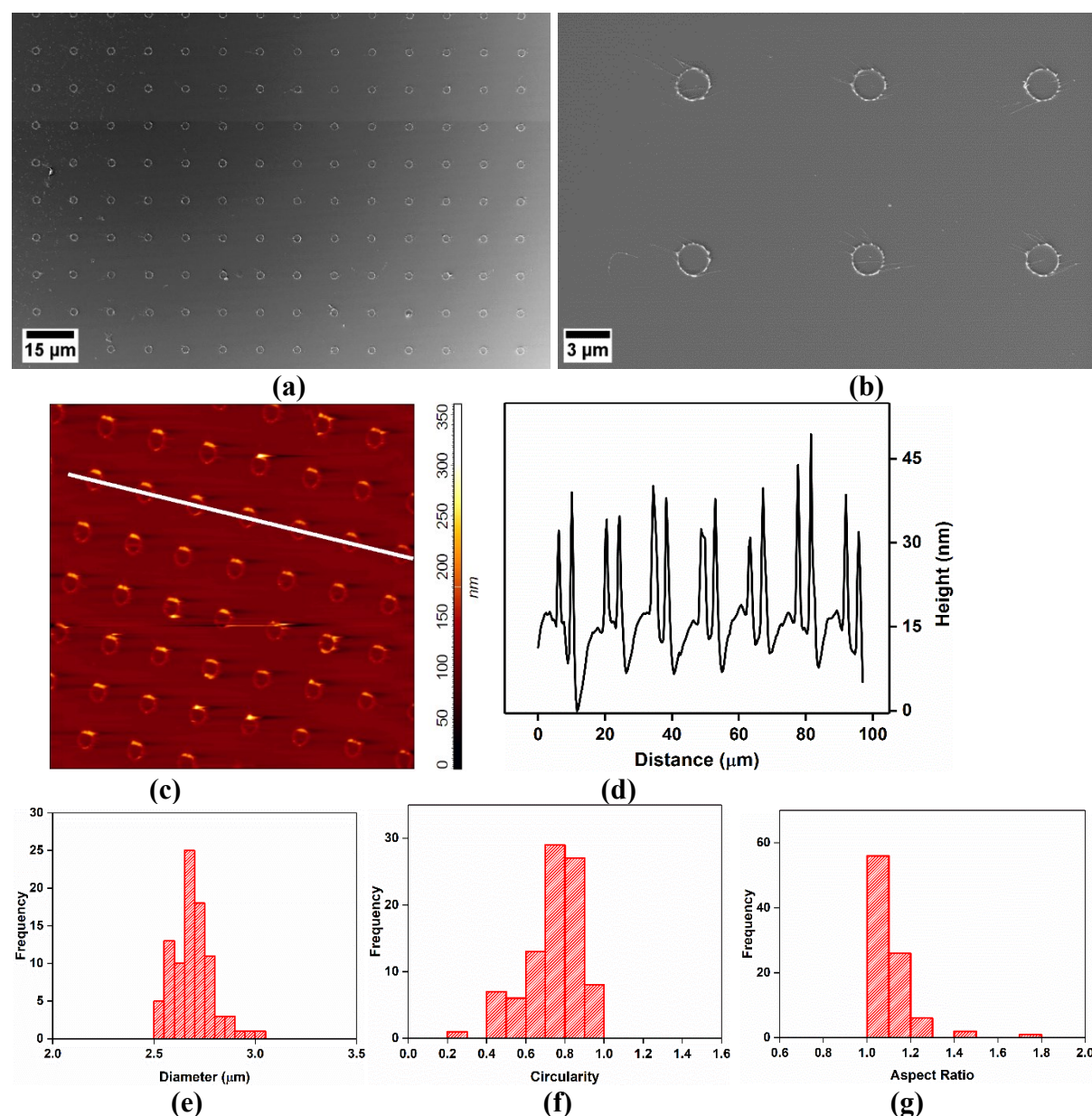


Figure 6-6 Imprinted hollow microrings of chitosan-graphene oxide (CS-GO) hydrogel on a silicon (Si) substrate fabricated with 7.87 kN m^{-2} imprint pressure. (a-b) SEM images; (a) large-area top view, and (b) detail top view. (c) AFM image ($100 \times 100 \mu\text{m}^2$), and (d) topographic line scan along the white line in c). (e-f) Histograms of (e) the diameters, (f) the circularities, and (g) the aspect ratios of 91 analyzed micron hollow microrings.

Table 6-1 Summary of all results of imprinted CS and CG-GO hollow microrings onto silicon substrates using two different imprinting pressures.

Samples	Imprinting pressure	Diameter d of hollow microrings	height h of hollow microrings	Width w of the rim
CS	3.95 kN m ⁻²	2.65 ± 0.17 μm	103.88 ± 13.82 nm	1.56 ± 0.35 nm
	7.87 kN m ⁻²	3.15 ± 0.09 μm	81.52 ± 7.57 nm	1.62 ± 0.30 nm
CS-GO	3.95 kN m ⁻²	2.50 ± 0.42 μm	29.31 ± 4.86 nm	1.73 ± 0.30 μm
	7.87 kN m ⁻²	2.67 ± 0.09 μm	37.34 ± 5.15 nm	1.84 ± 0.34 μm

6.2.2 Fabrication of titania (TiO₂) microrings

TiO₂ sol-gel solution was synthesized as described in section 3.3.3.1. Hollow microrings of TiO₂ were fabricated using the imprint method described in section 3.3.3.5. The TiO₂ microrings are prepared to generate a topographically patterned substrate to generate patterned assemblies of nanoparticles. The X-ray diffraction (XRD) pattern of a synthesized TiO₂ sample annealed at 450 °C is shown in Figure 6-7. The TiO₂ sol-gel solution was deposited on a cleaned FTO glass substrate and then treated thermally. The thermal treatment was the same as the fabrication of patterned TiO₂ holey films (see experimental section 3.3.1.3). After the thermal treatment, the TiO₂ film was scratched with the help of a scalpel from the FTO substrate and further analyzed in powder form. The crystalline nature of the sample was confirmed by the occurrence of well-defined sharp Bragg diffraction peaks. By comparison with reference pattern ICSD # 202243, the diffraction peaks at 2θ values of 25.33°, 37.97°, 47.97°, 54.72°, 62.78°, 69.74°, and 75.36° were assigned to the (101), (004), (200), (105), (204), (220), and (215) reflections of tetragonal anatase with space group I41/amd. The absence of reflections emerging from other polymorphs such as rutile or brookite indicated the exclusive presence of anatase. The obtained XRD pattern agrees with previously reported XRD patterns of sol-gel synthesized TiO₂ annealed at 450°C.[166]

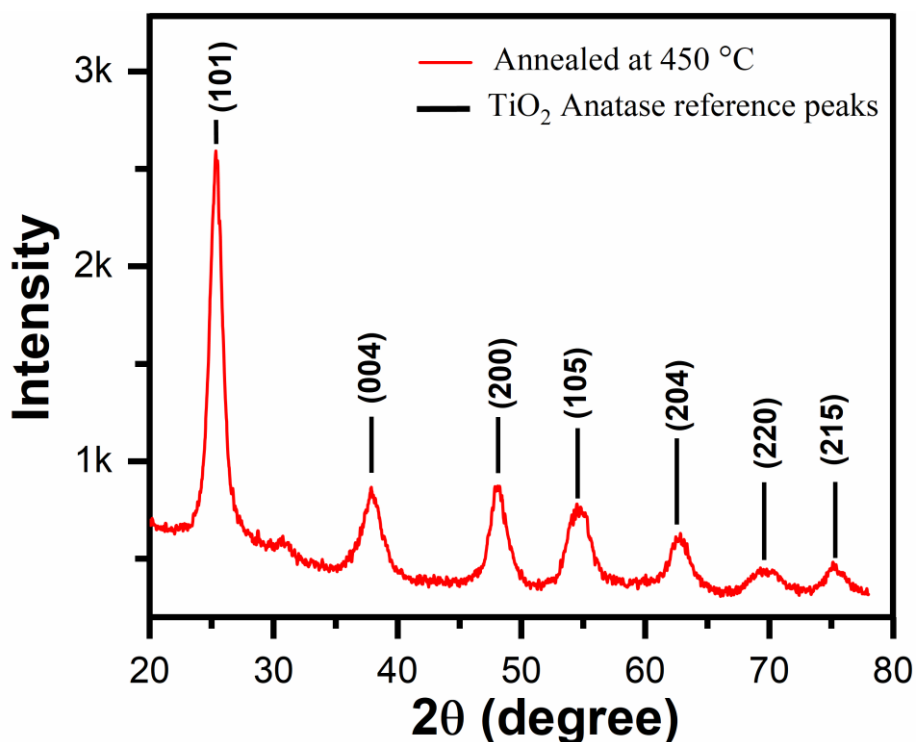


Figure 6-7 XRD pattern of sol-gel synthesized titania (TiO₂) showing the typical features of anatase phase (ICSD # 202243).

6.2.2.1 Morphological characterization of titania (TiO₂) microrings

Figure 6-8a-b shows the SEM images of hollow microrings of TiO₂ imprinted on a Si substrate with an imprint pressure of 3.95 kN m⁻². The hollow microrings of TiO₂ are hexagonally arranged and have long-range order with some defects. The hollow microrings' surface topography and height profile was characterized using atomic force microscopy (AFM). Figure 6-8c-d shows an AFM image to analyze the height of the hollow microrings. The average height of 6 hollow microrings amounted to 208.88±32.75 nm measured by AFM. A topographic line profile was extracted from the AFM image (Figure 6-8d). The average thickness of the rims calculated from 6 microrings from the AFM image amounted to 1.90±0.34 μm. A total of 109 hollow microrings of TiO₂ were evaluated from a binarized SEM image. The analyzed hollow microrings have a diameter of ≈ 3.35±0.13 μm, a circularity of ≈ 0.93±0.02, an average aspect ratio of ≈ 1.05±0.02 (Figure 6-8e-g).

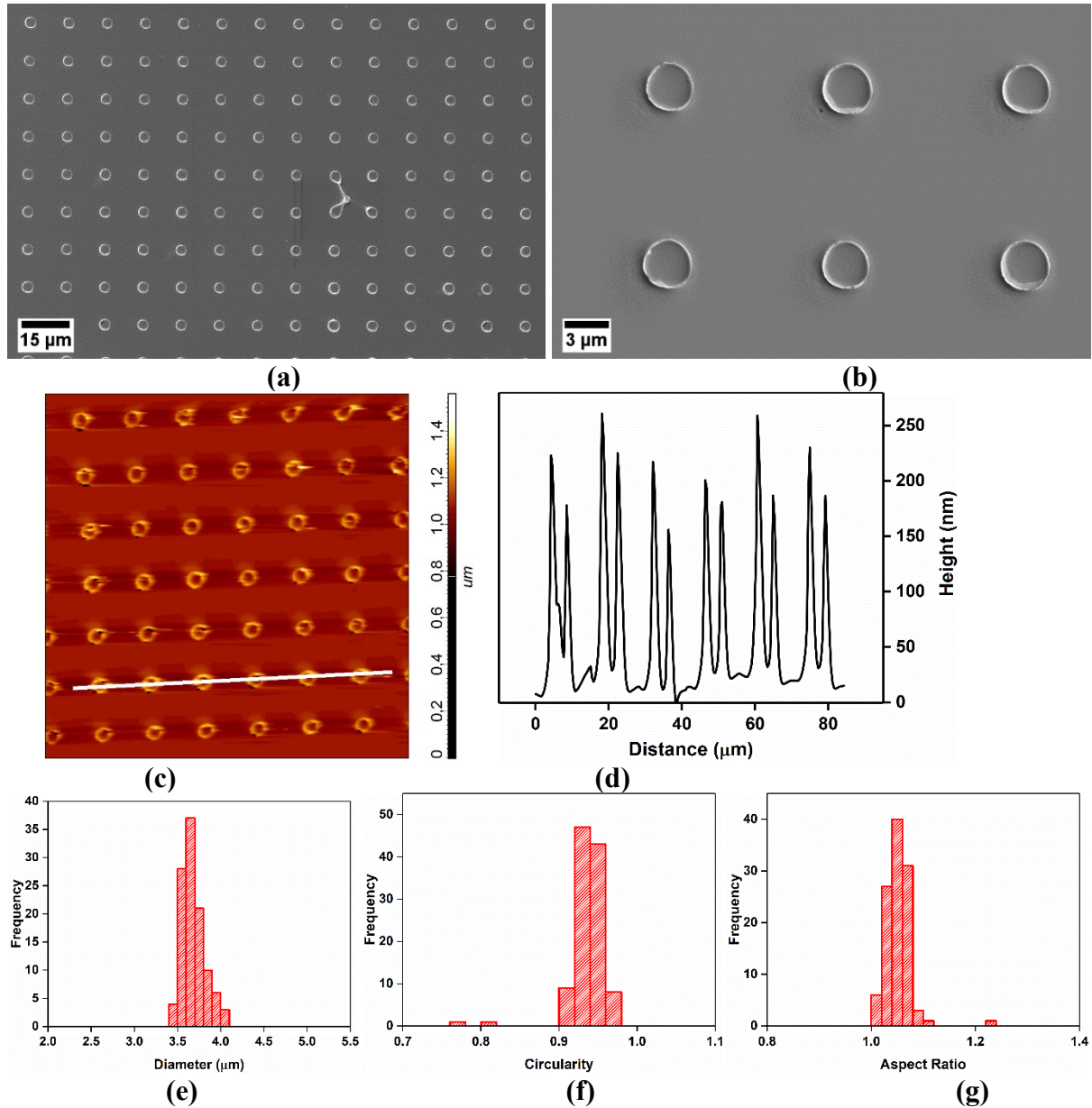


Figure 6-8 Imprinted hollow microrings of titania (TiO_2) on a silicon (Si) substrate fabricated with 3.95 kN m^{-2} imprint pressure. (a-b) SEM images; (a) large-area top view, and (b) detail top view. (c) AFM image ($100 \times 100 \mu\text{m}^2$), and (d) topographic line scan along the white line in c. (e-f) Histograms of (e) the diameters, (f) the circularities, and (g) the aspect ratios of 109 analyzed micron hollow rings.

Figure 6-9a-b shows the SEM images of hollow microrings of TiO_2 imprinted on a Si substrate with an imprint pressure of 7.87 kN m^{-2} . The hollow microrings of TiO_2 are hexagonally arranged and have long-range order with almost no defects. Figure 6-9c-d shows an AFM image to analyze the height of the hollow microrings, and the average height of 7 hollow

microrings amounted to $316.42 \pm 44.50 \text{ nm}$ measured by AFM. A topographic line profile was extracted from the measured AFM data (Figure 6-9d). The average thickness of the rims calculated from 7 microrings from the AFM image amounted to $2.07 \pm 0.37 \text{ }\mu\text{m}$. A total of 122 hollow microrings of TiO_2 were evaluated from a binarized SEM image, revealing a diameter of $\approx 4.50 \pm 0.08 \text{ }\mu\text{m}$, a circularity of $\approx 0.92 \pm 0.02$, an average aspect ratio of $\approx 1.13 \pm 0.02$ (Figure 6-9 e-g).

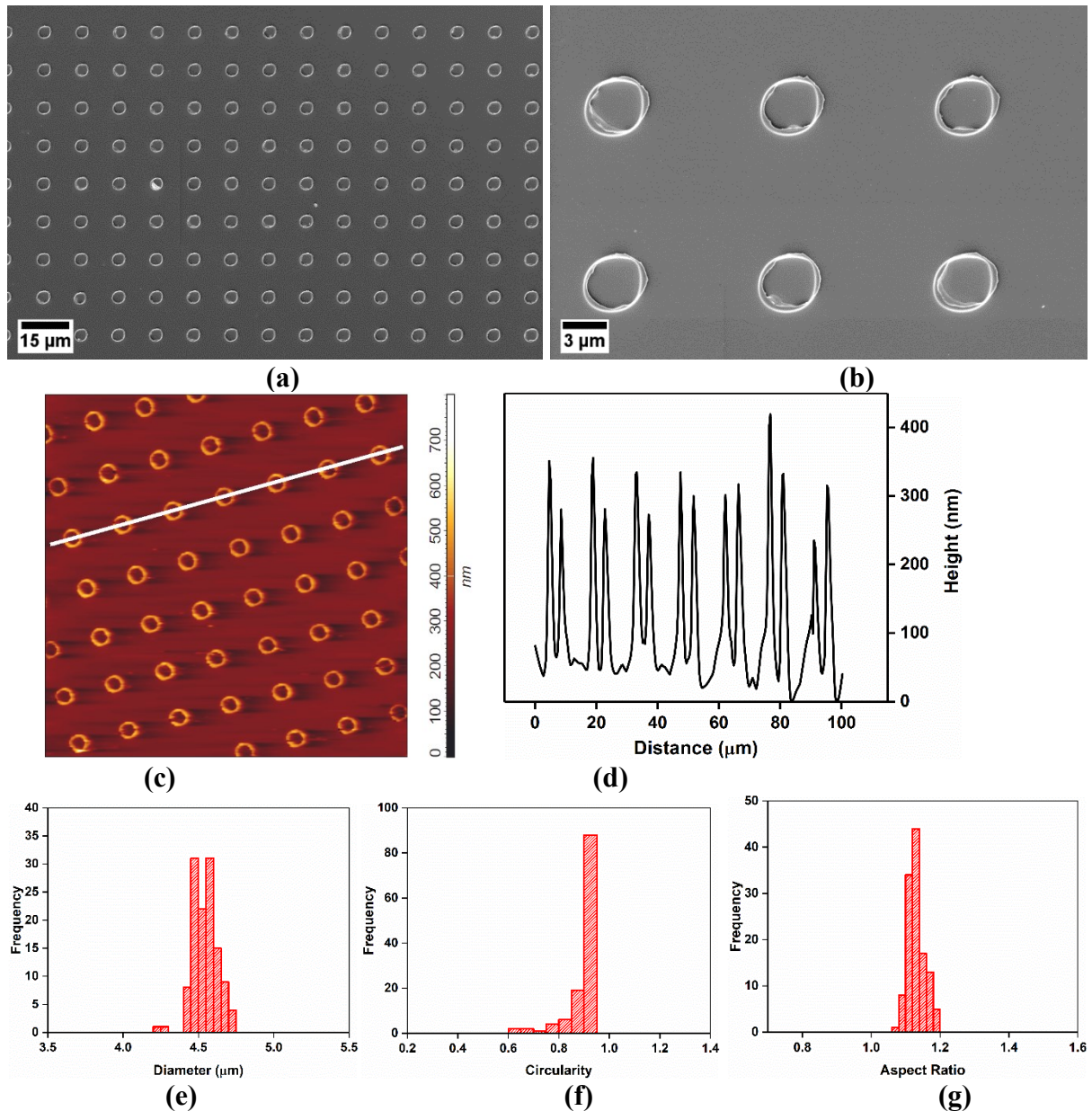
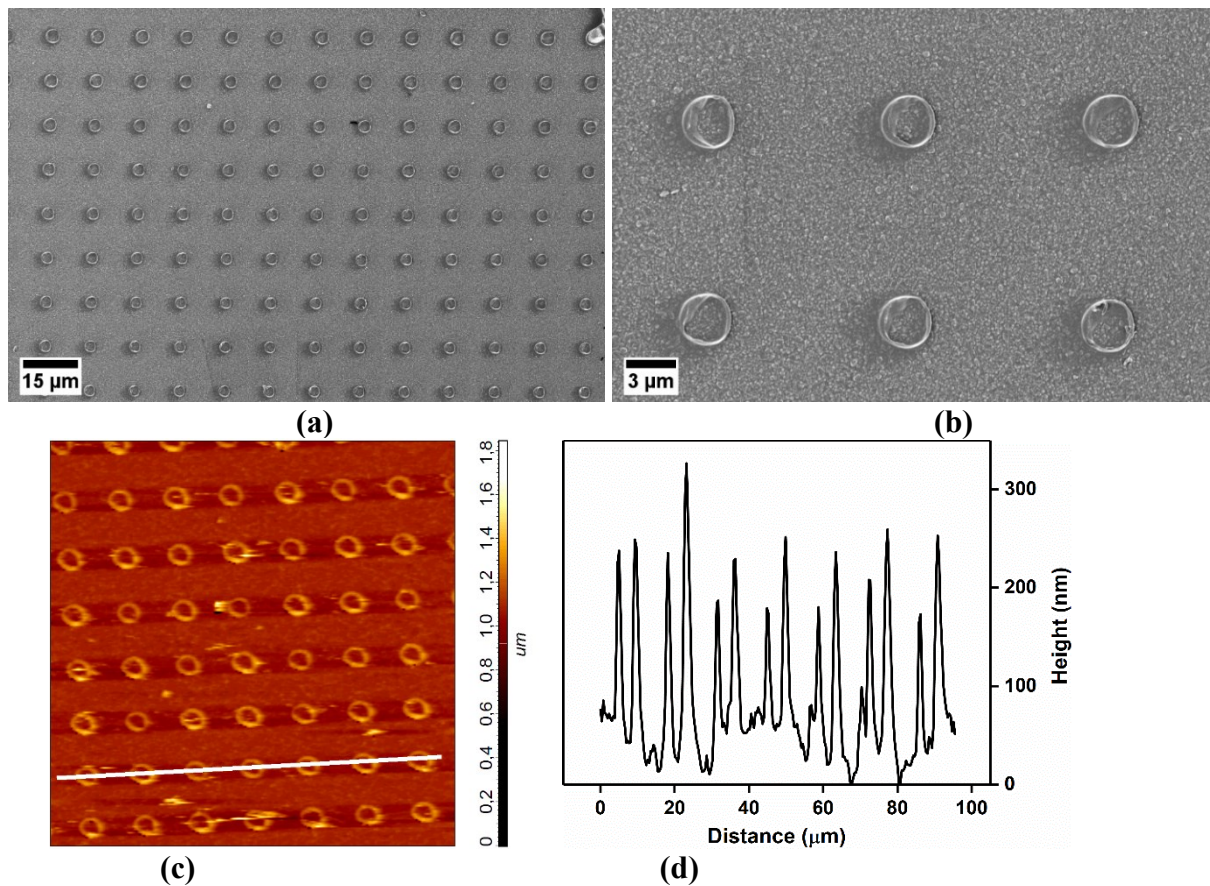


Figure 6-9 Imprinted titania (TiO_2) hollow microrings on a silicon (Si) substrate fabricated with 7.87 kN m^{-2} imprint pressure. (a-b) SEM images; (a) large-area top view, and (b) detail top view. (c) AFM image ($100 \times 100 \text{ }\mu\text{m}^2$), and (d) topographic line scan along the white line in c). (e-f) Histograms of (e) the diameters, (f) the circularities, and (g) the aspect ratios of 122 analyzed micron hollow rings.

Figure 6-10a-b shows SEM images of hollow microrings of TiO₂ imprinted on an FTO glass substrate with an imprint pressure of 7.87 kN m⁻². Figure 6-10c-d shows an AFM image to analyze the height of the hollow microrings, and the average height of the seven hollow microrings amounted to 228.87 ± 41.42 nm measured with AFM. A topographic line profile was extracted from the measured data (Figure 6-10d). The average thickness of the rims calculated from 7 microrings from the AFM image amounted to 1.98 ± 0.42 μ m. A total of 122 hollow microrings of TiO₂ were evaluated from a binarized SEM image, revealing a diameter of the hollow microrings of $\approx 3.90 \pm 0.21$ μ m, a circularity of $\approx 1.0 \pm 0.003$, and an average aspect ratio of $\approx 1.02 \pm 0.04$ (Figure 6-10e-g).



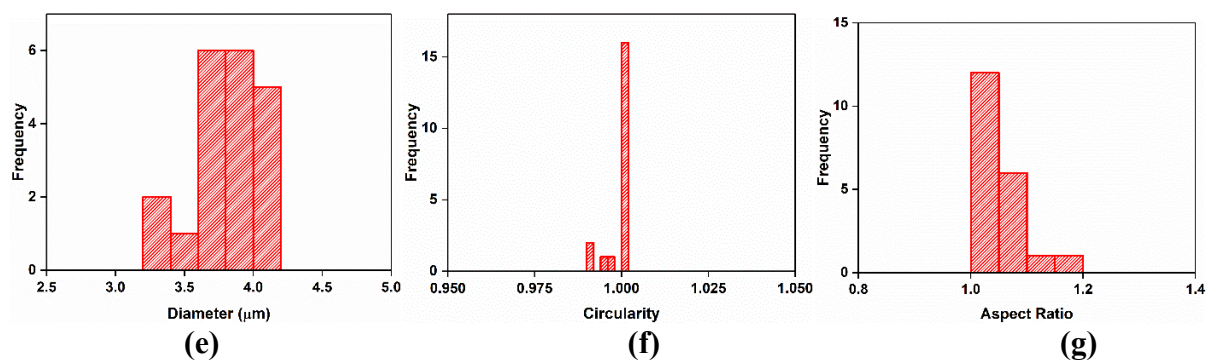


Figure 6-10 Imprinted titania (TiO_2) hollow microrings on an FTO (fluorine-doped tin oxide) substrate fabricated with 7.87 kN m^{-2} imprint pressure. (a-b) SEM images; (a) large-area top view, and (b) detail top view. (c) AFM image ($100 \times 100 \mu\text{m}^2$), and (d) topographic line scan along the white line in c). (e-f) Histograms of (e) the diameters, (f) the circularities, and (g) the aspect ratios of 122 analyzed micron hollow rings.

For the mapping of the elemental composition, EDX characterization was performed. Figure 6-11b-e reveals the distribution of the relevant elements on a hollow microring of TiO_2 imprinted on a Si substrate with an imprint pressure of 7.87 kN m^{-2} . Ti and O at the edge of the hollow microring evidence the successful fabrication of TiO_2 microrings.

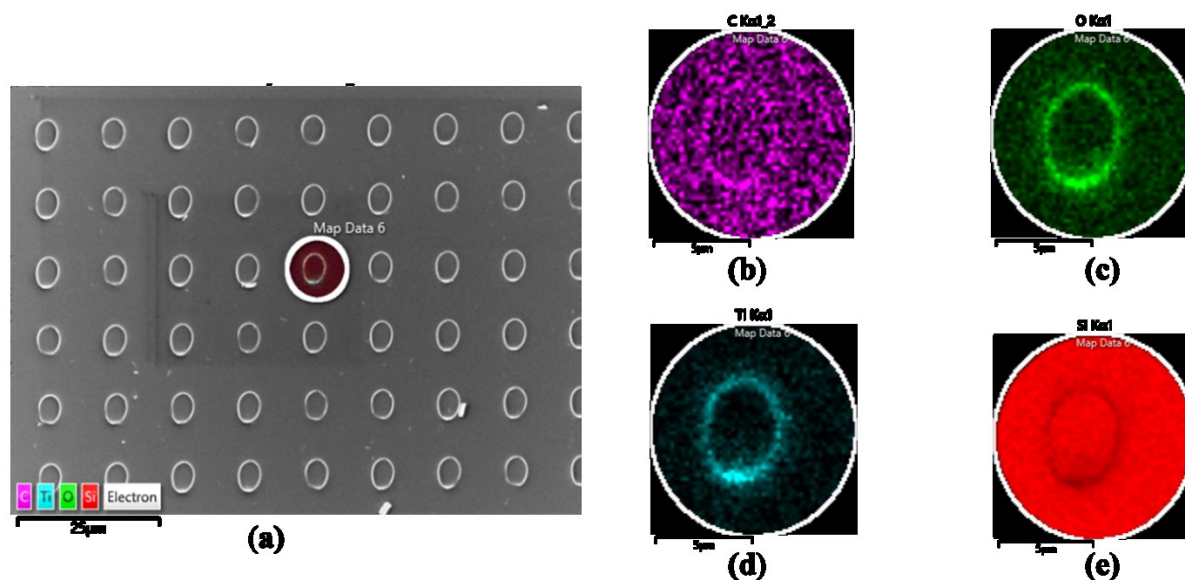


Figure 6-11 Imprinted titania (TiO_2) hollow microrings on a silicon (Si) substrate fabricated with 7.87 kN m^{-2} imprint pressure. (a) SEM image for the EDX elemental mapping. EDX elemental mappings of the encircled part of the SEM image are shown in a); EDX maps of (b) C $\text{K}\alpha_{1,2}$, (c) O $\text{K}\alpha_1$, (d) Ti $\text{K}\alpha_1$, and (e) Si $\text{K}\alpha_1$.

Table 6-2 Summary of all results of imprinted TiO₂ hollow microrings onto silicon substrates using two different imprinting pressures.

Samples	Imprinting pressure	Diameter d of hollow microrings	height h of hollow microrings	Width w of the rim
TiO ₂	3.95 kN m ⁻²	3.65 ± 0.13 μm	208.88 ± 32.75 nm	1.90± 0.34 μm
	7.87 kN m ⁻²	4.47 ± 0.08 μm	316.42 ± 44.50nm	2.07± 0.37 μm

6.2.3 Fabrication of Gold (Au) microrings

The gold precursor solution was synthesized as described in section 3.3.3.3. Au's hollow microrings were fabricated using the imprint method described in section 3.3.3.6.

6.2.3.1 Morphological characterization of gold (Au) microrings

Figure 6-12a-b shows the SEM images of hollow microrings of Au imprinted on a Si substrate with an imprint pressure of 3.95 kN m⁻². The hollow microrings of Au are hexagonally arranged and have long-range order with some defects. A total of 20 hollow microrings of Au were evaluated from a binarized SEM image. The analyzed hollow microrings have a diameter of $\approx 2.75 \pm 0.11$ μm, a circularity of $\approx 1.00 \pm 0.01$, an average aspect ratio of $\approx 1.07 \pm 0.06$ (Figure 6-12c-e).

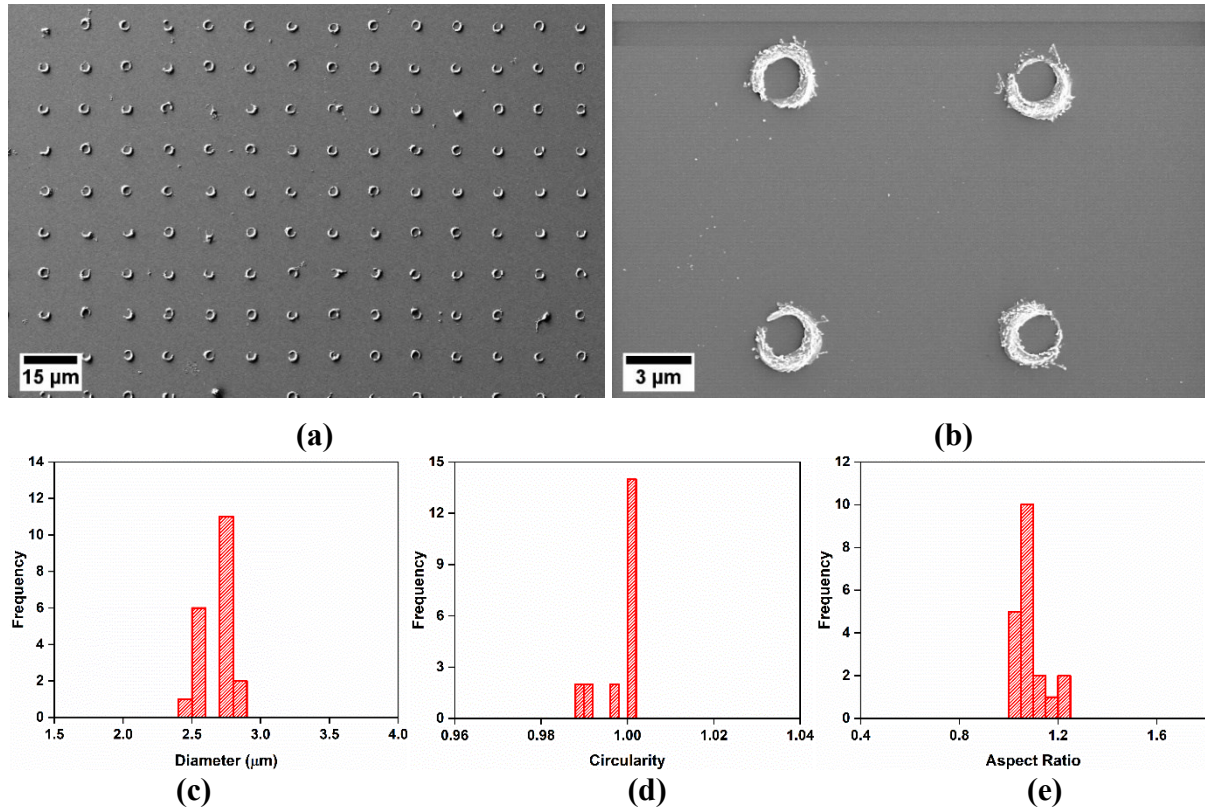


Figure 6-12 Imprinted gold (Au) hollow microrings on a silicon (Si) substrate fabricated with 3.95 kN m^{-2} imprint pressure and thermally treated at $140 \text{ }^\circ\text{C}$. (a-b) SEM images; (a) large-area top view, and (b) detail top view. (c-e) Histograms of (c) the diameters, (d) the circularities, and (e) the aspect ratios of 20 analyzed micron hollow microrings.

Figure 6-13a-b shows the SEM images of hollow microrings of Au imprinted on a Si substrate with an imprint pressure of 7.87 kN m^{-2} . The hollow microrings of Au are hexagonally arranged and have long-range order with many defects. A total of 20 hollow microrings of Au were evaluated from a binarized SEM image. The analyzed hollow microrings have a diameter of $3.90 \pm 0.018 \text{ } \mu\text{m}$, a circularity of $\approx 0.99 \pm 0.02$, and an average aspect ratio of $\approx 1.15 \pm 0.12$ (Figure 6-13c-e).

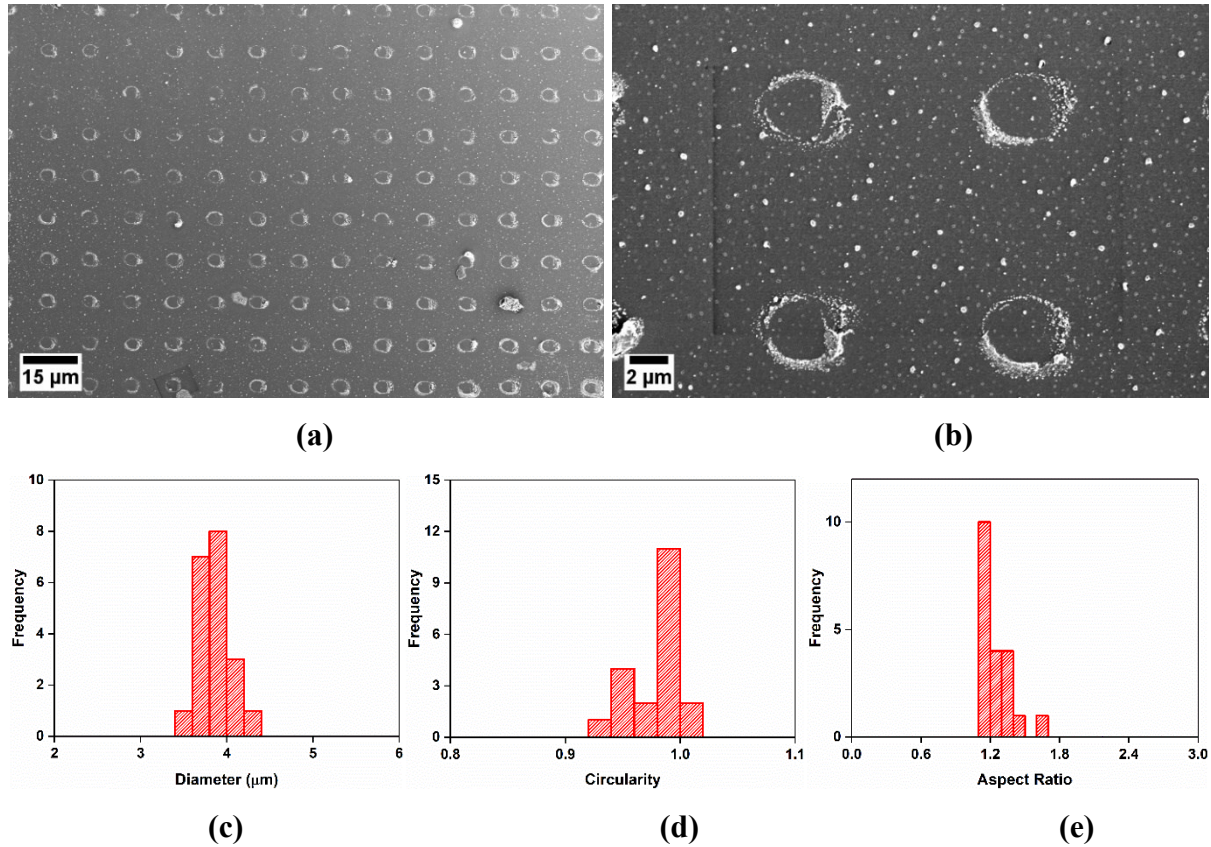


Figure 6-13 Imprinted gold (Au) hollow microrings on a silicon (Si) substrate fabricated with 7.87 kN m^{-2} imprint pressure and thermally treated at $450 \text{ }^\circ\text{C}$. (a-b) SEM images; (a) large-area top view, and (b) detail top view. (c-e) Histograms of (c) the diameters, (d) the circularities, and (e) the aspect ratios of 20 analyzed micron hollow rings.

For the mapping of the elemental composition, EDX characterization was performed. Figure 6-14b-g reveals the distribution of the relevant elements on a hollow microring of Au imprinted on a Si substrate with an imprint pressure of 7.87 kN m^{-2} . Au at the edge of the hollow microring is evidence of the successful fabrication of Au microrings.

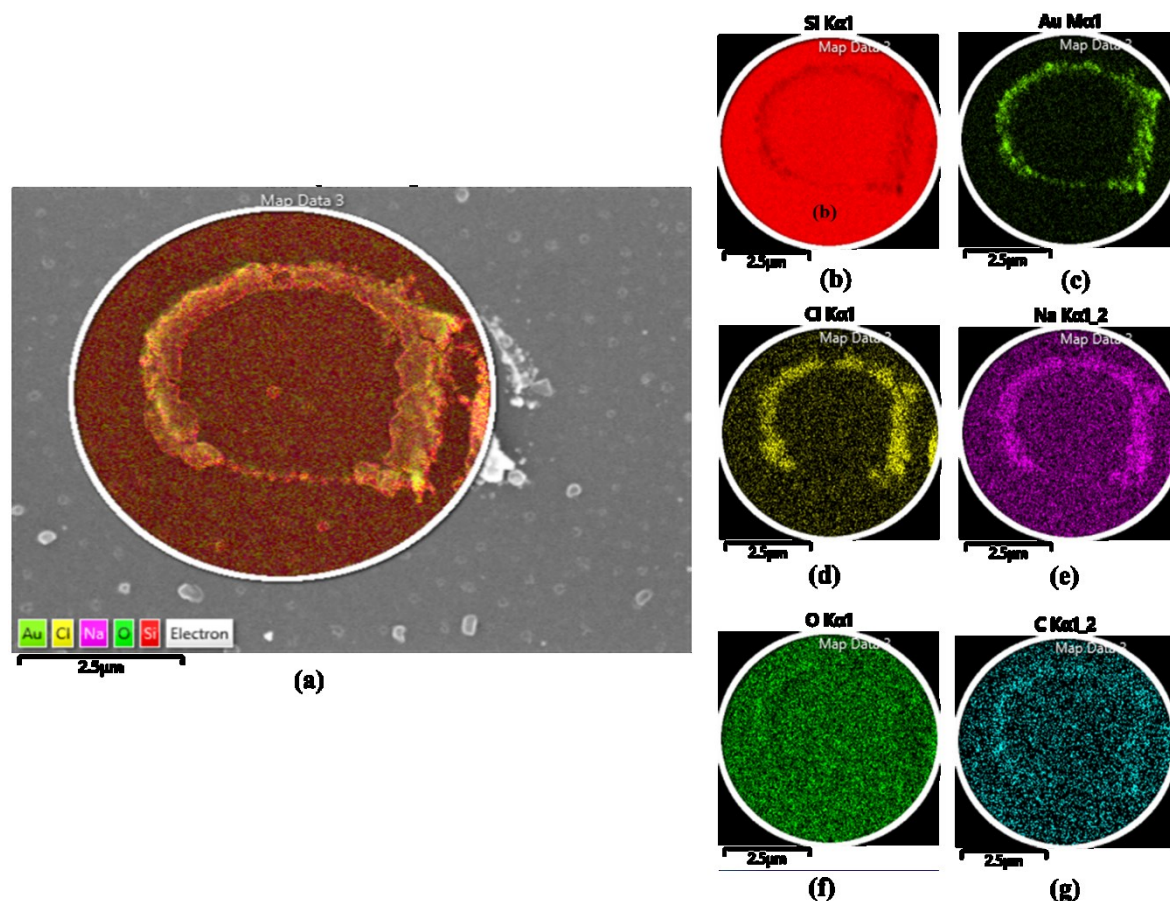


Figure 6-14 Imprinted gold (Au) hollow microrings on a silicon (Si) substrate fabricated with 7.87 kN m^{-2} imprint pressure and thermally treated at $450 \text{ }^\circ\text{C}$. (a) SEM image for the EDX elemental mapping. EDX elemental mappings of the encircled part of the SEM image are shown in a); EDX maps of (b) Si $K\alpha_1$, (c) Au $M\alpha_1$, (d) Cl $K\alpha_1$, (e) Na $K\alpha_{1,2}$, (f) O $K\alpha_1$, (g) C $K\alpha_{1,2}$.

Table 6-3 Summary of all results of imprinted gold (Au) hollow microrings on a silicon (Si) substrate using two different imprinting pressures.

Samples	Imprinting pressure	Diameter d of hollow microrings
Au	3.95 kN m^{-2}	$2.75 \pm 0.11 \text{ } \mu\text{m}$
	7.87 kN m^{-2}	$3.90 \pm 0.18 \text{ } \mu\text{m}$

6.3 Self-assembly of SiO₂ microparticles inside hollow microrings of TiO₂

Silica (SiO₂) microparticles with a diameter of 50nm were deposited into hollow microrings of TiO₂ through a method described in section 3.3.1.3.1. The SiO₂ microparticles with diameters of 50nm arranged themselves very homogeneously and well embedded inside some of the hollow microrings, as shown in Figure 6-15c. However, many left either half-filled or wholly empty, as shown in Figure 6-15a-b. The water contact angle, θ_{WCA} of TiO₂ microrings imprinted with an imprint pressure of 7.87 kN m⁻² on a Si substrate is approximately 108.6°±5.37°, while TiO₂ microrings containing SiO₂ microparticles 50nm in diameter are completely wettable. The water contact angles are the arithmetic mean of six measurements on different samples taken at 23 °C and relative humidity of 31%.

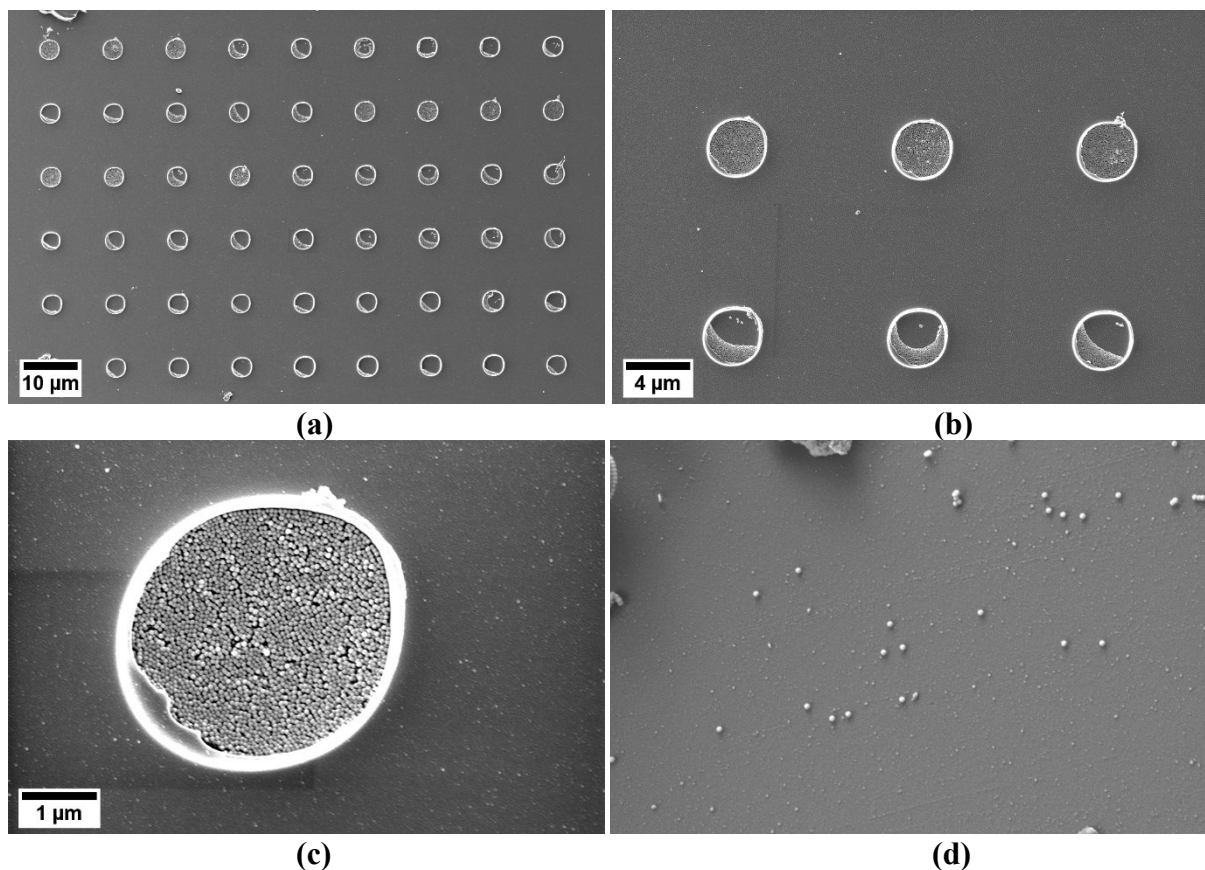


Figure 6-15 SEM images of hollow microrings of titania (TiO₂) imprinted with 7.87 kN m⁻² imprint pressure on a silicon substrate containing silica microparticles with a diameter of 50nm. (a) large view, (b-d) detailed view; (b) filled microrings, (c) a single microring filled with SiO₂ microparticles, and (d) SiO₂ microparticles between microrings.

6.4 Self-assembly of SiO₂ microparticles in hollow microrings of Au

Silica (SiO₂) microparticles with a diameter of 50nm were self-assembled into hollow microrings of Au through a method described in section 3.3.1.3.1. The SiO₂ microparticles with diameters of 50nm arranged themselves outside the Au microrings (Figure 6-16c). The water contact angles, θ_{WCA} of Au microrings imprinted at an imprint pressure of 7.87 kN m⁻² and thermally treated at 450 °C is approximately 0°. At the same time, after the deposition of SiO₂ microparticles with a diameter of 50nm, the substrate was also completely wettable.

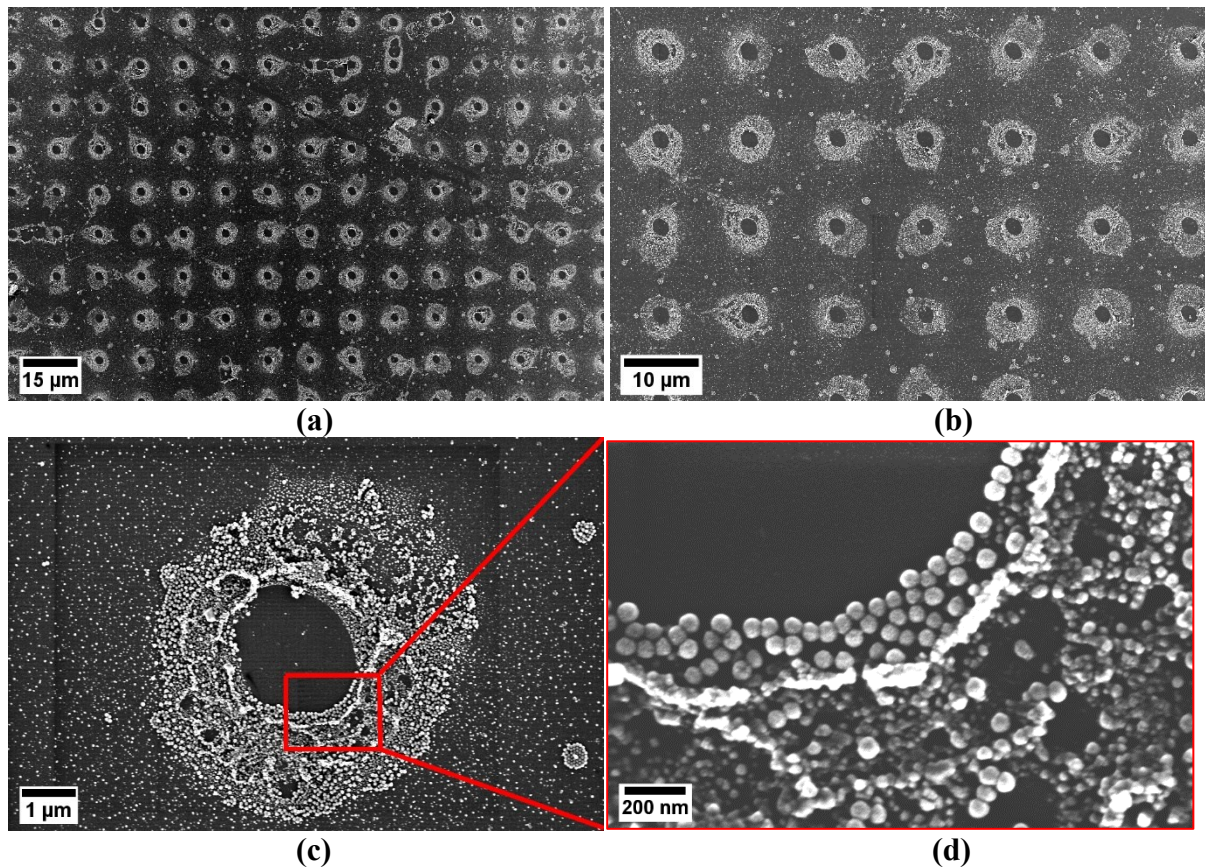


Figure 6-16 SEM images of hollow microrings of gold (Au) imprinted with 7.87 kN m⁻² imprint pressure on a silicon substrate after deposition of silica microparticles (diameter 50nm) assembled at the outer side of microrings (a) large view, (b-d) detailed view; (d) detailed view of the assembly of silica microparticles both inside and outside of Au microrings from the red region in (c).

7 Magnetic assisted insect-inspired capillary nanostamping (MA-IICN)

7.1 Design of stamps

7.1.1 PDMS secondary mold

PDMS secondary molds were obtained by pouring PDMS prepolymer onto silanized mSi. After curing, the PDMS molds had pillars at the positions of the mSi macropores (see section 3.3.1.1). The pore length ($\approx 0.79 \mu\text{m}$) and base diameter ($\approx 0.8 \mu\text{m}$) of the PDMS pillars (Figure 7-2a-b) approximately matched the dimensions of the macropores of the primary mSi mold ($0.8 \mu\text{m}$ pore length, $0.9 \mu\text{m}$ pore bottom) as can be seen in Figure 7-1a-b. The pillar depth ($\approx 6.99 \mu\text{m}$) and base opening diameter ($\approx 5.06 \mu\text{m}$) of the PDMS pillars (Figure 7-2c-d) approximately have the dimensions of the macropores of the primary mSi mold (total pore length of $7.26 \mu\text{m}$, $6.0 \mu\text{m}$ pore opening diameter, and $3.5 \mu\text{m}$ pore bottom diameter) can be seen in Figure 7-1c-d.

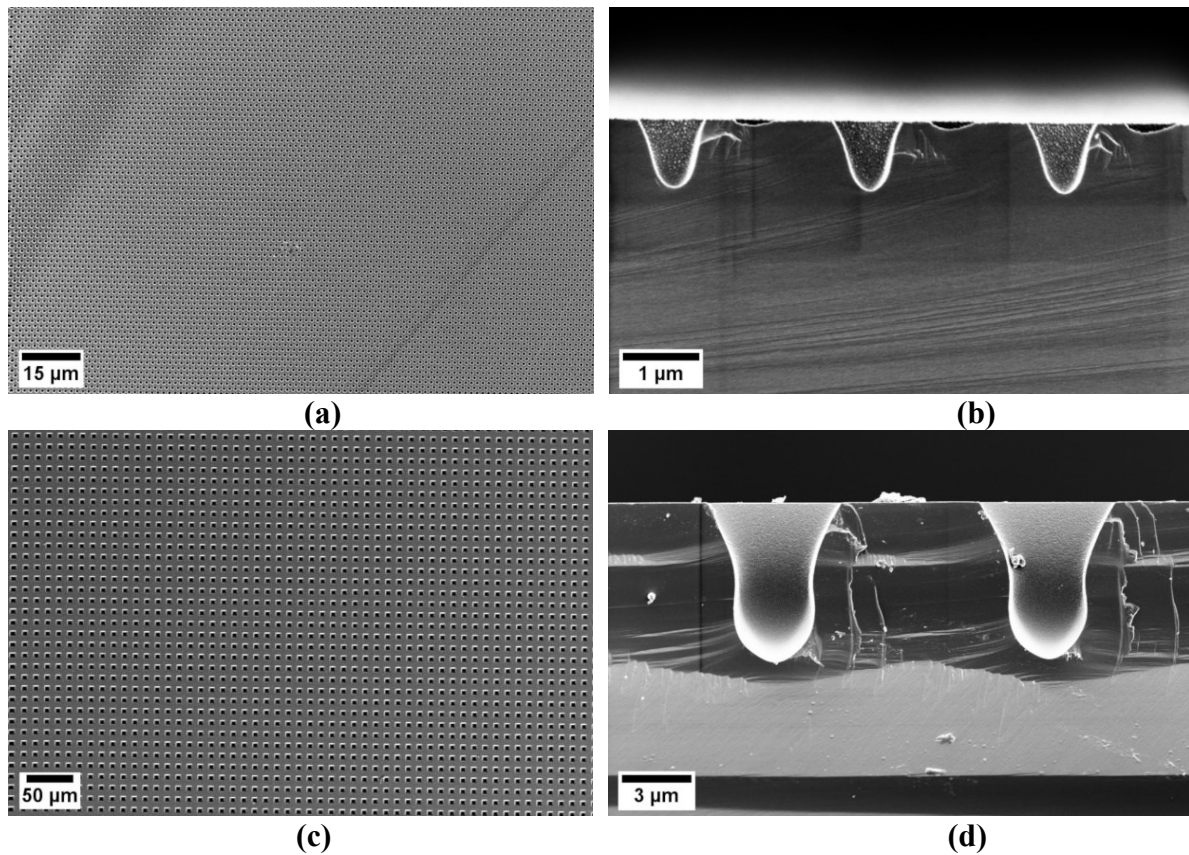


Figure 7-1 SEM images of macroporous silicon (mSi) primary mold; (a) the surface and (b) a cross-section of mSi with 0.9 μm pore base diameter, (c) the surface and (d) a cross-section of mSi with 3.5 μm pore bottom diameter.

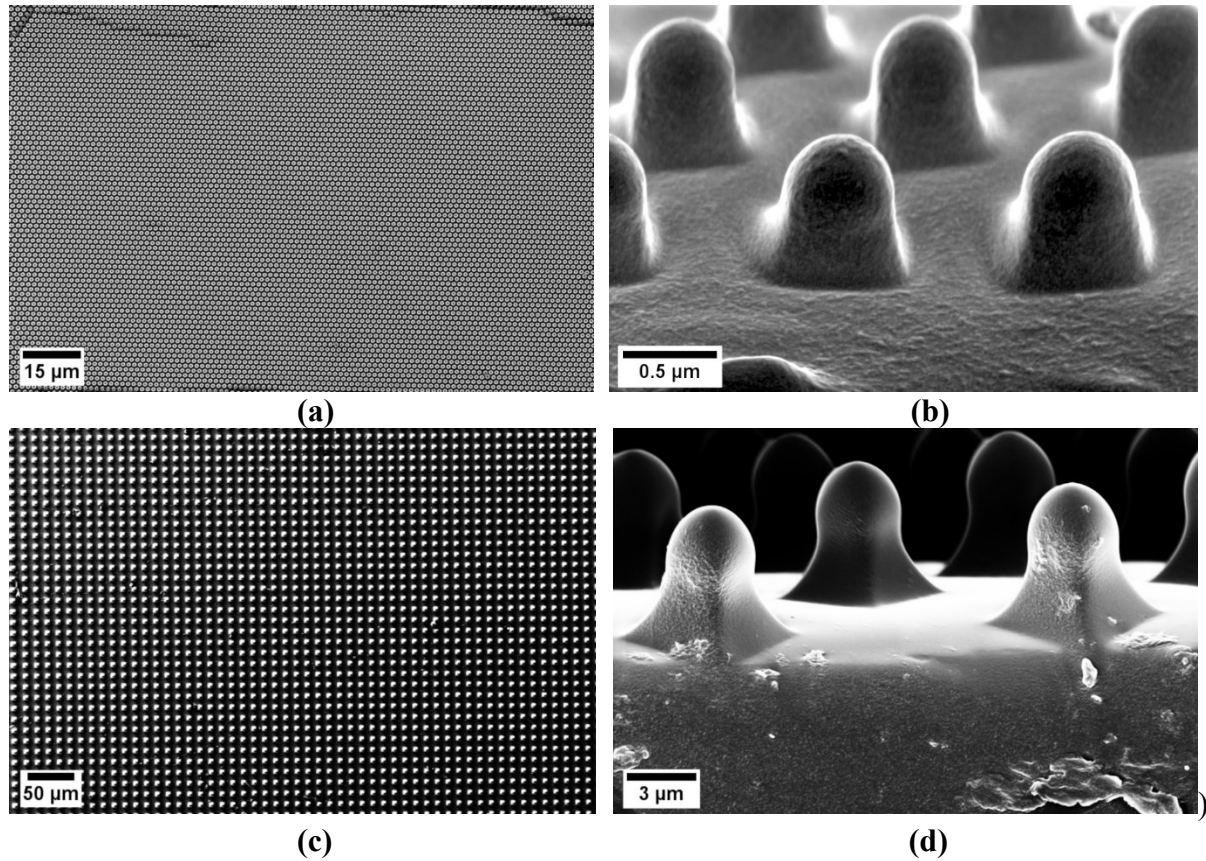


Figure 7-2 SEM images of PDMS secondary mold; (a) the surface and (b) a cross-section of a PDMS secondary mold with 0.9 μm pore base diameter, (a) the surface and (b) a cross-section of mSi mold with 3.5 μm pore bottom diameter.

7.1.2 Zinc oxide tetrapods (T-ZnO)

T-ZnO powder was synthesized as described in section 3.3.4.1. Figure 7-3 shows the X-ray diffraction (XRD) pattern of a synthesized T-ZnO powder. The crystalline nature of the sample was confirmed by the occurrence of well-defined sharp Bragg diffraction peaks. By comparison with reference spectrum ICSD # 067849, the diffraction peaks at 2θ values of 31.82° , 34.47° , 36.34° , 47.63° , 56.64° , 62.91° , 66.38° , 67.98° , 69.16° , and 76.99° were assigned to the (100), (002), (101), (102), (110), (103), (200), (112), (201), and (202) reflections of

hexagonal with the space group P63mc.[174] The morphology of tetrapod-shaped ZnO can be seen in Figure 7-4 g-j.

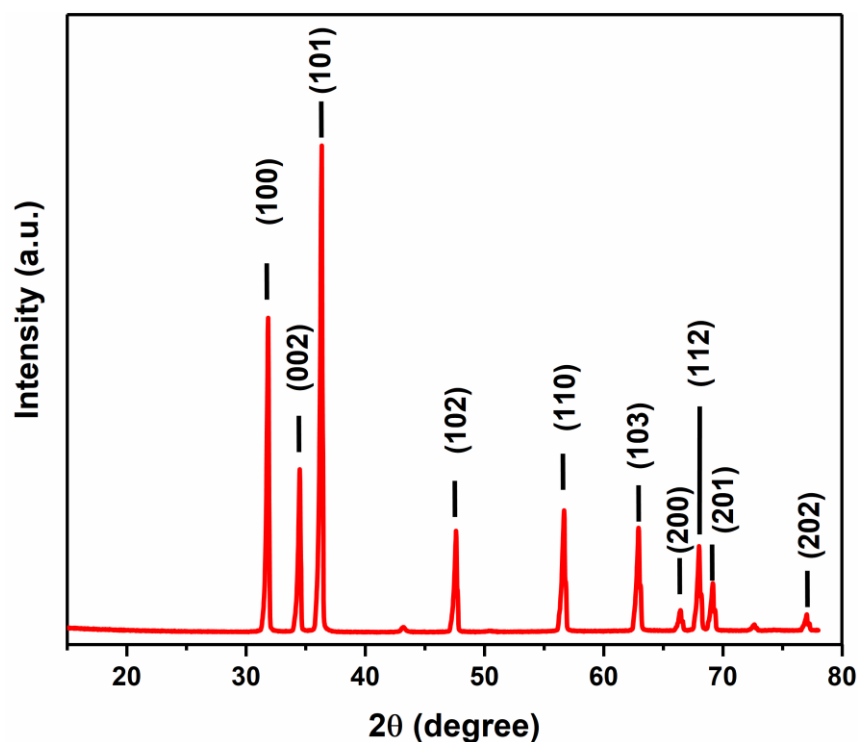
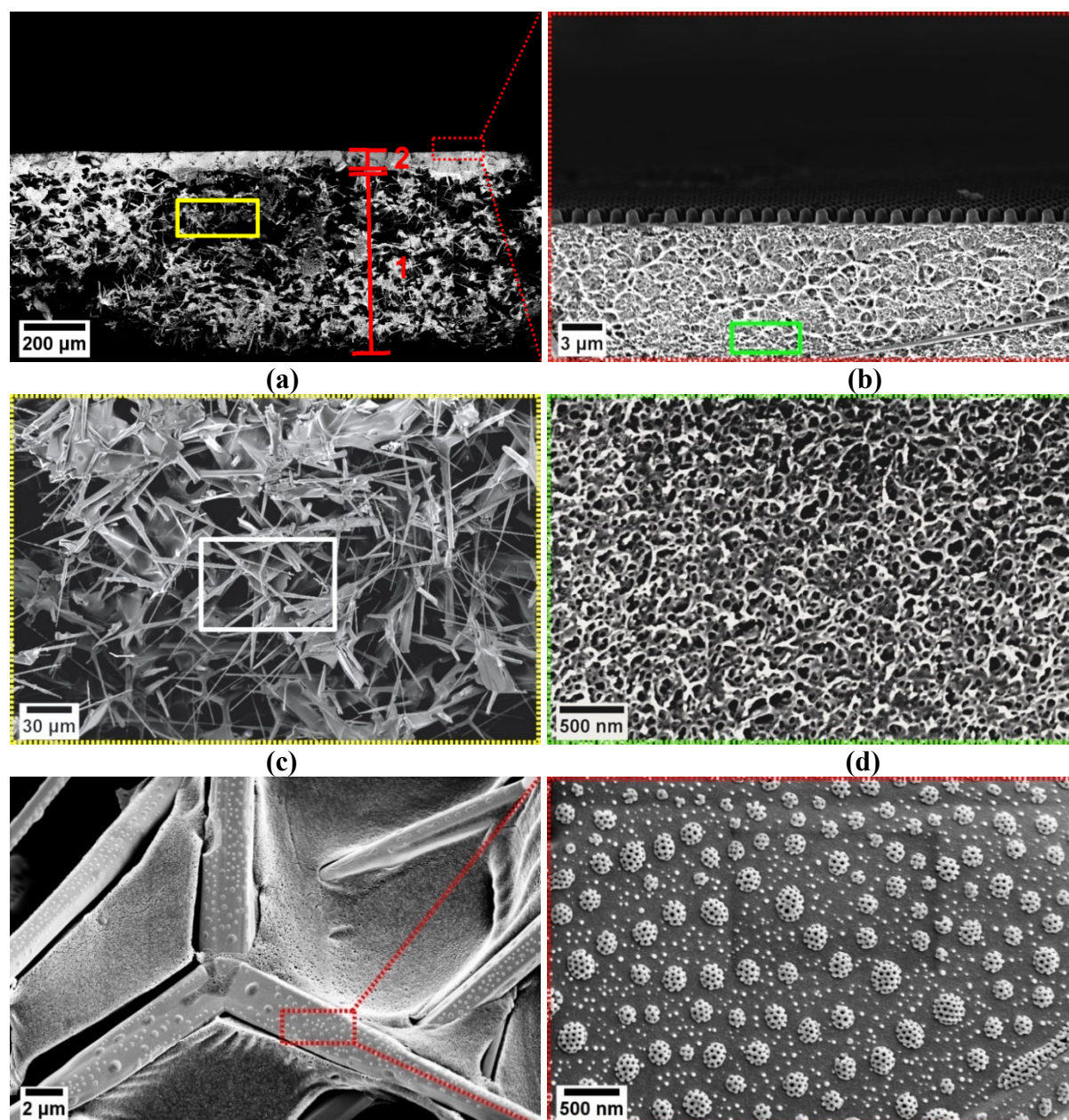


Figure 7-3 X-ray diffraction (XRD) pattern of synthesized zinc oxide tetrapod (T-ZnO) (ICSD # 067849).

7.1.3 PS-*b*-P2VP/T-ZnO porous composite stamp with tip contact surfaces (TC)

After fabricating the T-ZnO 3D pellets from T-ZnO powder (see section 3.3.4.2), the T-ZnO pellet was infiltrated with 10 wt.% of PS-*b*-P2VP solution in toluene. The PS-*b*-P2VP patterned film (stamping layer 2, see section 3.3.4.3.1; Figure 3-9) with tip-like contact surfaces were bounded to the T-ZnO layer (layer 1) with the method explained in section 3.3.4.3.1. The advantages of T-ZnO layer 1 are storing aqueous inks for multicycle stamping and the possibility of supplying inks to stamp contact surfaces from the reverse side. Figure 7-4 shows a composite stamp of porous block copolymer (PS-*b*-P2VP) and zinc oxide tetrapod (T-ZnO). The cross-sectional SEM image in Figure 7-4a displays a large view of the PS-*b*-P2VP stamping patterned layer 2 connected to T-ZnO layer 1. The thickness of T-ZnO layer 1 is

approximately 635 μm measured from the SEM cross-sectional image (Figure 7-4a) (1 mm thickness before infiltration of PS-*b*-P2VP step) attached to a PS-*b*-P2VP film with a thickness of approximately 65 μm measured from the SEM cross-sectional image (Figure 7-4a). The other advantage of T-ZnO layer 1 is to keep the PS-*b*-P2VP stamping layer 2 even and flat. The bending of PS-*b*-P2VP stamping layer 2 after pore generation in hot ethanol is prevented due to the rigidity of the T-ZnO support. Different arrangements of PS-*b*-P2VP polymer on the surfaces of the ZnO tetrapods in the T-ZnO layer 1 can be seen in Figure 7-4e-j. These structures possibly formed during the infiltration of PS-*b*-P2VP polymer in the 3D pellet. In Figure 7-4g-h, the ZnO tetrapods are connected with the help of PS-*b*-P2VP polymer.



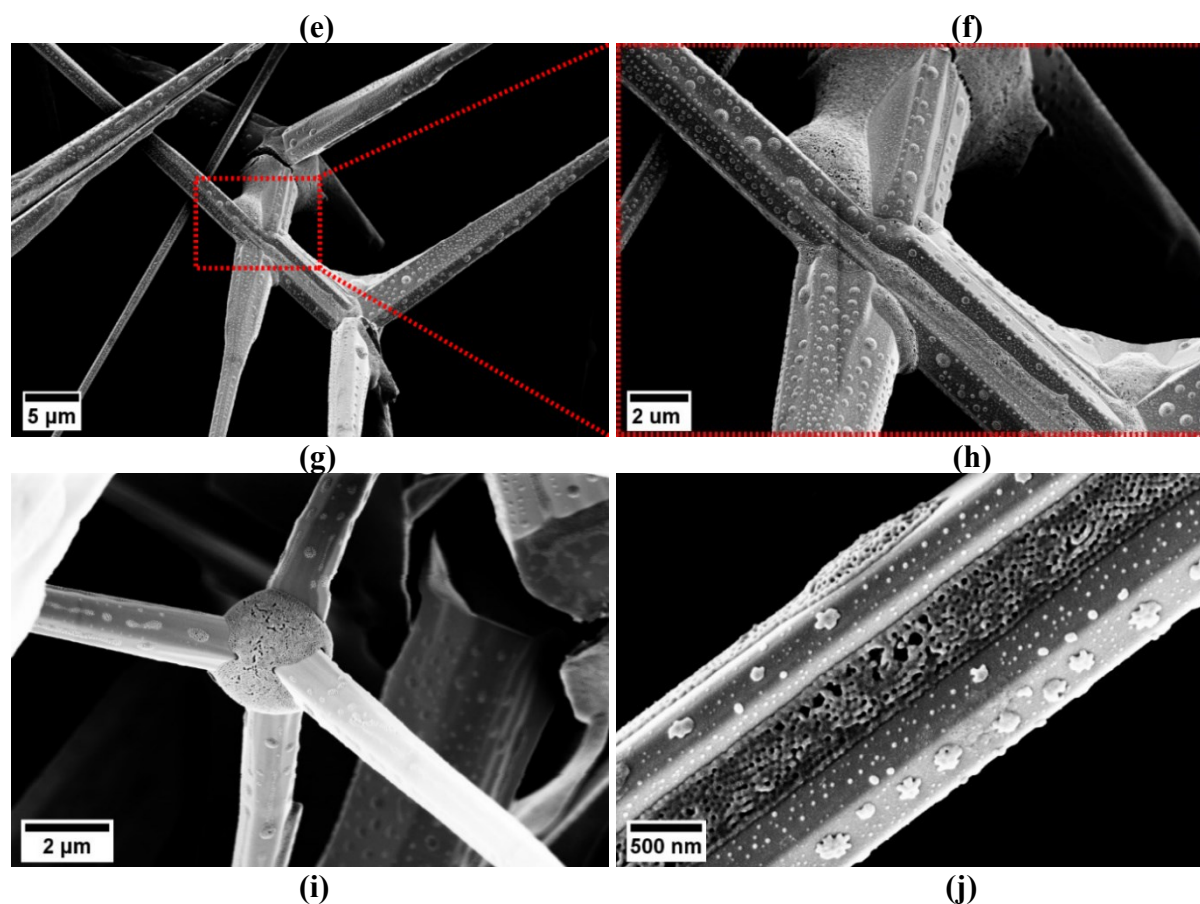


Figure 7-4 Porous block copolymer (PS-*b*-P2VP) and zinc oxide tetrapod (T-ZnO) composite stamps. (a-j) SEM images. (a) Large view and (b) magnified view cross-sectional image of a porous PS-*b*-P2VP stamping layer 2 patterned with round TC. (c) Detail cross-sectional view of porous T-ZnO layer 1 (from the yellow bordered region, a). (d) Detail cross-sectional view of porous PS-*b*-P2VP stamping layer 2 (from the green bordered region, b). (e-j) Detail images from the white-bordered region showing different arrangements of PS-*b*-P2VP polymer on top of ZnO tetrapod in T-ZnO layer 1.

As revealed by SEM images (Figure 7-5 a), the obtained polymer monolith perfectly replicated the structure of macropores from two different mSi templates. Figure 7-5b and 7-5c shows the cross-section of non-swelled PS-*b*-P2VP polymer contact surfaces and swelled PS-*b*-P2VP polymer TC, respectively. The depth of $\approx 0.9 \mu\text{m}$ and base diameter $\approx 0.7 \mu\text{m}$ approximately matched the dimensions of the primary silicon mold ($0.8 \mu\text{m}$ pore length, $0.9 \mu\text{m}$ pore bottom diameter, see Figure 7-1a-b).

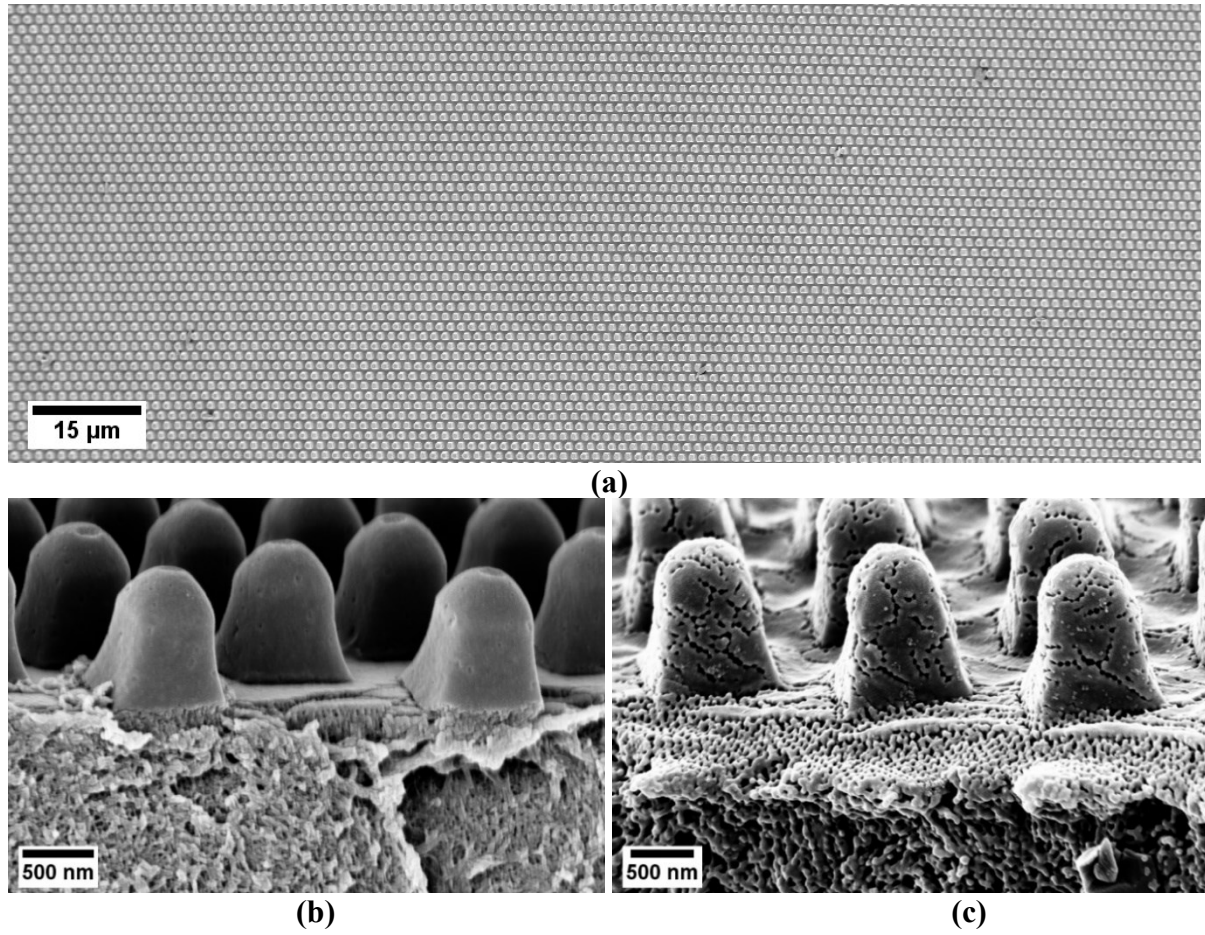


Figure 7-5 Porous block copolymer (PS-*b*-P2VP) and zinc oxide tetrapod (T-ZnO) composite stamps. (a-c) SEM images of porous block copolymer (PS-*b*-P2VP) stamping layer of a composite stamp having TC with diameters of $\approx 0.9 \mu\text{m}$. (a) Large top view of the porous PS-*b*-P2VP stamping layer 2 of a composite PS-*b*-P2VP/T-ZnO stamp. (b-c) Detail cross-sectional SEM views of PS-*b*-P2VP stamping layer 1 of a composite PS-*b*-P2VP/T-ZnO stamp. (b) Non-swelled contact surfaces of PS-*b*-P2VP stamping layer 2; (c) swelled contact surfaces of PS-*b*-P2VP stamping layer 2.

Figure 7-6c shows the contact surface of swelled PS-*b*-P2VP stamping layer 2 with polymer pillars having a height of $\approx 6.8 \mu\text{m}$ and a length of the top-side of the square-shaped pillars of $\approx 4.3 \mu\text{m}$. The dimensions of the pillars deviated little from the dimensions of the primary silicon mold ($7.26 \mu\text{m}$ pore depth, $3.5 \mu\text{m}$ pore bottom diameter, see Figure 7-1c-d).

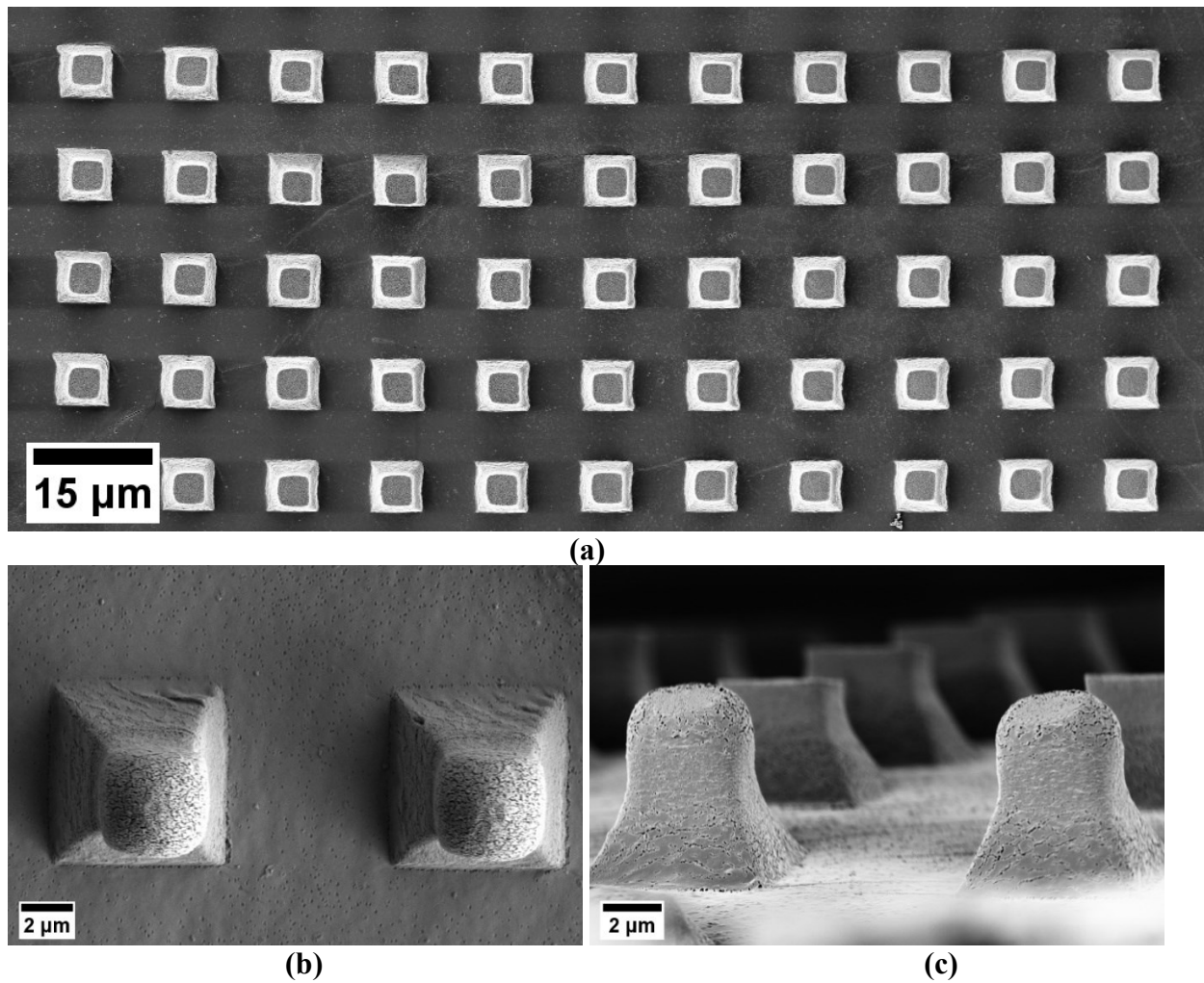


Figure 7-6 Porous block copolymer (PS-*b*-P2VP) and zinc oxide tetrapod (T-ZnO) composite stamps. (a-c) SEM images of porous block copolymer (PS-*b*-P2VP) stamping layer of a composite stamp having square TC with a side length $\approx 4.3 \mu\text{m}$. (a) Large top view of the porous PS-*b*-P2VP stamping layer 2 of a composite PS-*b*-P2VP/T-ZnO stamp, (b) Detail top view SEM views of PS-*b*-P2VP stamping layer 2 of a composite PS-*b*-P2VP/T-ZnO stamp, and (c) Detail cross-sectional SEM views of PS-*b*-P2VP stamping layer 2 of a composite PS-*b*-P2VP/T-ZnO stamp.

7.1.4 PS-*b*-P2VP/T-ZnO porous composite stamp with holey contact surfaces (HC)

The other variation of the topography of stamping layer 2 was a holey contact geometry fabricated following the procedure explained in detail in section 3.3.4.3.2. Figure 7-7 shows the top view SEM image of PS-*b*-P2VP stamping layer 2 of a PS-*b*-P2VP/T-ZnO porous composite stamp with a holey contact surface. As revealed by SEM images (Figure 7-7a-c), the obtained polymer monolith perfectly replicated the structure of the PDMS secondary mold. Figures 7-7b and 7-7c show the top view and cross-section of swelled PS-*b*-P2VP polymer HC of a PS-*b*-P2VP/T-ZnO porous composite stamp. The pore depth \approx of 0.9 μm and the top opening diameter \approx 0.9 μm approximately matched the dimensions of the secondary PDMS mold (0.79 μm pore length, 0.8 μm pore bottom diameter, see Figure 7-2a-b).

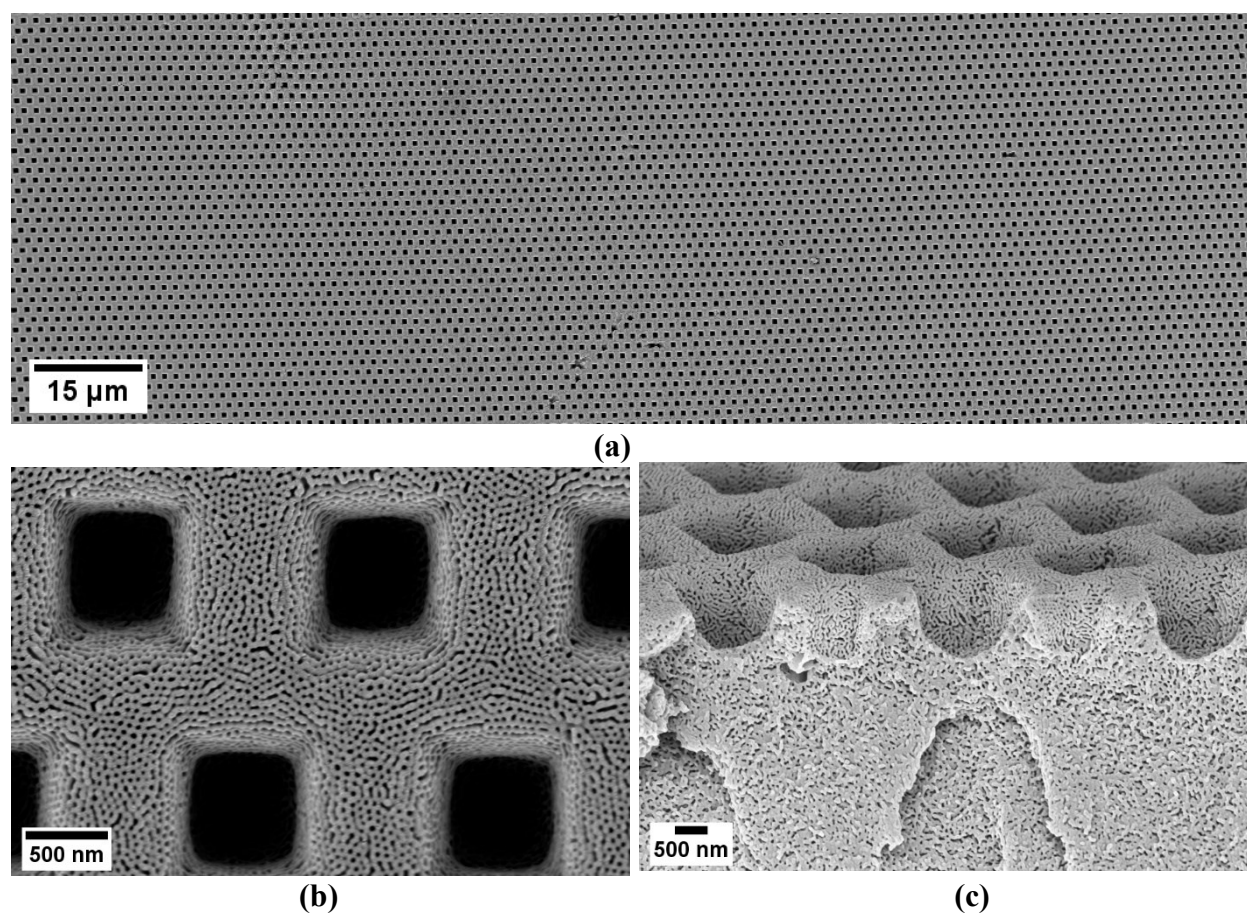


Figure 7-7 Porous block copolymer (PS-*b*-P2VP) stamping layer 2 of the holey contact surface (HC) composite stamps. (a-c) SEM images of porous block copolymer (PS-*b*-P2VP) stamping layer 2 of an HC composite stamp having contact surfaces of \approx 0.9 μm . (a) Large-area top view

of the porous PS-*b*-P2VP stamping layer 2 of a composite PS-*b*-P2VP/T-ZnO stamp. (b-c) Detail SEM views of PS-*b*-P2VP stamping layer 2 of a composite PS-*b*-P2VP/T-ZnO stamp. (b) Top view swelled contact surfaces of PS-*b*-P2VP stamping layer 2 and (d) Cross-sectional view of swelled contact surfaces of PS-*b*-P2VP stamping layer 2.

Figures 7-8a-b and 7-8c show the top view and cross-section of swelled PS-*b*-P2VP polymer HC of PS-*b*-P2VP/T-ZnO porous composite stamp, respectively, with a pore depth of $\approx 8.6 \mu\text{m}$ and length of the pore opening is $\approx 5.3 \mu\text{m}$. The dimensions deviate from the dimensions of the secondary PDMS mold ($6.99 \mu\text{m}$ pillar depth, $5.06 \mu\text{m}$ pore bottom diameter, see Figure 7-8c-d).

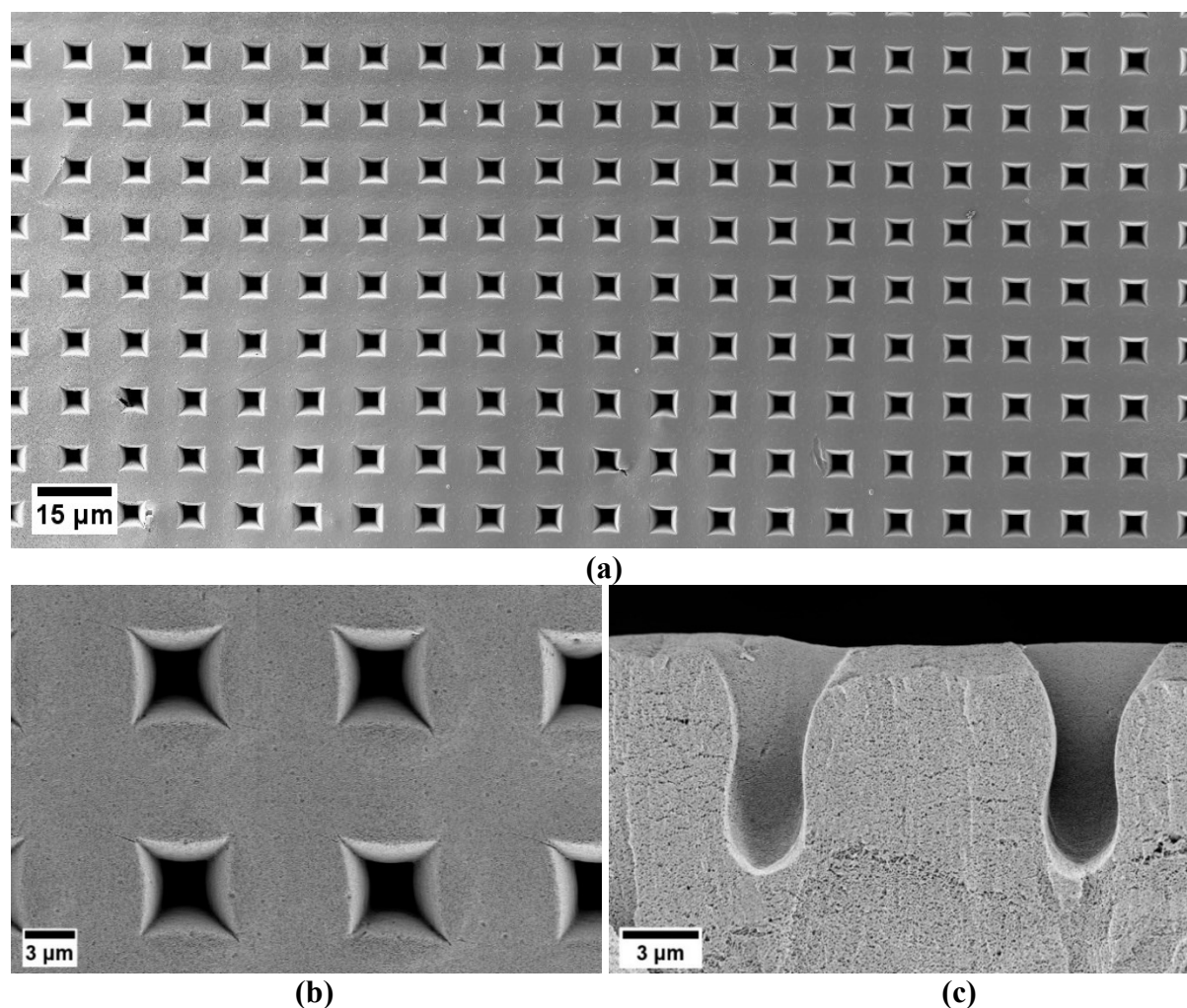


Figure 7-8 Porous block copolymer (PS-*b*-P2VP) stamping layer 2 of the holey contact surface (HC) composite stamps. (a-c) SEM images of porous block copolymer (PS-*b*-P2VP) stamping layer 2 of a composite stamp having HC of $\approx 5.3 \mu\text{m}$. (a) Large-area top view of the porous PS-*b*-P2VP stamping layer 2 of a composite PS-*b*-P2VP/T-ZnO stamp. (b-c) Detail SEM views

of PS-*b*-P2VP stamping layer 2 of a composite PS-*b*-P2VP/T-ZnO stamp. (b) Top view swelled contact surfaces of PS-*b*-P2VP stamping layer 2 and (d) Cross-sectional view of swelled contact surfaces of PS-*b*-P2VP stamping layer 2.

7.1.5 Stamping of magnetic nanoparticle model inks

This section discusses the stamping of model inks (ferrofluid, Fe₃O₄-10nm) and Fe₃O₄-5nm. Conventional superparamagnetic materials include Fe₃O₄, Fe₂O₃, MnFe₂O₄, FePt, and FeCo. For example, Fe₃O₄ magnetic nanoparticles aggregates attracted much attention. Magnetic nanoparticles have received significant attention because of their broad application range. Fe₃O₄ nanoparticles have many applications; such as biomedical engineering,[221] magnetic fluid hyperthermia (MFH),[222] biosensing,[223] gene delivery,[224] magnetic separation,[225] digital data storage [226] and design, and operation of machine elements.[227] So far, the deposition of small magnetic nanoparticle aggregates has remained challenging. The reasons may be magnetic inter-particle attractions, leading to a more significant accumulation of nanoparticles and a weak bonding force with the substrate, making it hard to print magnetic aggregates.[228]. Two model inks were selected: 1) 5 nm iron oxide superparamagnetic nanoparticles (magnetite, Fe₃O₄) in water (5mg/ml), and 2) an aqueous ferrofluid with magnetite (Fe₃O₄) particles (10 nm in diameter having a particle concentration of 1.2 vol-%. A ferrofluid is a dispersion of Fe₃O₄ magnetic nanoparticles, either sterically or electrostatically stabilized, and uses anionic surfactant. The 5 nm iron oxide superparamagnetic nanoparticles are unmodified nanoparticles. Magnetic particles act as nanomagnets comprising only one domain. Under ambient conditions, Brownian motion prevails, and the ferrofluids behave like an ordinary fluid. However, upon applying a magnetic field, the ferrofluid follows the modified Langevin theory and acts like a super magnetic fluid.[229] The interparticle magnetic interactions can significantly change the characteristics of the ensemble of nanoparticles aggregates, such as magnetization and coercivity.[230] Superparamagnetic properties are related to the nanoparticles' nanoscale sizes. Each nanoparticle acts as one individual crystalline magnetic domain with a net spin. The superparamagnetic nanoparticle aggregates can flip their magnetic spin triggered by an external magnetic field.[231] This follows the Neel relaxation model given in Equation 7-1.[232] Due to Neel relaxation and Brownian relaxation, there is no remnant magnetization in ferrofluids at room temperature after removing the

magnetic field.[233] Brownian relaxation changes the magnetic moment of magnetic particles in a solution by physical rotation of the whole particle under the applied field.[234] In this case, the Brownian relaxation time is given by Equation 7-2.[235] In the ferrofluid, it is perfectly possible to physically rotate the particles under the applied field, as the surfactant coating of ferrofluid nanoparticles is intended to keep the particles apart. Aggregates usually form, when the nanoparticles are not coated at all or incomplete surfactant coatings of nanoparticles in ferrofluid. The particles come closer and can result in large aggregates. Such aggregates can contain up to thousands of particles, resulting in the micro-sized entity. In the presence of the applied field, the direction of the moment of an individual particle in aggregate is pinned. Hence the aggregate develops a net moment, by rotation of complete nanoparticles aggregate rather than the switching of an individual nanoparticle within the aggregate. In this case, the Brownian rotation relaxation time is given by Equation 7-3.

$$\tau_N = \tau_0 \exp\left(\frac{KV}{k_bT}\right) \quad \text{Equation 7-1}$$

$$\tau_B = \frac{\pi(V_H^3)\eta}{2k_bT} \quad \text{Equation 7-2}$$

$$\tau_B = \frac{3V_H\eta}{k_bT} \quad \text{Equation 7-3}$$

Where, k_b is the Boltzmann constant, T is the absolute temperature, $\tau_0 \approx 10^{-9}$ s is the time constant, K is the anisotropy constant, η is the dynamic viscosity of the fluid, V_H is the hydrodynamic volume of the particle or aggregate, and V the volume of particle core.

The weak bonding force of magnetic nanoparticles with the substrate makes it hard to print magnetic aggregates with state-of-the-art methods.[228] In this work, methods have been devised with which magnetic nanoparticle aggregates can be printed easily on substrates. Aqueous magnetic inks were selected, and all stamping was performed with inks as received.

7.1.5.1 Setup I

In the setup I (see section 3.3.4.4.2.1), the stamp was glued to the PDMS layer with double-sided polyimide tape after infiltration of the model ink and then attached to the sample holder. The stamp holder approached a silanized Si counterpart substrate placed on a PDMS support, ensuring conformal contact. The contact results in ink transfer from the contact surfaces of the stamp to the silanized Si substrate. The apparent water contact angle on a silanized Si substrate is measured at $107.85^{\circ} \pm 0.55^{\circ}$ (not shown). After the detachment of the stamp from the Si substrate, stamped ink spots remained on the substrate surface. However, the stamping of magnetic nanoparticles aggregates was unsuccessful due to the reasons explained below. The deposited Fe_3O_4 -10nm nanoparticles aggregates have no order and many defects. A detailed, magnified SEM image shows the disorder and more significant agglomeration of stamped nanoparticle aggregates (Figure 7-10b). The reasons can be the magnetic inter-particle attractions, leading to a strong aggregation and a weak bonding force with the substrate, making it hard to print magnetic aggregates.[228] Van der Waals forces among the nanoparticle aggregates and anisotropic magnetic dipole interactions are responsible for the aggregation process; the schematic illustration is shown in Figure 7-9 displays the random orientation of magnetic nanoparticles. The aggregation resulting from interparticle interactions can drastically affect the magnetic properties too.[231] The interparticle interactions between magnetic nanoparticles influence the magnetic properties, for example, the superparamagnetic relaxation of the particles.[236] No external force field could not significantly result in ordered magnetic nanoparticle printing; the application of external magnetic fields in setups II, III, and IV discussed in the following sections was implemented. The external magnetic field application formed ordered magnetic nanoparticle arrays by stamping (see following sections).

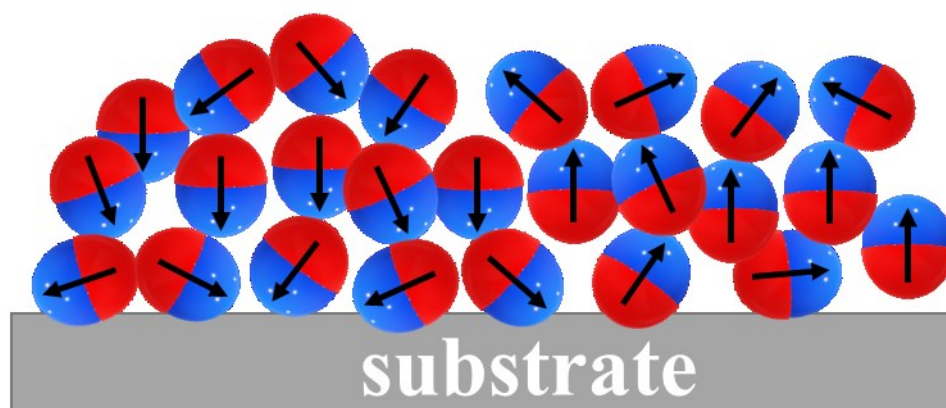


Figure 7-9 Schematic illustration of the accumulation of the magnetic nanoparticles without any external magnetic field.

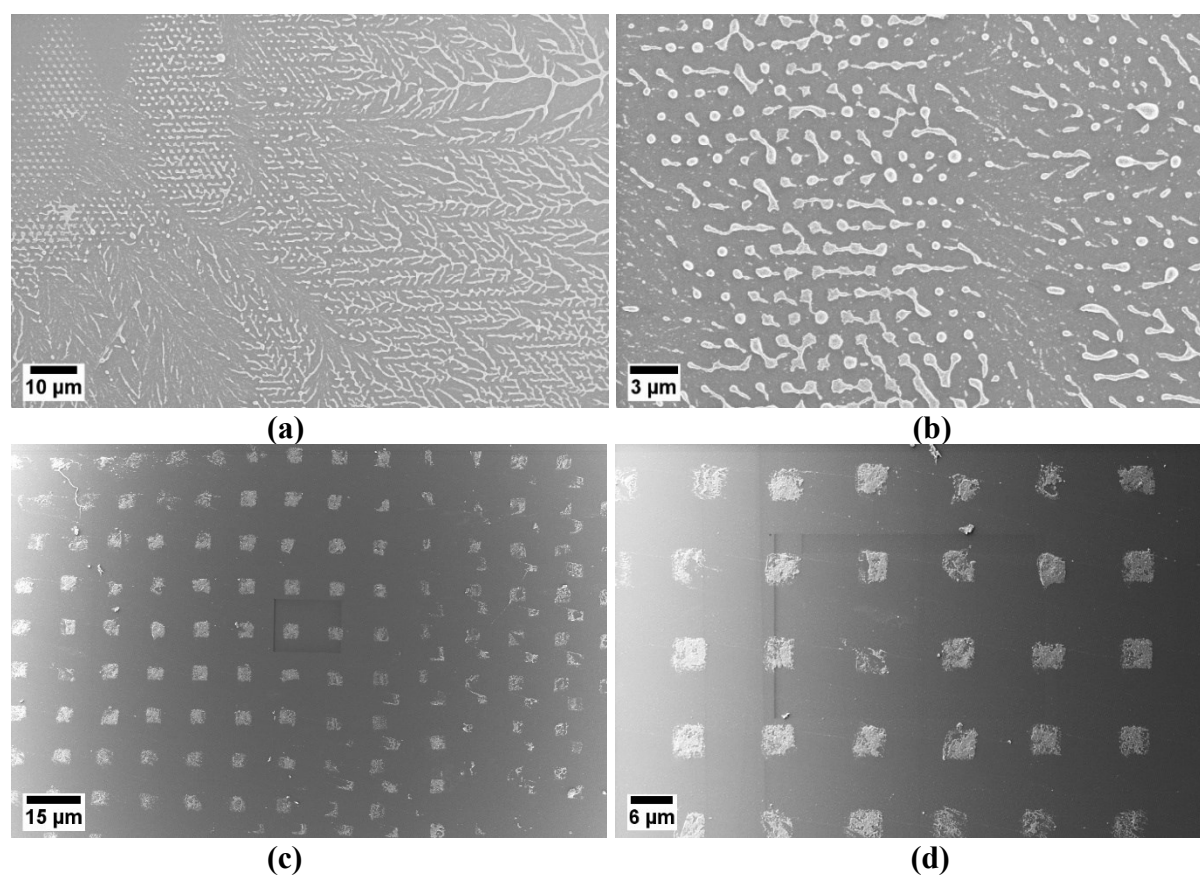


Figure 7-10 Magnetic nanoparticle aggregates (10nm Fe_3O_4 -ferrofluid) printed using an aqueous solution. (a-b) SEM images of magnetic nanoparticle spots printed with the experimental setup I using a PS-*b*-P2VP/T-ZnO composite nanoporous stamp (0.9 μm TC) at room temperature. (a) Large-area top view, and (b) top view at higher magnification. (c-d) Magnetic nanoparticle spots were printed with the experimental setup I using a PS-*b*-P2VP/T-ZnO composite nanoporous stamp (4.3 μm TC) at room temperature. (a) Large top view, and (b) Detail top view.

7.1.5.2 Setup II

Directing and controlling magnetic NP self-assembly with external magnetic fields has driven much interest in the scientific field of research. Magnetophoresis is a method wherewith spatially varying magnetic fields exert forces on nanoparticle aggregates. The force pulls the nanoparticle aggregates to the largest gradient field region.[237] In setup II, the magnetic nanoparticle aggregates were directed by placing a permanent external magnet either below (**out-of-plane**) or parallel the counter substrate (**in-plane**) (see section 3.3.4.4.2.2). The position of the magnets was not changed in the different experiments to ensure reproducibility. Figure 7-11 shows the schematics of **in-plane** and **out-of-plane** geometry setups. The Fe₃O₄ nanoparticle ink concentration gradient is higher near the magnets due to attraction towards a permanent external magnet.[238] One-dimensional aggregates or self-assembled superparamagnetic nanoparticle aggregates formed when applying a magnetic field.[239] The magnetic nanoparticles are magnetized along the direction of the magnetic field and orient themselves in the direction of external magnetic field lines.[240] The magnetic force (F_m) acting on a magnetic particle can be calculated by Equation 7-4.[241]

$$F_m = \frac{V_m \Delta \chi_m}{2\mu_0} \Delta H^2 \quad \text{Equation 7-4}$$

The magnetic pressure (p_m) used to pull the magnetic nanoparticles (ferrofluid) out of the macropores can be calculated by Equation 7-5.[242]

$$p_m \approx \mu_0 M_s H_0 \quad \text{Equation 7-5}$$

Where V_m is the volume of the magnetic particle, $\Delta \chi_m$ is magnetic susceptibility of the magnetic particles, μ_0 is vacuum permeability in units of (N m⁻¹), H is the magnetic field (A m⁻¹), M_s is saturation magnetization of the ferrofluid (A m⁻¹).

Capillary pressure [242] shown in Equation 7-6, can affect the magnetic pressure p_m .

$$p_\gamma \approx \frac{2\gamma}{d_y} \quad \text{Equation 7-6}$$

Where γ is the surface tension of the ferrofluid-air interface and $(d_y/2)$ is half the width of the channels and largest characteristic radius of the porous matrix. Generally, the ink transfer to the substrates also works without magnetic fields because of attractive van der Waals (vdW) forces. An additional pressure contribution would be related to the external magnetic field's vdW forces between ink and substrate.

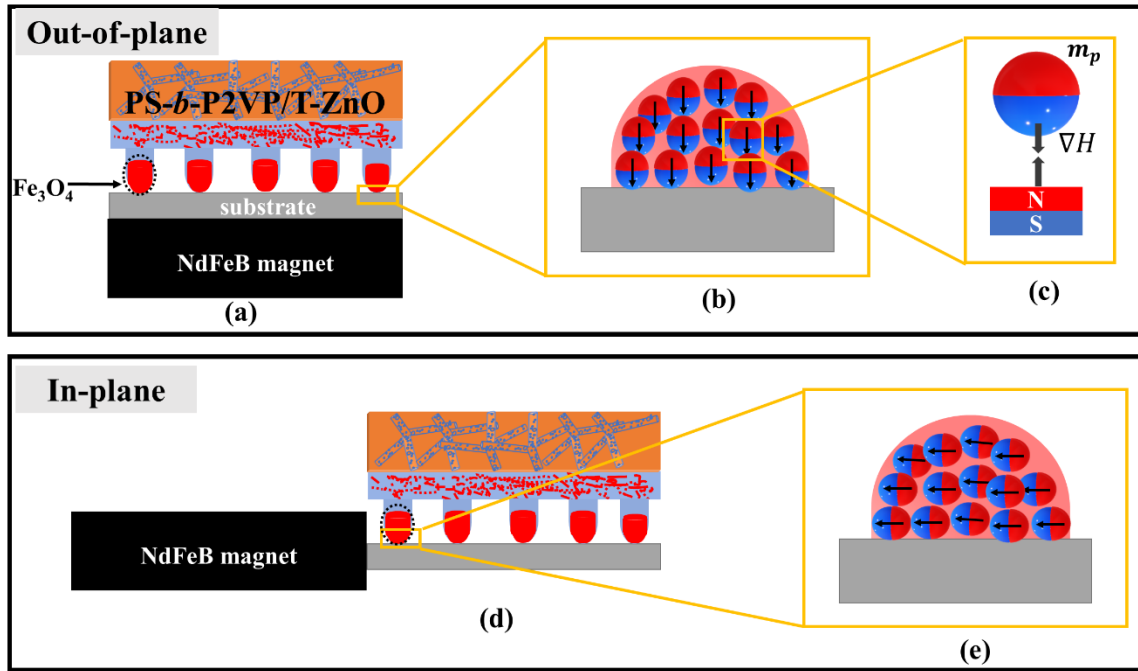


Figure 7-11 (a-c) Schematic illustration of the **out-of-plane** geometry, and (d-e) the **in-plane** geometry. (a, d) Detailed operation shows the particles' migration in the ferrofluid droplet at the contact element tips for ferrofluid ink. (b, e) The accumulation of the magnetic nanoparticle aggregates in the presence of the magnetic field, and (c) the solid dipole-dipole interaction among magnetic nanoparticle aggregates, resulting in the self-assembly of nanoparticle aggregates into parallel stacking, the m_p is effective dipole moment between particles under an external magnetic field H .

The shape of the ferrofluid droplet in an external magnetic field elongates with the increase in magnetic field strength. Due to mass conservation and contact angle decrease, ferrofluid droplet flows away from the contact line.[233] The interparticle attractions and repulsion forces are also responsible for the 3D conical structure,[243] as shown in Figure 7-12. The Rosensweig instability [244] is the most well-known and dramatic response of a ferrofluid, which results when ferrofluids surface perturbation causes bunching of the magnetic field lines, as shown in Figure 7-12. This bunching of field lines shows a spatial gradient in the field

strength, which is responsible for the attraction of the ferrofluid to the vital field region (tip of the perturbation). Suppose the magnetic field lines are oriented parallel to the ferrofluid surface. In that case, there is no generation of spikes, and an appropriate rotation of the magnets can cause spikes due to reorientation of the field lines.[245] As in our setups, the magnets are of finite size. Hence the field lines are non-uniform.[244] Ferrofluid spreading strongly depends on the geometry of the magnetic field.[233]

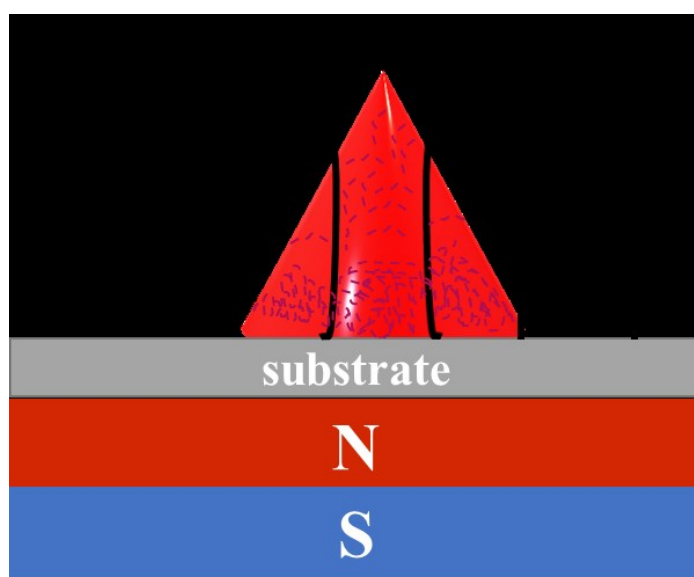


Figure 7-12 Schematic illustration of the magnetization of magnetic nanoparticles aggregates in the presence of a magnetic field. The ferrofluid surface perturbation results in a cone-like structure.

7.1.5.2.1 In-plane magnetic field

Figure 7-13 shows the SEM images of magnetic 10nm Fe_3O_4 -ferrofluid nanoparticle aggregates printed from an aqueous solution with a PS-*b*-P2VP/T-ZnO composite nanoporous stamp (0.9 μm TC) at room temperature using **in-plane** magnetic field setup II. The hexagonally arranged arrays of Fe_3O_4 -10nm nanoparticle aggregates have long-range order with many defects. Many bigger aggregates of ferrofluid can be seen (Figure 7-13a). After approximately 5 attempts, the stamping quality without many defects did not improve. Therefore, all following stamping experiments to form magnetic nanoparticle aggregates were conducted using **out-of-plane** magnetic fields (see sections below).

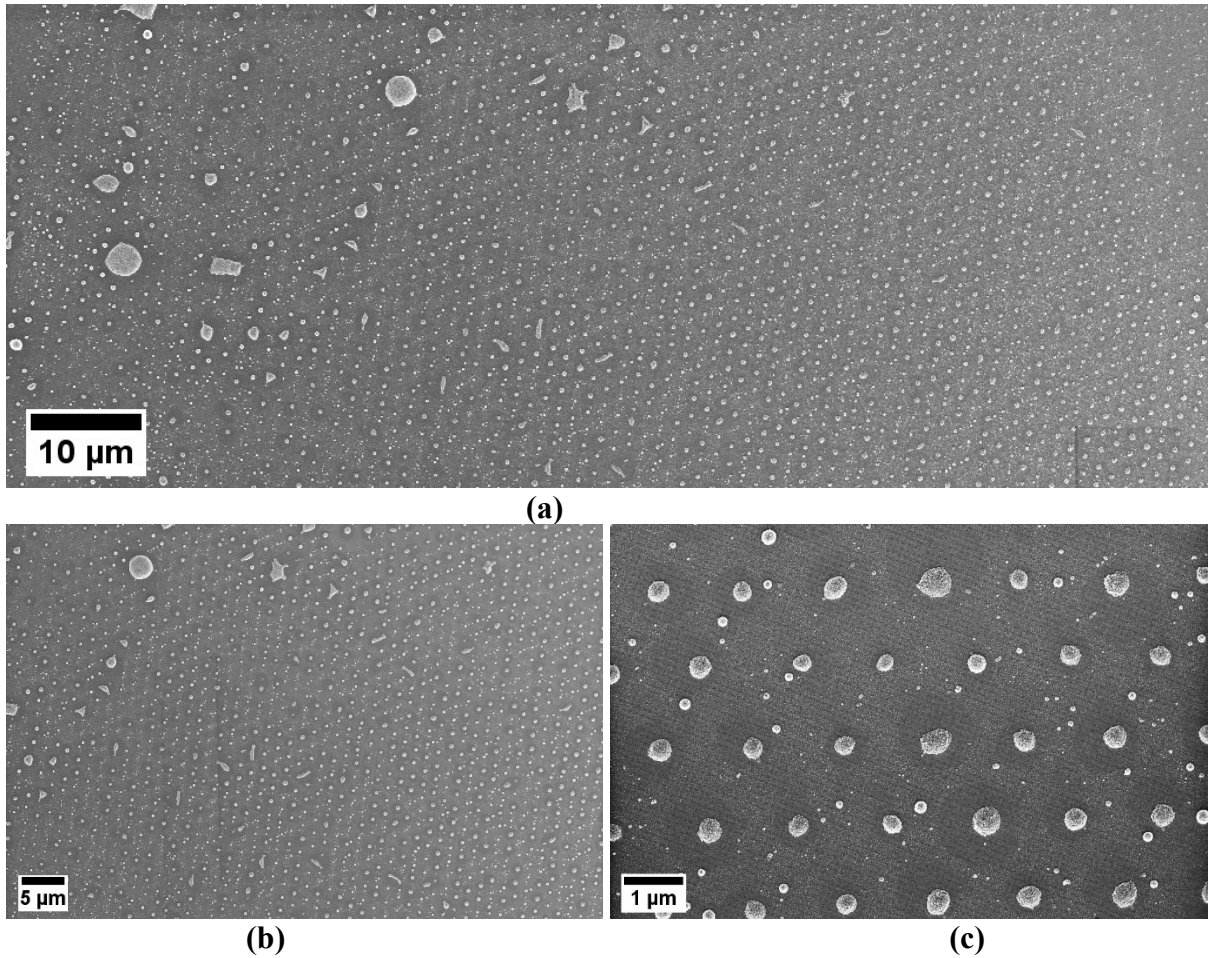


Figure 7-13 (a-c) SEM images of arrays of magnetic nanoparticle aggregates (10nm Fe_3O_4 -ferrofluid) printed from an aqueous solution by using the experimental setup II with PS-*b*-P2VP/T-ZnO composite nanoporous stamp (0.9 μm TC) at room temperature using **in-plane** geometry. The **in-plane** magnetic field lines parallel the substrate (at $H \approx 0.33\text{T}$). (a) Large-area top view, and (b-c) detail top views.

7.1.5.2.2 Out-of-plane magnetic field

7.1.5.2.2.1 Effect of external magnetic field

The magnetic flux density generally increases with the increase in the number of magnets and decreasing in the distance between the magnets.[246] To change the strength of the external magnetic field, additional magnets were added below the silanized Si substrate, starting with only one, two, three, and four (NdFeB, 20*5mm² (diameter*height) external permanent magnets below the counterpart substrate. The magnetic field strengths measured using a Gaussmeter as a magnetic flux density sensor amounted to $\approx 0.18\text{T}$, $\approx 0.26\text{T}$, $\approx 0.30\text{T}$, and \approx

0.33T for one, two, three, or four external permeant magnets, respectively. The Gaussmeter was placed on top of the magnets to measure the magnetic field strength value. Figure 7-14 shows SEM images of magnetic 10nm Fe₃O₄-Ferrofluid nanoparticle aggregates printed from an aqueous solution with a PS-*b*-P2VP/T-ZnO composite nanoporous stamp (0.9 μm TC) at room temperature under different magnetic field strengths. With the increase in magnetic field strength, the stamped arrays of nanoparticle aggregates show long-range order having very few defects. The best result was achieved when four external permanent magnets (NdFeB, 20*5mm² (diameter*height), Grade 52)) with $H \approx 0.33\text{T}$ were placed below silanized Si substrate. Hence, all the results are shown below for setup II obtained with $H \approx 0.33\text{T}$. With the increase in magnetic field strength, the magnetic pressure p_m generates a strong force on the ferrofluid according to Equation 7-5.[242]. In the non-uniform magnetic field, the contact angle of ferrofluid to substrate surface first increases and then decreases linearly with increasing field strength.[247] The magnetic field is not uniform over the whole magnet area in our setup and is essential to consider.

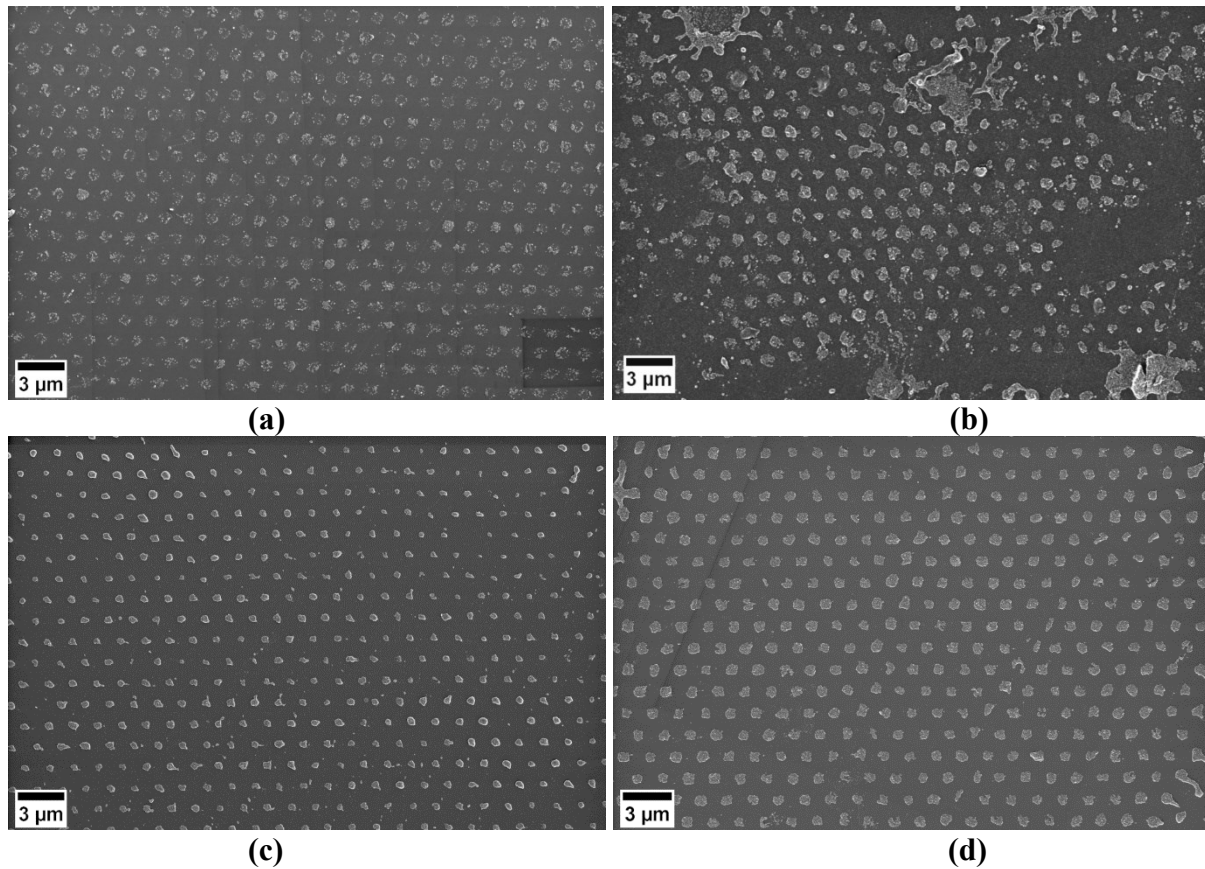


Figure 7-14 (a-d) SEM images of printed magnetic nanoparticle aggregates (10nm Fe₃O₄-ferrofluid) from an aqueous solution by using the experimental setup II with PS-*b*-P2VP/T-ZnO composite nanoporous stamp (0.9 μm TC) at room temperature. The number of the external permanent magnets (NdFeB, 20*5 mm² (diameter*height), Grade 52 located below the counterpart substrates (**out-of-plane**) are (a) one ($H \approx 0.18\text{T}$), (b) two ($H \approx 0.26\text{T}$), (c) three ($H \approx 0.30\text{T}$) and (d) four ($H \approx 0.33\text{T}$).

7.1.5.2.2.2 Stamping by tip contact surfaces (TC) composite stamps

Figure 7-15a-c shows the SEM images of magnetic 10nm Fe₃O₄-ferrofluid nanoparticle aggregates printed from an aqueous solution with a PS-*b*-P2VP/T-ZnO composite nanoporous stamp (0.9 μm TC) at room temperature. The hexagonally arranged arrays of Fe₃O₄-10nm nanoparticle aggregates have long-range order and few defects (Figure 7-15a). The order of stamped nanoparticle aggregates can be seen from detailed magnified SEM images (Figure 7-15b-c).

The surface topography and height profile of stamped nanoparticle aggregates are characterized using atomic force microscopy (AFM). Figure 7-15d-e shows an AFM image to analyze the heights of the stamped nanoparticle aggregates. The average height of 7 evaluated 10nm Fe₃O₄ nanoparticle aggregates amounted to $44.80 \pm 6.58\text{nm}$. The measurement was done using the contact mode and by extracting a line profile from the measured data (Figure 7-15d). As AFM is a very sensitive method, obtaining a good AFM image is challenging. A total of 332 stamped 10nm Fe₃O₄-ferrofluid nanoparticle aggregates were analyzed from a binarized SEM image and evaluated according to the procedure described in chapter 3.1.4. The analyzed aggregates of magnetic nanoparticle aggregates have a diameter of $\approx 675 \pm 62\text{ nm}$, a circularity of $\approx 0.87 \pm 0.07$, an average aspect ratio of $\approx 1.1 \pm 0.19$ (Figure 7-15f-h).

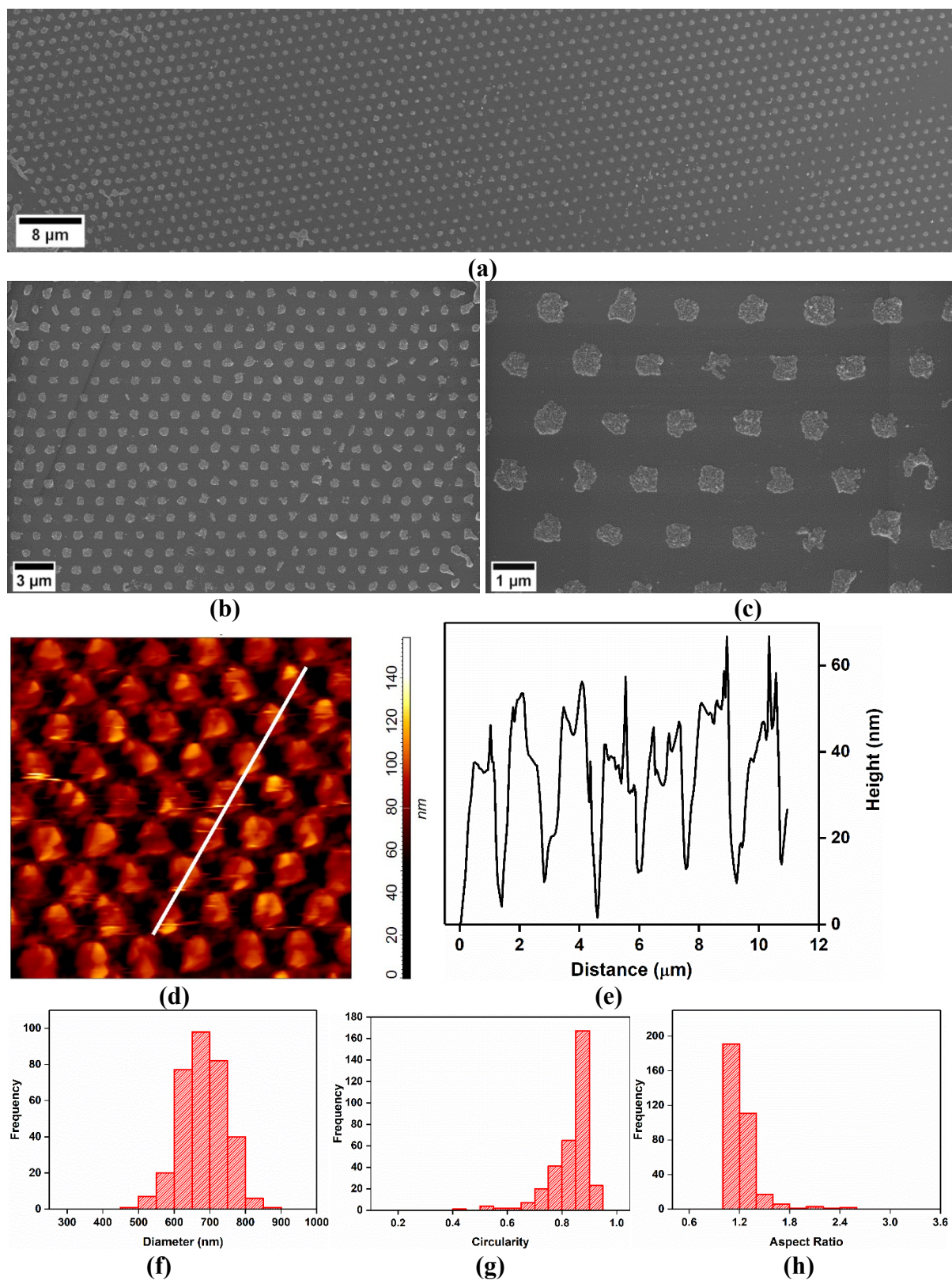


Figure 7-15 (a-c) SEM images of arrays of magnetic nanoparticle aggregates (10nm Fe_3O_4 -ferrofluid) printed from an aqueous solution by using the experimental setup II (**out-of-plane** external magnetic field, $H \approx 0.33\text{T}$) with PS-*b*-P2VP/T-ZnO composite nanoporous stamp ($0.9 \mu\text{m}$ TC) at room temperature. (a) Large-area top view, and (b-c) detail top SEM views. (d) AFM image ($12 \times 12 \mu\text{m}^2$) of stamped magnetic nanoparticle aggregates, and (e) line scan

along the white line in d) showing the height of the stamped magnetic nanoparticle aggregates. Histograms of 332 analyzed stamped magnetic nanoparticle aggregates showing (f) the diameters, (g) the circularities, and (h) the aspect ratios of the Fe_3O_4 stamped magnetic nanoparticle aggregates.

Figure 7-16a-b shows SEM images of magnetic 5nm Fe_3O_4 nanoparticle aggregates printed from a 5 mg/mL aqueous solution with a PS-*b*-P2VP/T-ZnO composite nanoporous stamp (0.9 μm TC) at room temperature. The hexagonally arranged arrays of Fe_3O_4 -5nm nanoparticle aggregates have long-range order with very few defects (Figure 7-16a). The order of the stamped nanoparticle aggregates can be seen from a detailed magnified SEM image (Figure 7-16b). 34 stamped nanoparticles aggregate in a binarized SEM image were analyzed according to the procedure described in chapter 3.1.4. The analyzed particles have a diameter of $\approx 775 \pm 44$ nm, a circularity of $\approx 1.005 \pm 0.01$, and an average aspect ratio of $\approx 1.025 \pm 0.09$ (Figure 7-16c-e).

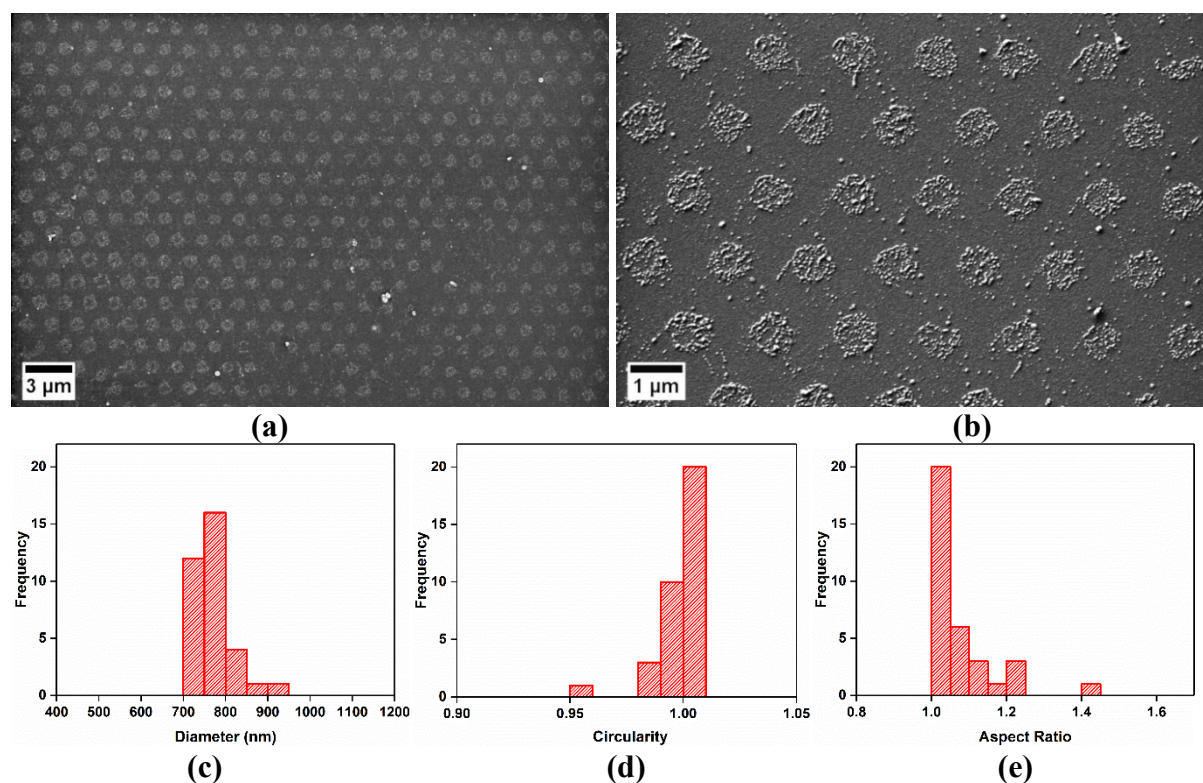


Figure 7-16 (a-b) SEM images of printed magnetic nanoparticle aggregates (5nm Fe_3O_4) from an aqueous solution by using the experimental setup II (**out-of-plane** external magnetic field, $H \approx 0.33\text{T}$) with a PS-*b*-P2VP/T-ZnO composite nanoporous stamp (0.9 μm TC) at room temperature. (a) Large-area top view, and (b) detail. Histograms of (c) the diameters, (d) the

circularities, and (e) the aspect ratios of 34 analyzed stamped magnetic 5nm Fe₃O₄ nanoparticle aggregates.

Figure 7-17a-c shows SEM images of magnetic 10nm Fe₃O₄-ferrofluid nanoparticle aggregates printed from an aqueous solution with a PS-*b*-P2VP/T-ZnO composite nanoporous stamp (4.3 μm TC) at room temperature. The square lattice of rectangular Fe₃O₄-10nm nanoparticle aggregates has long-range order and with very minimal defects (Figure 7-17a). The order of the stamped nanoparticle aggregates can be seen from detailed magnified SEM images (Figure 7-17b-c). As seen from the detailed magnified SEM image in Figure 7-17c, the square arrays are not altogether containing dense nanoparticle aggregates.

The surface topography and height profile of stamped nanoparticle aggregates are characterized using atomic force microscopy (AFM). Figure 7-17d-e shows an AFM image to analyze the heights of the stamped nanoparticle aggregates. The average height of 7 evaluated nanoparticle aggregates amounted to 42.33±4.55nm. The measurement was done with AFM using the contact mode and by extracting a line profile of the measured data (Figure 7-17e). The stamped nanoparticle aggregates were analyzed according to the procedures described in chapter 3.1.4. A total of 189 stamped nanoparticle aggregates was evaluated from binarized SEM images. The analyzed nanoparticles aggregates have a square edge length of $\approx 4.25 \pm 0.70 \mu\text{m}$, an average aspect ratio of $\approx 1.1 \pm 0.19$ (Figure 7-17f-h). The plotline profile was extracted by Image J from the white line in the SEM image (Figure 7-17b) shown in Figure 7-17 h. The edge side length of the stamped square arrays amounts to $\approx 4.1 \pm 0.40 \mu\text{m}$.

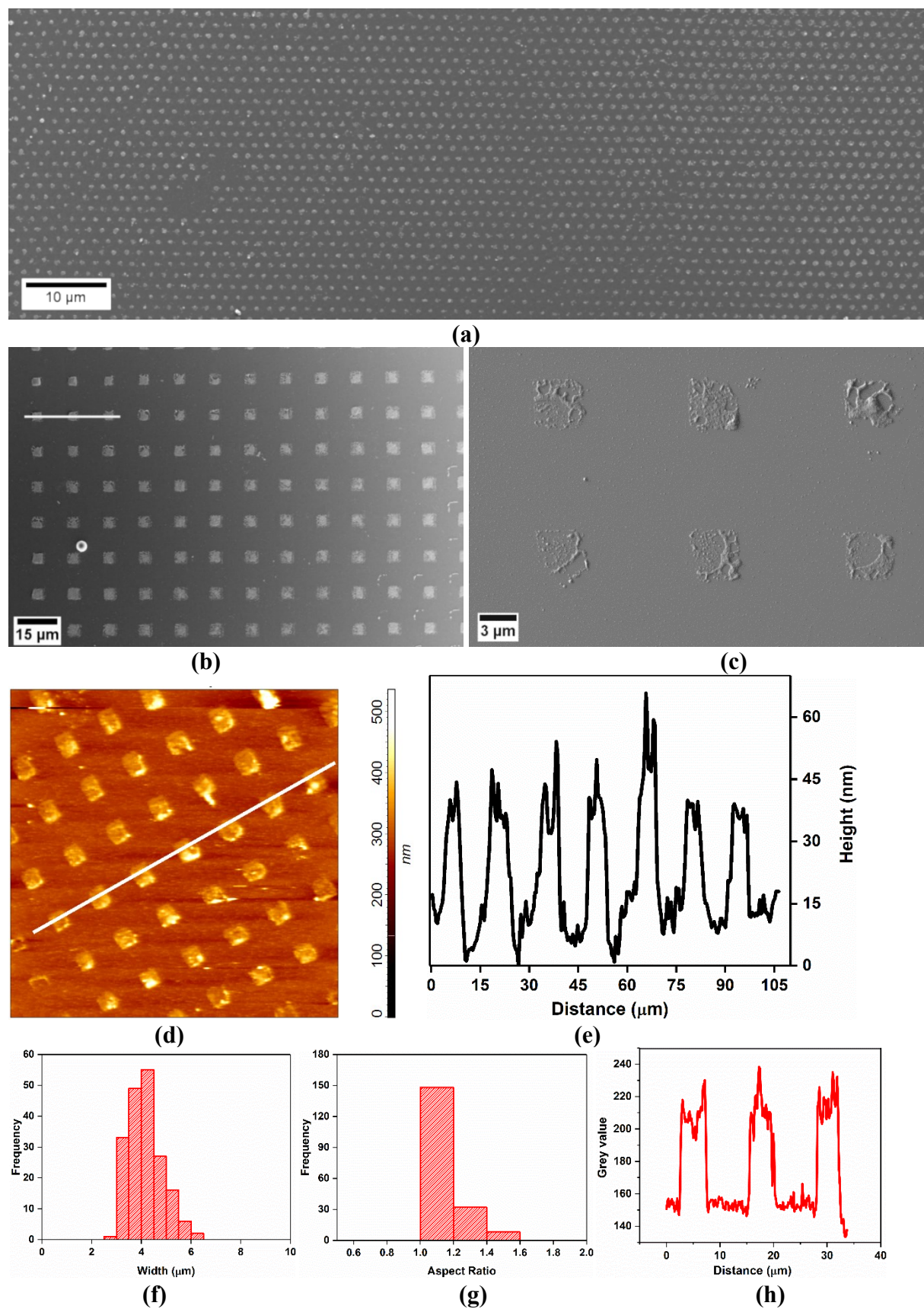


Figure 7-17 (a-c) SEM images of printed magnetic nanoparticle aggregates (10nm Fe_3O_4 -ferrofluid) from an aqueous solution by using the experimental setup II (**out-of-plane** external magnetic field, $H \approx 0.33\text{T}$) with a PS-*b*-P2VP/T-ZnO composite nanoporous stamp ($4.3 \mu\text{m}$)

TC) at room temperature. (a) Large-area top view, and (b-c) detail top SEM views. (d) AFM image ($100 \times 100 \mu\text{m}^2$) of stamped magnetic nanoparticle aggregates, and (e) line scan along the white line in d) showing the height of the stamped magnetic nanoparticle aggregates. Histograms of 189 analyzed stamped magnetic nanoparticles aggregates showing (f) the edge length, (g) the aspect ratios, and (h) the plotline profile (white line in Figure 7-17b)) of the Fe_3O_4 stamped magnetic nanoparticle aggregates.

7.1.5.2.2.3 Stamping by holey contact surfaces (HC) composite stamps

Figure 7-18a-b shows SEM images of rims of magnetic 10nm Fe_3O_4 -ferrofluid nanoparticle aggregates printed from an aqueous solution with a PS-*b*-P2VP/T-ZnO composite nanoporous stamp ($0.9 \mu\text{m}$ HC) at room temperature, which surrounds hexagonal holes.

The arrays of rims consisting of Fe_3O_4 -10nm nanoparticles have long-range order with a few defects (Figure 7-18a). There is a more significant agglomeration of nanoparticles at the contact sites between the stamp contact surface and substrate, as shown in Figure 7-18a. A total of 22 holes from Figure 7-18b was analyzed from a binarized SEM image according to the procedure described in chapter 3.1.5 The analyzed holes have a diameter of $\approx 1.42 \pm 0.062 \mu\text{m}$, a circularity of $\approx 0.99 \pm 0.03$, and an average aspect ratio of $\approx 1.075 \pm 0.081$ (Figure 7-18c-e).

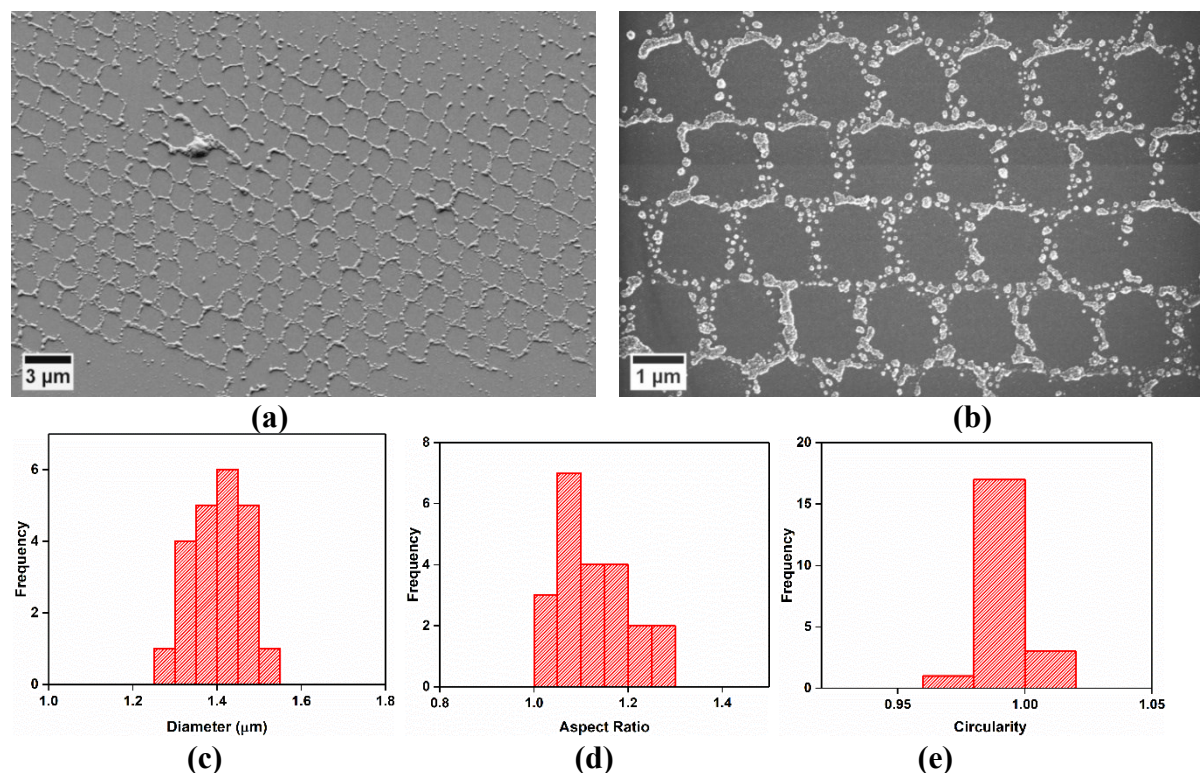


Figure 7-18 (a-b) SEM images of printed magnetic nanoparticle aggregates (10nm Fe₃O₄-ferrofluid) from an aqueous solution by using the experimental setup II (**out-of-plane** external magnetic field, $H \approx 0.33\text{T}$) with a PS-*b*-P2VP/T-ZnO composite nanoporous stamp (0.9 μm HC) at room temperature. (a) Large-area top view, and (b) detail top view. Histograms of (c) the diameters, (d) the circularities, and (e) the aspect ratios of 22 analyzed holes.

Figure 7-19a-b shows SEM images of holes of magnetic 10nm Fe₃O₄-ferrofluid nanoparticles printed from an aqueous solution with a PS-*b*-P2VP/T-ZnO composite nanoporous stamp (5.3 μm HC) at room temperature. The arrays of holes surrounded by rims consisting of Fe₃O₄-10nm nanoparticles have long-range order with minimal defects (Figure 7-19a). A total of 22 square holes analyzed from a binarized SEM image was according to the procedure described in chapter 3.1.5. The analyzed holes have a width of $\approx 5.19 \pm 0.19 \mu\text{m}$ and an average aspect ratio of $\approx 1.05 \pm 0.05$ (Figure 7-19c-d). The extraction of the plotline profile calculated by Image J from the white line (Figure 7-19a) is shown in Figure 7-19e. The side length of the stamped square-arrays amounts to $\approx 6.09 \pm 0.29 \mu\text{m}$.

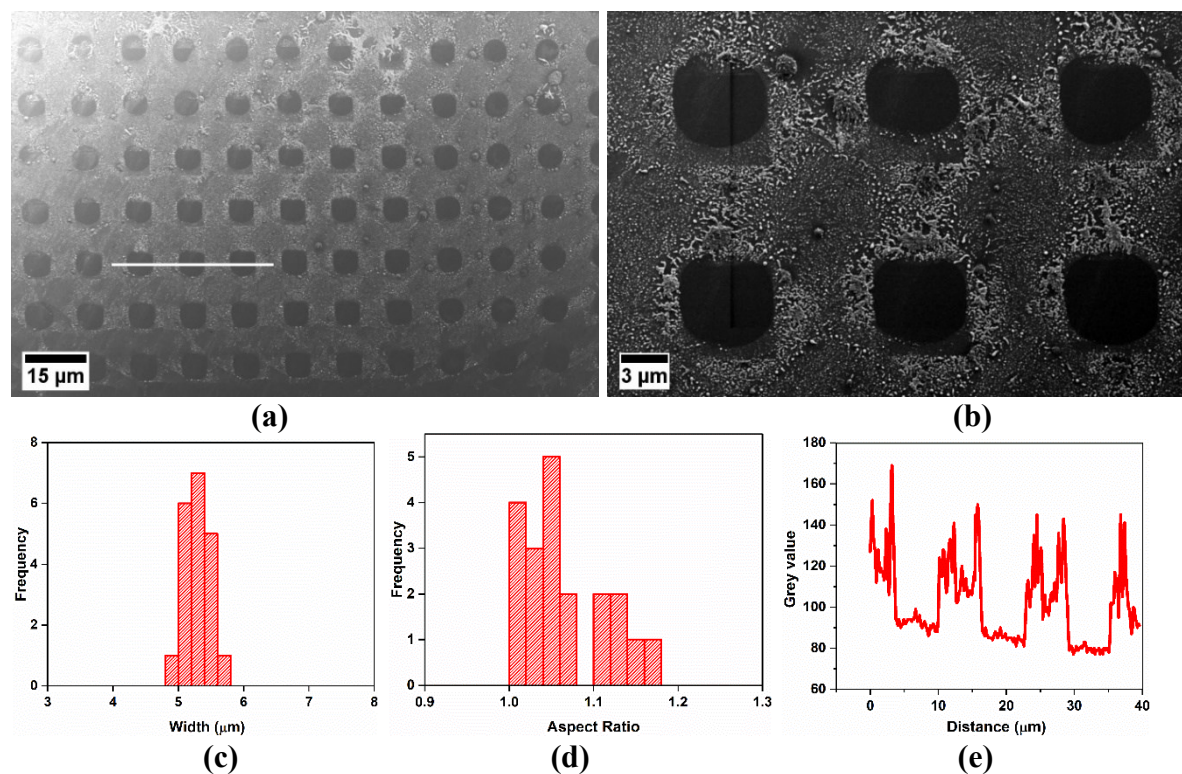


Figure 7-19 (a-b) SEM images of printed magnetic nanoparticles aggregates holes (10nm Fe₃O₄-ferrofluid) from an aqueous solution by using experimental setup II (**out-of-plane**

external magnetic field, $H \approx 0.33\text{T}$) with a PS-*b*-P2VP/T-ZnO composite nanoporous stamp ($5.3\ \mu\text{m}$ HC) at room temperature. (a) Large-area top view, and (b) detail top view. Histograms of (c) edge length and (e) the aspect ratios of 22 holes surrounded by rims of magnetic 10nm Fe_3O_4 -ferrofluid nanoparticle. (c) The plotline profile (white line in Figure 7-19a).

As described in section 7.1.3, the advantages of T-ZnO layer 1 are the storage of aqueous inks for multicycle stamping and the possibility of supplying inks to stamp contact surfaces from the reverse side. Here, ten stamping cycles were carried out without refilling the stamp. Hence, it is unnecessary to refill or use a new stamp. A single stamp can be used for many cycles. Figure 7-20 shows the results of successive stamping of magnetic 10nm Fe_3O_4 -Ferrofluid nanoparticle aggregates from an aqueous solution with PS-*b*-P2VP/T-ZnO composite nanoporous stamp ($4.3\ \mu\text{m}$ tip contact surfaces) at room temperature by using setup II (**out-of-plane**, $H \approx 0.33\ \text{T}$) without reinking. The order of the stamped magnetic nanoparticle aggregates can be seen for the 1st, 3rd, 6th and 10th cycles.

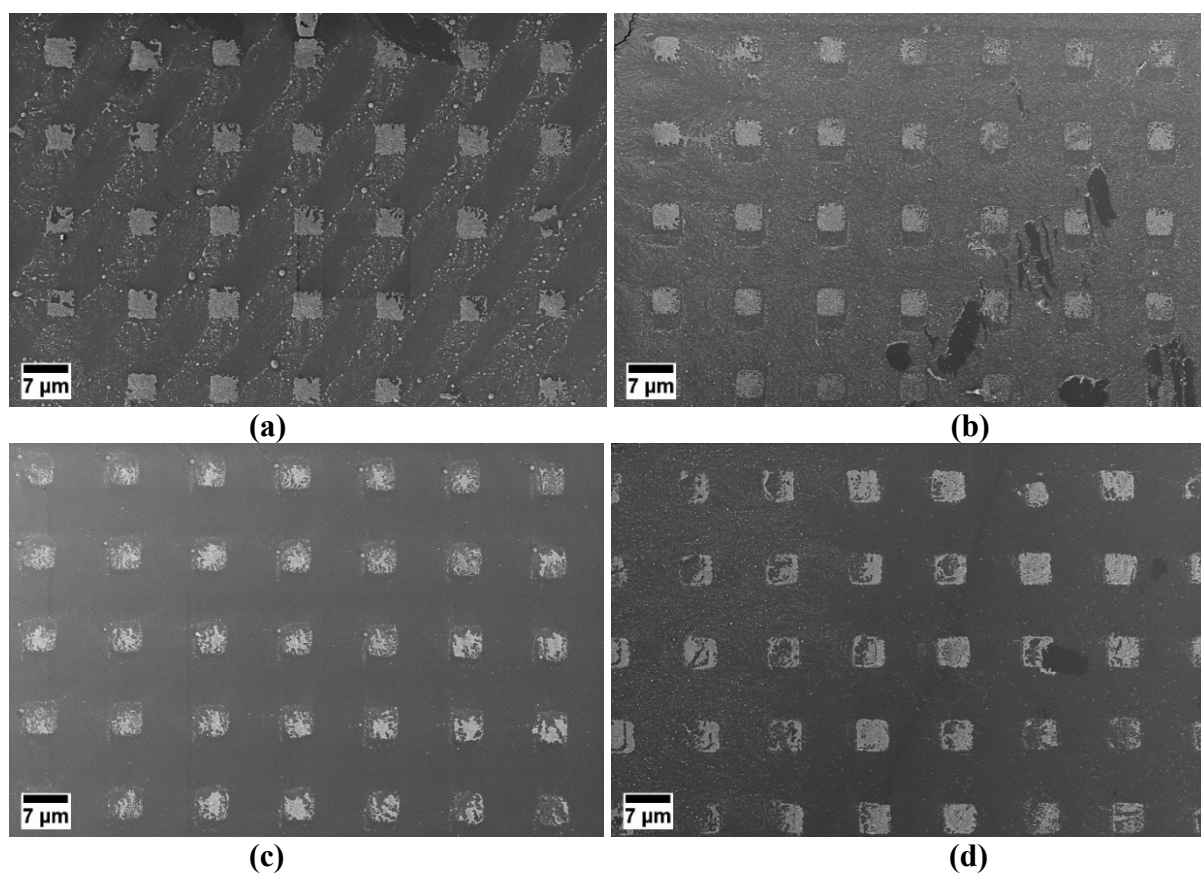


Figure 7-20 SEM images of magnetic 10nm Fe₃O₄-Ferrofluid nanoparticle aggregates printed from an aqueous solution using setup II with a PS-*b*-P2VP/T-ZnO composite nanoporous stamp (4.3 μm tips contact surfaces) at room temperature (**out-of-plane** external magnetic field, $H \approx 0.33\text{T}$). (a) 1st, (a) 3rd, (c) 6th, and (d) 10th stamping cycle.

7.1.5.3 Setup III

In setup III, the magnetic nanoparticle aggregates were directed by a permanent external magnet either below (**out-of-plane**) or parallel to the counter substrate (**in-plane**) (see section 3.3.4.4.2.3), and with the incorporation of a permanent external magnet (NdFeB, 6*1mm² (diameter*height), Grade 52) into the PDMS layer glued to the stamp holder with double-sided polyimide tape. In this setup, the stamp part is strongly attracted to the substrate by magnetic force because of the high-strength magnets below the silanized Si substrate. The detachment of the stamp part was done carefully because due to magnetic attraction force, the stamp is firmly attached to the substrate. For this, before detaching the stamp from the substrate, the substrate was held with the help of a non-magnetic tweezer from a side part. The magnetic field is not uniform over the whole magnet area; this is essential to consider. The position of magnets below the counterpart substrates was kept the same from experiment to experiment for the sake of reproducibility. The possible forces that act on nanoparticle aggregates in the magnetic field [248] are shown in Figure 7-21b. The magnetic nanoparticles are magnetized along the direction of the magnetic field and orient themselves in the direction of external magnetic field lines, and the magnetic force (F_m) acting on a magnetic particle can be calculated by Equation 7-4.[241] The magnetic force between two bar magnets can be calculated using Equation 7-7.[249]

$$F_z = \frac{(B_0^2 \cdot A^2) \cdot (L^2 + R^2)}{(\pi \cdot \mu_0) \cdot L^2} \cdot \left(\left(\frac{1}{x^2} + \frac{1}{(x+2 \cdot L)^2} \right) - \frac{2}{(x+L)^2} \right) \quad \text{Equation 7-7}$$

Where F_z is a force between two bar magnets (N), B_0 is flux density very close to each pole (T), A is the area of each pole (m²), L is the length of each magnet (m), R is the radius of each magnet (m), μ_0 is the vacuum permeability, and x is the separation between the two magnets (m).

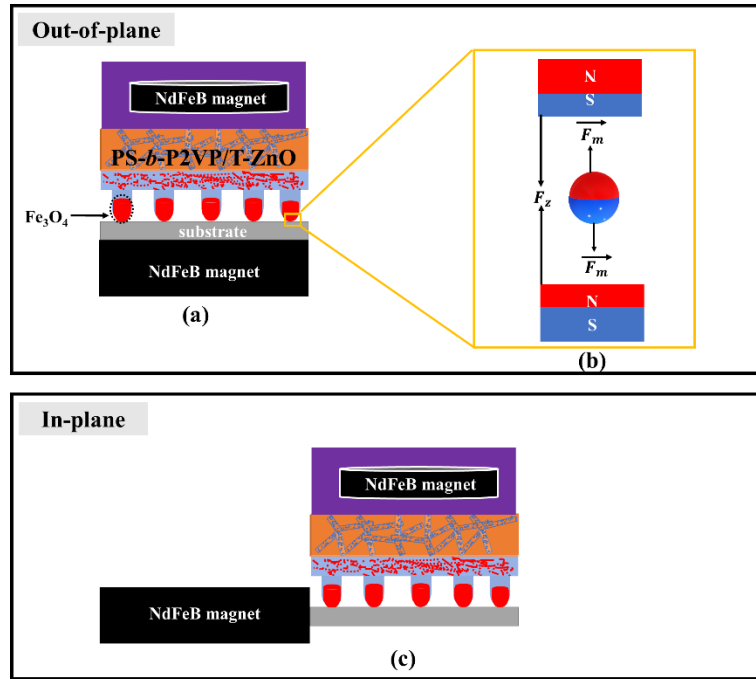


Figure 7-21 (a-b) Schematic illustration of **out-of-plane** geometry, and (c) **in-plane** geometry. (a) Detailed operation step showing the migration of the particles in the ferrofluid droplet at contact element tips for magnetic nanoparticle ferrofluid ink and (b) the strong dipole-dipole interaction among magnetic nanoparticles aggregates, resulting in the self-assembly of nanoparticle aggregates into parallel stacking, the F_z is force between two bar magnets, under an external magnetic field H .

7.1.5.3.1 In-plane magnetic field

Figure 7-22 shows SEM images of magnetic 10nm Fe₃O₄-ferrofluid nanoparticle aggregates printed from an aqueous solution with a PS-*b*-P2VP/T-ZnO composite nanoporous stamp (0.9 μm TC) at room temperature. The hexagonally arranged arrays of Fe₃O₄-10nm nanoparticle aggregates have long-range order and can be seen in Figure 7-22a. The printing resulted in many defects, and many larger aggregates of ferrofluid can be seen (Figure 7-22b). The quality of the stamped patterns did not improve in subsequent repetitions of the stamping experiments; hereafter, all following stamping experiments were conducted using **out-of-plane** magnetic field configurations (see sections below).

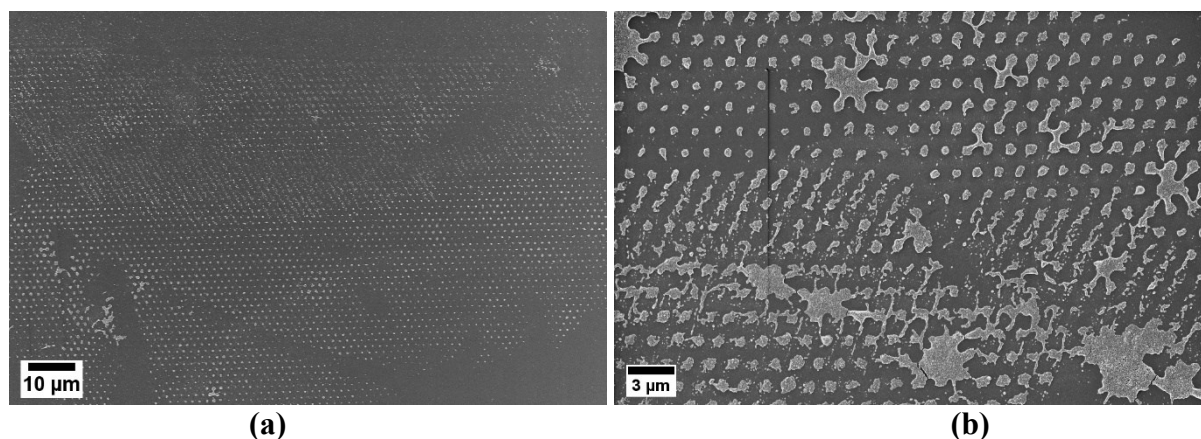


Figure 7-22 (a-b) SEM images of printed magnetic nanoparticle aggregates (10nm Fe_3O_4 -ferrofluid) from an aqueous solution by using the experimental setup III with a PS-*b*-P2VP/T-ZnO composite nanoporous stamp (0.9 μm TC) at room temperature using **in-plane** geometry – the **in-plane** magnetic field lines are parallel to the substrate (at $H \approx 0.33\text{T}$). (a) Large-area top view, and (b) detail top views.

7.1.5.3.2 Out-of-plane magnetic field

7.1.5.3.2.1 Effect of external magnetic field

As described in section 7.1.5.2.2.1, the magnetic flux density generally increases with a decrease in distance between the magnets or the increase in the number of magnets.[246] To change the strength of the external magnetic field, one, two, three, or four NdFeB external permeant magnets with a diameter of 20 mm and a height of 5mm were added below the silanized Si counter substrate. The magnetic field strength H measured using a Gaussmeter, a magnetic flux density sensor, amounted to $\approx 0.20\text{T}$, $\approx 0.27\text{T}$, $\approx 0.35\text{T}$, and $\approx 0.37\text{T}$ for one, two, three, or four external permeant magnets, respectively. Figure 7-23 shows SEM images of magnetic 10nm Fe_3O_4 -ferrofluid nanoparticle aggregates printed from an aqueous solution with a PS-*b*-P2VP/T-ZnO composite nanoporous stamp (0.9 μm TC) at room temperature under different magnetic field strengths. The obtained arrays of stamped nanoparticle aggregates show an increasingly better long-range order (Figure 7-23d) than stamped nanoparticle aggregates with low magnetic field strength. The best result was achieved when four external permanent magnets (NdFeB, 20*5mm² (diameter*height), Grade 52)) with $H \approx 0.37\text{T}$ were

placed below the silanized Si substrate. Hence, all results are shown below for setup III arrangements obtained with $H \approx 0.37\text{T}$.

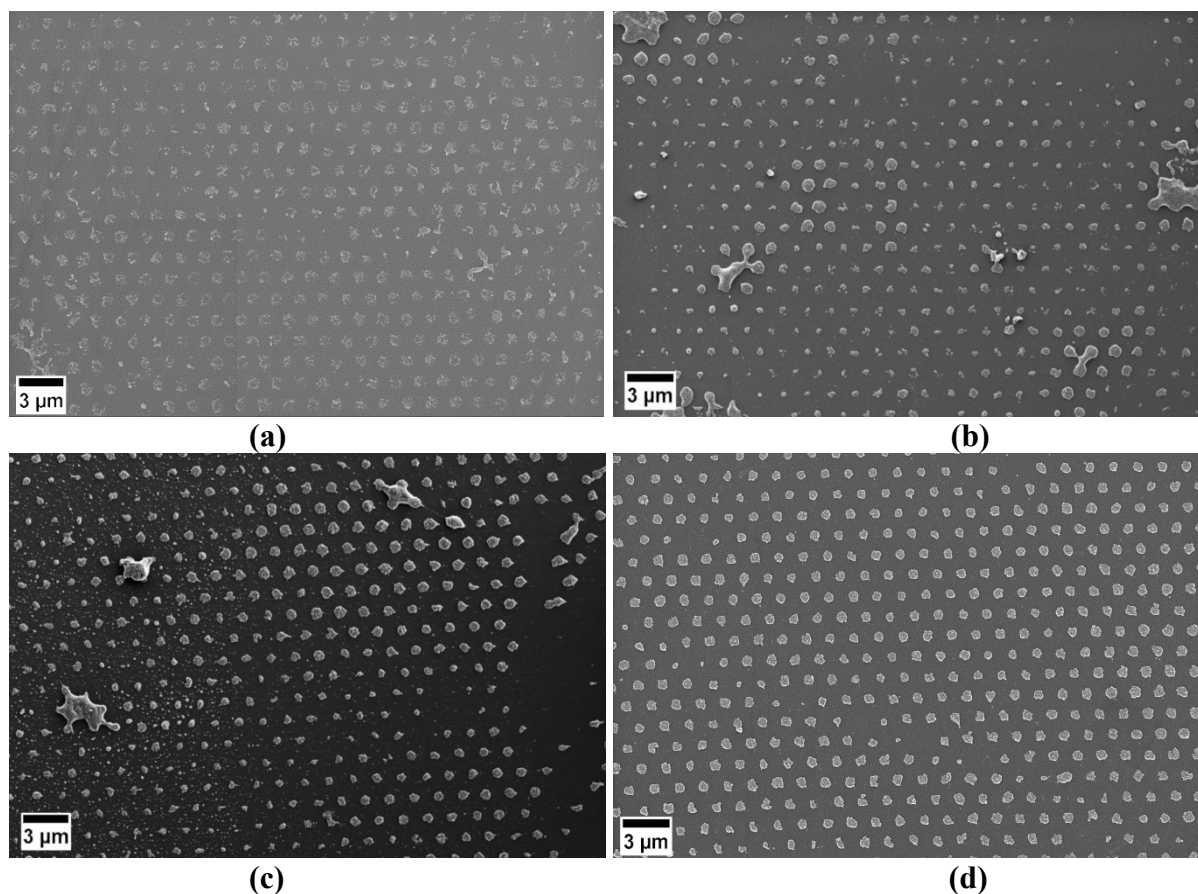


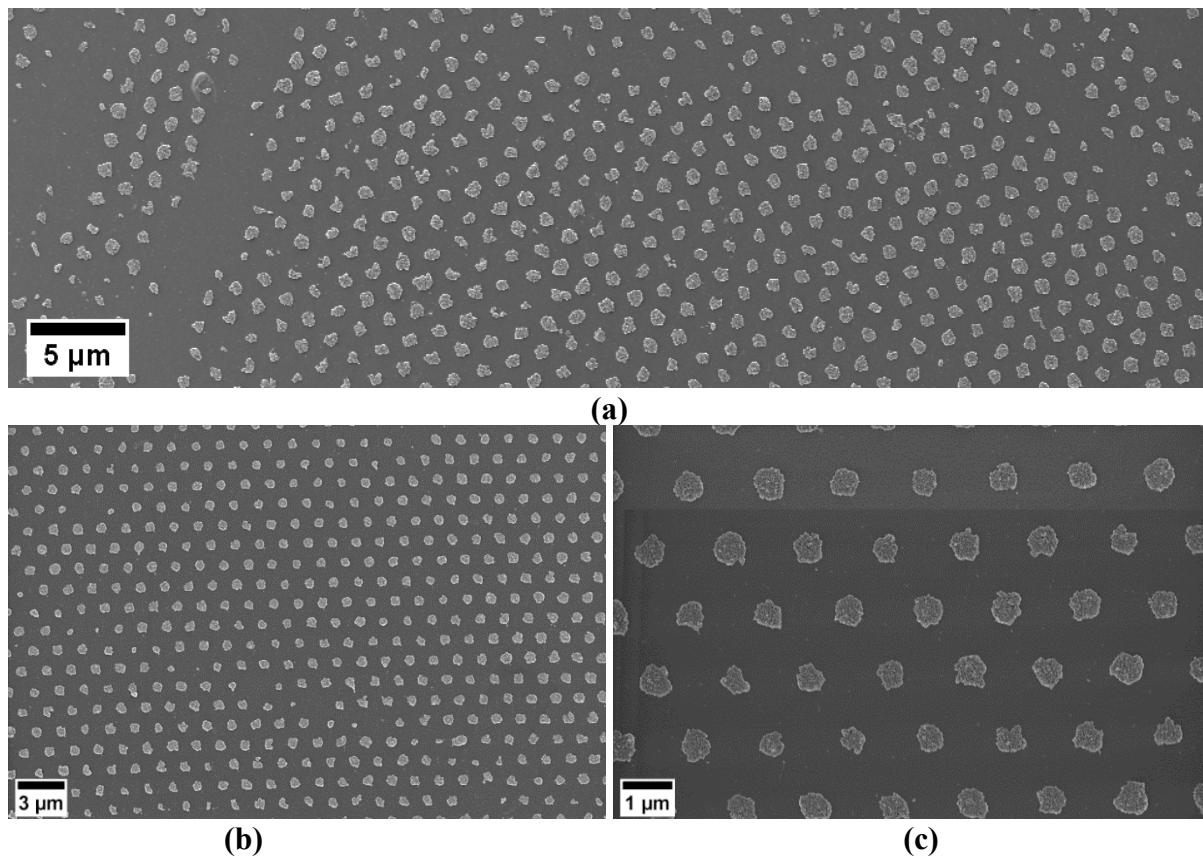
Figure 7-23 (a-d) SEM images of magnetic nanoparticle aggregates (10nm Fe₃O₄.ferrofluid) printed from an aqueous solution by using the experimental setup III with a PS-*b*-P2VP/T-ZnO composite nanoporous stamp (0.9 μm TC) at room temperature. The number of the external permanent magnets (NdFeB, 20*5 mm² (diameter*height), Grade 52 located below the counterpart substrates (**out-of-plane**) are: (a) one, $H \approx 0.20\text{ T}$; (b) two, $H \approx 0.27\text{ T}$; (c) three, $H \approx 0.35\text{ T}$ and (d) Four, $H \approx 0.37\text{ T}$.

7.1.5.3.2.2 Stamping by tip contact surface (TC) composite stamps

Figure 7-24a-c shows the SEM images of magnetic 10nm Fe₃O₄.ferrofluid nanoparticle aggregates printed from an aqueous solution with a PS-*b*-P2VP/T-ZnO composite nanoporous stamp (0.9 μm TC) at room temperature. The hexagonally arranged arrays of Fe₃O₄-10nm

nanoparticle aggregates have long-range order and few defects (Figure 7-24a). The order of stamped nanoparticle aggregates can be seen from detailed magnified SEM images (Figure 7-24b-c).

The surface topography and height profiles of stamped nanoparticle aggregates were characterized using atomic force microscopy (AFM). Figure 7-24d-e shows an AFM image to analyze the heights of the stamped nanoparticle aggregates. The average height of the 7 evaluated 10nm Fe₃O₄ nanoparticle aggregates amounted to 61.85±8.96nm. The measurement was done by AFM using the contact mode, and a line profile was extracted from the measured data (Figure 7-24b). A total of 428 stamped 10nm Fe₃O₄-ferrofluid nanoparticle aggregates in a binarized SEM image were evaluated according to the procedure described in section 3.1.5. The analyzed aggregates of magnetic nanoparticles have a diameter of $\approx 625\pm 59$ nm, a circularity of $\approx 0.89\pm 0.05$, and an average aspect ratio of $\approx 1.15\pm 0.13$ (Figure 7-24f-h).



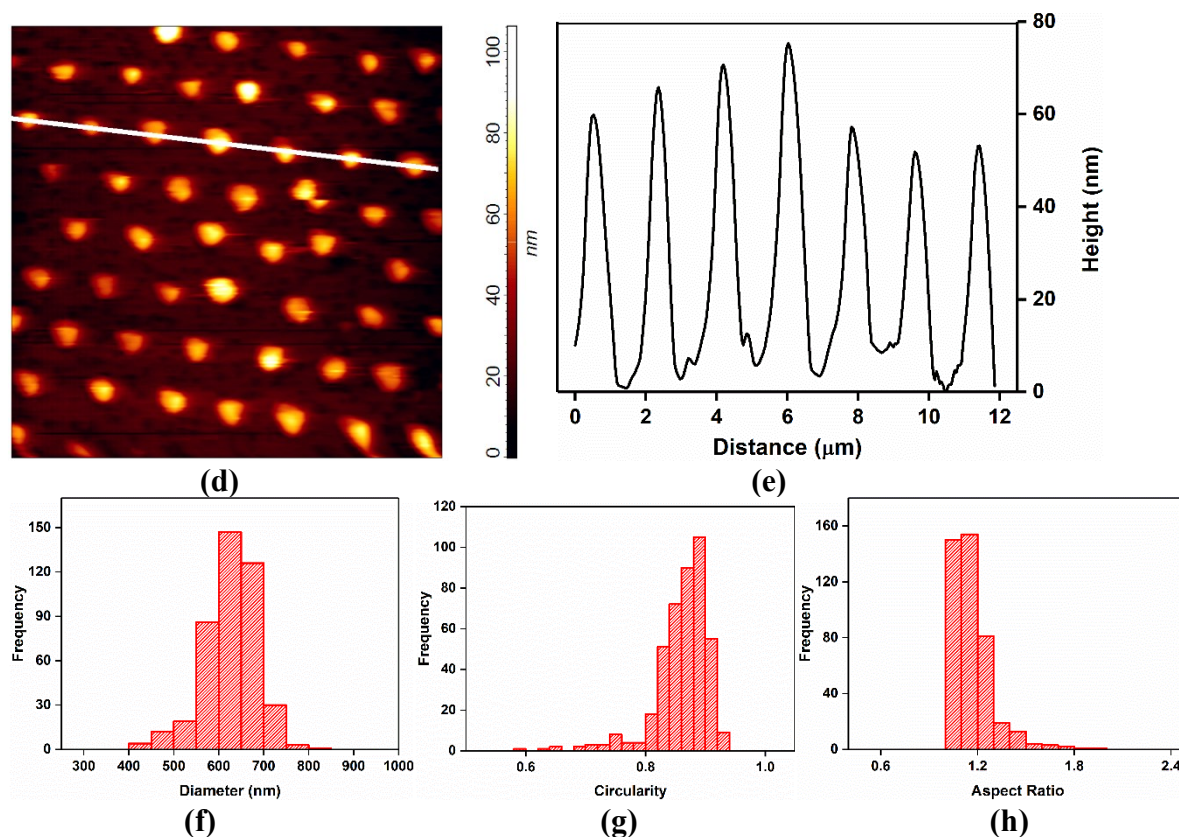


Figure 7-24 (a-c) SEM images of arrays of magnetic nanoparticle aggregates (10nm Fe_3O_4 -ferrofluid) printed from an aqueous solution by using the experimental setup III (**out-of-plane** external magnetic field, $H \approx 0.37\text{T}$) with PS-*b*-P2VP/T-ZnO composite nanoporous stamp (0.9 μm TC) at room temperature. (a) Large-area top view, and (b-c) detail top SEM views. (d) Atomic Force Microscopy (AFM) image ($12 \times 12 \mu\text{m}^2$) of stamped magnetic nanoparticle aggregates, and (e) The line scan of the white line in d) shows the height of the stamped magnetic nanoparticle aggregates. Histograms of 428 analyzed stamped magnetic nanoparticle aggregates showing (f) the diameters, (g) the circularities, and (h) the aspect ratios of the Fe_3O_4 stamped magnetic nanoparticle aggregates.

Figure 7-25a-b shows SEM images of magnetic 5nm Fe_3O_4 nanoparticle aggregates printed from an aqueous solution with a PS-*b*-P2VP/T-ZnO composite nanoporous stamp (0.9 μm TC) at room temperature. The hexagonally arranged arrays of Fe_3O_4 -5nm nanoparticle aggregates have long-range order and many defects (Figure 7-25a). A total of 20 nanoparticle aggregates from a binarized SEM image was evaluated according to the method described in section 3.1.4. The analyzed nanoparticle aggregates have a diameter of $\approx 725 \pm 153$ nm, a circularity of $\approx 0.875 \pm 0.140$, and an average aspect ratio of $\approx 1.3 \pm 0.30$ (Figure 7-25c-e).

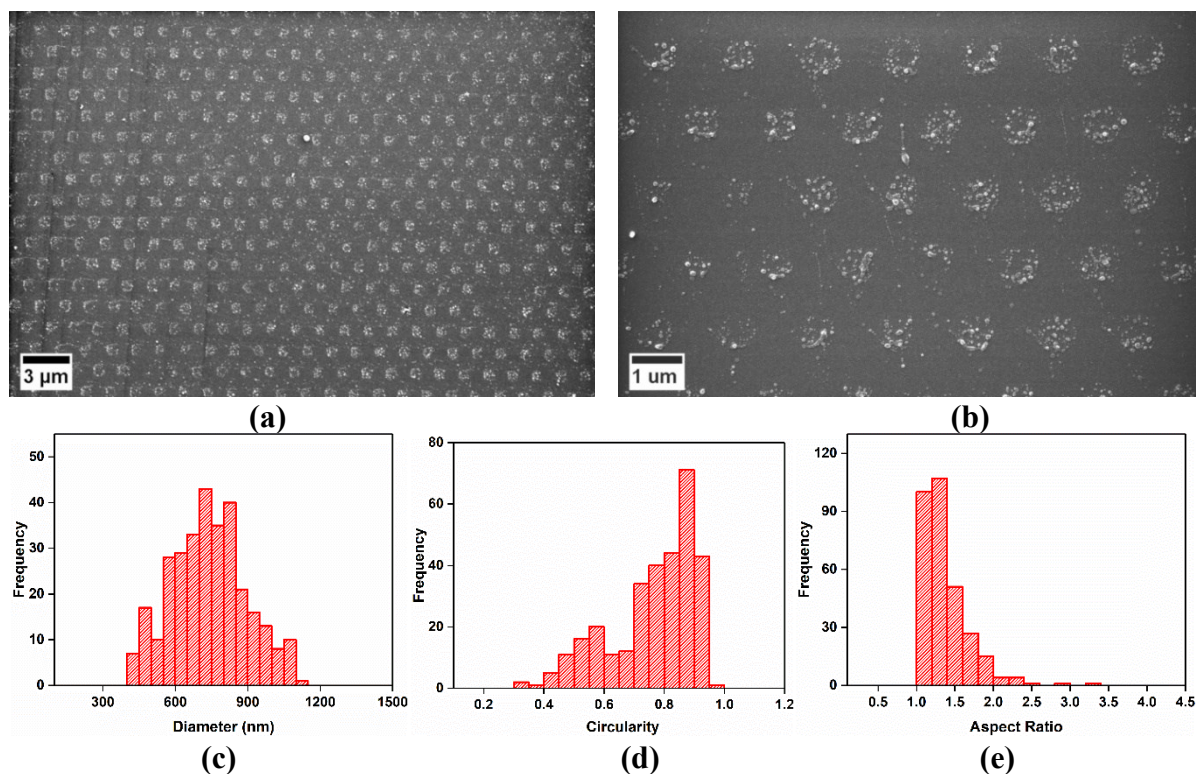


Figure 7-25 (a-b) SEM images of printed magnetic nanoparticle aggregates ($5\text{nm Fe}_3\text{O}_4$) from an aqueous solution by using the experimental setup III (**out-of-plane** external magnetic field, $H \approx 0.37\text{T}$) with PS-*b*-P2VP/T-ZnO composite nanoporous stamp ($0.9\ \mu\text{m TC}$) at room temperature. (a) Large-area top view and (b) detail top view. Histograms of (a) the diameters, (b) the circularities, and (c) the aspect ratios of 20 stamped magnetic $5\text{nm Fe}_3\text{O}_4$ nanoparticle aggregates.

Figure 7-26a-c shows SEM images of magnetic $10\text{nm Fe}_3\text{O}_4$ -ferrofluid nanoparticle aggregates printed from an aqueous solution with a PS-*b*-P2VP/T-ZnO composite nanoporous stamp ($4.3\ \mu\text{m TC}$) at room temperature. The square lattice of rectangular Fe_3O_4 - 10nm nanoparticle aggregates has long-range order and a limited number of defects (Figure 7-26a). The order of the stamped nanoparticle aggregates can be seen from detailed magnified SEM images (Figure 7-26b). As seen from the detailed magnified SEM image in Figure 7-26b, the square lattice is altogether containing dense nanoparticle aggregates.

The surface topography and height profiles of stamped nanoparticle aggregates were characterized using atomic force microscopy (AFM). Figure 7-26c-d shows an AFM image to analyze the stamped nanoparticles aggregates height. The average height of the 7 stamped nanoparticle aggregates amounted to $59.55 \pm 12.91\text{nm}$ measured by AFM. The measurement

was done with AFM using the contact mode; a line profile was extracted from the measured data (Figure 7-26d). A total of 18 stamped nanoparticle aggregates in a binarized SEM image were evaluated according to the method described in section 3.1.4. The analyzed aggregates have an edge length of $\approx 4.50 \pm 0.23 \mu\text{m}$ and an average aspect ratio of $\approx 1.05 \pm 0.15$ (Figure 7-26e-g). The plotline profile extracted with Image J along the white line in Figure 7-26a is shown in Figure 7-26g. The edge length of the stamped square arrays amounted to $\approx 3.98 \pm 0.39 \mu\text{m}$.

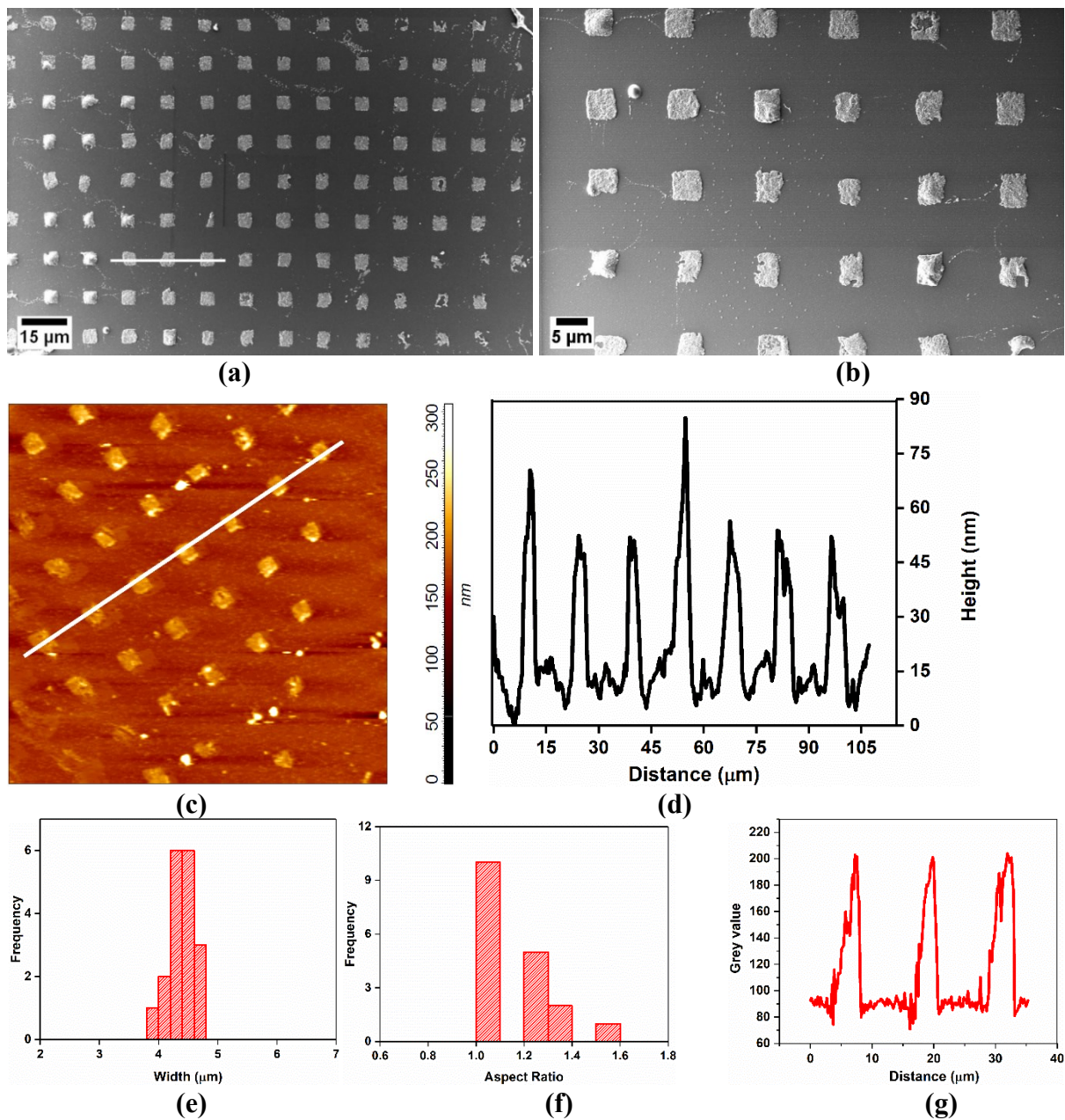
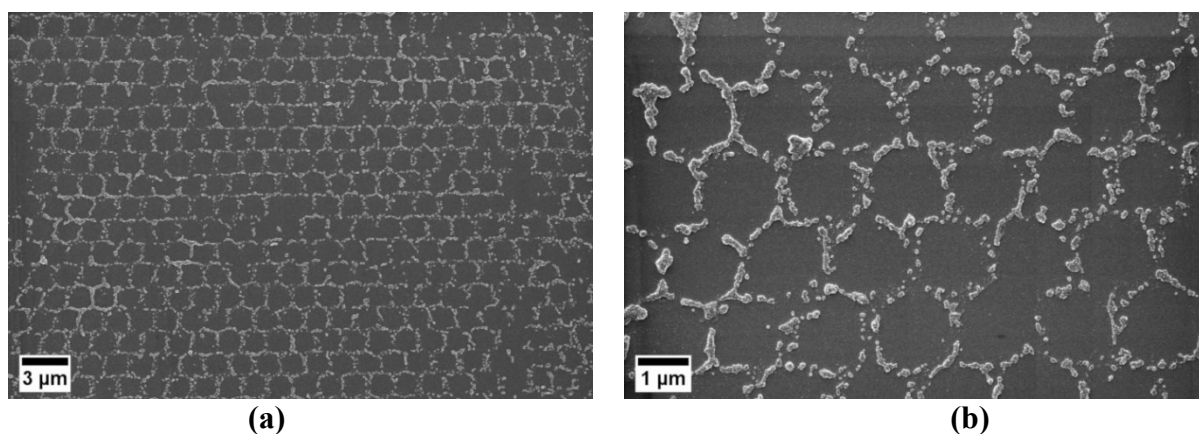


Figure 7-26 (a-b) SEM images of arrays of magnetic nanoparticle aggregates (10nm Fe₃O₄-ferrofluid) printed from an aqueous solution by using the experimental setup III (**out-of-plane** external magnetic field, $H \approx 0.37\text{T}$) with a PS-*b*-P2VP/T-ZnO composite nanoporous stamp (4.3 μm TC) at room temperature. (a) Large-area top view, and (b) detail top view. (c) AFM image (100 x 100 μm^2) of stamped magnetic nanoparticle aggregates, and (d) line scan of the white line in c) showing the height of the stamped magnetic nanoparticle aggregates. Histograms of e) the square dot edge length and (f) the aspect ratio of 18 magnetic 10nm Fe₃O₄-Ferrofluid nanoparticle aggregates. (g) Line profile along the white line in Figure 7-26a of the Fe₃O₄ stamped magnetic nanoparticle aggregates.

7.1.5.3.2.3 Stamping by holey contact surface (HC) composite stamps

Figure 7-27a-b shows SEM images of arrays of rims of magnetic 10nm Fe₃O₄-ferrofluid nanoparticles printed from an aqueous solution with PS-*b*-P2VP/T-ZnO composite nanoporous stamp (0.9 μm HC) at room temperature, which surrounds hexagonal holes. The arrays of hexagonally arranged holes encompassed by Fe₃O₄-10nm nanoparticle aggregates rims have long-range order with some defects (Figure 7-27a). A total of 20 holes from binarized SEM images were evaluated according to the method described in section 3.1.4. The analyzed holes have a diameter of $\approx 1.25 \pm 0.10 \mu\text{m}$, a circularity of $\approx 0.97 \pm 0.110$, and an average aspect ratio of $\approx 1.12 \pm 0.08$ (Figure 7-27c-e).



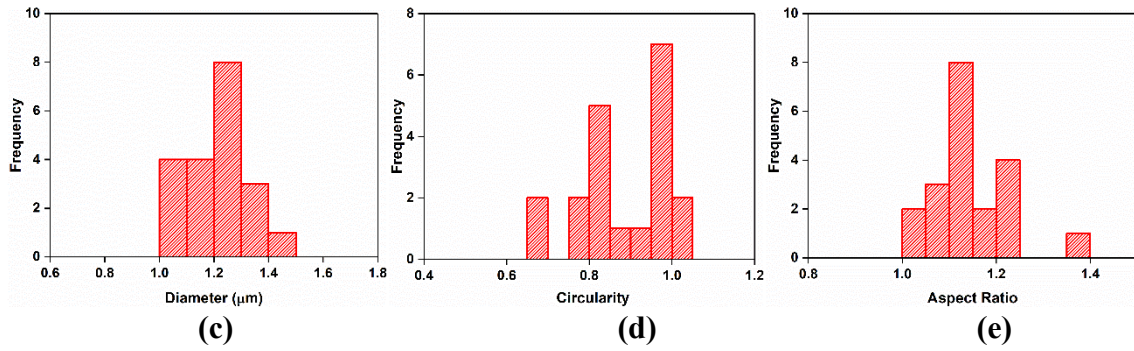
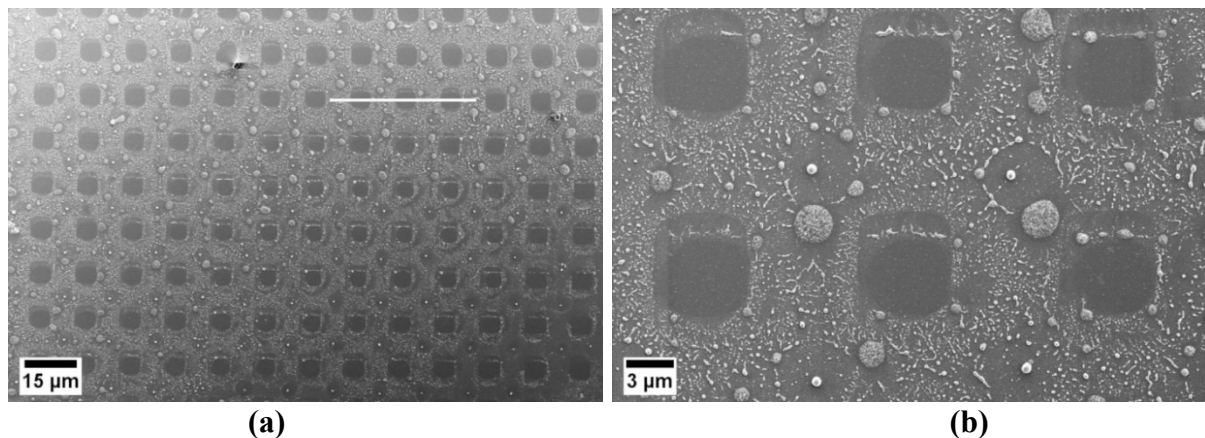


Figure 7-27 (a-b) SEM images of magnetic nanoparticle aggregates holes (10nm Fe_3O_4 -ferrofluid) printed from an aqueous solution by using the experimental setup III (**out-of-plane** external magnetic field, $H \approx 0.37\text{T}$) with a PS-*b*-P2VP/T-ZnO composite nanoporous stamp (0.9 μm HC) at room temperature. (a) Large-area top view, and (b) detail top view. Histograms of (c) the diameters, (d) the circularities, and (e) the aspect ratios of 20 analyzed holes.

Figure 7-28a-b shows SEM images of a holey film of magnetic 10nm Fe_3O_4 -ferrofluid nanoparticles printed from an aqueous solution with a PS-*b*-P2VP/T-ZnO composite nanoporous stamp (5.3 μm HC) at room temperature. The hole arrays have long-range order with few agglomeration defects (Figure 7-28a). 20 square holes from binarized SEM images were evaluated according to the method described in section 3.1.4. The analyzed holes have a diameter of $\approx 5.25 \pm 1.02 \mu\text{m}$ and an average aspect ratio of $\approx 1.05 \pm 0.015$ (Figure 7-28c-d). The extraction of the plotline profile obtained with Image J along the white line in Figure 7-28a is shown in Figure 7-28e. The side edge length of the square holes amounts to $\approx 5.57 \pm 0.5 \mu\text{m}$.



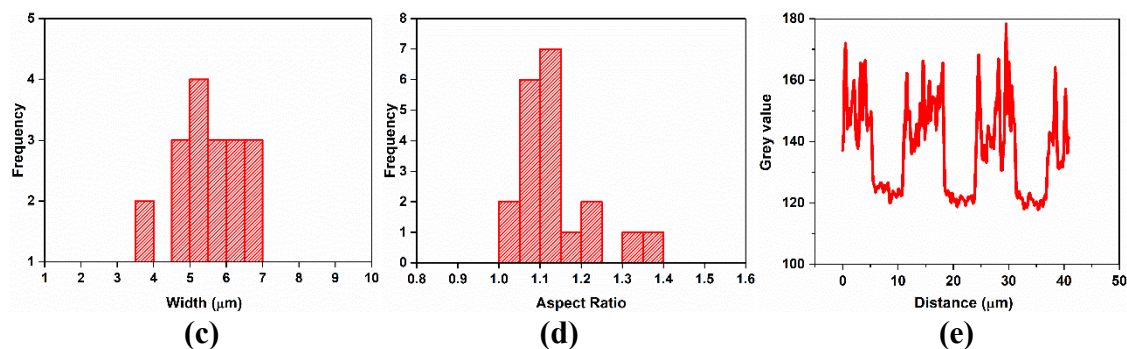
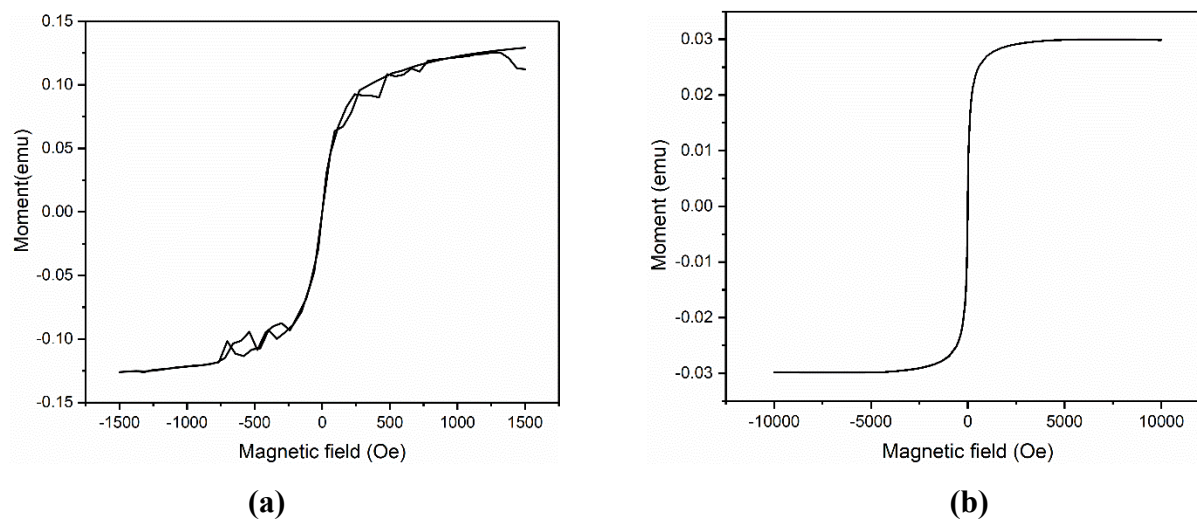


Figure 7-28 (a-b) SEM images of magnetic nanoparticle aggregates holes (10nm Fe_3O_4 -ferrofluid) printed from an aqueous solution by using the experimental setup III (**out-of-plane** external magnetic field, $H \approx 0.37\text{T}$) with a PS-*b*-P2VP/T-ZnO composite nanoporous stamp (5.3 μm HC) at room temperature. (a) Large-area top view, and (b) detail top view. Histograms of (c) edge length, and (d) the aspect ratios of 20 holes in a film consisting of magnetic 10nm Fe_3O_4 -Ferrofluid nanoparticle aggregates (e) The plotline profile (white line in Figure 7-28a).

Figure 7-29a-b shows a typical magnetic hysteresis loop for 50 μL of Fe_3O_4 (10 nm) ferrofluids in a vial and Fe_3O_4 (10 nm) ferrofluid nanoparticles spin-coated on a silicon substrate. The spin-coating was done at 1000 rpm for 60 sec. The ferrofluid shows superparamagnetic characteristics as there is no hysteresis in the magnetization curves (Figure 7-29a-b). Fe_3O_4 (10 nm) ferrofluid nanoparticle aggregates printed on a silanized Si substrate showed diamagnetic characteristics. The reason may be a too-small amount of deposited magnetic nanoparticles aggregates on the silanized Si substrate (Figure 7-29c).



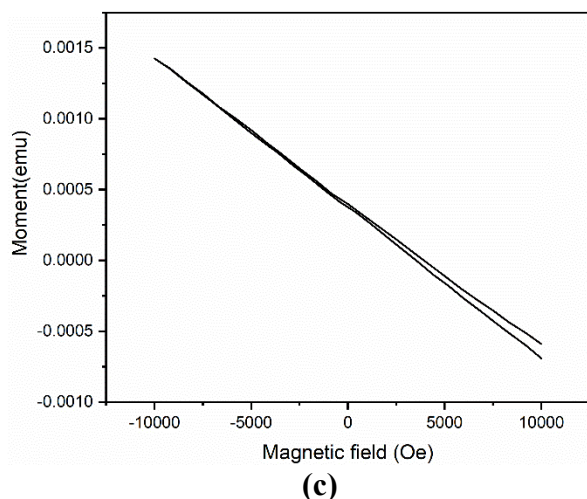


Figure 7-29 Hysteresis loops of (a) 50 μL of Fe_3O_4 (10 nm) ferrofluid in a vial, (b) Fe_3O_4 (10 nm) ferrofluid nanoparticles spin-coated on a silicon substrate, and (c) magnetic nanoparticle aggregates (10nm Fe_3O_4 -ferrofluid) printed from an aqueous solution by using the experimental setup III (**out-of-plane**, $H \approx 0.37\text{T}$) with a PS-*b*-P2VP/T-ZnO composite nanoporous stamp (4.3 μm TC) at room temperature.

7.1.5.4 Setup IV

In setup IV, the magnetic nanoparticle aggregates were stamped with the help of an external magnetic field generated in a vibrating sample magnetometer (VSM) at room temperature (see section 3.3.4.4.2.4). After infiltration of a PS-*b*-P2VP/T-ZnO composite stamp with 10nm Fe_3O_4 -ferrofluid ink, the stamp was attached to the silanized silicon counter substrate with transparent double-sided adhesive tape (tesa). The stamp attached to the substrate was glued to the VSM sample holder rod and placed carefully at the central position between the electromagnets, as shown in Figure 7-30 a and c for **in-plane** and **out-of-plane** geometry respectively.

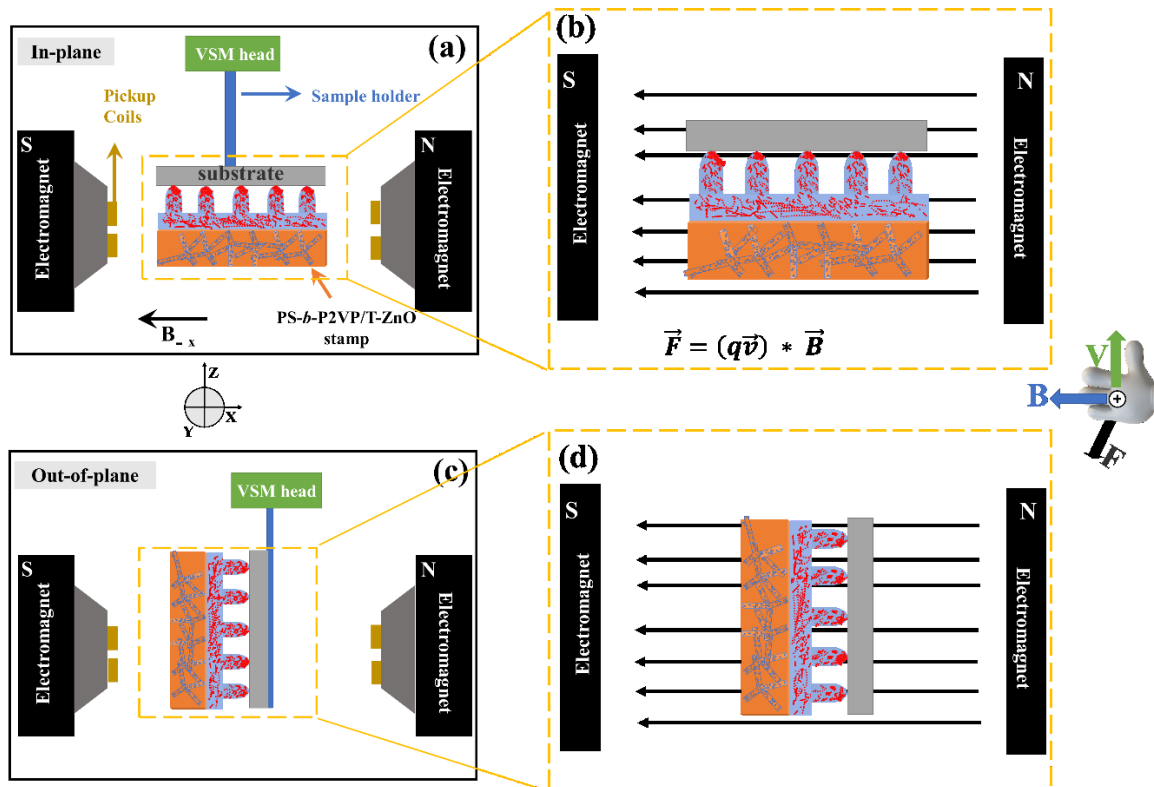


Figure 7-30 (a-b) Schematic illustration of **in-plane** geometry, and (c-d) **out-of-plane** geometry. As shown, the magnetic field lines run (b) parallel and (d) perpendicular to the counterpart surface. Solid black lines show magnetic field lines. B_{-x} is magnetic flux density, \vec{F} is the Lorentz force, and \vec{v} is velocity of particles. According to the right-hand rule, \vec{F} is perpendicular to \vec{B} and \vec{v} .

7.1.5.4.1 Out-of-plane magnetic field

Figure 7-31 shows the SEM images of magnetic 10nm Fe_3O_4 -ferrofluid nanoparticle aggregates printed from an aqueous solution with a PS-*b*-P2VP/T-ZnO composite nanoporous stamp (0.9 μm TC) at room temperature. The Fe_3O_4 -10nm nanoparticle aggregates are largely disordered. Many bigger aggregates of nanoparticles can be seen. The stamping procedure was ineffective in the **out-of-plane** geometry and did not yield precisely stamped spots. The disorder and agglomeration of the stamped nanoparticles can be seen in Figure 7-31. The reasons may be the strong magnetic inter-particle attractions, leading to a strong agglomeration and a weak bonding force with the substrate, making it hard to print magnetic aggregates.[228] The other reason may be the arrangement of a sample with a VSM sample holder rod, which is vertical;

however, setups II and III yielded printing results with long-range order in the **out-of-plane** geometry, having fewer defects (see sections 7.1.5.2.2 and 7.1.5.3.2).

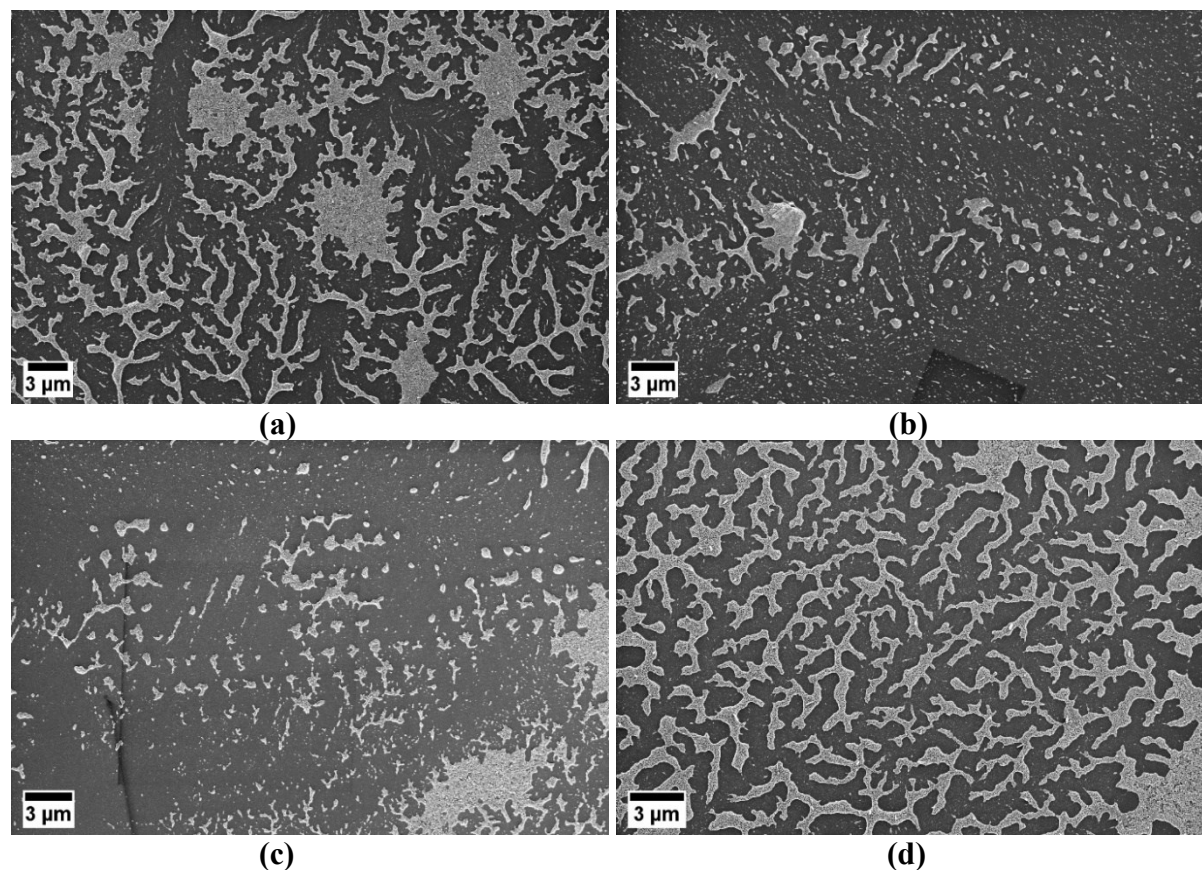
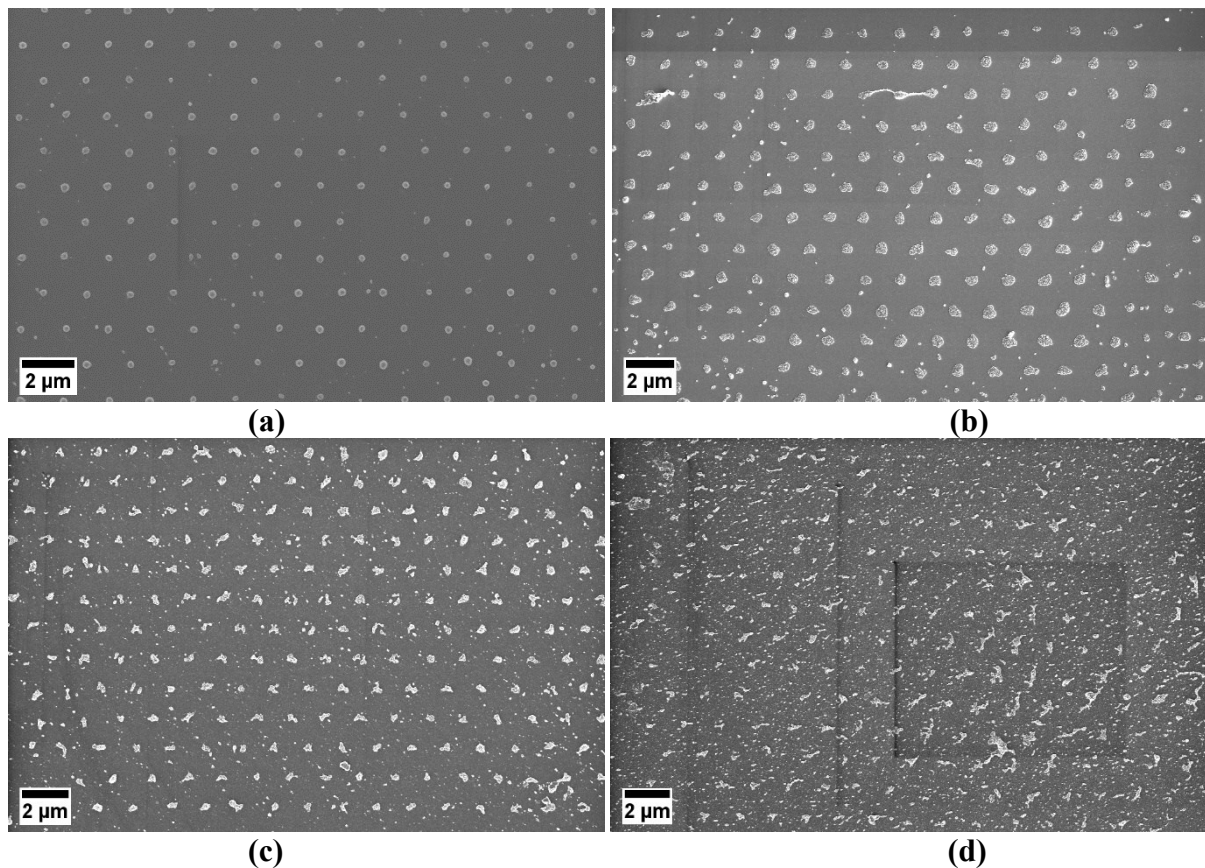


Figure 7-31 SEM images of magnetic 10nm Fe_3O_4 -ferrofluid nanoparticle aggregates printed from an aqueous solution using setup IV with a PS-*b*-P2VP/T-ZnO composite nanoporous stamp (0.9 μm TC) at room temperature using **out-of-plane** geometry; (a) $H \approx 0.2$ T, (b) $H \approx 0.6$ T, (c) $H \approx 1.0$ T, and (d) $H \approx 1.4$ T.

7.1.5.4.2 In-plane magnetic field

7.1.5.4.2.1 Effect of magnetic field exposure time

During the **in-plane** geometry, the magnetic field exposure time was varied. Figure 7-32 shows the printing of magnetic nanoparticle aggregates with a magnetic field strength H value of 1.4T at room temperature in the **in-plane** geometry under different exposure times for 10 s, 40 s, 70 s, 100 s, 180 s, 300 s, and 600 s. The stamped nanoparticle aggregate arrays show less order with many defects with increasing magnetic field exposure time. The best reproducibility was achieved by applying a magnetic field exposure time of 10s. Hence, all results shown below were obtained with setup IV at $H \approx 1.4\text{T}$ under the magnetic field exposure times for 10 s.



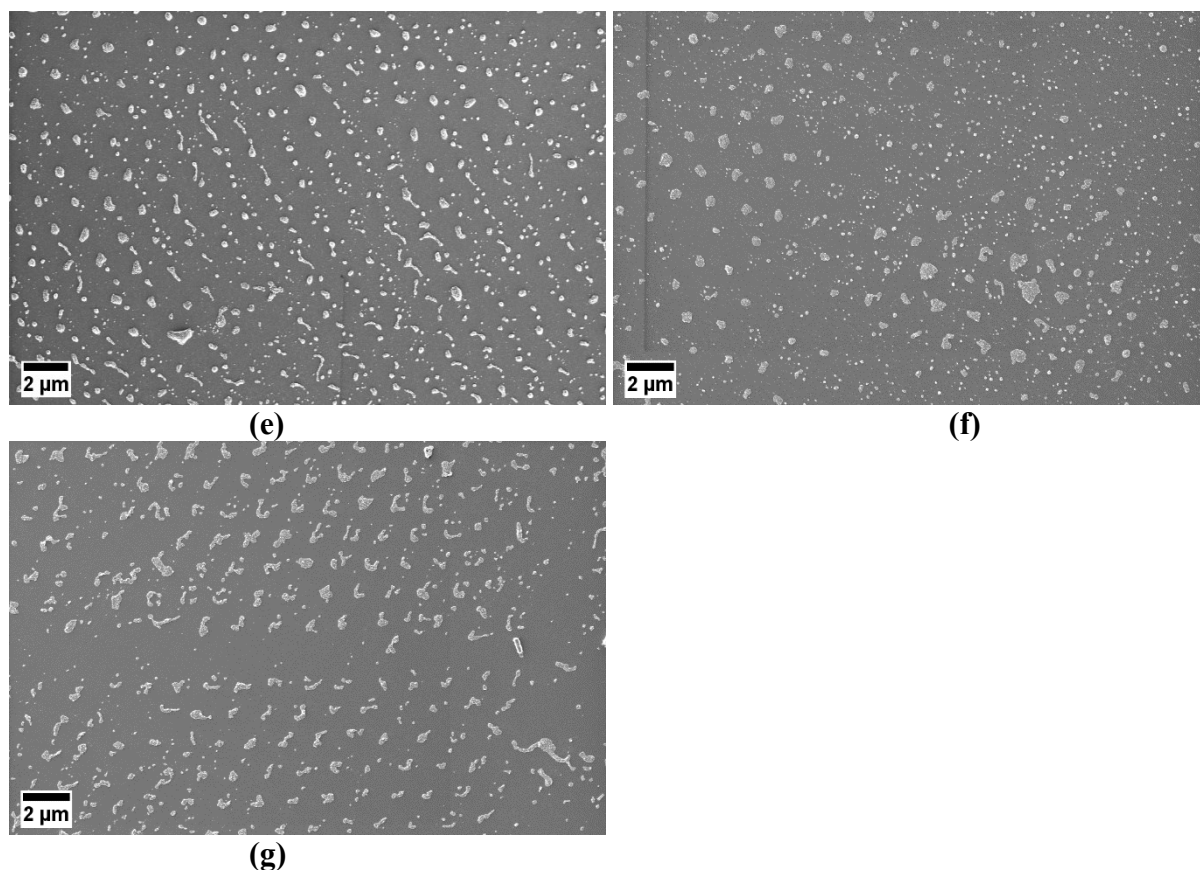


Figure 7-32 (a-g) SEM images of magnetic nanoparticle aggregates (10nm Fe_3O_4 -ferrofluid) printed from an aqueous solution by using the experimental setup IV (**in-plane** magnetic field, $H \approx 1.4\text{T}$) with a PS-*b*-P2VP/T-ZnO composite nanoporous stamp (0.9 μm TC) at room temperature. The **in-plane** magnetic field was applied for (a) 10 sec, (b) 40 sec, (c) 70 sec, (d) 100 sec, (e) 180 sec, (f) 300 sec, and (g) 600 sec.

7.1.5.4.2.2 Effect of external magnetic field

To test the effect of the external magnetic field strength, the printing of magnetic nanoparticle aggregates was done with magnetic field strength H values of 0.2T, 0.6T, 1.0T, and 1.4T at room temperature in the **in-plane** geometry with an exposure time to the magnetic field for 10 s. Figure 7-33 shows SEM images of magnetic 10nm Fe_3O_4 -ferrofluid nanoparticle aggregates printed from an aqueous solution with a PS-*b*-P2VP/T-ZnO composite nanoporous stamp (0.9 μm TC) at room temperature under different magnetic field strengths. The stamped nanoparticle aggregates arrays show increasingly better long-range order with few defects (Figure 7-33d). The best reproducibility was achieved by applying a magnetic field of 1.4T. Hence, all results shown below were obtained with setup IV obtained with $H \approx 1.4\text{T}$.

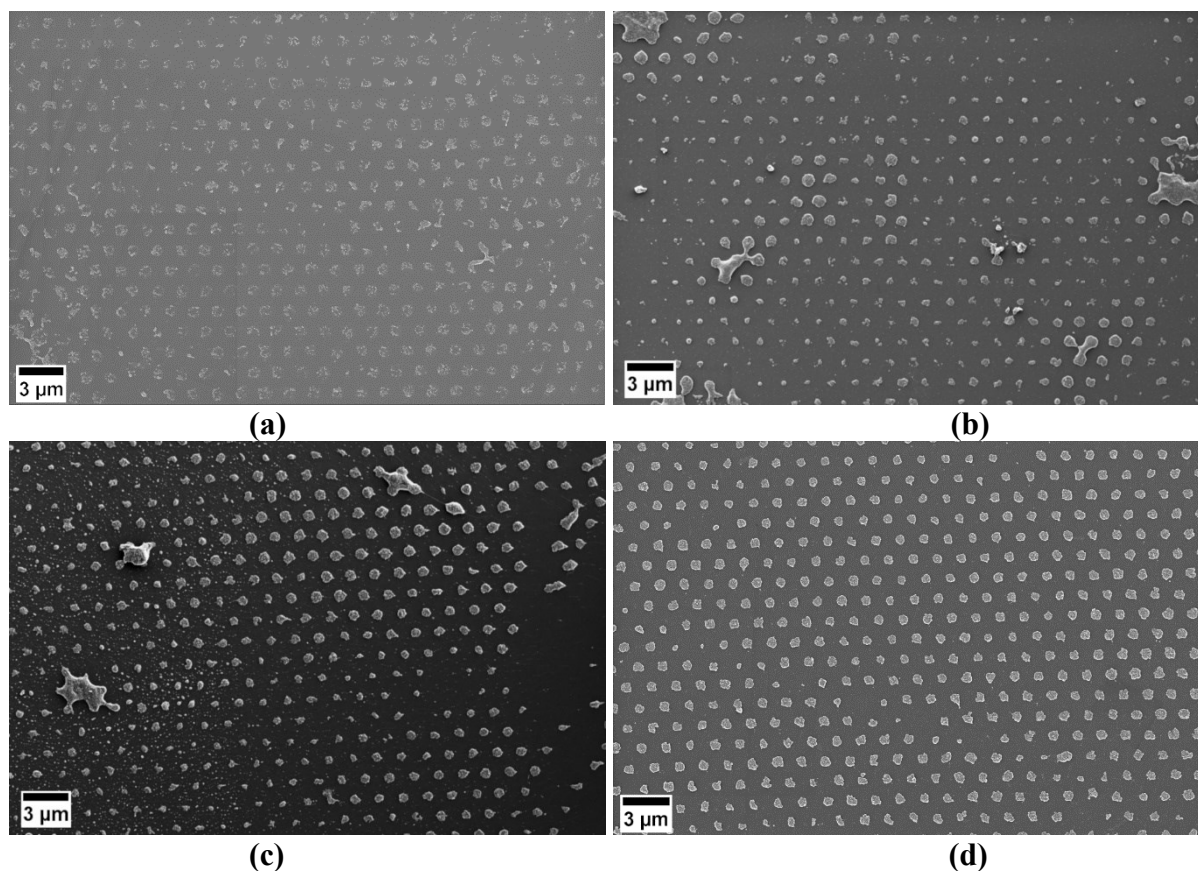


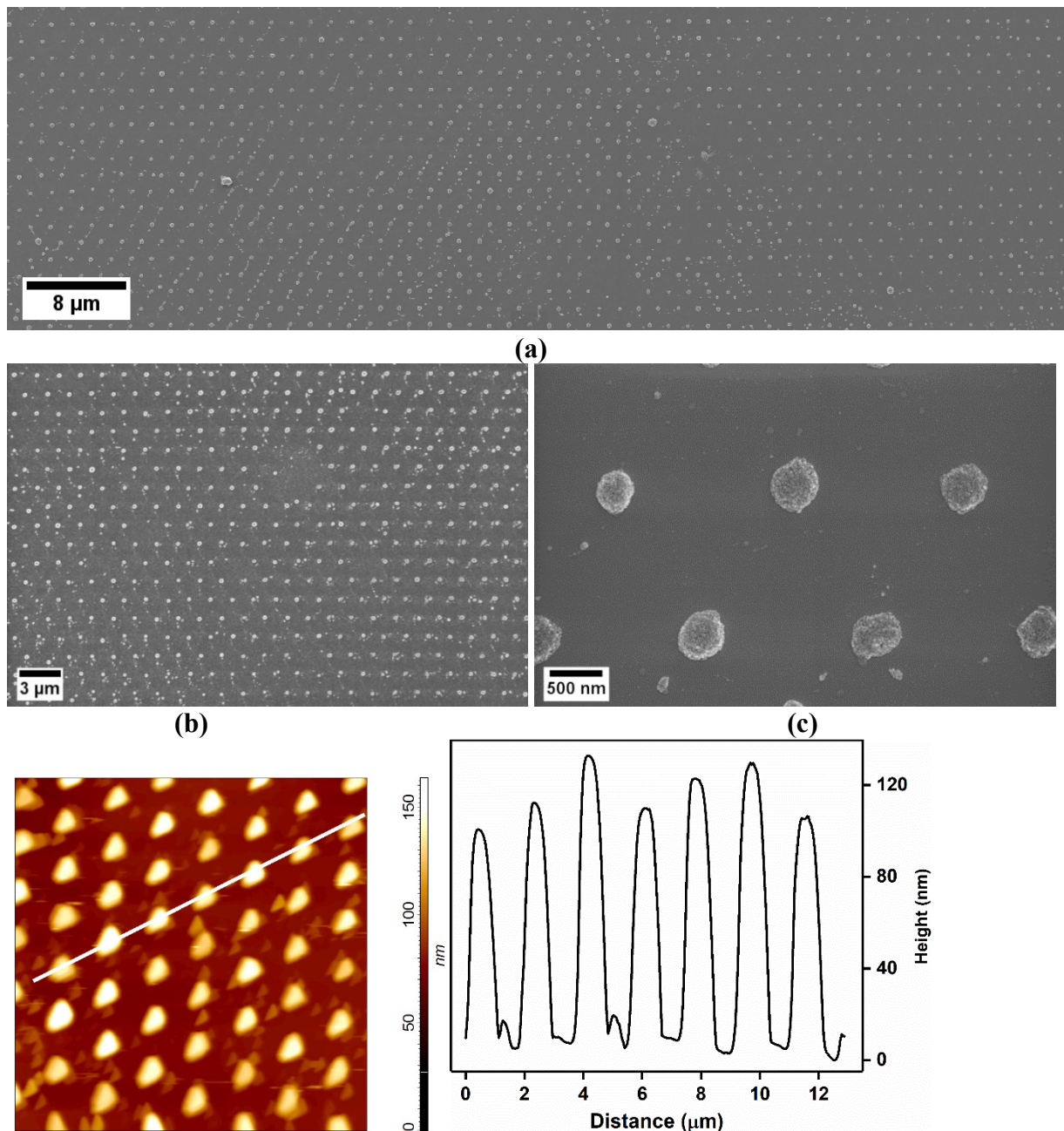
Figure 7-33 SEM images of magnetic 10nm Fe_3O_4 -Ferrofluid nanoparticle aggregates printed from an aqueous solution using setup IV with a PS-*b*-P2VP/T-ZnO composite nanoporous stamp (0.9 μm TC) at room temperature. The external magnetic field strength in **in-plane** geometry; (a) $H \approx 0.2$ T, (b) $H \approx 0.6$ T, (c) $H \approx 1.0$ T, and (d) $H \approx 1.4$ T.

7.1.5.4.2.3 Stamping by tip contact surface (TC) composite stamps

Figure 7-34a-c shows the SEM images of magnetic 10nm Fe_3O_4 -ferrofluid nanoparticle aggregates printed from an aqueous solution with PS-*b*-P2VP/T-ZnO composite nanoporous stamp (0.9 μm TC) at room temperature. The hexagonally arranged arrays of Fe_3O_4 -10nm nanoparticles aggregates have long-range order and few defects (Figure 7-34a). The order of the stamped nanoparticle aggregates can be seen from detailed magnified SEM images (Figure 7-34b-c).

The stamped nanoparticle aggregates surface topography and height profile were characterized by atomic force microscopy (AFM). Figure 7-34d-e shows an AFM image to analyze the

heights of the stamped nanoparticle aggregates. The average height of 7 evaluated 10nm Fe₃O₄ nanoparticle aggregates amounted to 115.74±12.30nm. The measurement was done by AFM using the contact mode and by extracting a line profile of the measured data (Figure 7-34e). A total of 158 stamped 10nm Fe₃O₄ ferrofluid nanoparticle aggregates in a binarized SEM image were evaluated according to the method described in section 3.1.4. The analyzed magnetic nanoparticle aggregates have a diameter of $\approx 325\pm 74$ nm, a circularity of $\approx 0.97\pm 0.038$, and an average aspect ratio of $\approx 1.05\pm 0.13$ (Figure 7-34f-h).



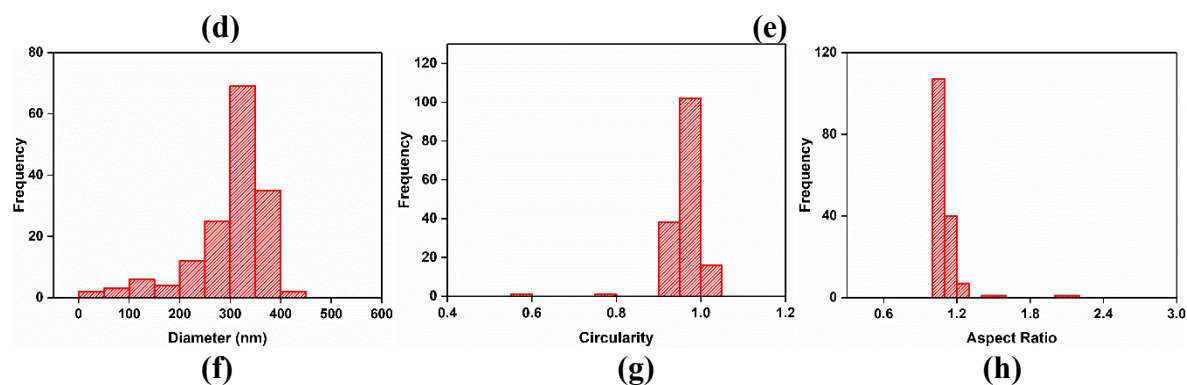


Figure 7-34 (a-c) SEM images of arrays of magnetic nanoparticle aggregates (10nm Fe_3O_4 -ferrofluid) printed from an aqueous solution by using the experimental setup IV (**in-plane** external magnetic field, $H \approx 1.4\text{T}$) with a PS-*b*-P2VP/T-ZnO composite nanoporous stamp (0.9 μm TC) at room temperature. (a) Large-area top view, and (b-c) detail top views. (d) AFM image ($12 \times 12 \mu\text{m}^2$) of stamped magnetic nanoparticle aggregates, and (e) line scan of the white line in d) showing the heights of the stamped magnetic nanoparticle aggregates. Histograms of 158 analyzed stamped magnetic nanoparticles aggregates showing (f) the diameters, (g) the circularities, and (h) the aspect ratios of the Fe_3O_4 stamped magnetic nanoparticle aggregates.

Figure 7-35a-c shows SEM images of magnetic 10nm Fe_3O_4 -ferrofluid nanoparticle aggregates printed from an aqueous solution with a PS-*b*-P2VP/T-ZnO composite nanoporous stamp (4.3 μm TC) at room temperature. The square lattice of rectangular Fe_3O_4 -10nm nanoparticle aggregates has long-range order and a limited number of defects (Figure 7-35a).

The surface topography and height profile of stamped nanoparticle aggregates were characterized using atomic force microscopy (AFM). Figure 7-35c-d shows an AFM image to analyze the heights of the stamped nanoparticle aggregates. The average height of the 7 stamped nanoparticle aggregates amounted to $164.47 \pm 28.29\text{nm}$. The measurement was done by AFM using the contact mode and extracting a line profile of the measured data (Figure 7-35d). A total of 108 stamped aggregates from Figure 7-35a in a binarized SEM image was evaluated and analyzed according to the method described in section 3.1.4. The analyzed square aggregates have an edge length of $\approx 4.1 \pm 0.23 \mu\text{m}$ and an average aspect ratio of $\approx 1.05 \pm 0.13$ (Figure 7-35e-g). The line profile along the white line in Figure 7-35a obtained by ImageJ is shown in Figure 7-35g. The side length of the stamped square arrays amounts to $\approx 4.4 \pm 0.11 \mu\text{m}$.

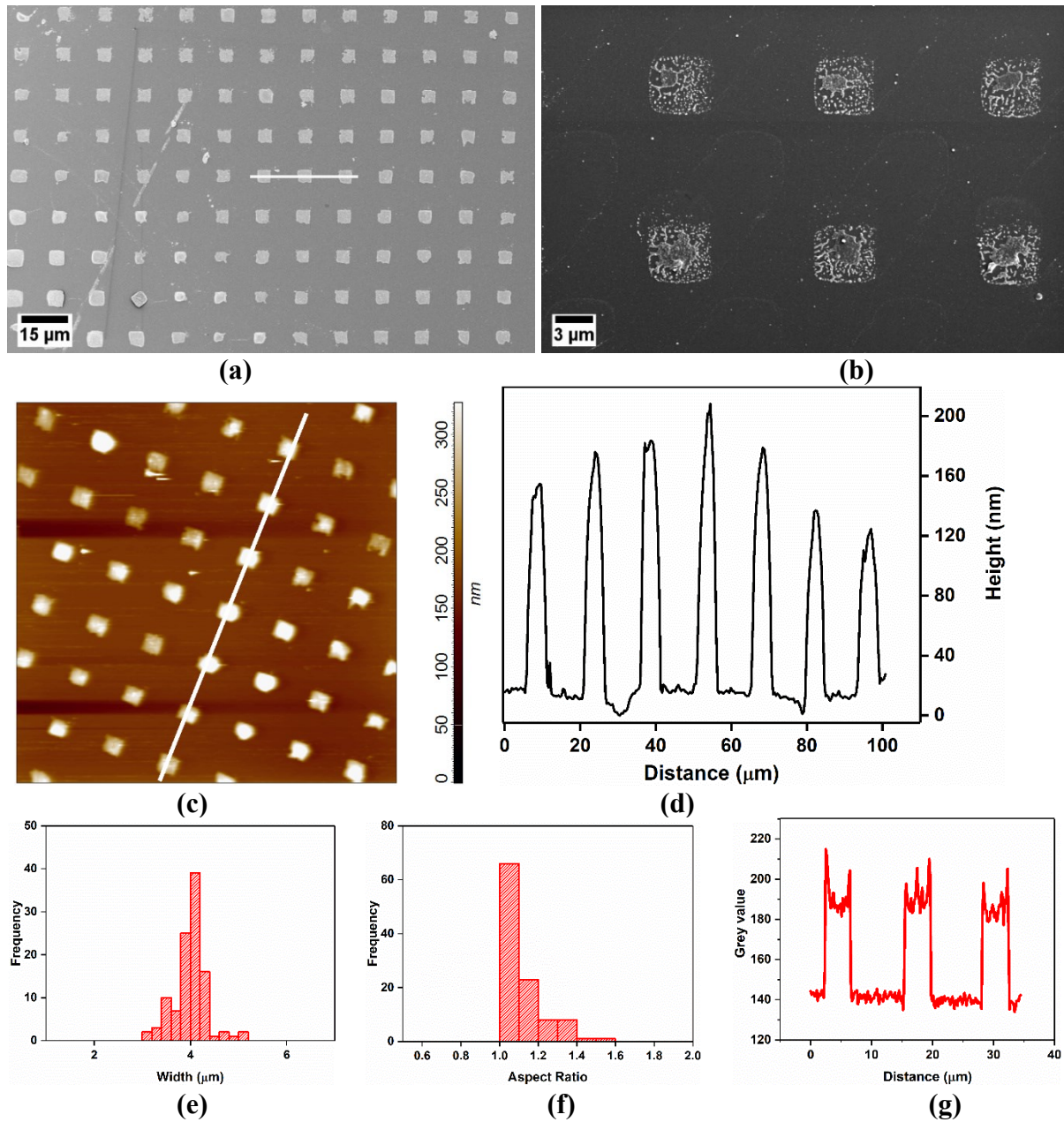


Figure 7-35 (a-b) SEM images of magnetic nanoparticle aggregates (10nm Fe_3O_4 -ferrofluid) printed from an aqueous solution by using the experimental setup IV (**in-plane** external magnetic field, $H \approx 1.4\text{T}$) with a PS-*b*-P2VP/T-ZnO composite nanoporous stamp (4.3 μm TC) at room temperature. (a) Large-area top view, and (b) detail top view. (c) AFM image ($100 \times 100 \mu\text{m}^2$) of stamped magnetic nanoparticle aggregates, and (d) line scan of the white line in c) showing the height of the stamped magnetic nanoparticle aggregates. Histograms of e) the square dot edge length and (f) the aspect ratio of 108 magnetic 10nm Fe_3O_4 -Ferrofluid nanoparticle aggregates. (g) Line profile along the white line in Figure 7-35a of the Fe_3O_4 stamped magnetic nanoparticle aggregates.

Table 7-1 and 7-2 summarize all results of (10nm Fe₃O₄-ferrofluid) magnetic nanoparticle aggregates printed from an aqueous solution using different setups.

Table 7-1 Summary of all results of magnetic nanoparticle aggregates (10nm Fe₃O₄-ferrofluid) printed from an aqueous solution. The printing results are with setup II (**out-of-plane** external magnetic field, $H \approx 0.33\text{T}$).and setup III (**out-of-plane** external magnetic field, $H \approx 0.37\text{T}$). The results for experimental setup IV are shown here with (**in-plane** external magnetic field, $H \approx 1.4\text{T}$, 10 sec exposure time).

Stamp	Printing Setup	Average diameter d , or edge side length, l	Aspect ratio, AR	Height, h of the stamped spot
PS- <i>b</i> -P2VP/T-ZnO (0.9 μm TC)	II	$d \approx 675 \pm 62 \text{ nm}$	1.1 \pm 0.19	44.80 \pm 6.58 nm
	III	$d \approx 625 \pm 59 \text{ nm}$	1.15 \pm 0.13	61.83 \pm 8.83 nm
	IV	$d \approx 325 \pm 74 \text{ nm}$	1.05 \pm 0.13	115.74 \pm 12.30 nm
PS- <i>b</i> -P2VP/T-ZnO (4.3 μm TC)	II	$l \approx 4.25 \pm 0.70 \mu\text{m}$	1.1 \pm 0.19	42.33 \pm 4.55 nm
	III	$l \approx 4.50 \pm 0.23 \mu\text{m}$	1.05 \pm 0.15	59.55 \pm 12.91nm
	IV	$l \approx 4.1 \pm 0.23 \mu\text{m}$	1.05 \pm 0.13	164.4 \pm 28.29nm

Table 7-2 Summary of all results of magnetic nanoparticle aggregates (10nm Fe₃O₄-ferrofluid) printed from an aqueous solution. The printing results are with setup II (**out-of-plane** external magnetic field, $H \approx 0.33\text{T}$).and setup III (**out-of-plane** external magnetic field, $H \approx 0.37\text{T}$).

Stamp	Printing Setup	Average diameter d , or edge side length, l	Aspect ratio, AR
PS- <i>b</i> -P2VP/T-ZnO (0.9 μm HC)	II	$d \approx 1.42 \pm 0.062 \mu\text{m}$	1.075 \pm 0.08
	III	$d \approx 1.25 \pm 0.10 \mu\text{m}$	1.12 \pm 0.08
PS- <i>b</i> -P2VP/T-ZnO (5.3 μm HC)	II	$l \approx 5.19 \pm 0.19 \mu\text{m}$	1.05 \pm 0.05
	III	$l \approx 5.25 \pm 1.02 \mu\text{m}$	1.05 \pm 0.02

8 Conclusion

In this thesis, patterning methods to fabricate various functional particle patterns were developed. Two classes of model substrates were selected; topographically patterned and smooth substrates.

For the first model system, i.e., topographically patterned substrates, direct imprinting was used to topographically pattern substrates of different materials. These topographically patterned substrates were then used to self-assemble silica (SiO_2) microparticles, which were further modified in a site-selective way for specific applications.

- Different sizes of SiO_2 microparticles were self-assembled inside the macropores of macroporous TiO_2 substrates. The wettability of $p\text{TiO}_2$ holey films changed from hydrophobic ($\theta_{WCA} \approx 108.5^\circ \pm 3.1^\circ$) to super-hydrophilic characteristics ($\theta_{WCA} \approx 0^\circ$) after deposition of SiO_2 microparticles with different diameters into the $p\text{TiO}_2$ macropores ($p\text{TiO}_2\text{-SiO}_2$). The surface chemistry of self-assembled SiO_2 microparticles inside the TiO_2 macropores was modified by three different routes to make the substrates hydrophobic: (1) adsorption of a) cycloazasilane, b) FDTS, and c) 1-dodecanethiol, (2) Au metal caps coated on the SiO_2 particles inside the TiO_2 macropores by thermal evaporation, and (3) PS-*b*-P2VP rods attached to the silica particles. All the chemical surface treatments increased the apparent water contact angles (θ_{WCA}), making the modified substrates more hydrophobic with a maximum apparent $\theta_{WCA} \approx 134.5^\circ \pm 3.4^\circ$ for $p\text{TiO}_2\text{-SiO}_2(143\text{nm})@\text{FDTS}@\text{PS-}b\text{-P2VP}$. $p\text{TiO}_2\text{-SiO}_2(143\text{nm})@\text{FDTS}@\text{PS-}b\text{-P2VP}$ is substrate fabricated by modifying $p\text{TiO}_2\text{-SiO}_2(143\text{ nm})$ template with FDTS and then PS-*b*-P2VP rods. For wettability switching from hydrophilic to hydrophobic, the infiltrated self-assembled SiO_2 particles were detached from the macropores with adhesive carbon tape, so that the native hydrophobic state is restored ($\theta_{WCA} \approx 118.5^\circ \pm 5.2^\circ$). For wettability switching from hydrophobic to hydrophilic, the transition occurred by heating the substrates to 600 °C for 30 mins. High adhesion of water droplets to the patterned TiO_2 and all modified patterned TiO_2 substrates having SiO_2 microparticles were observed for all hydrophobic states, and even upon tilting and vigorously moving substrates, the droplets remained strongly pinned. Evaporation dynamics studies of water droplets were performed on all modified surfaces, including sessile water droplet shape evolution during evaporation. For samples modified with

either cycloazasilane or with a gold metallic layer, the contact base radius remains nearly constant until a dimensionless evaporation time ($t^*=t_e/t_c$) of 0.8. In the case of samples modified with either 1-dodecanethiol on the gold film or with FDTS, the contact base radius remained nearly constant until a dimensionless evaporation time ($t^*=t_e/t_c$) of 0.6 so that the constant contact radius (CCR) mode dominated.

- In the second example of a topographically patterned surface, macroporous substrates of the block copolymers PS-*b*-P2VP and PS-*b*-P4VP were fabricated. SiO₂ microparticles were deposited inside the macroporous-nanoporous substrates for site-selective orthogonal modifications to fabricate Janus particles. The modification method was developed to selectively modify self-assembled SiO₂ microparticles inside PS-*b*-P2VP and PS-*b*-P4VP macroporous substrates with a continuous nanoporous fine structure. The top side of the embedded gold-coated SiO₂ microparticles was modified with 1-dodecanethiol, and the bottom side of the embedded SiO₂ microparticles inside the PS-*b*-P4VP macropores was modified with APTES using a home-built device. SiO₂ microparticles with a diameter of 0.755 μm inside a patterned PS-*b*-P2VP substrate were modified with ≈ a 20 nm thick gold layer on the top side and K₂Cr₂O₇ on the bottom side.
- In the third example of topographically patterned surfaces, smooth substrates were structured with hollow microrings of chitosan (C.S.), chitosan-graphene oxide (CS-GO), gold (Au), and TiO₂. Two imprinting pressures with values of ≈ 3.95 kN m⁻² and ≈ 7.87 kN m⁻² were applied to form the hollow microring patterns. For all investigated materials, the hollow microrings imprinted with a pressure of 7.87 kN m⁻² have a narrower diameter distribution with a larger diameter, and larger widths of the rims, than to microrings imprinted with a pressure of 3.95 kN m⁻². The microrings of TiO₂ were used as confinement structures for SiO₂ microparticles. The wettability of TiO₂ microrings imprinted with an imprint pressure of 7.87 kN m⁻² on a Si substrate changed from hydrophobic ($\theta_{WCA} \approx 108.6^\circ \pm 5.37^\circ$) to super-hydrophilic characteristics ($\theta_{WCA} \approx 0^\circ$) after deposition of SiO₂ microparticles with a diameter of 50 nm into the microrings.

On the second class of model substrates, i.e., smooth silanized Si substrates, magnetic nanoparticles were stamped. A capillary stamping approach combined with an external permanent magnetic field or electromagnets was realized to print magnetic nanoparticle-based inks. PS-*b*-P2VP/T-ZnO composite stamps with either tip contact surfaces (round or square-shaped) or with holey contact surfaces having round or square-shaped holes were used to stamp 10nm Fe₃O₄-ferrofluid and 5nm Fe₃O₄ magnetic nanoparticle inks. The advantages of T-ZnO layer 1 are storing aqueous inks for multicycle stamping and the possibility of supplying inks to stamp contact surfaces from the reverse side. The significant advantages of the printing method include overcoming the tedious printing of nanoparticles, the need for re-inking steps, and the simplicity of the method.

- No external force field (setup I) could not significantly result in ordered magnetic nanoparticle printing. Application of external magnetic fields (setups II, III, and IV) resulted in the formation of ordered arrays of magnetic nanoparticle aggregates by stamping. The magnetic nanoparticle aggregates were directed by placing a permanent external magnet (setup II and III) either below (**out-of-plane**) or parallel to the counter substrate (**in-plane**). The stamping quality without many defects did not improve during the **in-plane** magnetic field application. The stamped nanoparticle aggregate arrays showed an increasingly better long-range order with **out-of-plane** magnetic fields (setup II and III). The effect of the external permanent magnetic field was tested by adding additional magnets below the silanized Si substrates. The values of the magnetic field H (**out-of-plane**) amounted to $\approx 0.18\text{T}$, $\approx 0.26\text{T}$, $\approx 0.30\text{T}$, $\approx 0.33\text{T}$ for setup II and $\approx 0.20\text{T}$, $\approx 0.27\text{T}$, $\approx 0.35\text{T}$, $\approx 0.37\text{T}$ for setup III, respectively. Long-range order of stamped nanoparticle aggregate arrays without defects was realized with 0.33T (**out-of-plane**) for setup II (**out-of-plane**) and 0.37T for setup III, respectively.
- With setup IV, magnetic nanoparticle aggregates were stamped with the help of an external magnetic field generated in a vibrating sample magnetometer (VSM) at room temperature. The stamping procedure was ineffective in the **out-of-plane** geometry and did not yield precisely stamped spots, while in the **in-plane** geometry, the stamped nanoparticle aggregate arrays show increasingly better long-range order with few defects. During stamping in the **in-plane** geometry, the magnetic field exposure time was varied with a magnetic field strength value of 1.4T at room

temperature. In the **in-plane** geometry under different magnetic field H exposure times for 10 s, 40 s, 70 s, 100 s, 180 s, 300 s, and 600 s, the best reproducibility was achieved with a magnetic field H exposure time of 10s. To test the effect of the external magnetic field strength, the printing of magnetic nanoparticle aggregates was done with H values of 0.2T, 0.6T, 1.0T, and 1.4T at room temperature in the **in-plane** geometry with a magnetic field H exposure time for 10 s. High-quality arrays of magnetic nanoparticle aggregates were achieved by applying a magnetic field of 1.4T.

- For stamping with PS-*b*-P2VP/T-ZnO (0.9 μm tip contact surfaces) composite stamps, the lowermost average diameter d of magnetic nanoparticle aggregates stamped (10nm Fe_3O_4 -ferrofluid) amounted to $\approx 325\pm 74$ nm, and a height of 115.74 ± 12.30 nm was obtained by using setup IV (**in-plane** external magnetic field, $H \approx 1.4\text{T}$, 10 sec exposure time) over the larger surface area.

9 References

- [1] N. Mitin, A. Pikulin, Interference surface patterning using colloidal particle lens arrays, *Optics Letters*, 45 (2020) 6134-6137.
- [2] S.M. Yang, S.G. Jang, D.G. Choi, S. Kim, H.K. Yu, Nanomachining by colloidal lithography, *Small*, 2 (2006) 458-475.
- [3] Y. Yin, Y. Lu, B. Gates, Y. Xia, Template-assisted self-assembly: a practical route to complex aggregates of monodispersed colloids with well-defined sizes, shapes, and structures, *J. Am. Chem. Soc.*, 123 (2001) 8718-8729.
- [4] J. Huang, A.R. Tao, S. Connor, R. He, P. Yang, A general method for assembling single colloidal particle lines, *Nano letters*, 6 (2006) 524-529.
- [5] H. Zheng, Y. Zhou, C.F. Ugwu, A. Du, I.I. Kravchenko, J.G. Valentine, Large-Scale Metasurfaces Based on Grayscale Nanosphere Lithography, *ACS Photonics*, (2021).
- [6] B.H. Lee, H. Shin, M.M. Sung, Patterning a two-dimensional colloidal crystal by water-mediated particle transfer printing, *Chemistry of Materials*, 19 (2007) 5553-5556.
- [7] M. Schmidt, M. Philippi, M. Münzner, J.M. Stangl, R. Wieczorek, W. Harneit, K. Müller-Buschbaum, D. Enke, M. Steinhart, Capillary nanostamping with spongy mesoporous silica stamps, *Advanced Functional Materials*, 28 (2018) 1800700.
- [8] R. Abbel, E.R. Meinders, *Printing Technologies for Nanomaterials*, Wiley-VCH Verlag GmbH & Co. KGaA2017.
- [9] S.M. Yang, G.A. Ozin, Opal chips: Vectorial growth of colloidal crystal patterns inside silicon wafers, *Chemical Communications*, Royal Society of Chemistry, 2000, pp. 2507-2508.
- [10] D. Xia, A. Biswas, D. Li, S.R.J. Brueck, Directed self-assembly of silica nanoparticles into nanometer-scale patterned surfaces using spin-coating, *Advanced Materials*, Wiley-VCH Verlag, 2004, pp. 1427-1432.
- [11] R. van Dommelen, P. Fanzio, L. Sasso, Surface self-assembly of colloidal crystals for micro- and nano-patterning, *Advances in Colloid and Interface Science*, Elsevier B.V., 2018, pp. 97-114.
- [12] P. Liu, J. Peng, Y. Chen, M. Liu, W. Tang, Z.-H. Guo, K. Yue, A general and robust strategy for in-situ templated synthesis of patterned inorganic nanoparticle assemblies, *Giant*, 8 (2021) 100076.
- [13] Y. Lu, Y. Yin, Y. Xia, Self-assembly approach to the fabrication of patterned, two-dimensional arrays of microlenses of organic polymers, *Advanced Materials*, John Wiley & Sons, Ltd, 2001, pp. 34-37.
- [14] M. Asbahi, F. Wang, Z. Dong, J.K.W. Yang, K.S.L. Chong, Directed self-assembly of sub-10 nm particle clusters using topographical templates, *Nanotechnology*, 2016.
- [15] N.J. Wittenberg, T.W. Johnson, L.R. Jordan, X. Xu, A.E. Warrington, M. Rodriguez, S.H. Oh, Formation of biomembrane microarrays with a squeegee-based assembly method, *Journal of Visualized Experiments*, J Vis Exp, 2014.
- [16] E. Miele, S. Raj, Z. Baraissov, P. Král, U. Mirsaidov, Dynamics of Templated Assembly of Nanoparticle Filaments within Nanochannels, *Advanced Materials*, Wiley-VCH Verlag, 2017.
- [17] J. Cui, Y. Li, H. Yuan, N. Gao, K. Feng, W. Li, K. Zhou, X. Yin, G. Li, Gram-scale fabrication of patchy nanoparticles with tunable spatial topology and chemical functionality, *Nano Research*, (2021) 1-7.

- [18] X. Fan, J. Yang, X.J. Loh, Z. Li, Polymeric janus nanoparticles: recent advances in synthetic strategies, materials properties, and applications, *Macromolecular rapid communications*, 40 (2019) 1800203.
- [19] Y. Liu, T. Xiao, C. Bao, Y. Fu, X. Yang, Fabrication of novel Janus membrane by nonsolvent thermally induced phase separation (NTIPS) for enhanced performance in membrane distillation, *Journal of membrane science*, 563 (2018) 298-308.
- [20] E. Poggi, J.-P. Bourgeois, B. Ernoult, J.-F. Gohy, Polymeric Janus nanoparticles templated by block copolymer thin films, *RSC Advances*, 5 (2015) 44218-44221.
- [21] H. Wu, W. Yi, Z. Chen, H. Wang, Q. Du, Janus graphene oxide nanosheets prepared via Pickering emulsion template, *Carbon*, 93 (2015) 473-483.
- [22] D. Liu, R. Aleisa, Z. Cai, Y. Li, Y. Yin, Self-assembly of superstructures at all scales, *Matter*, 4 (2021) 927-941.
- [23] Y. Zhu, F. Sun, H. Qian, H. Wang, L. Mu, J. Zhu, A biomimetic spherical cactus superhydrophobic coating with durable and multiple anti-corrosion effects, *Chemical Engineering Journal*, Elsevier B.V., 2018, pp. 670-679.
- [24] S.G. Ullattil, P. Periyat, Sol-gel synthesis of titanium dioxide, *Sol-Gel Materials for Energy, Environment and Electronic Applications*, Springer 2017, pp. 271-283.
- [25] Z. Duan, Y. Zhao, Y. Ren, J. Jia, L. Ma, J. Cui, Y. Wang, G. Zhao, Facile micro-patterning of ferromagnetic CoFe₂O₄ films using a combined approach of sol-gel method and UV irradiation, *Ceramics International*, 45 (2019) 369-377.
- [26] D. Lv, L. Sheng, J. Wan, J. Dong, H. Ouyang, H. Jiao, J. Liu, Bioinspired hierarchically hairy particles for robust superhydrophobic coatings: Via a droplet dynamic template method, *Polymer Chemistry*, Royal Society of Chemistry, 2019, pp. 331-335.
- [27] X. Yun, Z. Xiong, Y. He, X. Wang, Superhydrophobic lotus-leaf-like surface made from reduced graphene oxide through soft-lithographic duplication, *RSC Advances*, Royal Society of Chemistry, 2020, pp. 5478-5486.
- [28] Y. Yang, H. He, Y. Li, J. Qiu, Using Nanoimprint Lithography to Create Robust, Buoyant, Superhydrophobic PVB/SiO₂ Coatings on wood Surfaces Inspired by Red roses petal, *Scientific Reports*, Nature Publishing Group, 2019, pp. 1-9.
- [29] B. Radha, S.H. Lim, M.S.M. Saifullah, G.U. Kulkarni, Metal hierarchical patterning by direct nanoimprint lithography, *Scientific Reports*, Nature Publishing Group, 2013, pp. 1-8.
- [30] P. Ma, Z. Xu, M. Wang, L. Lu, M. Yin, X. Chen, D. Li, W. Ren, Fast fabrication of TiO₂ hard stamps for nanoimprint lithography, *Materials Research Bulletin*, Elsevier Ltd, 2017, pp. 253-259.
- [31] K.I. Nakamatsu, S. Matsui, Nanoimprinting using liquid-phase hydrogen silsesquioxane, *Japanese Journal of Applied Physics, Part 2: Letters*, IOP Publishing, 2006, pp. L546.
- [32] J. Zhu, Y. Tian, X. Liu, C. Yang, Lithography-induced hydrophobic surfaces of silicon wafers with excellent anisotropic wetting properties, *Microsystem Technologies*, Springer Verlag, 2019, pp. 735-745.
- [33] L. Zhang, N. Zhao, J. Xu, Fabrication and application of superhydrophilic surfaces: A review, *Journal of Adhesion Science and Technology*, Taylor & Francis, 2014, pp. 769-790.
- [34] J. Willmann, D. Stocker, E. Dörsam, Characteristics and evaluation criteria of substrate-based manufacturing. Is roll-to-roll the best solution for printed electronics?, *Organic Electronics*, 15 (2014) 1631-1640.
- [35] A. Carlson, A.M. Bowen, Y. Huang, R.G. Nuzzo, J.A. Rogers, Transfer printing techniques for materials assembly and micro/nanodevice fabrication, *Advanced Materials*, 24 (2012) 5284-5318.
- [36] Y. Feng, X. Liu, K. Li, F. Gong, J. Shen, Y. Lou, Glass Flow Evolution and the Mechanism of Antireflective Nanoprotrusion Arrays in Nanoholes by Direct Thermal Imprinting, *ACS Applied Materials & Interfaces*, 13 (2021) 16968-16977.

- [37] H. Choi, P.T. Nguyen, C.V. Tran, J.B. In, Micro-patterned metal current collectors for high aspect ratio flexible graphene supercapacitors, *Applied Surface Science*, Elsevier B.V., 2020, pp. 145432.
- [38] N. Sitpathom, T. Muangnapoh, J.M. Dawes, Opal-templated films for optical strain sensing, *Optics Express*, The Optical Society, 2020, pp. 16280.
- [39] R. Lou, G. Zhang, G. Li, X. Li, Q. Liu, G. Cheng, Design and fabrication of dual-scale broadband antireflective structures on metal surfaces by using nanosecond and femtosecond lasers, *Micromachines*, MDPI AG, 2020, pp. 20.
- [40] J. Zhan, H. Xu, Y. Zhong, Q. Wu, Z. Liu, Surface modification of patterned electrospun nanofibrous films via the adhesion of DOPA-bFGF and DOPA-ponericin G1 for skin wound healing, *Materials and Design*, Elsevier Ltd, 2020, pp. 108432.
- [41] W. Liu, R. Pan, M. Cai, X. Luo, C. Chen, G. Jiang, X. Hu, H. Zhang, M. Zhong, Oil-triggered switchable wettability on patterned alternating air/lubricant-infused superamphiphobic surfaces, *Journal of Materials Chemistry A*, Royal Society of Chemistry, 2020, pp. 6647-6660.
- [42] M. Geissler, Y. Xia, Patterning: Principles and some new developments, *Advanced Materials*, 16 (2004) 1249-1269.
- [43] Y. Xia, B. Gates, Y. Yin, Building complex structures from monodisperse spherical colloids, *Australian Journal of Chemistry*, CSIRO PUBLISHING, 2001, pp. 287-290.
- [44] C. Stelling, A. Mark, G. Papastavrou, M. Retsch, Showing particles their place: Deterministic colloid immobilization by gold nanomeshes, *Nanoscale*, Royal Society of Chemistry, 2016, pp. 14556-14564.
- [45] M. Fujita, O. Koike, Y. Yamaguchi, Direct simulation of drying colloidal suspension on substrate using immersed free surface model, *Journal of Computational Physics*, 281 (2015) 421-448.
- [46] G.S. Lazarov, N.D. Denkov, O.D. Velev, P.A. Kralchevsky, K. Nagayama, Formation of two-dimensional structures from colloidal particles on fluorinated oil substrate, *Journal of the Chemical Society, Faraday Transactions*, 90 (1994) 2077-2083.
- [47] R. van Dommelen, P. Fanzio, L. Sasso, Surface self-assembly of colloidal crystals for micro-and nano-patterning, *Advances in colloid and interface science*, 251 (2018) 97-114.
- [48] R. Bhardwaj, X. Fang, P. Somasundaran, D. Attinger, Self-assembly of colloidal particles from evaporating droplets: role of DLVO interactions and proposition of a phase diagram, *Langmuir*, 26 (2010) 7833-7842.
- [49] Z. Li, Z. Guo, Bioinspired surfaces with wettability for antifouling application, *Nanoscale*, Royal Society of Chemistry, 2019, pp. 22636-22663.
- [50] M. Shirazi, S. Kord, Y. Tamsilian, Novel smart water-based titania nanofluid for enhanced oil recovery, *Journal of Molecular Liquids*, Elsevier B.V., 2019, pp. 112064.
- [51] E.B. Caldon, J.M.C. Albayalde, A.M.P. Aglosolos, K.S. Bautista, M.D. Tavora, S.A.P. Cabalza, J.R.O. Diaz, M.D. Mulato, Titania-Containing Recycled Polypropylene Surfaces with Photo-Induced Reversible Switching Wettability, *Journal of Polymers and the Environment*, Springer New York LLC, 2019, pp. 1564-1571.
- [52] W. Barthlott, C. Neinhuis, Purity of the sacred lotus, or escape from contamination in biological surfaces, *Planta*, Springer, 1997, pp. 1-8.
- [53] A. Otten, S. Herminghaus, How Plants Keep Dry: A Physicist's Point of View, *Langmuir*, American Chemical Society, 2004, pp. 2405-2408.
- [54] K. Koch, I.C. Blecher, G. König, S. Kehraus, W. Barthlott, The superhydrophilic and superoleophilic leaf surface of *Ruellia devosiana* (Acanthaceae): a biological model for spreading of water and oil on surfaces, *Functional Plant Biology*, CSIRO, 2009, pp. 339.
- [55] C. Neinhuis, W. Barthlott, Characterization and distribution of water-repellent, self-cleaning plant surfaces, *Annals of Botany*, Oxford University Press, 1997, pp. 667-677.

- [56] L. Feng, S. Li, H. Li, J. Zhai, Y. Song, L. Jiang, D. Zhu, Super-hydrophobic surface of aligned polyacrylonitrile nanofibers, *Angewandte Chemie - International Edition*, John Wiley & Sons, Ltd, 2002, pp. 1221-1223.
- [57] C. Guo, L. Feng, J. Zhai, G. Wang, Y. Song, L. Jiang, D. Zhu, Large-area fabrication of a nanostructure-induced hydrophobic surface from a hydrophilic polymer, *ChemPhysChem*, Wiley-VCH Verlag, 2004, pp. 750-753.
- [58] Y. Wang, S. Vitas, I. Burgert, E. Cabane, Beech wood cross sections as natural templates to fabricate superhydrophobic surfaces, *Wood Science and Technology*, Springer Verlag, 2019, pp. 985-999.
- [59] M. Ghasemlou, F. Daver, E.P. Ivanova, B. Adhikari, Bio-inspired sustainable and durable superhydrophobic materials: From nature to market, *Journal of Materials Chemistry A*, Royal Society of Chemistry, 2019, pp. 16643-16670.
- [60] M. Yi, L. Liu, L. Wu, X. Li, Research on sliding angles of water droplets on the hierarchical structured superhydrophobic surfaces, *Applied Physics A: Materials Science and Processing*, Springer, 2020, pp. 1-9.
- [61] T.L. Liu, C.-J.C. Kim, Contact Angle Measurement of Small Capillary Length Liquid in Super-repelled State, *Scientific reports*, 7 (2017) 740.
- [62] D. Bonn, J. Eggers, J. Indekeu, J. Meunier, Wetting and spreading, *Reviews of Modern Physics*, American Physical Society, 2009, pp. 739-805.
- [63] D.H. Everett, Manual of symbols and terminology for physicochemical quantities and units, appendix II: Definitions, terminology and symbols in colloid and surface chemistry, *Pure and Applied Chemistry*, 31 (1972) 577-638.
- [64] L. Leger, *Spreading of Liquids on Solid Surfaces*, Springer, Boston, MA, 1988, pp. 721-740.
- [65] F. Brochard-Wyart, J.M. de Gennes, D. Quéré, P.G. de Gennes, Spreading of Nonvolatile Liquids in a Continuum Picture, *Langmuir*, Academic Press, 1991, pp. 335-338.
- [66] T. Young, III. An essay on the cohesion of fluids, *Philosophical Transactions of the Royal Society of London*, The Royal Society, 1805, pp. 65-87.
- [67] A. Alizadeh Pahlavan, L. Cueto-Felgueroso, G.H. McKinley, R. Juanes, Thin Films in Partial Wetting: Internal Selection of Contact-Line Dynamics, *Physical Review Letters*, American Physical Society, 2015, pp. 034502.
- [68] R.N. Wenzel, Resistance of solid surfaces to wetting by water, *Industrial and Engineering Chemistry*, American Chemical Society, 1936, pp. 988-994.
- [69] A.B.D. Cassie, S. Baxter, Wettability of porous surfaces, *Transactions of the Faraday Society*, The Royal Society of Chemistry, 1944, pp. 546-551.
- [70] A. Giacomello, S. Meloni, M. Chinappi, C.M. Casciola, Cassie-baxter and wenzel states on a nanostructured surface: Phase diagram, metastabilities, and transition mechanism by atomistic free energy calculations, *Langmuir*, American Chemical Society, 2012, pp. 10764-10772.
- [71] R. Raj, S. Adera, R. Enright, E.N. Wang, High-resolution liquid patterns via three-dimensional droplet shape control, *Nature communications*, 5 (2014) 1-8.
- [72] A. Rudawska, Assessment of surface preparation for the bonding/adhesive technology, *Surface Treatment in Bonding Technology*; Elsevier: Amsterdam, The Netherlands, (2019) 227-275.
- [73] L. Gao, T.J. McCarthy, How Wenzel and Cassie were wrong, *Langmuir*, American Chemical Society, 2007, pp. 3762-3765.
- [74] F.E. Bartell, J.W. Shepard, Surface roughness as related to hysteresis of contact angles. II. The systems paraffin-3 molar calcium chloride solution-air and paraffin-glycerol-air, *Journal of Physical Chemistry*, American Chemical Society, 1953, pp. 455-458.

- [75] C. Extrand, Contact angles and hysteresis on surfaces with chemically heterogeneous islands, *Langmuir*, 19 (2003) 3793-3796.
- [76] C. Jothi Prakash, R. Prasanth, Approaches to design a surface with tunable wettability: a review on surface properties, *Journal of Materials Science*, 56 (2021) 108-135.
- [77] Z. Yang, X. Liu, Y. Tian, Hybrid Laser Ablation and Chemical Modification for Fast Fabrication of Bio-inspired Super-hydrophobic Surface with Excellent Self-cleaning, Stability and Corrosion Resistance, *Journal of Bionic Engineering*, Springer, 2019, pp. 13-26.
- [78] R. Fürstner, W. Barthlott, C. Neinhuis, P. Walzel, Wetting and self-cleaning properties of artificial superhydrophobic surfaces, *Langmuir*, American Chemical Society 2005, pp. 956-961.
- [79] C.H. Xue, Q.Q. Fan, X.J. Guo, Q.F. An, S.T. Jia, Fabrication of superhydrophobic cotton fabrics by grafting of POSS-based polymers on fibers, *Applied Surface Science*, Elsevier B.V., 2019, pp. 241-248.
- [80] Y. Cai, D. Chen, N. Li, Q. Xu, H. Li, J. He, J. Lu, A smart membrane with antifouling capability and switchable oil wettability for high-efficiency oil/water emulsions separation, *Journal of Membrane Science*, Elsevier B.V., 2018, pp. 69-77.
- [81] T. Lv, Z. Cheng, E. Zhang, H. Kang, Y. Liu, L. Jiang, Self-Restoration of Superhydrophobicity on Shape Memory Polymer Arrays with Both Crushed Microstructure and Damaged Surface Chemistry, *Small*, Wiley-VCH Verlag, 2017, pp. 1503402.
- [82] H. Gao, Y. Liu, S. Li, G. Wang, Z. Han, L. Ren, A biomimetic surface with switchable contact angle and adhesion for transfer and storage of microdroplets, *Nanoscale*, Royal Society of Chemistry, 2018, pp. 15393-15401.
- [83] H. Gao, Y. Liu, G. Wang, S. Li, Z. Han, L. Ren, Switchable Wettability Surface with Chemical Stability and Antifouling Properties for Controllable Oil-Water Separation, *Langmuir*, American Chemical Society, 2019, pp. 4498-4508.
- [84] R. Wang, K. Hashimoto, A. Fujishima, M. Chikuni, E. Kojima, A. Kitamura, M. Shimohigoshi, T. Watanabe, Light-induced amphiphilic surfaces [4], *Nature*, Nature Publishing Group, 1997, pp. 431-432.
- [85] R. Wang, K. Hashimoto, A. Fujishima, M. Chikuni, E. Kojima, A. Kitamura, M. Shimohigoshi, T. Watanabe, Photogeneration of highly amphiphilic TiO₂ surfaces, *Advanced Materials*, John Wiley & Sons, Ltd, 1998, pp. 135-138.
- [86] M. Miyauchi, A. Nakajima, T. Watanabe, K. Hashimoto, Photocatalysis and photoinduced hydrophilicity of various metal oxide thin films, *Chemistry of Materials*, American Chemical Society, 2002, pp. 2812-2816.
- [87] D. Fattakhova-Rohlfing, A. Zaleska, T. Bein, Three-dimensional titanium dioxide nanomaterials, *Chemical Reviews*, 2014, pp. 9487-9558.
- [88] T. Shibata, N. Sakai, K. Fukuda, Y. Ebina, T. Sasaki, Structural study of photoinduced hydrophilicity of titania nanosheet film, *Materials Science and Engineering: B*, Elsevier, 2009, pp. 12-15.
- [89] S. Banerjee, D.D. Dionysiou, S.C. Pillai, Self-cleaning applications of TiO₂ by photo-induced hydrophilicity and photocatalysis, *Applied Catalysis B: Environmental*, Elsevier, 2015, pp. 396-428.
- [90] J. Wang, B. Mao, J.L. Gole, C. Burda, Visible-light-driven reversible and switchable hydrophobic to hydrophilic nitrogen-doped titania surfaces: correlation with photocatalysis, *Nanoscale*, Royal Society of Chemistry, 2010, pp. 2257.
- [91] J.L. Garcia-Cordero, Z.H. Fan, Sessile droplets for chemical and biological assays, *Lab on a Chip*, 17 (2017) 2150-2166.
- [92] D. Brutin, V. Starov, Recent advances in droplet wetting and evaporation, *Chem. Soc. Rev.*, 47 (2018) 558-585.

- [93] M.N. MacGregor-Ramiasa, K. Vasilev, Questions and Answers on the Wettability of Nano-Engineered Surfaces, *Adv. Mater. Interfaces*, 4 (2017) 1700381.
- [94] Y.X. Zuo, L.Z. Zheng, C. Zhao, H. Liu, Micro-/Nanostructured Interface for Liquid Manipulation and Its Applications, *Small*, 16 (2020) 1903849.
- [95] S. Zhou, L. Jiang, Z.C. Dong, Bioinspired Surface with Superwettability for Controllable Liquid Dynamics, *Adv. Mater. Interfaces*, 8 (2021) 2000824.
- [96] D. Quéré, Wetting and roughness, *Annu. Rev. Mater. Res.*, 38 (2008) 71-99.
- [97] R.J. Archer, B. Becher-Nienhaus, G.J. Dunderdale, A. Hozumi, Recent Progress and Future Directions of Multifunctional (Super)Wetting Smooth/Structured Surfaces and Coatings, *Adv. Funct. Mater.*, 30 (2020) 1907772.
- [98] M.N. Valipour, F.C. Birjandi, J. Sargolzaei, Super-non-wettable surfaces: A review, *Colloids Surf. A: Physicochem. Eng. Asp.*, 448 (2014) 93-106.
- [99] D.Y. Zang, S. Tarafdar, Y.Y. Tarasevich, M.D. Choudhury, T. Dutta, Evaporation of a Droplet: From physics to applications, *Phys. Rep.*, 804 (2019) 1-56.
- [100] R.G. Picknett, R. Bexon, Evaporation of Sessile or Pendant Drops in Still Air, *J. Coll. Interf. Sci.*, 61 (1977) 336-350.
- [101] R.D. Deegan, O. Bakajin, T.F. Dupont, G. Huber, S.R. Nagel, T.A. Witten, Capillary flow as the cause of ring stains from dried liquid drops, *Nature*, 389 (1997) 827-829.
- [102] J.Z. Sun, M.X. Kuang, Y.L. Song, Control and Application of "Coffee Ring" Effect in Inkjet Printing, *Prog. Chem.*, 27 (2015) 979-985.
- [103] D. Mampallil, H.B. Eral, A review on suppression and utilization of the coffee-ring effect, *Adv. Colloid Interface Sci.*, 252 (2018) 38-54.
- [104] M.E.R. Shanahan, Simple Theory of Stick-Slip Wetting Hysteresis, *Langmuir*, 11 (1995) 1041-1043.
- [105] B.Y. Xiong, J.J. Li, C.Q. He, X.Q. Tang, Z.Z. Lv, X.F. Li, X.Q. Yan, Effect of pore morphology and surface roughness on wettability of porous titania films, *Materials Research Express*, 7 (2020).
- [106] T. Adachi, S.S. Latthe, S.W. Gosavi, N. Roy, N. Suzuki, H. Ikari, K. Kato, K.-I. Katsumata, K. Nakata, M. Furudate, T. Inoue, T. Kondo, M. Yuasa, A. Fujishima, C. Terashima, Photocatalytic, superhydrophilic, self-cleaning TiO₂ coating on cheap, lightweight, flexible polycarbonate substrates, *Applied Surface Science*, 458 (2018) 917-923.
- [107] X. Zhou, S. Yu, J. Zang, Z. Lv, E. Liu, Y. Zhao, Colorful nanostructured TiO₂ film with superhydrophobic–superhydrophilic switchable wettability and anti-fouling property, *Journal of Alloys and Compounds*, Elsevier Ltd, 2019, pp. 257-266.
- [108] Y. Pan, W. Kong, B. Bhushan, X. Zhao, Rapid, ultraviolet-induced, reversibly switchable wettability of superhydrophobic/superhydrophilic surfaces, *Beilstein Journal of Nanotechnology*, Beilstein-Institut Zur Forderung der Chemischen Wissenschaften, 2019, pp. 866-873.
- [109] T. Kobayashi, S. Konishi, Acceleration of wettability switching on TiO₂ thin films under ultraviolet irradiation and direct current bias voltage, *Surface and Coatings Technology*, Elsevier B.V., 2019, pp. 80-86.
- [110] H. Kang, H. Lai, Z. Cheng, Y. Liu, L. Jiang, Restoration of superwetting switching on TiO₂ coated shape memory polymer arrays, *Chemical Engineering Journal*, Elsevier B.V., 2020, pp. 124996.
- [111] W.J. Hong, M. Kang, The super-hydrophilicities of Bi-TiO₂, V-TiO₂, and Bi-V-TiO₂ nano-sized particles and their benzene photodecompositions with H₂O addition, *Materials Letters*, North-Holland, 2006, pp. 1296-1305.
- [112] W.Y. Gan, S.W. Lam, K. Chiang, R. Amal, H. Zhao, M.P. Brungs, Novel TiO₂ thin film with non-UV activated superwetting and antifogging behaviours, *Journal of Materials Chemistry*, 17 (2007) 952-954.

- [113] V. Zorba, X. Chen, S.S. Mao, Superhydrophilic TiO₂ surface without photocatalytic activation, *Applied Physics Letters*, American Institute of Physics AIP, 2010, pp. 093702.
- [114] W.Y. Gan, S.W. Lam, K. Chiang, R. Amal, H. Zhao, M.P. Brungs, Novel TiO₂ thin film with non-UV activated superwetting and antifogging behaviours, *Journal of Materials Chemistry*, The Royal Society of Chemistry, 2007, pp. 952-954.
- [115] H. Su, C.-A.H. Price, L. Jing, Q. Tian, J. Liu, K. Qian, Janus particles: design, preparation, and biomedical applications, *Materials today bio*, 4 (2019) 100033.
- [116] Y. Li, S. Chen, S. Demirci, S. Qin, Z. Xu, E. Olson, F. Liu, D. Palm, X. Yong, S. Jiang, Morphology evolution of Janus dumbbell nanoparticles in seeded emulsion polymerization, *Journal of colloid and interface science*, 543 (2019) 34-42.
- [117] Y. Nonomura, S. Komura, K. Tsujii, Adsorption of disk-shaped Janus beads at liquid-liquid interfaces, *Langmuir*, 20 (2004) 11821-11823.
- [118] D. Kilinc, A. Lesniak, S.A. Rashdan, D. Gandhi, A. Blasiak, P.C. Fannin, A. Von Kriegsheim, W. Kolch, G.U. Lee, Mechanochemical Stimulation of MCF7 Cells with Rod-Shaped Fe-Au Janus Particles Induces Cell Death Through Paradoxical Hyperactivation of ERK, *Advanced healthcare materials*, 4 (2015) 395-404.
- [119] H. Zhao, F. Liang, X. Qu, Q. Wang, Z. Yang, Conelike Janus composite particles, *Macromolecules*, 48 (2015) 700-706.
- [120] M. Feyen, C. Weidenthaler, F. Schüth, A.-H. Lu, Regioselectively controlled synthesis of colloidal mushroom nanostructures and their hollow derivatives, *J. Am. Chem. Soc.*, 132 (2010) 6791-6799.
- [121] J.-B. Fan, H. Liu, Y. Song, Z. Luo, Z. Lu, S. Wang, Janus particles synthesis by emulsion interfacial polymerization: Polystyrene as seed or beyond?, *Macromolecules*, 51 (2018) 1591-1597.
- [122] L. Tian, B. Li, X. Li, Q. Zhang, Janus dimers from tunable phase separation and reactivity ratios, *Polymer Chemistry*, 11 (2020) 4639-4646.
- [123] G.I. Dar, M.Z. Iqbal, Multifunctional biocompatible Janus nanostructures for biomedical applications, *Current Opinion in Biomedical Engineering*, 10 (2019) 79-88.
- [124] B. Wang, B. Li, B. Zhao, C.Y. Li, Amphiphilic Janus gold nanoparticles via combining "solid-state grafting-to" and "grafting-from" methods, *J. Am. Chem. Soc.*, 130 (2008) 11594-11595.
- [125] L. Hong, S. Jiang, S. Granick, Simple method to produce Janus colloidal particles in large quantity, *Langmuir*, 22 (2006) 9495-9499.
- [126] J.S.J. Tan, C.H. Wong, Z. Chen, Janus Particle Preparation through UV-Induced Partial Photodegradation of Spin-Coated Particle Films, *Langmuir*, 37 (2021) 8167-8176.
- [127] L. Cheng, G. Hou, J. Miao, D. Chen, M. Jiang, L. Zhu, Efficient synthesis of unimolecular polymeric Janus nanoparticles and their unique self-assembly behavior in a common solvent, *Macromolecules*, 41 (2008) 8159-8166.
- [128] W. Zhang, J. He, H. Bao, X. Dong, Polymeric Janus nanoparticles from triblock terpolymer micellar dimers, *RSC advances*, 5 (2015) 104223-104227.
- [129] J.-R. Li, G.C. Henry, J.C. Garno, Fabrication of nanopatterned films of bovine serum albumin and staphylococcal protein A using latex particle lithography, *Analyst*, 131 (2006) 244-250.
- [130] M. Bayati, P. Patoka, M. Giersig, E.R. Savinova, An approach to fabrication of metal nanoring arrays, *Langmuir*, 26 (2010) 3549-3554.
- [131] F. Yan, W.A. Goedel, The preparation of mesoscopic rings in colloidal crystal templates, *Angewandte Chemie International Edition*, 44 (2005) 2084-2088.
- [132] F. Yan, W.A. Goedel, Preparation of mesoscopic gold rings using particle imprinted templates, *Nano Letters*, 4 (2004) 1193-1196.

- [133] A. Kumar, G.M. Whitesides, Features of gold having micrometer to centimeter dimensions can be formed through a combination of stamping with an elastomeric stamp and an alkanethiol “ink” followed by chemical etching, *Applied physics letters*, 63 (1993) 2002-2004.
- [134] S. Qiu, J. Ji, W. Sun, J. Pei, J. He, Y. Li, J.J. Li, G. Wang, Recent Advances in Surface Manipulation Using Micro-contact Printing for Biomedical Applications, *Smart Materials in Medicine*, (2021).
- [135] J.-C. Cau, L. Ludovic, N. Marie, L. Adriana, P. Vincent, Magnetic field assisted microcontact printing: A new concept of fully automated and calibrated process, *Microelectronic engineering*, 110 (2013) 207-214.
- [136] H.O. Jacobs, G.M. Whitesides, Submicrometer patterning of charge in thin-film electrets, *Science*, 291 (2001) 1763-1766.
- [137] H.W. Kang, J. Leem, S.H. Ko, S.Y. Yoon, H.J. Sung, Vacuum-assisted microcontact printing (μ CP) for aligned patterning of nano and biochemical materials, *Journal of Materials Chemistry C*, 1 (2013) 268-274.
- [138] R.S. Moirangthem, Magnetic force assisted thermal nanoimprint lithography (MF-TNIL) for cost-effective fabrication of 2D nanosquare array, *Nano Express*, 1 (2020) 010039.
- [139] V. Santhanam, R.P. Andres, Microcontact printing of uniform nanoparticle arrays, *Nano Letters*, 4 (2004) 41-44.
- [140] X.Y. Ling, I.Y. Phang, D.N. Reinhoudt, G.J. Vancso, J. Huskens, Transfer-Printing and Host– Guest Properties of 3D Supramolecular Particle Structures, *ACS applied materials & interfaces*, 1 (2009) 960-968.
- [141] T. Kraus, L. Malaquin, H. Schmid, W. Riess, N.D. Spencer, H. Wolf, Nanoparticle printing with single-particle resolution, *Nature nanotechnology*, 2 (2007) 570-576.
- [142] J. Yao, X. Yan, G. Lu, K. Zhang, X. Chen, L. Jiang, B. Yang, Patterning colloidal crystals by lift-up soft lithography, *Advanced Materials*, 16 (2004) 81-84.
- [143] D. Deganello, J. Cherry, D. Gethin, T. Claypole, Patterning of micro-scale conductive networks using reel-to-reel flexographic printing, *Thin Solid Films*, 518 (2010) 6113-6116.
- [144] S. Kim, H. Sojoudi, H. Zhao, D. Mariappan, G.H. McKinley, K.K. Gleason, A.J. Hart, Ultrathin high-resolution flexographic printing using nanoporous stamps, *Science Advances*, American Association for the Advancement of Science, 2016, pp. e1601660-e1601660.
- [145] J. Benson, C.M. Fung, J.S. Lloyd, D. Deganello, N.A. Smith, K.S. Teng, Direct patterning of gold nanoparticles using flexographic printing for biosensing applications, *Nanoscale research letters*, 10 (2015) 1-8.
- [146] D. Qin, Y. Xia, G.M. Whitesides, Soft lithography for micro-and nanoscale patterning, *Nature protocols*, 5 (2010) 491.
- [147] M. Runge, H. Hübner, A. Grimm, G. Manoharan, R. Wiczorek, M. Philippi, W. Harneit, C. Meyer, D. Enke, M. Gallei, Capillary stamping of functional materials: parallel additive substrate patterning without ink depletion, *Advanced Materials Interfaces*, 8 (2021) 2001911.
- [148] H. Xu, X.Y. Ling, J. van Bennekom, X. Duan, M.J. Ludden, D.N. Reinhoudt, M. Wessling, R.G. Lammertink, J. Huskens, Microcontact printing of dendrimers, proteins, and nanoparticles by porous stamps, *J. Am. Chem. Soc.*, 131 (2009) 797-803.
- [149] M. Philippi, C. You, C.P. Richter, M. Schmidt, J. Thien, D. Liße, J. Wollschläger, J. Piehler, M. Steinhart, Close-packed silane nanodot arrays by capillary nanostamping coupled with heterocyclic silane ring opening, *RSC advances*, 9 (2019) 24742-24750.
- [150] P. Hou, R. Kumar, B. Oberleiter, R. Kohns, D. Enke, U. Beginn, H. Fuchs, M. Hirtz, M. Steinhart, Scanner-Based Capillary Stamping, *Advanced Functional Materials*, 30 (2020) 2001531.

- [151] S.Y. Chou, P.R. Krauss, P.J. Renstrom, Nanoimprint lithography, *Journal of Vacuum Science & Technology B: Microelectronics and Nanometer Structures Processing, Measurement, and Phenomena*, 14 (1996) 4129-4133.
- [152] R. Ganesan, J. Dumond, M.S. Saifullah, S.H. Lim, H. Hussain, H.Y. Low, Direct patterning of TiO₂ using step-and-flash imprint lithography, *ACS nano*, 6 (2012) 1494-1502.
- [153] L.M. Cox, A.M. Martinez, A.K. Blevins, N. Sowan, Y. Ding, C.N. Bowman, Nanoimprint lithography: Emergent materials and methods of actuation, *Nano Today*, 31 (2020) 100838.
- [154] J. Man, H. Yang, Y. Wang, H. Chen, F. Xiong, Study on controllable surface morphology of the micro-pattern fabricated on metallic foil by laser shock imprinting, *Optics & Laser Technology*, 119 (2019) 105669.
- [155] M. Mühlberger, I. Bergmair, A. Klukowska, A. Kolander, H. Leichtfried, E. Platzgummer, H. Loeschner, C. Ebm, G. Grützner, R. Schöftner, UV-NIL with working stamps made from Ormostamp, *Microelectronic Engineering*, 86 (2009) 691-693.
- [156] K.H. Hsu, P.L. Schultz, P.M. Ferreira, N.X. Fang, Electrochemical nanoimprinting with solid-state superionic stamps, *Nano Letters*, 7 (2007) 446-451.
- [157] Y.J. Weng, S.Y. Yang, Applying magnetic soft mold imprint technology with ultraviolet light-emitting-diode array on the fabrication of microlens arrays, *Polymers for Advanced Technologies*, 22 (2011) 748-752.
- [158] G. Greczynski, L. Hultman, C 1s peak of adventitious carbon aligns to the vacuum level: dire consequences for material's bonding assignment by photoelectron spectroscopy, *ChemPhysChem*, 18 (2017) 1507.
- [159] M. Schmidt, M. Philippi, M. Münzner, J.M. Stangl, R. Wiczorek, W. Harnleit, K. Müller-Buschbaum, D. Enke, M. Steinhart, Capillary Nanostamping with Spongy Mesoporous Silica Stamps, *Advanced Functional Materials*, John Wiley & Sons, Ltd, 2018, pp. 1800700.
- [160] L. Papula, *Mathematische Formelsammlung*, Springer2017.
- [161] P. Hou, M. Steinhart, Immobilization of Water Drops on Hydrophobic Surfaces by Contact Line Pinning at Nonlithographically Generated Polymer Microfiber Rings, *Advanced Materials Interfaces*, Wiley-VCH Verlag, 2018, pp. 1801191.
- [162] J. Wang, H. Li, H. Li, C. Zuo, H. Wang, Thermal stability and optimal photoinduced hydrophilicity of mesoporous TiO₂ thin films, *Journal of Physical Chemistry C*, 2012, pp. 9517-9525.
- [163] H. Li, J. Wang, H. Li, S. Yin, T. Sato, High thermal stability thick wall mesoporous titania thin films, *Materials Letters*, North-Holland, 2009, pp. 1583-1585.
- [164] B. Bonelli, S. Esposito, F.S. Freyria, Mesoporous Titania: Synthesis, Properties and Comparison with Non-Porous Titania, *Titanium Dioxide*, InTech, 2017.
- [165] K. Liu, H. Fu, K. Shi, B. Xin, L. Jing, W. Zhou, Hydrophilicity and formation mechanism of large-pore mesoporous TiO₂ thin films with tunable pore diameters, *Nanotechnology*, 2006, pp. 3641-3648.
- [166] P. Ma, Z. Xu, M. Wang, L. Lu, M. Yin, X. Chen, D. Li, W. Ren, Fast fabrication of TiO₂ hard stamps for nanoimprint lithography, *Materials Research Bulletin*, Pergamon, 2017, pp. 253-259.
- [167] Y. Kameya, H. Yabe, Optical and superhydrophilic characteristics of TiO₂ coating with subwavelength surface structure consisting of spherical nanoparticle aggregates, *Coatings*, MDPI AG, 2019, pp. 547.
- [168] P. Hou, R. Kumar, B. Oberleiter, R. Kohns, D. Enke, U. Beginn, H. Fuchs, M. Hirtz, M. Steinhart, Scanner-Based Capillary Stamping, *Advanced Functional Materials*, Wiley-VCH Verlag, 2020.

- [169] A. Eichler-Volf, L. Xue, A. Kovalev, E.V. Gorb, S.N. Gorb, M. Steinhart, Nanoporous monolithic microsphere arrays have anti-adhesive properties independent of humidity, *Materials*, 2016, pp. 1-12.
- [170] Z. Xu, M. Yin, J. Sun, G. Ding, L. Lu, P. Chang, X. Chen, D. Li, 3D periodic multiscale TiO₂ architecture: a platform decorated with graphene quantum dots for enhanced photoelectrochemical water splitting, *Nanotechnology*, 27 (2016) 115401.
- [171] X. Yang, Y. Tu, L. Li, S. Shang, X.-m. Tao, Well-dispersed chitosan/graphene oxide nanocomposites, *ACS applied materials & interfaces*, 2 (2010) 1707-1713.
- [172] M. Abd Elmoula, E. Panaitescu, M. Phan, D. Yin, C. Richter, L.H. Lewis, L. Menon, Controlled attachment of gold nanoparticles on ordered titania nanotube arrays, *Journal of Materials Chemistry*, 19 (2009) 4483-4487.
- [173] Y.K. Mishra, S. Kaps, A. Schuchardt, I. Paulowicz, X. Jin, D. Gedamu, S. Freitag, M. Claus, S. Wille, A. Kovalev, Fabrication of macroscopically flexible and highly porous 3D semiconductor networks from interpenetrating nanostructures by a simple flame transport approach, *Particle & Particle Systems Characterization*, 30 (2013) 775-783.
- [174] Y.K. Mishra, G. Modi, V. Cretu, V. Postica, O. Lupan, T. Reimer, I. Paulowicz, V. Hrkac, W. Benecke, L. Kienle, Direct growth of freestanding ZnO tetrapod networks for multifunctional applications in photocatalysis, UV photodetection, and gas sensing, *ACS applied materials & interfaces*, 7 (2015) 14303-14316.
- [175] M. Thommes, K. Kaneko, A.V. Neimark, J.P. Olivier, F. Rodriguez-Reinoso, J. Rouquerol, K.S.W. Sing, Physisorption of gases, with special reference to the evaluation of surface area and pore size distribution (IUPAC Technical Report), *Pure and Applied Chemistry*, Walter de Gruyter GmbH, 2015, pp. 1051-1069.
- [176] L.X. Du, Z.T. Jiang, R. Li, Preparation of porous titania microspheres for HPLC packing by sol-gel method, *Materials Letters*, 2013, pp. 17-20.
- [177] S.K. Das, S. Darmakolla, A.J. Bhattacharyya, High lithium storage in micrometre sized mesoporous spherical self-assembly of anatase titania nanospheres and carbon, *Journal of Materials Chemistry*, Royal Society of Chemistry, 2010, pp. 1600.
- [178] F.-J. Haug, P. Schwaller, J. Wloka, J. Patscheider, A. Karimi, M. Tobler, Stoichiometry dependence of hardness, elastic properties, and oxidation resistance in TiN/SiN_x nanocomposites deposited by a hybrid process, *Journal of Vacuum Science & Technology A: Vacuum, Surfaces, and Films*, American Vacuum Society, 2004, pp. 1229-1234.
- [179] P. Michaels, M.T. Alam, S. Ciampi, W. Rouesnel, S.G. Parker, M.H. Choudhury, J.J. Gooding, A robust DNA interface on a silicon electrode, *Chemical Communications*, The Royal Society of Chemistry, 2014, pp. 7878-7880.
- [180] R. Purbia, R. Borah, S. Paria, Carbon-Doped Mesoporous Anatase TiO₂ Multi-Tubes Nanostructures for Highly Improved Visible Light Photocatalytic Activity, *Inorganic Chemistry*, American Chemical Society, 2017, pp. 10107-10116.
- [181] Z. He, M. Liu, L. Liu, G. Tong, W. Wu, X. Wang, Distinct plasmon resonance enhanced microwave absorption of strawberry-like Co/C/Fe/C core-shell hierarchical flowers: Via engineering the diameter and interparticle spacing of Fe/C nanoparticles, *RSC Advances*, Royal Society of Chemistry, 2019, pp. 22644-22655.
- [182] P.M. Dietrich, N. Graf, T. Gross, A. Lippitz, S. Krakert, B. Schupbach, A. Terfort, W.E.S. Unger, Amine species on self-assembled monolayers of omega-aminothiolates on gold as identified by XPS and NEXAFS spectroscopy, *Surf Interface Anal*, 42 (2010) 1184-1187.
- [183] R.A. Shircliff, P. Stradins, H. Moutinho, J. Fennell, M.L. Ghirardi, S.W. Cowley, H.M. Branz, I.T. Martin, Angle-resolved XPS analysis and characterization of monolayer and multilayer silane films for DNA coupling to silica, *Langmuir*, American Chemical Society, 2013, pp. 4057-4067.

- [184] J.S. Stevens, A.C. De Luca, M. Pelendritis, G. Terenghi, S. Downes, S.L.M. Schroeder, Quantitative analysis of complex amino acids and RGD peptides by X-ray photoelectron spectroscopy (XPS), *Surf Interface Anal*, John Wiley & Sons, Ltd, 2013, pp. 1238-1246.
- [185] K. Khadka, N.C. Strandwitz, G.S. Ferguson, Byproduct-Free Route to Aminosiloxane Monolayers on Silicon/Silicon Dioxide, *Langmuir*, American Chemical Society, 2017, pp. 1639-1645.
- [186] G. Greczynski, L. Hultman, C 1s Peak of Adventitious Carbon Aligns to the Vacuum Level: Dire Consequences for Material's Bonding Assignment by Photoelectron Spectroscopy, *ChemPhysChem*, Wiley-VCH Verlag, 2017, pp. 1507-1512.
- [187] J.B. Yoo, H.J. Yoo, H.J. Jung, H.S. Kim, S. Bang, J. Choi, H. Suh, J.H. Lee, J.G. Kim, N.H. Hur, Titanium oxynitride microspheres with the rock-salt structure for use as visible-light photocatalysts, *Journal of Materials Chemistry A*, Royal Society of Chemistry, 2016, pp. 869-876.
- [188] L. Tao, S. Ramachandran, C.T. Nelson, M. Lin, L.J. Overzet, M. Goeckner, G. Lee, C.G. Willson, W. Wu, W. Hu, Durable diamond-like carbon templates for UV nanoimprint lithography, *Nanotechnology*, 2008.
- [189] J. Cech, R. Taboryski, Stability of FDTS monolayer coating on aluminum injection molding tools, *Applied Surface Science*, Elsevier B.V., 2012, pp. 538-541.
- [190] M. Li, X. Huang, W. Luo, Y. Chen, F. Han, X. Cheng, Thermal degradation behavior of self-assembled monolayer surfactant on silicon substrate, *Journal of Vacuum Science & Technology B*, American Vacuum Society, 2020, pp. 032602.
- [191] X. Liu, Y. Bai, J. Xu, Q. Xu, L. Xiao, L. Sun, J. Weng, Y. Zhao, Robust Amphiphobic Few-Layer Black Phosphorus Nanosheet with Improved Stability, *Advanced Science*, John Wiley and Sons Inc., 2019, pp. 1901991.
- [192] J.-P. Sylvestre, A.V. Kabashin, E. Sacher, M. Meunier, J.H.T. Luong, Nanoparticle size reduction during laser ablation in aqueous solutions of cyclodextrins, in: P.R. Herman, J. Fieret, A. Pique, T. Okada, F.G. Bachmann, W. Hoving, K. Washio, X. Xu, J.J. Dubowski, D.B. Geohegan, F. Traeger (Eds.) *Photon Processing in Microelectronics and Photonics III*, SPIE, 2004, pp. 84.
- [193] S.D. Techane, L.J. Gamble, D.G. Castner, X-ray photoelectron spectroscopy characterization of gold nanoparticles functionalized with amine-terminated alkanethiols, *Biointerphases*, American Vacuum Society, 2011, pp. 98-104.
- [194] L. Qie, W. Chen, X. Xiong, C. Hu, F. Zou, P. Hu, Y. Huang, Sulfur-Doped Carbon with Enlarged Interlayer Distance as a High-Performance Anode Material for Sodium-Ion Batteries, *Advanced Science*, Wiley, 2015.
- [195] R.M. Petoral, K. Wermelin, E. Dahlstedt, J. Hellberg, K. Uvdal, Adsorption of n-butyl-substituted tetrathiafulvalene dodecanethiol on gold, *Journal of Colloid and Interface Science*, Academic Press, 2005, pp. 388-393.
- [196] Y.W. Yang, L.J. Fan, High resolution XPS study of decanethiol on Au(111): Single sulfur-gold bonding interaction, *Langmuir*, American Chemical Society, 2002, pp. 1157-1164.
- [197] M.-C. Bourg, A. Badia, R.B. Lennox, Gold-Sulfur Bonding in 2D and 3D Self-Assembled Monolayers: XPS Characterization, *The Journal of Physical Chemistry B*, American Chemical Society, 2000, pp. 6562-6567.
- [198] D.G. Castner, K. Hinds, D.W. Grainger, X-ray photoelectron spectroscopy sulfur 2p study of organic thiol and bisulfide binding interactions with gold surfaces, *Langmuir*, American Chemical Society, 1996, pp. 5083-5086.
- [199] M. Philippi, C. You, C.P. Richter, M. Schmidt, J. Thien, D. Liße, J. Wollschläger, J. Piehler, M. Steinhart, Close-packed silane nanodot arrays by capillary nanostamping coupled with heterocyclic silane ring opening, *RSC Advances*, Royal Society of Chemistry, 2019, pp. 24742-24750.

- [200] I. Dziegielewski, J.L. Weyher, W. Dzwolak, On the hydrophobicity of modified Ga-polar GaN surfaces, *Applied Physics Letters*, American Institute of Physics AIP, 2013, pp. 043704.
- [201] C. Cao, F. Wang, M. Lu, Superhydrophobic CuO coating fabricated on cotton fabric for oil/water separation and photocatalytic degradation, *Colloids and Surfaces A: Physicochemical and Engineering Aspects*, Elsevier B.V., 2020, pp. 125033.
- [202] N. Yokoi, K. Manabe, M. Tenjimayashi, S. Shiratori, Optically transparent superhydrophobic surfaces with enhanced mechanical abrasion resistance enabled by mesh structure, *ACS Applied Materials and Interfaces*, American Chemical Society, 2015, pp. 4809-4816.
- [203] H.K. Park, S.W. Yoon, Y.R. Do, Superhydrophobicity of 2D SiO₂ hierarchical micro/nanorod structures fabricated using a two-step micro/nanosphere lithography, *Journal of Materials Chemistry*, Royal Society of Chemistry, 2012, pp. 14035-14041.
- [204] H. Reddy, U. Guler, A.V. Kildishev, A. Boltasseva, V.M. Shalaev, Temperature-dependent optical properties of gold thin films, *Optical Materials Express*, The Optical Society, 2016, pp. 2776.
- [205] W. Han, E. Stepula, M. Philippi, S. Schlücker, M. Steinhart, Evaluation of 3D gold nanodendrite layers obtained by templated galvanic displacement reactions for SERS sensing and heterogeneous catalysis, *Nanoscale*, Royal Society of Chemistry, 2018, pp. 20671-20680.
- [206] K.A. Baldwin, D.J. Fairhurst, Classifying dynamic contact line modes in drying drops, *Soft Matter*, Royal Society of Chemistry, 2015, pp. 1628-1633.
- [207] M.W. Yang, S.Y. Lin, A method for correcting the contact angle from the theta/2 method, *Colloids Surf. A: Physicochem. Eng. Asp.*, 220 (2003) 199-210.
- [208] E. Pensa, E. Cortés, G. Corthey, P. Carro, C. Vericat, M.H. Fonticelli, G. Benítez, A.A. Rubert, R.C. Salvarezza, The chemistry of the sulfur-gold interface: in search of a unified model, *Accounts of chemical research*, 45 (2012) 1183-1192.
- [209] M. Lazghab, K. Saleh, P. Guigon, Functionalisation of porous silica powders in a fluidised-bed reactor with glycidoxypropyltrimethoxysilane (GPTMS) and aminopropyltriethoxysilane (APTES), *Chemical Engineering Research and Design*, 88 (2010) 686-692.
- [210] H. Wang, P. Bai, J. Xie, B. Liu, C. Wang, J. Xu, X. Wang, Enhancement of sensitivity of silica photonic crystals to carbon dioxide by APTES modification, *Optical Materials*, 113 (2021) 110816.
- [211] S. Issa, F. Cousin, M. Bonnevide, D. Gigmes, J. Jestin, T.T. Phan, Poly (ethylene oxide) grafted silica nanoparticles: efficient routes of synthesis with associated colloidal stability, *Soft Matter*, (2021).
- [212] V. Colvin, A. Goldstein, A. Alivisatos, Semiconductor nanocrystals covalently bound to metal surfaces with self-assembled monolayers, *J. Am. Chem. Soc.*, 114 (1992) 5221-5230.
- [213] V. Srinivasan, E. Stiefel, A. Elsberry, R. Walton, X-ray photoelectron spectra of inorganic molecules. 21. Sulfur 2p chemical shifts associated with the binding of thiol and thioether groups of transition metal ions, *J. Am. Chem. Soc.*, 101 (1979) 2611-2614.
- [214] D.G. Castner, K. Hinds, D.W. Grainger, X-ray photoelectron spectroscopy sulfur 2p study of organic thiol and disulfide binding interactions with gold surfaces, *Langmuir*, 12 (1996) 5083-5086.
- [215] Y.-T. Li, Y.-Y. Yang, Y.-X. Sun, Y. Cao, Y.-S. Huang, S. Han, Electrochemical fabrication of reduced MoS₂-based portable molecular imprinting nanoprobe for selective SERS determination of theophylline, *Microchimica Acta*, 187 (2020) 1-11.
- [216] T.G. Avval, C.V. Cushman, S. Bahr, P. Dietrich, M. Meyer, A. Thißen, M.R. Linford, Dimethyl sulfoxide by near-ambient pressure XPS, *Surface Science Spectra*, 26 (2019) 014020.
- [217] B. Ballarin, D. Barreca, E. Boanini, E. Bonansegna, M.C. Cassani, G. Carraro, S. Fazzini, A. Mignani, D. Nanni, D. Pinelli, Functionalization of silica through thiol-yne radical

chemistry: a catalytic system based on gold nanoparticles supported on amino-sulfide-branched silica, *RSC advances*, 6 (2016) 25780-25788.

[218] X. Zheng, Q. Wang, W. Du, Effects of Imprinting Pressure on the Damage of Flexible Composite Mould and Pattern Quality during UV Nanoimprinting, *Micromachines*, 10 (2019) 706.

[219] M. Abolhassani, C.S. Griggs, L.A. Gurtowski, J.A. Mattei-Sosa, M. Nevins, V.F. Medina, T.A. Morgan, L.F. Greenlee, Scalable chitosan-graphene oxide membranes: the effect of GO size on properties and cross-flow filtration performance, *ACS omega*, 2 (2017) 8751-8759.

[220] D. Ho, J. Zou, B. Zdyrko, K.S. Iyer, I. Luzinov, Capillary force lithography: the versatility of this facile approach in developing nanoscale applications, *Nanoscale*, 7 (2015) 401-414.

[221] V.V. Mody, A. Singh, B. Wesley, Basics of magnetic nanoparticles for their application in the field of magnetic fluid hyperthermia, *European Journal of Nanomedicine*, 5 (2013) 11-21.

[222] A. Hajalilou, L. Ferreira, M.M. Jorge, C. Reis, M. Cruz, Superparamagnetic Ag-Fe₃O₄ composites nanoparticles for magnetic fluid hyperthermia, *Journal of Magnetism and Magnetic Materials*, 537 (2021) 168242.

[223] A. Ramzannezhad, A. Bahari, A. Hayati, H. Najafi-Ashtiani, Magnetic nanobiosensors in detecting Microalbuminuria (MAU), using Fe₃O₄ nanorods synthesized via microwave-assisted method, *Materials Science and Engineering: B*, 268 (2021) 115123.

[224] S. Yildiz, K. Solak, M. Acar, A. Mavi, Y. Unver, Magnetic Nanoparticles Mediated-Gene Delivery for Simpler and More Effective Transformation of *Pichia pastoris*, *Nanoscale Advances*, (2021).

[225] H. Rong, T. Gao, Y. Zheng, L. Li, D. Xu, X. Zhang, Y. Hou, M. Yan, Fe₃O₄@ silica nanoparticles for reliable identification and magnetic separation of *Listeria monocytogenes* based on molecular-scale physiochemical interactions, *Journal of Materials Science & Technology*, 84 (2021) 116-123.

[226] Y. Gu, G. Valentino, E. Mongeau, Ferrofluid-based reconfigurable optofluidic switches for integrated sensing and digital data storage, *Applied optics*, 53 (2014) 537-543.

[227] M. Kole, S. Khandekar, Engineering applications of ferrofluids: A review, *Journal of Magnetism and Magnetic Materials*, (2021) 168222.

[228] X.-F. Guan, D. Chen, Z.-Y. Quan, F.-X. Jiang, C.-H. Deng, G.A. Gehring, X.-H. Xu, Morphology and magnetic properties of Fe₃O₄ nanodot arrays using template-assisted epitaxial growth, *Nanoscale research letters*, 10 (2015) 1-6.

[229] M. Jadav, R. Patel, R. Mehta, Influence of magnetic field on evaporation of a ferrofluid droplet, *Journal of Applied Physics*, 122 (2017) 145302.

[230] D. Balaev, S. Semenov, A. Dubrovskiy, S. Yakushkin, V. Kirillov, O. Martyanov, Superparamagnetic blocking of an ensemble of magnetite nanoparticles upon interparticle interactions, *Journal of Magnetism and Magnetic Materials*, 440 (2017) 199-202.

[231] F. Arteaga-Cardona, N.G. Martha-Aguilar, J.O. Estevez, U. Pal, M.Á. Méndez-Rojas, U. Salazar-Kuri, Variations in magnetic properties caused by size dispersion and particle aggregation on CoFe₂O₄, *SN Applied Sciences*, 1 (2019) 412.

[232] X. Wang, H. Gu, Z. Yang, The heating effect of magnetic fluids in an alternating magnetic field, *Journal of magnetism and magnetic materials*, 293 (2005) 334-340.

[233] M. Latikka, M. Backholm, J.V. Timonen, R.H. Ras, Wetting of ferrofluids: Phenomena and control, *Current Opinion in Colloid & Interface Science*, 36 (2018) 118-129.

[234] V. Franco, B. Dodrill, *Magnetic Measurement Techniques for Materials Characterization*, Springer, 2021.

- [235] A. Fletcher, J. Downs, W. Frost, D. Clarke, K. O'Grady, A. Hirohata, Magnetic braille using ferrofluids, *Journal of Physics D: Applied Physics*, 54 (2021) 215001.
- [236] M. Xu, C.R. Bahl, C. Frandsen, S. Mørup, Interparticle interactions in agglomerates of α -Fe₂O₃ nanoparticles: influence of grinding, *Journal of colloid and interface science*, 279 (2004) 132-136.
- [237] J.B. Tracy, T.M. Crawford, Magnetic field-directed self-assembly of magnetic nanoparticles, *MRS bulletin*, 38 (2013) 915-920.
- [238] B. Ma, C. Xu, J. Chi, J. Chen, C. Zhao, H. Liu, A versatile approach for direct patterning of liquid metal using magnetic field, *Advanced Functional Materials*, 29 (2019) 1901370.
- [239] J. Hajduová, M. Uchman, I. Šafařík, M. Šafaříková, M. Šlouf, S. Pispas, M. Štěpánek, Aggregation of superparamagnetic iron oxide nanoparticles in dilute aqueous dispersions: Effect of coating by double-hydrophilic block polyelectrolyte, *Colloids and Surfaces A: Physicochemical and Engineering Aspects*, 483 (2015) 1-7.
- [240] R.S. Rikken, R.J. Nolte, J.C. Maan, J.C. van Hest, D.A. Wilson, P.C. Christianen, Manipulation of micro-and nanostructure motion with magnetic fields, *Soft matter*, 10 (2014) 1295-1308.
- [241] S. Oh, S.H. Jung, H. Seo, M.-K. Min, B. Kim, Y.K. Hahn, J.H. Kang, S. Choi, Magnetic activated cell sorting (MACS) pipette tip for immunomagnetic bacteria separation, *Sensors and Actuators B: Chemical*, 272 (2018) 324-330.
- [242] W. Wang, J.V. Timonen, A. Carlson, D.-M. Drotlef, C.T. Zhang, S. Kolle, A. Grinthal, T.-S. Wong, B. Hatton, S.H. Kang, Multifunctional ferrofluid-infused surfaces with reconfigurable multiscale topography, *Nature*, 559 (2018) 77-82.
- [243] E.B. Joyee, A. Szmelter, D. Eddington, Y. Pan, Magnetic field-assisted stereolithography for productions of multimaterial hierarchical surface structures, *ACS Applied Materials & Interfaces*, 12 (2020) 42357-42368.
- [244] K.J. Terhune, L.B. King, B.D. Prince, N. Jain, B.S. Hawkett, The effects of magnetic surface stress on electro spray of an ionic liquid ferrofluid, 52nd AIAA/SAE/ASEE Joint Propulsion Conference, 2016, pp. 4549.
- [245] L. Huang, T. Hädrich, D.L. Michels, On the accurate large-scale simulation of ferrofluids, *ACM Transactions on Graphics (TOG)*, 38 (2019) 1-15.
- [246] N. Angrisani, F. Foth, M. Kietzmann, S. Schumacher, G.L. Angrisani, A. Christel, P. Behrens, J. Reifenrath, Increased accumulation of magnetic nanoparticles by magnetizable implant materials for the treatment of implant-associated complications, *Journal of nanobiotechnology*, 11 (2013) 1-10.
- [247] N. Nam-Trung, Micro-magnetofluidics: interactions between magnetism and fluid flow on the microscale, *Microfluid Nanofluid*, 12 (2012) 1-16.
- [248] S. Ge, A. Nemiroski, K.A. Mirica, C.R. Mace, J.W. Hennek, A.A. Kumar, G.M. Whitesides, Magnetic levitation in chemistry, materials science, and biochemistry, *Angewandte Chemie International Edition*, 59 (2020) 17810-17855.
- [249] https://en.wikipedia.org/wiki/Force_between_magnets#cite_note-tri-c-3.

10 Appendix

10.1 List of abbreviations

XPS	X-ray photoelectron spectroscopy
SEM	SEM
AFM	Atomic Force Microscopy
BET	Brunauer-Emmett-Teller
BJH	Barret, Joyner and Halenda
EDX	Energy-dispersive X-ray spectroscopy
NIL	Nanoimprint lithography
PS μ M	Phase separation micromolding
MA-IICN	Magnetic assisted insect-inspired capillary nanostamping
WCA	water contact angle
QCM	Quartz crystal microbalance
VSM	Vibrating-sample magnetometer
μ CP	Microcontact printing
J.P.s	Janus particles
J.M.s	Janus membranes
FDTS	1H,1H,2H,2H-Perfluorodecyltrichlorosilane
M_n	Average molecular mass by number
M_w	Average molecular mass by weight
PDMS	Polydimethylsiloxane
PS- <i>b</i> -P2VP	poly(styrene- <i>block</i> -2-vinyl pyridine)
PS- <i>b</i> -P4VP	Poly(styrene- <i>block</i> -4-vinyl pyridine)
EtOH	Ethanol
DMF	Dimethylformamide
HAuCl ₄ x H ₂ O	Hydrogen tetrachloroaurate (III) hydrate
KOH	Potassium hydroxide
NaOH	Sodium hydroxide

SiO ₂	Silica
TiO ₂	Titania
CS	Chitosan
GO-CS	Chitosan-graphene oxide
K ₂ Cr ₂ O ₇	Potassium dichromate
HCl	Hydrochloric acid
Fe ₃ O ₄	Magnetite
Au	Gold
Ti	Titanium
T-ZnO	Zinc oxide tetrapods
AcAc	Glacial acetic acid
APTES	3-Aminopropyl)triethoxysilane
e.g.	For example
RT	Room temperature
AR	Aspect ratio
FTO	Fluorine-doped tin oxide-coated glass
mSi	Macroporous silicon templates
TC	Tip like contact surfaces
HC	Holey contact surfaces

10.2 List of publications

Gazenbiller, Eugen, **Qaiser Ali Khan**, Beatriz Rico-Oller, Angelika Hackner, Thomas Meer, Theo Hack, Benedikt Langer *et al.* "Semiconducting properties of surface-treated titanium and their effect on peel resistance: Experimental and modelling studies." *International Journal of Adhesion and Adhesives* (2021): 103049.

Alarслан, Fatih, Laura Vittadello, Jonas Klein, **Qaiser Ali Khan**, Christian Kijatkin, Markus Haase, Helmut Schäfer, Mirco Imlau, and Martin Steinhart. "Thin patterned lithium niobate films by parallel additive capillary stamping of aqueous precursor solutions." *Advanced Engineering Materials* (2021): 2101159.

Eichler-Volf, Anna, Yara Alsaadawi, Fernando Vazquez Luna, **Qaiser Ali Khan**, Simon Stierle, Chi Xu, Michael Heigl *et al.* "Sensitivity of PS/CoPd Janus particles to an external magnetic field." *RSC Advances* 11, no. 28 (2021): 17051-17057.

Zahra, Qurat Ul Ain, **Qaiser Ali Khan**, and Zhaofeng Luo. "Advances in Optical Aptasensors for Early Detection and Diagnosis of Various Cancer Types." *Frontiers in Oncology* 11 (2021): 632165-632165.

Khan, Qaiser Ali, Ahmed Shaur, Tayyab Ali Khan, Yasir F. Joya, and M. S. Awan. "Characterization of reduced graphene oxide produced through a modified Hoffman method." *Cogent Chemistry* 3, no. 1 (2017): 1298980.

10.3 Curriculum vitae

Qaiser Ali KHAN

E-mail: qaiserali.k@hotmail.com

khan@uos.de

Date of birth: 02. April 1991

12/2017-12/2021

Scientific co-worker

Institute of Chemistry of new materials, Universität Osnabrück, Germany

Research topic: Substrate functionalization with functional particle patterns

Supervisor: Prof. Dr. Martin Steinhart

10/2014-09/2017

M.Sc. in Materials science and Engineering

Faculty of Engineering, Christian-Albrechts-Universität zu Kiel, Germany

Research topic: Electrochemical stability of pre-treated titanium surfaces for aeronautical applications

Supervisors: Prof. Dr. Mikhail Zheludkevich, Dr. rer. nat. Daniel Höche

10/2010-06/2014

B.Sc. in Materials Engineering

Department of Materials Science and Engineering, Ghulam Ishaq Khan Institute (GIKI), Pakistan

Research topic: Synthesis of graphene by combined chemical and thermal methods and characterizations

Supervisor: Dr. Yasir Faheem Joya

10.4 Declaration

I hereby declare that the presented thesis

“Substrate functionalization with functional particle patterns”

describes my own work unless otherwise acknowledged in the text. The thesis research was carried out at Institute für Chemie neuer Materialien, Fachbereich Biologie / Chemie, Universität Osnabrück, Germany, under the supervision of Prof. Dr. Martin Steinhart. All the sources are cited as a list of references. I further declare that this work has not been submitted to any other institution for an academic degree purpose.

Qaiser Ali Khan

January 2022, Osnabrück